A Study of InP-based Strained Layer Heterostructures.

A thesis by

Paul Nicholas Stavrinou

submitted to the University of London for the degree of Ph.D

Department of Electronic and Electrical Engineering
University College London

November 1994

to my mother and father,
and to jessica

Abstract

The small layer dimensions required in low dimensional structures, such as multiple quantum wells (MQW), allows constituent materials to be used which are lattice *mis*matched in bulk form. The primary aim of this thesis is the study of InP based electroabsorption devices which comprise lattice *mis*matched induced strained layer MQW material.

Experimental and theoretical investigations are undertaken into the band-edge electronic structure and associated optical properties of strained $InAs_xP_{1-x}$/ InP quantum wells. The devices are designed for application around 1.06 µm and, for the first time, demonstrate growth of this QW system by solid source molecular beam epitaxy. Modelling is also used to study the properties of three layer InP/ $InAs_xP_{1-x}$/ $In_zGa_{1-z}As$ QW's which are proposed for their internal staircase-like potential. The associated effective built-in field allows a blue shift of the fundamental absorption edge and offers improved device performance over the conventional red shifting MQW devices.

Theoretical descriptions of MQW subband states are based on the effective Hamiltonian model (**k.p**) which includes coupling between conduction and valence bands as well as the effects of biaxial strain. The approach is extensively discussed and alternative approximations for describing band-edge structure are assessed. To account for the presence of an electric field, a tunnelling resonance method using a **k.p** description is used to find the quasi-bound states of the structure. Excitonic properties are computed using variational techniques thereby giving the ability to simulate optical absorption spectra using phenomenological broadening of both the exciton line and the continuum. Excellent agreement is found with experiment.

Optical absorption spectroscopy and bias dependent photocurrent spectra from p-i(MQW)-n structures is presented along with supporting cross-section TEM and X-ray diffraction measurements. In the context of these results, limits to pseudomorphically strained growth and routes to strain relaxation are discussed. The latter is shown to be an important factor in determining the absorption characteristics of devices.

Contents

Chapter 1. **Introduction**

§1.1 Demand for Optical Technology.

The areas of telecommunications and computing have much to gain from optical technology (J.E Midwinter 1985). For example, the introduction of optical fibre has almost entirely displaced co-axial cable in the long distance terrestrial trunk telecommunications network (P Cochrane 1990). Coding (and decoding) of optical signals at either end of the fibre system, is obviously central to fibre optic communications. Electro-optic devices, such as optical modulators (and detectors), are often used, where the information from electronic data is coded onto (decoded from) an optical beam. As the complexity and performance of systems develop, the use of optical technology within the network itself has increasingly attracted more interest. Advanced electro-optic devices are seen to be promising components in self-routing optical systems and optical switching (see J.E Midwinter 1990 and references therein for further information). However, the role of optics technology is by no means limited to the long haul telecommunication networks.

A growing development of very large scale integration (VLSI) technology leads to ever increasing integrated circuit packing densities. In the face of increased functionality per unit area and larger operating speeds resulting from integration, improvements are often constrained by the problem of interfacing the chip within an overall system. Greater demands are placed on the number of chip input and output channels and their capacity in order to meet its increased information needs (see e.g. Dickinson and Prise 1990). A number of studies have been carried out which compare system requirements for interfacing with either electrical tracks or optical techniques. These suggest that in power terms, optical links are superior to electrical ones over distances longer than approximately 1mm at bit rates of 1 GHz (Feldman *et al* 1988, D.A.B Miller 1989). Therefore optimum architectures can be envisaged which exploit the high capacity interconnect capabilities of optics and the processing power of electronics. Such systems may consist of small electronic islands, performing processing tasks at very high speeds, interconnected by optical links formed from electro-optic modulators (see J.E Midwinter 1988 , Parry *et al* 1989). Another method of increasing the capacity of processing systems, in addition to operating at higher speeds, is to operate on information in parallel. Arrays comprising electro-optic devices are proving to be effective as digital photonic logic planes in experiments on parallel processing and switching systems (Tooley and Wakelin 1993).

From this brief discussion, it should be clear that electro-optic devices play an important role in many leading technologies. Semiconductor devices are promising candidates, and among other things, are applicable to opto-electronic integrated circuits (OEICs) in which optical and electronic devices are integrated onto one chip (see e.g. Parry *et al* 1989, D.A.B Miller 1989). An impressive range of electro-optic semiconductor devices are based on heterostructures, more specifically quantum well properties. The emphasis in this thesis is on the development of heterostructures rather than their integration or application. An introduction to heterostructures and their application now appears in most text books relating to semiconductor physics/electronics, in addition, publications specifically dedicated to heterostructures are now available (e.g. Weisbuch and Vinter 1991). Hence in the following sections, a brief description of heterostructures is given in relation to their electro-absorption properties. Following this in §1.3, key areas of quantum well technology are noted with an emphasis on electro-absorption devices. It is predominantly the latter device types in which the present work is concerned with.

§1.2 Introduction to Heterostructures.

Heterostructures such as multiple quantum wells (MQW) or superlattices (SL) physically comprise alternating layers of different semiconductor materials grown on a thick semiconductor substrate. For suitable constituent layer thickness, the modulation of electronic properties, i.e. band gap etc, along the growth direction results in quantum confinement effects. The distribution of electron states for the structure is strongly modified by the confinement and the heterostructure takes an asymmetric electronic form, quite different from that of a bulk semiconductor (see e.g. M Alterelli 1986). From an engineering point of view, a significant point is that the subsequent optical and electronic properties of such structures may be tailored through both the choice of constituent materials and the dimensions along the growth direction. In effect, producing artificial materials, i.e. the heterostructure as a whole, that may be used in existing semiconductor devices or form the basis of new devices (see various applications described in Weisbuch and Vinter 1991 and references therein).

The realization of heterostructures has been made possible by the remarkable achievements in the growth control of semiconductor material. Growth of heterostructures is typically by molecular beam epitaxy (MBE) or metal organic vapour deposition, although recently several hybrid techniques have been developed, e.g. gas source MBE (GSMBE) and chemical beam epitaxy (CBE). It is beyond the scope of this thesis to describe the various growth methods in detail and the reader is asked to consult the various reviews on the subject, e.g. for MBE (B.A Joyce 1985, A.C Gossard 1986) and for MOCVD (Stringfellow 1985); more recent reviews appear in Stradling and Klipstein (1990). An outline of the MBE technique is given in §5.2.1, including some growth details relating to structures investigated in Chapter 5.

§1.2.1 III-V semiconductors.

Experimental and theoretical investigations into III-V semiconductors have continued to increase over the past three decades, the later stages predominantly driven by the fabrication of opto-electronic devices. All the electronic and optical properties of semiconductors are described by the concept of band structure which in turn arises from the chemical and crystalline properties of the solid (see e.g. Bassani and Parravicini 1975, R.A Smith 1978). Alloying of binary III-V semiconductors, e.g. InAs and GaAs to produce $In_xGa_{1-x}As$, provides further band structure modifications and varies the energy band edge between the two binary III-V constituents.

The wealth of work, particularly on the electronic band structure of such materials, provides an excellent starting point to develop *artificial* materials through heterostructure design. Heterostructures formed from III-V materials demand a knowledge of the individual material properties in order to predict the resulting composite band structure. Electronic band structures are typically displayed as energy-wavevector diagrams covering the whole Brillouin zone, detailing the relationship between the energy, E, of the particle (electron or hole) and the corresponding wavevector for a particular crystal direction, i.e. E(**k**), (Bassani and Parravicini 1975, R.A Smith 1978). For E(**k**) dispersions close to the band edge, the concept of an effective mass for a particular band is conveniently used, i.e.

$$\frac{1}{m^*} = \frac{1}{\hbar^2}\frac{d^2E(\mathbf{k})}{d\mathbf{k}^2} \tag{1.1}$$

In the present work only the energy region very close to the band edge is important, i.e. at the centre (Γ-point) of the Brillouin zone. Consequently, the descriptions of the constituent layers may be reduced to this region (Chapter 3), which greatly simplifies calculations required for heterostructure modelling (Chapter 4).

§1.2.2 Bulk band line-ups.

An important issue in heterostructures is how the constituent materials line up at the *abrupt* interface, in relation to their band edges. For two bulk semiconductors, A and B, with band gaps E_g^A and E_g^B, such that $E_g^A > E_g^B$, at least two possible configurations of the structure ABA can be envisaged (below).

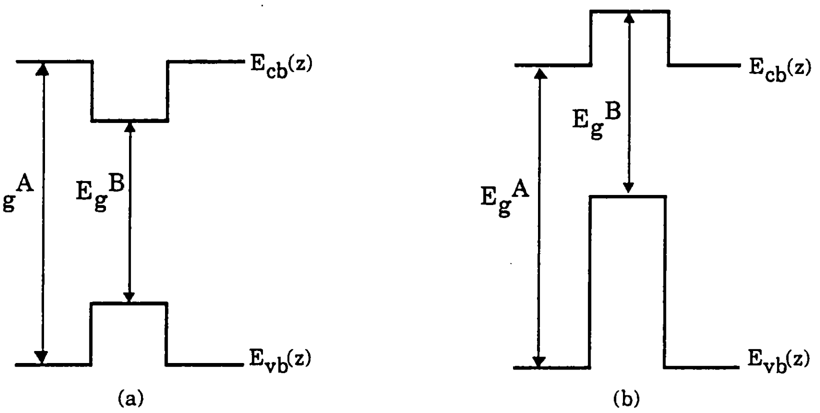

Figure 1-1. *The bulk band line-ups for (a) Type I and (b) Type II ABA heterostructure. (Growth is assumed along z)*

The large majority of heterostructures designed for electro-absorption devices rely on the type I line up, where the larger band gap material, e.g. $Al_xGa_{1-x}As$ (A), forms a potential barrier for both electrons and holes residing near the band edge of the B material (e.g. GaAs). In a type II configuration (Fig.1-1b), a potential barrier is due to the B layer in the conduction band, whereas in the valence band the potential barrier is due to the A layer. Heterostructure systems comprised of GaAs/InP are expected to show a type II line up (Gershoni *et al* 1988). The structures presented in Chapter 5 exhibit a type I line up, while the investigations in Chapter 6 describes a structure that uses both type I and type II line ups.

The precise determination of the band line-ups for a particular set of materials remains a difficult area. Experimental determination of band offsets is largely based on optical spectroscopy. The offset is generally determined by fitting the calculated excitonic transitions to those observed. However, for most symmetric quantum wells, the lower transition energies are relatively insensitive to the band offset which can lead to large uncertainties in the deduced values. Furthermore, the accuracy of the model used becomes an issue, particularly if higher order transitions are to be fitted. Recent work has demonstrated that by growth of the appropriate asymmetric heterostructures, the normally *forbidden* transitions become visible which can significantly improve the accuracy to which offsets can be measured or fitted to (Kopf *et al* 1992).

First principle calculations of the band offsets at semiconductor interfaces have been carried out, although the computational complexities of such calculations often restrict their use in investigating a wide range of material systems. Many of the common lattice-matched systems, and a few strained systems, have been investigated and typically demonstrate good qualitative agreement with experiment (a useful discussion of the various models is given by People and Jackson 1990).

In an attempt to obviate the computations required in self consistent type methods and yet still provide some indication of band line-ups, several *semi*-empirical methods have been developed. Probably the most widely used is the model-solid theory (MST) developed by Van de Walle and Martin (1987) which uses simple closed form expressions to predict band offsets in both lattice-matched and lattice-mismatched (strained) systems. [note: a clear demonstration of its use is given by People and Jackson 1990] Another straightforward model, uses a semi-empirical-tight-binding method (SETB) and a set of *universal* parameters optimized for the majority of III-V semiconductors (Anderson and Jones 1991). Both of these were used in the present work and found to predict reasonably well the distribution of the confinement potential inferred from experimental observations, i.e. for InAsP/InP the confinement potential is shared in favour of the conduction band, (cf. Chapter 5). However while both the MST and SETB methods are indeed useful, experimentally determined offset parameters are preferentially considered in this thesis.

§1.2.3 Properties of quantum wells.

A *conventional* quantum well (QW) is described by the type I configuration (e.g. GaAs/AlGaAs, InGaAs/InP). Introducing a coordinate representation, the growth (and hence confinement) direction is along the z direction, the dimensions of the layers perpendicular to z (i.e. x and y or $\parallel$) are several orders of magnitude larger and so confinement is along one dimension. The electrons and holes close to the band edge in the well material, are free to move in the plane of layer ($\parallel$) whereas their motion along (z) is strongly affected by the potential confinement. The effect of the confinement potential gives rise to a discrete set energies for which the electrons and holes are *bound* for motion along (z), (see figure below).

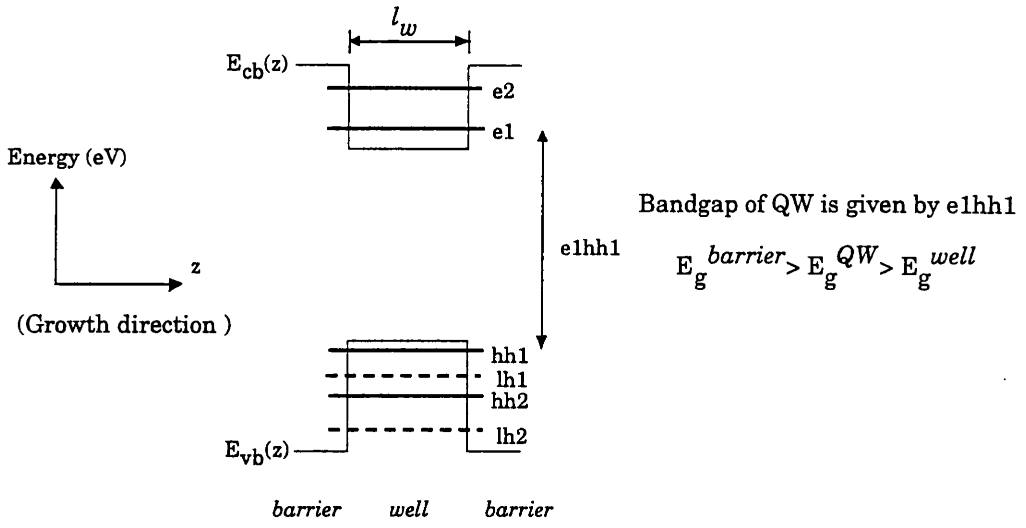

Figure 1-2. *A schematic showing the quantized states for a quantum well (type I).*

Since the allowed energies occur at finite k_z with respect to the well material, (i.e. not at the bulk band edge), distinct heavy- and light-hole states are found for the heterostructure valence band. [note: the valence band states are degenerate at **k**=0 but separate for $k_z>0$ due to the difference in effective mass, cf. (1.1), (see e.g. Schmitt-Rink *et al* 1989)].

For the simplest single particle picture, the $E(k_{||})$ dispersion (i.e. governing motion in the the plane of the QW) of each confined state is parabolic, $E \propto k_{||}^2$. In this case for each of the *sub*bands, the 2-D density of states is constant for energies larger than the confined state, with the confined state representing the bottom of the subband (see e.g. G. Bastard, 1988, chps.1,3). [note: this picture is not as accurate for hole states, since both the nature and close proximity of light and heavy holes induces strong mixing for $k_{||} \neq 0$, resulting in highly non-parabolic dispersions (see e.g. Bastard and Brum 1986)]. The joint or reduced density of states, (DOS), for transitions between particular electron and hole subbands follows a similar trend, and demonstrates a step-like structure with constant plateaus for each of the allowed e*n*h*n* transitions. Selection rules govern the strength of optical transitions between subbands, and are discussed in greater detail in §4.4.3. Essentially, the strength is proportional to the square of the e*n*-h*n* overlap integral in the direction perpendicular to the layers (z), (Fig.1-4). Typically in a symmetric QW, as in Fig.1-2, an approximate rule is that transitions occur between subbands providing $\Delta n=0$, such as e1hh1, e1lh1, e2hh2 etc.

The strong confinement of particles along one direction also has an important affect on the formation of exciton states between conduction and valence subbands (discussed in further detail in. §4.4). An exciton can be thought of as an orbiting electron-hole pair (e-h), bound together by a mutual Coulomb interaction. In bulk materials, this interaction manifests itself in the absorption spectrum near the band edge; excitonic peaks occur at energies slightly below the band gap by an amount representing the binding energy of the e-h pair. Similar reasoning applies to QW structures where exciton formation can be associated between each set of conduction and valence subbands. However, for well widths less than the bulk exciton diameter (~150Å for GaAs), the confinement of electron and hole states along (z) causes the exciton states to be more bound (ie. larger binding energy), leading to an enhancement of excitonic effects. (Schmitt-Rink *et al* 1989). The effect on the room temperature absorption spectrum is dramatic. For bulk samples the exciton peak is barely visible, whereas in QW structures clear excitonic peaks are observed before each corresponding subband plateau, particular in the case of e1hh1 transitions, (Fig.1-3).

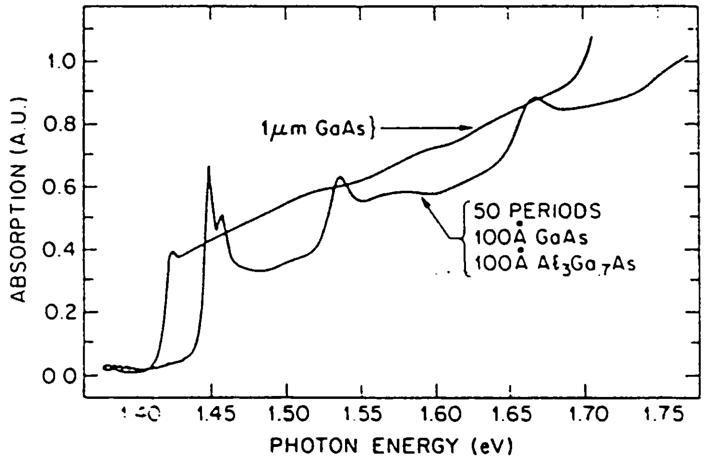

Figure.1-3. *Comparison of room temperature absorption spectra from a bulk GaAs sample and a GaAs/AlGaAs MQW sample. [after Schmitt-Rink et al 1989]*

A large range of devices exploiting room temperature quantum well optical properties rely on the consequences of electric fields applied perpendicular to the layers. The situation is illustrated in figure 1-4 including the resulting absorption spectrum near the band edge. As field is applied, the band edge exciton peaks, n=1hh and n=1lh, shift to lower energies and their peak height decreases. The overall description has been termed the quantum confined Stark effect (QCSE) following the intial investiagtions by Miller and co-workers (1984, 1985).

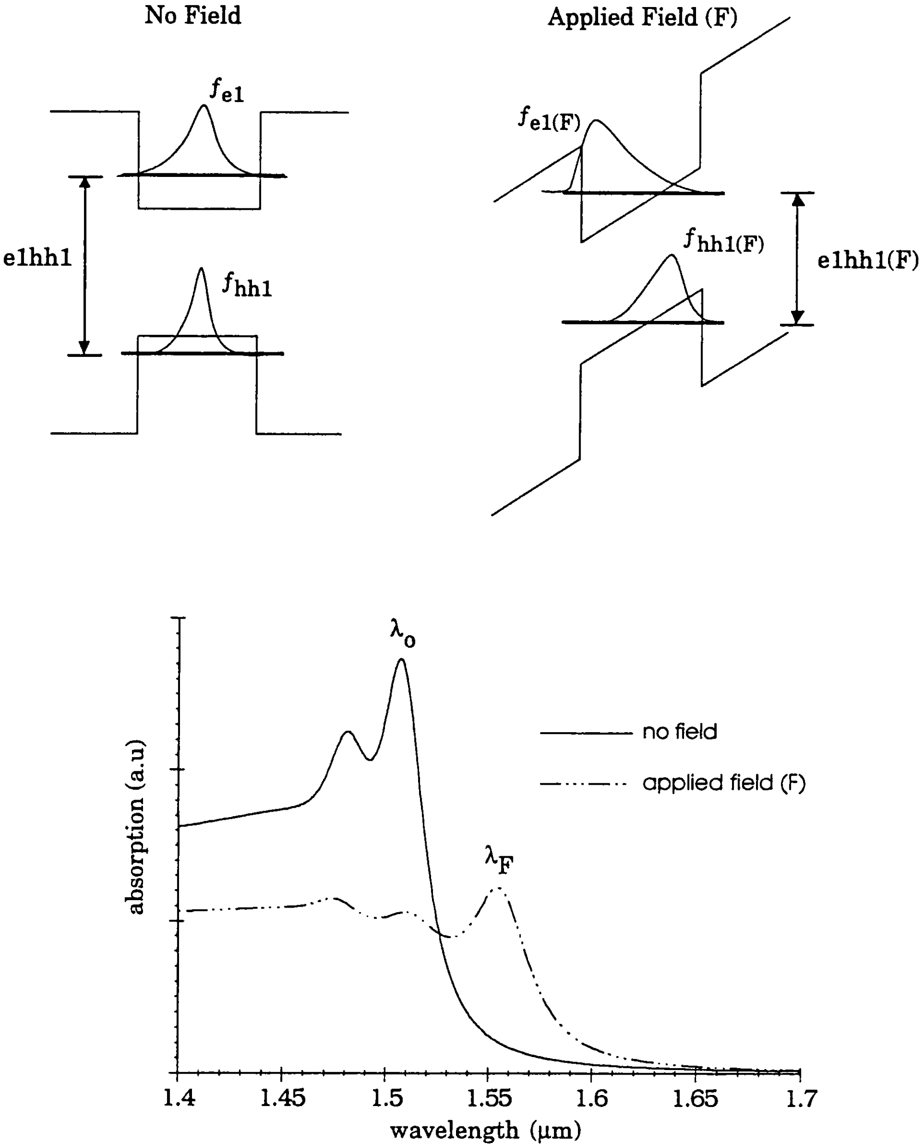

Figure. 1-4. *Illustrating the quantum confined Stark effect (QCSE). (upper plot) Schematic showing the effect of an applied field across a QW. The band gap of the QW reduces with field, i.e. elhhl>elhhl(F). In addition the localization of the carrier envelope functions (along z) are illustrated. (lower plot) Schematic of the band edge absorption with applied field (i.e. the QCSE). The red shift of the elhhl exciton transition,* λ_o *to* λ_F*, is largely due to the decrease in QW band gap.*

Calculations of the excitonic transition shift with field (i.e. λ_o to λ_F), show the dominant term is the energy shift of the associated subband, i.e. elhhl(F) in Fig.1-4 (Miller *et al* 1985, G. Bastard 1988), that is the reduction in binding energy of the e-h pair with field is small in comparison. However, the presence of the Coulomb attraction, albeit weaker, is important, since it maintains the exciton formation for large applied fields, e.g. up to ~10^5 kV/cm in typical GaAs/AlGaAs QWs (Miller *et al* 1984, 1985). The retention of exciton peaks with field is a result of the confinement along (z). As field is applied the carriers are pulled to the opposite interfaces within the well, the potential barriers somewhat hinder carrier escape, and since the well width is *less* than the bulk exciton diameter some degree of Coulomb interaction is maintained. This is in contrast with fields applied parallel to the layers (i.e. along $\parallel$), which demonstrates rapid ionization of the exciton, and subsequent broadening of the band edge, for much smaller applied fields ($<10^4$ kV/cm), qualitatively similar to bulk materials (Miller *et al* 1985).

The QCSE is a feature of quantum wells which underlies many of the devices based on heterostructures. It is particularly relevant for the present work, such that a description of the QCSE is a topic that is presented in subsequent chapters.

§1.3 Heterostructure Device Technology.

Many properties arising from heterostructures such as quantum wells have made a significant impact on device technology. This section highlights the principal areas with the emphasis on electro-absorption devices with which the present work is mainly concerned.

§1.3.1 Electronic devices.

High speed electronic devices are key elements in the development of electronic systems for data processing or analogue signal handling. Devices employing heterostructure technology may be divided into two classes, namely those involving transport of charge *along* the layer plane, and those utilizing *perpendicular* transport, i.e. perpendicular to the layers. The first class are essentially variations on the Field Effect Transistor (FET) principle (see e.g. Sze), with the transport defined along a channel. In one such structure, a heterojunction comprising n-doped $Al_xGa_{1-x}As$ and undoped GaAs results in electrons being transferred to the GaAs side at the interface, through equalizing the Fermi level (see e.g. Weisbuch and Vinter (1991), chp. 5). A potential well is formed at the heterojunction interface giving rise to a 2-D electron gas (2DEG) which acts as a conducting channel for the structure. Because of the spatial separation of the electrons (in the GaAs layer) and ionised donors (in the AlGaAs layer), impurity scattering is reduced which leads to higher electron mobilities in the channel. Structures of this type are known by several acronyms, the most commonly used are high electron mobility transistors (HEMT) or modulation doped FET (MODFET). Improvements and variations to the design, i.e. inclusion of buffer layers and additional heterojunctions, have developed these structures to the stage where both high speed performance and power requirements are better than traditional Si MOSFET and GaAs MESFET technologies (Solomon and Morkoç 1984). They are also noted for their low noise figure, which makes them particular attractive for use as amplifiers in receivers (see Weisbuch and Vinter 1991, §21).

In the case of vertical transport devices, the confinement properties of quantum wells are directly exploited in some devices. An actively studied device has been the resonant tunnelling diode (RTD), essentially comprising a isolated barrier/well/barrier structure (see e.g. Capasso *et al* 1986). A confined state in the well region enhances the *tunnelling* probability of electrons incident at that energy, this 'resonant tunnelling' leads to increased transport of electrons *across* the structure. An electric field applied across the structure increases the energy of the electrons through the structure. A peak in the I-V curve results at the resonant condition, in that at higher fields the current through the structure reduces. Such devices therefore exhibit negative differential resistance (NDR) which may be used (with external circuitry) as microwave oscillators (see e.g. Brown *et al* 1989). Other vertical transport devices such as heterojunction bipolar transistors (HBT) and various 'hot' electron structures have also benefited from the advent of heterojunction technology, including several variants utilizing NDR behaviour to increase functionality of the device characteristics (see Weisbuch and Vinter 1991, p164).

§1.3.2 Quantum well lasers.

One of the main impacts of heterostructures is in the area of semiconductor lasers, the general area is now well documented with several books covering the subject in some detail (see e.g. P.S Zory, Jr. 1993). The 2-D density of states in QW structures has provided significant achievements in QW laser diodes, over the bulk (3-D DOS) counterparts. Improvements include increased gain at low injection currents and an increase in the rate of change of gain with injection current. Typically, several QWs (MQW) will form the active region of the structure, which themselves can be enclosed in a larger potential well or graded region. With the larger band gap material enclosing the active region, the refractive index difference (higher in the lower band gap active region), can serve to provide optical confinement, (cf. separate confinement heterostructures (SCH) and variants described in §23 from Weisbuch and Vinter (1991). The injected carriers, which are mainly localised in the well region, radiatively recombine between the confined states, lasing therefore occurs at energies determined by the QW band edge. Through varying the well width the quantum well band edge may be tuned, and so provide some flexibility in the design lasing wavelength. While in principle this is true, practical laser structures are often of the distributed feedback type (DFB), employing a corrugated grating acting as a distributed Bragg reflector (DBR) which can define single wavelength operation and aid in sideband suppression (see review by Koch and Koren 1990). Overall the improvements going from 3-D to 2-D DOS in devices have already provided low power, low threshold semiconductor lasers (cf. a recent publication entirely devoted to QW lasers is edited by P.S Zory, Jr. 1993).

In recent years, a new laser configuration has been developed; namely the vertical cavity surface emitting laser (VCSEL). Quantum wells again form the active region which is placed within a cavity, typically defined by semiconductor Bragg stacks (see review by Jewell *et al* 1991). The geometry of the VCSEL allied with their low power usage allows arrays of such lasers to be fabricated giving rise to range of possible applications, e.g. optical interconnection of electronic islands.

The above, rather crude, outline is by no means representative of the overall area which combines many disciplines. Sophisticated device design, e.g. three stage DFB structures, VCSEL cavity modifications, along with advances in material physics, e.g. band structure engineering for the active region, continue to place QW lasers at the forefront of semiconductor technology. Although such lasers are now commercially available, the improvements in growth, availability of materials and design suggests the development of QW lasers will continue to be an active area of research. A statement suitably verified by the recent development of quantum cascade lasers (see report by E.P O'Reilly 1994 for further information and references).

§1.3.3 Electro-absorption devices.

Many device types utilize the resolution of enhanced excitonic absorption in quantum well structures. For applied electric fields, the Stark shift and persistence of the exciton peaks produce absorption changes at the band edge, $\Delta\alpha$, that are significantly larger than bulk counterparts, e.g. $\Delta\alpha\sim450$ cm^{-1} for bulk GaAs compared to $\Delta\alpha\sim5000$ cm^{-1} for GaAs/AlGaAs MQW structures (Jelley *et al* 1989). Devices such as electro-absorption modulators are obvious candidates to make use of the larger field induced absorption changes (see e.g. Wood *et al* 1984). For example, intensity modulation of an incident optical beam can be best achieved if the beam has a wavelength λ_0 or λ_F (cf. Fig.1-4). The modulating signal can then be *written* onto the beam intensity by a pulse train of applied field.

In order to apply the electric field across the quantum well the structure is placed in the intrinsic region of a p-i-n diode, (Fig.1-5), such that the p and n layers have a larger band gap than the QW layers (i.e. larger than e1hh1). Contacting to the p and n layers permits an electric field to be applied, the field strength is given approximately by V_{appl}/L_i, where V_{appl} is the applied *reverse* bias and L_i is the length of the intrinsic region. It should also be noted that since the device is essentially a p-i-n diode, it can also act as a photodiode thereby giving important duality of function to the device.

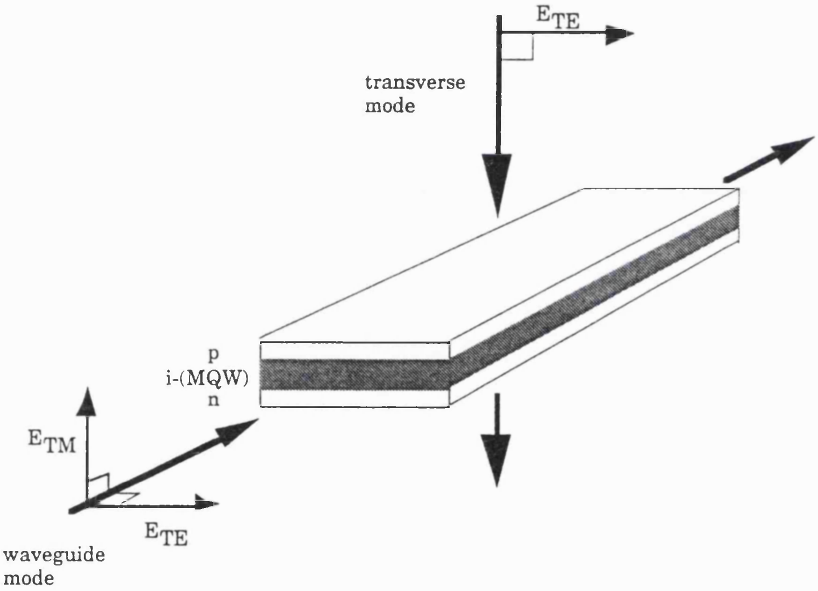

Figure 1-5 *A Schematic showing two basic device geometries i.e. waveguide and transverse operation along with the electric field vectors. It should be noted that in a transverse structure two modes of device are available; transmission (illustrated above) and reflection where the output beam is reflected back through the device.*

Electro-absorption devices, such as modulators can be fabricated into two geometries, (Fig.1-5). As a waveguide, with light incident parallel to the layers (||) (see review by Wood 1988), or as a transverse structure with light incident perpendicular to the layers (z) (Wood *et al* 1984). The structures investigated in this thesis, (Chapter 5), are of the transverse type. To achieve significant modulation ($\sim e^{-\Delta\alpha . L_i}$), the intrinsic region comprises *multiple* quantum wells, where typically 50-100 repeats of the QW are used in the intrinsic region. Conversely, waveguide structures require only a few QW since a large absorption length is already available by the physical length of the device.

In multiple period structures the barrier width is very important and determines many of the properties. It is useful to recall the terminology that is often used to distinguish various structures (Chemla and Miller 1985). In a multiple layer structure, each QW has its own confined states and associated wavefunction which, although largely localised in the well layer, penetrates into the barrier layer. Providing the barrier layer is sufficiently thick, i.e. thicker than the penetration length, the wavefunctions from adjacent wells do not overlap and the properties of the MQW are well described by those from a single QW. [note: it is assumed the MQW comprises identical repeats of the QW.] When the barrier width is less than the penetration length, the wavefunctions overlap and the carriers are no longer confined to a single QW. In this situation the structure is commonly referred to as a superlattice (SL), or coupled quantum wells (CQW) if the interaction is between two quantum wells only. The resulting electro-absorption properties of these structures has attracted considerable interest for use in various devices (see e.g. for SL, Bluese *et al* 1988a,b and for CQW, Lee *et al* 1989, Atkinson *et al* 1990). In this thesis, the interest is in MQW structures exploiting the properties of single QWs (i.e. the QCSE). The question of the barrier width is clearly important. The work in Chapter 4 (§4.2) addresses this point in more detail.

With regard to device performance, the operating voltage should be as low as possible to ease the burden on the driver circuitry, and at the same time the absorption change must provide sufficient modulation. The basic p-i-n transverse modulator relies on a large optical active absorption length to provide sufficient modulation. In principle the number of QWs forming the MQW region could be increased to provide this; however increasing the length of the intrinsic region increases the applied bias required to achieve a given electric field, and hence absorption change. Many workers have demonstrated how this problem can be circumvented through the design of double or multiple pass modulators (Boyd *et al* 1987, Whitehead *et al* 1989). Incorporating the MQW within a Fabry-Perot cavity increases the number of passes and hence optical length while maintaining a comparatively small physical length. With further optimization, the Fabry-Perot designs have led to dramatic improvements in device performance (Zouganelli *et al* 1991). The designs, although initially developed for the GaAs/AlGaAs system, have since been extended for InP based longer wavelength MQWs with some success (Moseley *et al* 1990, Yoo *et al* 1994). However the development of InP based semiconductor mirrors defining the cavity continues to be topic of interest (e.g. Guy *et al* 1994), and further improvements in device performance may be expected.

Other p-i-n devices that exploit the electro-absorption properties of quantum wells are a range of bistable optical switches known as SEEDs (Self-Electro-optic Effect Device). SEEDs offer logic operations in the optical domain utilizing the QCSE to provide two distinct operating states determined by the intensity of the incoming beam (see D.A.B Miller 1990, Lentine and Miller 1993, for comprehensive reviews on the subject). The basic operation of SEED and some applications are briefly discussed in Chapter 6.

Absorption changes at the band edge give rise to changes in refractive index, via the Kramers-Krönig relations (see e.g. Bassani and Parravicini 1975). Thus in addition to intensity modulation, *phase* modulation is also a possibility and has been demonstrated in waveguide devices (Koren *et al* 1987, Zucker *et al* 1988). These electro-refraction effects have been used to produce directional couplers or intersectional switches, where the path of the light can be switched between possible output ports (Cada *et al* 1991, Schimomura *et al* 1992). Switches of this kind can serve a large number of crossover ports and could be useful components in optical routing architectures.

Electric-field modulation of the band edge absorption via the QCSE is not the only method available for possible applications. Quenching of the exciton can also modulate the exciton spectra and has been used to design various devices. For example, in the barrier reservoir and quantum well electron transfer structure (BRAQWET) a highly doped barrier is employed. Modulating an applied electric field sweeps the carriers in and out of the well. Carriers (electrons) in the well, essentially fill up the subband and screen the Coulomb interaction thus inhibiting the formation of the exciton resonance (Schmitt-Rink *et al* 1989). A key distinction in these devices is that although electric field is applied, the resulting absorption (and refractive index) changes are not via the QCSE but obtained by band filling effects (Blum *et al* 1991, Zucker *et al* 1991). High power and high speed modulation is fundamentally dictated by the escape time of electrons entering and leaving the wells (assuming the device is small enough not to be limited by the RC time constant). Similar considerations also apply to QCSE devices which rely on the escape of both carriers from the well, i.e. electrons and particularly holes (see e.g. Fox *et al* 1991). Although the dependence on only one type of carrier in BRAQWETs and related structures, which is typically the fastest escaping carrier (electron), has suggested significant advantages may be achieved with these structures (Zucker *et al* 1991). However, it should be noted, the subject of carrier escape in (multi)-quantum well devices, and the implications on device performance, continues to be an area of active research.

Modulation by exciton quenching may also be achieved through high intensity optical pumping of the structure (see e.g. Chemla and Miller 1985, Schmitt-Rink *et al* 1989). The underlying principle is similar to structures such as BRAQWETs, in relation to the band filling and absorption quenching, although through optical excitation *both* types of carriers are placed in the wells. Absorption and refraction changes are similarly induced as a function of optical power, thereby leading towards all-optical control of modulation/switching (e.g. Chemla and Miller 1985, Li Kam Wa *et al* 1985).

§1.4 Concluding Remarks.

A brief description of the confinement effects in heterostructures has been presented, specifically for the use in (M)QW electro-absorption structures. Viewed as a *constructed* material, the band gap of the heterostructure, defined by e1hh1, may be varied through changing the well width. The exciton states associated with this band gap following accordingly. To a first approximation, the absorption band edge (i.e. e1hh1-E_B where E_B is the exciton binding energy) can be tailored to lie between the bulk band edge of the well and barrier materials. In practise well widths of 50-150Å are typically used, which for the GaAs/AlGaAs system can vary the band edge by approximately 90 meV (810 nm to 860 nm). Growth on InP substrates, using the lattice matched InGaAs/InP system offers similar energy changes for varying well width but covers a wavelength range approximately between 1.44 μm to 1.62 μm, due to the smaller bulk band gap of the well layer. Selecting the band edge absorption to occur at a specific wavelength is clearly beneficial in device design, particularly in view certain operating wavelength requirements for applications, e.g. in long haul telecommunications the requirement is to operate around 1.55 μm which corresponds to the low loss optical fibre window. However, changing the well width may not be advantageous for a particular device, since it is well known the performance of the electro-absorption properties, i.e. Stark shift and absorption, are well width dependent (see e.g. Brum and Bastard 1985, Whitehead *et al* 1988). An obvious solution is to change the constituent bulk materials, to satisfy both a particular operating wavelength and prescribed electro-absorption properties. For example, the use of quaternary layers which act as the well material; InGaAsP/InP (e.g. Temkin *et al* 1987) and InGaAlAs/AlInAs (Wakita *et al* 1988) are MQW structures where the bulk band gap for the well material is varied by the adjusting the group III and V mole fractions, while still remaining lattice matched to InP substrate. However as early as 1982 it was suggested by Osbourn that lattice *mis*matched layers could be used in heterostructures (Osbourn 1982). Among other things this increased the range of materials available for heterostructures and hence provided further flexibility in the design of heterostructure devices. The work in this thesis investigates the use of lattice mismatched layers in heterostructures, specifically for MQW electro-absorption devices. The basic ideas behind the use of lattice mismatched materials is presented in the following chapter.

References.

Alterelli M, *"Band Structure, Impurities and Excions in Superlattices"* in *Heterojunctions and Semiconductor Superlattices,* edited by Allan G, Bastard G, Boccara N, Lannoo M and Voos M, Springer Verlag, Berlin, (1986), pp 12-37.

Anderson N.G, and Jones S.D, *"Optimized Tight-Binding Valence Bands and Heterojunction Offsets in Strained III-V Semiconductors"*, J. Appl. Phys., **70**, (1991), pp 4342-4356.

Atkinson D, Parry G, Rivers A, and Roberts J.S, *"Modelling of Low Voltage Electroabsorption in Coupled Quantum Wells with Applications to Low-Voltage Optical Modulation"* Semicond. Sci. Technol. **5**, (1990), pp 516-524.

Bassani F, and Pastori Parravicini, G in *Electronic States and Optical Transitions in Solids* edited by R.A. Ballinger, Pergamon Press, (1975).

Bar-Joseph I, Klingshirn C, Miller D.A.B, Chemla D.S, Koren U, and Miller B.I, *"Quantum Confined Stark Effect in InGaAs/InP Quantum Wells Grown by Organometallic Vapor Phase Epitaxy"*, Appl. Phys. Lett., **50**, (1987), pp 1010-1012.

Bastard G, and Brum J.A, *"Electronic States in Semiconductor Heterostructures"* IEEE J. Quantum Electron. vol. JQE-22, (1986) pp 1625-1644.

Bastard G, *Wave Mechanics Applied to Semiconductor Heterostructures,* Les Editions de Physique, Paris, (1988).

Bleuse J, Bastard G, and Voisin P, *"Electric-Field-Induced Localization and Oscillatory Electro-Optical Properties of Semiconductor Superlattices"*, Phys. Rev. Lett. **60**, (1988a), pp 220-223.

Bleuse J, Voisin P, Allovon M, and Quillec M, *"Blue Shift of the Absorption Edge in AlGaInAs-GaInAs Superlattices: Proposal for an Original Electro-Optical Modulator"*, Appl. Phys. Lett. **53**, (1988b), pp 2632-2634.

Blum O, Zucker J.E, Chang T.Y, Sauer N.J, Divino M, Jones K.L, and Gastafson T.K, *"High Contrast Electron-Transfer GaAs-AlGaAs Multiple Quantum Well*

Waveguide Modulator", IEEE Photon. Technol. Lett., **3**, (1991), pp 327-329.

Brown E.R, Sollner T.C.L.G, Parker C.D, Goodhue W.D, and Chen C.L, *"Oscillations up to 420 Ghz in GaAs/AlAs Resonant Tunnelling Diodes"*, Appl. Phys. Lett., **55**, (1989), pp 1777-1779.

Brum J.A, and Bastard G, *"Electric-Field-Induced Dissociation of Excitons in Semiconductor Quantum Wells"* Phys. Rev. **B 31**, (1985), pp 3893-3898.

Cada M, Keyworth B.P, Glinski J.M, SpringThorpe A.J, Rolland C, and Hill K.O, *"Electro-optic Switching in a p-i-n Doped Multiple Quantum Well Directional Coupler"*, J. Appl. Phys., **69**, (1991), pp 1760-1762.

Capasso F, Mohammend K, and Cho A.Y, *"Resonant Tunnelling Through Double Barriers, Perpendicular Quantum Transport Phenomena in Superlattices, and Their Device Applications"*, IEEE J. Quantum Electron., JQE-**22**, (1986), pp 1853-1869.

Chemla D.S, and Miller D.A.B, *"Room-Temperature Excitonic Nonlinear-Optical Effects in Semiconductor Quantum-Well Structures"* J. Opt. Soc. Am. B **2**, (1985), pp 1155-1173.

Cochrane P, *"Future Directions in Long Haul Fibre Optic Systems"*, British Telecom Technol. Journal, **8**, (1990), pp 5-17

Dickinson A, and Prise M.E, *"Free-Space Optical Interconnection Scheme"*, Appl. Optics, **29**, (1990), pp-2001-2005.

Feldman M.R, Esener S.C, Guest C.C, and Lee S.H, *"Comparison between Optical and Electrical Interconnects Based on Power and Speed Considerations"*, Appl. Optics, **27**, (1988), pp1742-1751

Gershoni D, Temkin H, Vandenberg J.M, Chu S.N.G, Hamm R.A, and Panish M.B, *"Type I to Type II Superlattice Transition in Strained Layers of* $In_xGa_{1-x}As$ *Grown on InP"*, Phys. Rev. Lett., **60**, (1988), pp 448-451.

Gossard A.C, *"Growth of Microstructures by Molecular Beam Epitaxy"*, IEEE J. Quantum Electron., JQE-**22**, (1986), pp 1649-1655.

Guy P, Woodbridge K, Haywood S.K, and Hopkinson M, *"Highly Doped 1.55 μm* $Ga_xIn_{1-x}As/InP$ *Distributed Bragg Reflector Stacks"*, Electron. Lett., **30**, (1994), pp 1526-1527.

Fox A.M, Miller D.A.B, Livescu G, Cunningham J.E, Jan W.Y, *"Quantum Well Carrier Sweep Out: Relation to Electroabsorption and Exciton Saturation"*, IEEE J. Quantum Electron., JQE-**27**, (1991), pp 2281-2295.

Jelley K.W, Engelmann R.W.H, Alavi K, and Lee H, "*Well Size Related Limitations on Maximum Electroabsorption in GaAs/AlGaAs Multiple Quantum Well Structures*", Appl. Phys. Lett., **55**, (1989), pp 70-72.

Jewell J.L, Harbison J.P, Scherer A, Lee Y.H, and Florez L.T, "*Vertical Cavity Surface Emitting Lasers: Design, Growth, Fabrication, Characterization*", IEEE J. Quantum Electron. vol. JQE-**27**, (1991), pp 1332-1346.

Joyce B, "*Molecular Beam Epitaxy*", Rep. Prog. Phys. **48**, (1985), pp 1637-1697.

Koch T.L, and Koren U, "*Semiconductor Lasers for Coherent Optical Fiber Communications*", J. Lightwave Technol., **8**, (1990), pp 274-293.

Kopft R.F, Herman M.H, Lamont Schnoes M, Perley A.P, Livescu G, and Ohring M, "*Band Offset Determination in Analog Graded Parabolic and Triangular Quantum Wells of GaAs/AlGaAs and GaInAs/AlInAs*", J. Appl. Phys. **71**, (1992), pp 5004-5011.

Koren U, Koch T.L, Presting H, and Miller B.I, "*InGaAs/InP Multiple Quantum Well Waveguide Phase Modulator*", Appl. Phys. Lett., **50** , (1987), pp 368-370.

Lee J, Vassell M.O, Koteles E.S, and Elman B, "*Excitonic Spectra of Asymmetric Coupled Double Quantum Wells in Electric Fields*", Phys. Rev. **B 39**, (1989), pp 10133-10143.

Lentine A.L, and Miller D.A.B, "*Evolution of the SEED Technology-Bistable Logic Gates to Optoelectronic Smart Pixels*", IEEE J. Quantum Electron. vol. JQE-**29**, (1993), pp 655-669.

Li Kam Wa O, Sitch J.E, Mason N.J, Roberts J.S and Robson P.N, "*All Optical Multiple Quantum Well Waveguide Switch*", Electron. Lett., **21**, (1985), pp 26-28.

Midwinter J.E, "*Light Electronics, Myth or Reality*", IEE Proceedings, Vol. **132**, Pt. J (6), (1985), pp 371-382.

Midwinter J.E, "*Digital Optics, Smart Interconnect or Optical Logic ?*", Physics Technology, **19**, (1988), pp 101-108.

Midwinter J.E, "*Photonics in Switching: The Next 25 Years of Optical Communications?*", Inaugural address at IEE, 10th Oct. 1990, paper 8366J.

Miller D.A.B, Chemla D.S, Damen T.C, Gossard A.C, Wiegmann W, Wood T.H, and Burrus C.A, "*Band Edge Electroabsorption in Quantum Well Structures: The Quantum Confined Stark Effect*" Phys. Rev. Lett. **53**, (1984), pp 2173-2176.

Miller D.A.B, Chemla D.S, Damen T.C, Gossard A.C, Wiegmann W, Wood T.H, and Burrus C.A, "*Electric Field Dependence of Optical Absorption Near the Band Gap of Quantum Well Structures*", Phys. Rev. **B 32**, (1985), pp 1043-1060.

Miller D.A.B, "*Optics for Low-Energy Communication Inside Digital Processors: Quantum Detectors, Sources and Modulators as Efficient Impedance Converters*", Optics Lett., **14**, (1989), pp 146-148.

Miller D.A.B, "*Quantum-Well Self-Electro-Optic Effect Devices*", Opt. & Quant. Electron. **22**, (1990), pp S61-S98.

Moseley A.J, Thompson J, Kearley M.Q, Robbins D.J, Goodwin M.J, "*Low Voltage InGaAs/InP Multiple Quantum Well Reflective Fabry-Perot Modulator*", Electron. Lett., **26**, (1990), pp 913-914.

O'Reilly E.P, "*Quantum Cascade Laser has no Role for Holes*", article in Physics World, July (1994), pp 24-25.

Osbourn G.C, "*Strained-Layer Superlattices from Lattice Mismatched Materials*", J. Appl. Phys., **53**, (1982), pp 1586-1589.

Oudar J.L, Kuselewicz R, Sfez B, Michel J.C, and Planel R, "*Prospects for Further Threshold Reduction in Microresonators*", Opt. & Quant. Electron. **24**, (1992), pp S193-S208.

Parry G, Whitehead M, and Midwinter J.E, "*Digital Optoelectronic Devices and Systems*", Chp.13 in *GaAs Technology and its Impact on Circuits and Systems,* edited by D.Haig, IEE Circuits and Systems Series 1, published by Peter Peregrinus Ltd., UK, (1989).

People R, and Jackson S.A, in *Semiconductors and Semimetals, Vol. 32 : Strained-Layer Superlattices:Physics*, Chapter 4, vol.ed T.P Pearsall, Academic Press, New York, (1990), pp 119-174.

Stradling R.A and Klipstein P.C (editors), *Growth and Characterisation of Semiconductors*, Adam Higler, Bristol, (1990).

Stringfellow G.B, in *Semiconductors and Semimetals, Vol. 22 : Part A. Material Growth Techniques*, Chapter 3, eds Willardson R.K and Beer A.C, Academic Press, New York, (1990), pp 209-259.

Schmitt-Rink S, Chemla D.S, and Miller D.A.B, "*Linear and Nonlinear Optical Properties of Semiconductor Quantum Wells*" Advances in Physics, Vol.**38**, (1989) pp89-188.

Schimomura K, Tanaka N, Aizawa T, and Arai S, "*2V Drive Voltage Switching Operation in 1.55 μm GaInAs/InP MQW Intersectional Waveguide Optical Switch*", Electron. Lett., **28**, (1992), pp 2017-2019.

Smith R.A, *Semiconductors*, 2^{nd} edition, Cambridge University Press, (1978), in particular chapter 11.

Solomon P.M, and Morkoç H, "*Modulation-Doped GaAs/AlGaAs Heterojunction Field-Effect Transistors (MODFET's), Ultrahigh-Speed Device for Supercomputers*", IEEE Trans. on Electron Devices, ED-**31**, (1984), pp 1015-1027.

Sze S.M, *Physics of Semiconductor Devices*, chapters 6,7 and 8, John Wiley & Sons, New York, (1981).

Temkin H, Gershoni D, Panish M.B, "*InGaAsP/InP Quantum Well Modulators Grown by Gas Source Molecular Beam Epitaxy*", Appl. Phys. Lett., **50**, (1987), pp 1776-1778.

Tooley F.A.P, and Wakelin S, "*Design of a Symmetrical Self-Electro-Optic-Effect-Device Cellular-Logic Image-Processor*", Appl. Optics, **32**, (1993), pp 1850-1862.

Van de Walle C.G, and Martin R.M, "*Theoretical Study of Band Offsets at Semiconductor Interfaces*", Phys. Rev. **B35**, (1987), pp 8154-8165.

Wakita K, Kotaka L, Asai H, Nojima S, and Mikami O, "*High Effeciency Electroabsorption in Quaternary AlGaInAs Quantum Well Optical Modulators*", Electron. Lett., **24**, (1988), pp 1324-25.

Weisbuch C and Vinter B, in *Quantum Semiconductor Structures: Fundamentals and Applications*, Academic Press, (1991).

Whitehead M, Stevens P, Rivers A, Parry G, Roberts J.S, Mistry P, Pate M, and Hill G, "*Effects of Well Width on the Characteristics of GaAs/AlGaAs Multiple Quantum Well Electroabsorption Modulators*", Appl. Phys. Lett., **53**, (1988), pp 956-958.

Whitehead M, Rivers A, Parry G, Roberts J.S, and Button C, "*Low-Voltage Multiple Quantum Well Reflection Modulator with On:Off Ratio >100:1*", Electron. Lett., **25**, (1989), pp 984-985.

Whitehead M, "*Optimisation of Normal Incidence GaAs-AlGaAs Multiple Quantum Well Optical Modulators*", Ph.D Thesis, University of London, (1990).

Wood T.H, Burras C.A, Miller D.A.B, Chemla D.S, Damen T.C, Gossard A.C, and Wiegmann W, "*High Speed Optical Modulation with GaAs/GaAlAs Quantum Wells in a p-i-n Diode Structure*", Appl. Phys. Lett., **44**, (1984), pp 16-18.

Wood T.H, *"Multiple Quantum Well (MQW) Waveguide Modulators"*, J. Light. Tech., **6**, (1988), pp 743-757.

Yoo S.J.B, Bhat R, Caneau C, Koza M.A, Gamelin T, and Lee T.P, *"High Performance 1.5 μm Operation of Asymmetric Fabry-Perot Modulators"*, CLEO '94, (1994), paper CThE5.

Zory, Jr. P.S, (editor) of *Quantum Well Lasers*, Academic Press, New York, (1993).

Zouganeli P, Whitehead M, Stevens P.J, Rivers A.W, Parry G, and Roberts J.S, *"High Tolerances for a Low-Voltage High-Contrast, Low-Insertion-Loss, Asymmetric Fabry-Perot Modulator"*, IEEE Photon. Technol. Lett., **3**, (1991), pp 733-735.

Zucker J.E, Hendrickson T.L, and Burrus C.A, *"Low Voltage Phase Modulation in GaAs/AlGaAs Quantum Well Optical Waveguides"*, Electron. Lett., **24**, (1988), pp 112-113.

Zucker J.E, Jones K.L, Wegener M, Chang T.Y, Sauer N.J, Divino M.D, and Chemla D.S, *"Multi-GigaHertz-Bandwidth Intensity Modulators using Tunable-Electron-Density Multiple Quantum Well Waveguides"*, Appl. Phys. Lett., **59**, (1991), pp 201-203.

Chapter 2. **Introduction to the Use of Strained layers in Heterostructures.**

During the development of heterostructures, it became apparent that the use of thin layers (typically <200Å) relaxes the requirement of using lattice matched constituent materials (G.C Osbourn 1982). Coherently strained multilayer structures were envisaged, consisting of thin alternating layers of materials which are lattice mismatched in bulk form. The thin layers elastically deform such that the lattice constant in the interface planes is the same throughout the structure. A considerable amount of work has since been carried out on strained layer heterostructures, demonstrating further *engineering* of band structure through strain and quantum confinement. A brief introduction to some of the concepts involved and the effects on the band structure is presented here. Further detailed explanations can be found in the literature (see e.g. E.P O'Reilly 1989, T.P Pearsall 1990, J Singh 1993). The chapter finishes with some comments on strain relaxation in multiple quantum well structures.

§2.1 Description of Stress and Strain.

The effect of an external force on a crystal lattice is to distort the lattice in some manner (see e.g. Nye 1957). This applied force (per unit area), or stress, can be described in terms of *stress* tensors, σ_{ij}, individually representing an *ij* component of the force acting on the crystal lattice. The case suitable for the work in this thesis, is $i=j$, which simply implies the stress is acting perpendicular to the six faces of the cubic lattice. [note: the so called, *shear* components of stress, where $i \neq j$, are relevant for structures grown along (111) (Mailhiot and Smith 1989)]. To proceed with forming a mathematical description of the lattice distortion, a set of *strain* tensors are introduced, e_{ij}. Each component of the strain tensor describes the distortion of the lattice away from its unstrained shape. As with the stress tensors, only the normal components, $i=j$, are relevant for the present work.

Relating how a particular stress leads to a particular strain or lattice distortion is a generalization of Hooke's Law, that is providing the elastic limits of the material are not exceeded, the strain is proportional to the magnitude of the applied stress (see for e.g. Feynman, Leighton and Sands, chp. 38, 1964). Neglecting the shear components of stress, the relationship between stress and strain tensors can be written as:

$$\begin{pmatrix} \sigma_{xx} \\ \sigma_{yy} \\ \sigma_{zz} \end{pmatrix} = \begin{pmatrix} C_{11} & C_{12} & C_{12} \\ C_{12} & C_{11} & C_{12} \\ C_{12} & C_{12} & C_{11} \end{pmatrix} \begin{pmatrix} e_{xx} \\ e_{yy} \\ e_{zz} \end{pmatrix} \qquad (2.1)$$

where the crystal axes are orthogonal and taken to lie along the x,y and z axes. The C_{ij} are known as the elastic coefficients of the material and are well documented for all III-V semiconductors (e.g. Landolt-Börnstein 1982, 1989). The above relationship assumes the crystal has cubic symmetry such that all off-diagonal terms are equal, and all diagonal terms are equal. In this sense, only two elastic coefficients need be considered, C_{11} and C_{12}. The form of (2.1) shows that one type of stress leads to three components of strain. Examples of the types of stress relevant in the present work are shown below, along with the corresponding lattice deformation through the strain components.

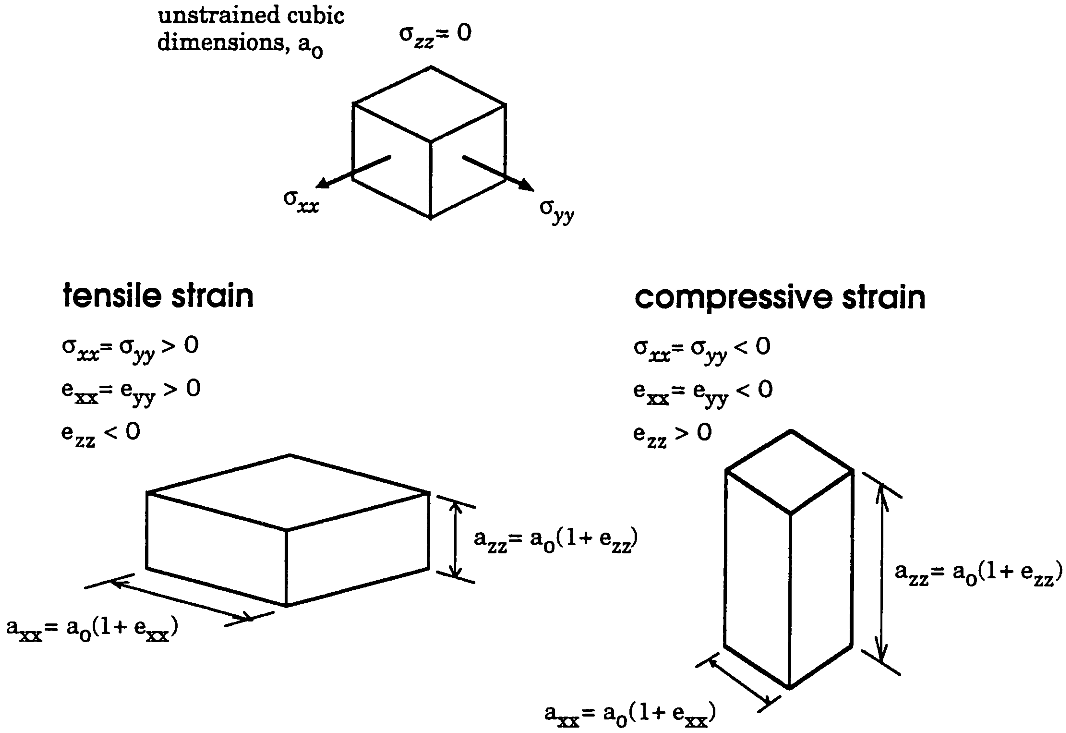

Figure 2-1. *A schematic demonstrating two types of biaxial strain on a cubic cell.*

Equal stress applied to all four x and y faces of the cubic cell sets $\sigma_{xx} = \sigma_{yy}$, and no stress applied to the z faces, i.e. $\sigma_{zz} = 0$, provides a simple picture of lattice mismatched induced stress encountered in thin layer growth. For this situation the crystal is under *biaxial* strain, and the two types of biaxial strain are illustrated (Fig. 2-1). For outward directed stress ($\sigma_{xx}>0$), the resulting strain is referred to as biaxial *tensile* strain, while inward directed stress ($\sigma_{xx}<0$), gives rise to biaxial *compressive* strain. Using (2.1), the relationship between the strain tensors describing the lattice deformation can be found. Recalling $\sigma_{xx} = \sigma_{yy}$, this implies the strain in both x and y directions is equal, i.e. $e_{xx} = e_{yy}$.. Setting $\sigma_{zz} = 0$ in (2.1), the third equation gives,

$$e_{zz} = -\frac{2C_{12}}{C_{11}} e_{xx} \tag{2.2}$$

With C_{11} and C_{12} always positive, a lattice deformation along x (or y) produces a deformation of the opposite sense along z (cf. Fig.2-1).

The strain tensors are central to describing the electronic properties of a strained material, this is covered later in the thesis (§3.3). In practise the in-plane strain tensor (e_{zz}) is determined from considering the lattice mismatch between bulk layers, then applying (2.2), both tensors describing the lattice distortion are known.

§2.2 Strained Layers.

§2.2.1 Growth and critical thickness.

The ability to realize strained layers in practical structures was undoubtedly due to the growth advancements that were instrumental in the development of heterostructures (see T.P Pearsall 1990,chapter 1 for further information). A strained layer is formed through growth of a thin epilayer (with lattice constant a_0^{epi}) on a substrate (a_0^s) such that $a_0^s \neq a_0^{epi}$, (Fig2-2). The epilayer deforms to take on the lattice constant in the plane of the substrate. Terms such as pseudomorphic or coherent growth are often used to describe the situation, since interfacial coherence is maintained. The strain energy, arising from the lattice match, is accommodated by the deformation of the epilayer. For a thick substrate, the in-plane strain of the epilayer is described from the bulk lattice constants a_0^{epi} and a_0^s. Specifically,

$$e_{xx}(=e_{yy}) = \frac{a_0^s - a_0^{epi}}{a_0^{epi}} \tag{2.3}$$

The resulting deformation in the growth direction is determined from (2.2).

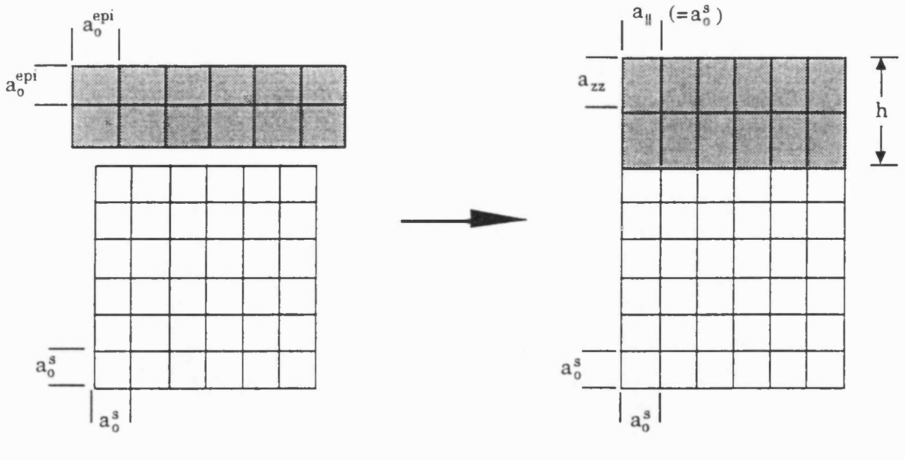

Figure 2-2. *A schematic showing the deformation of an epilayer through the lattice mismatch induced strain. (illustrated for biaxial compression).*

Coherent growth of an epilayer in this manner cannot go on indefinitely. The accommodated strain energy increases with epilayer thickness, h, such that above a certain *critical* thickness, h_c, the introduction of dislocations to relieve the strain energy becomes thermodynamically more favorable (see e.g. E.P O'Reilly 1989 and references therein). With the introduction of dislocations, the lattice mismatch is then partially accommodated by the lattice strain *and* partially by the introduction of misfit dislocations at interface. The epilayer is then said to be relaxed, usually by some percentage amount, and the in-plane strain tensor description of the epilayer from (2.3) no longer holds. For $h<h_c$ the strained epilayer is expected to be thermodynamically stable against dislocation formation, due to the energy barrier that must be overcome to generate dislocations (E.P O'Reilly 1989). In view of the energy (or force) considerations, the critical thickness depends somewhat on the lattice mismatch of the materials, in fact a representative value of single layer critical thickness often quoted is 100Å%, i.e. for a 1% mismatch, h_c~100Å (E.P O'Reilly 1989 and references therein).

Although so far discussed in terms of a single epilayer, similar reasoning lies behind the growth of heterostructures such as (multi-) quantum wells and superlattices comprising lattice mismatched bulk constituents. Generally growth on a thick substrate (or buffer layer) fixes the dominant lattice constant for the structure, i.e. the in-plane lattice constant to which the subsequent layers deform. Accordingly, above *some* critical thickness, the strain is relieved through the generation of dislocations. However, both the relaxation process and the critical thickness can substantially differ from the single epilayer layer case mentioned above (further discussed in §2.3). Interestingly, with a multi-layer structure, it is possible to employ alternating layers which are under compressive and tensile strain in equal respects in relation to the substrate (or buffer). For approximately the same well and barrier thickness (below the individual h_c) the *net* strain in one period becomes zero and growth of these alternating layers could in principle continue indefinitely (People and Jackson 1990, cf. InAsP/InGaP MQW on InP from Woodward *et al* 1992).

Briefly then, epitaxial growth of high quality layers that are lattice mismatched in bulk form may be achieved through the elastic accommodation of strain. For a mismatch of ~1%, thicknesses up to 100Å should be possible which is compatible with attaining the desired confinement effects from quantum well structures (cf. §1.2). The following section describes the modifications on the band structure due to strain which are relevant to quantum well band structures where one (or both) of the constituent layers may be strained. Further discussions on critical thickness and relaxation mechanisms, particularly in multi-quantum well structures, are presented in §2.4.

§2.2.2 Band structure modifications through strain.

The manner in which lattice mismatch induced strain effects the band structure is commonly described using deformation potentials (E.P O'Reilly 1989 and references therein). These are constants of the material which describe the shift per unit strain of the band edges and can be obtained from the usual sources (eg. Landolt and Börnstein 1982, 1989). Many of the strain effects on the quantum well band structure can be understood by considering the change in band structure with strain of the constituent bulk layers (Fig.2-3). The situation described here is for growth on (100) substrates, relevant to the devices studied in the present work.

The total strain in a layer can be resolved into a hydrostatic component, $e_{vol} = e_{xx} + e_{yy} + e_{zz} = 2e_{\|} + e_{zz}$ which describes the change in crystal volume, and an axial component, $e_{ax} = e_{zz} - e_{\|}$. The hydrostatic component acts on the band edges, ie. resulting in a change of band gap from the bulk value. In the valence band, the axial component lifts the degeneracy between the heavy- and light-hole bands at the zone centre. For realizable strains, the splitting of the heavy- and light-hole band edges can be large, eg. approximately 60 meV for $e_{\|} \approx 1\%$.

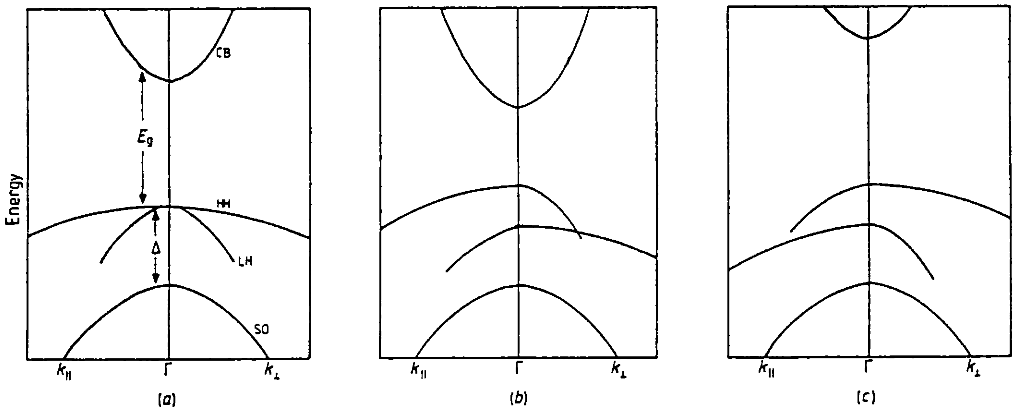

Figure 2-3. *A schematic representation of the band structure of (a) an unstrained direct gap semiconductor. (b) the structure under biaxial tension and (c) the structure under biaxial compression. [from E.P O'Reilly 1989].*

To clarify the notation used above (with respect to QW geometry), the perpendicular direction corresponds to the growth (z) direction and the parallel direction would correspond to the plane of the quantum well layers. The distinction is important, since from the above figure, the axial component of strain is seen to introduce an anisotropic valence band. Under compressive strain, (Fig.2-4c), the highest valence band is heavy along the growth (and hence confinement) direction and comparatively light in the plane of the layers, cf. (2.1). This is contrary to the situation of tensile strain, illustrated in Fig.2-4b. For a given type of strain, the apparent mass reversal illustrated above is qualitatively similar to that encountered in the valence band states of QW structures, and in similar way can be understood from a **k.p** description of the band structure (Bastard and Brum 1986, E.P O'Reilly 1989). Further comments appear later on. The splitting of the valence band leads to separate *bulk* energy gaps for heavy-hole to conduction band and light-hole to conduction band transitions. An additional consideration arises from the shift of the band edges, in that compressive strain tends to increase the *mean* band gap while tensile strain reduces it.

In a quantum well structure, where the well layer is strained, the shifts of the band edges have a direct bearing on the QW band edges, i.e. e1hh1, e1lh1 etc. The confinement energies are determined by the dispersion ($k_\perp$) along the growth (confinement) axis. Recalling the unstrained QW case in §1.2.3, where the heavy-and light-hole *bulk* band edges are degenerate at $k_\perp=0$ and correspond to the bottom of the valence band potential well, the difference in effective mass results in the bound states occurring at different energies with respect to their *degenerate* bulk band edges. Considering the ground states, hh1 and lh1, the magnitude of the separation is primarily determined by the well width and the effective masses, and in all cases hh1 is higher in energy than lh1 (cf. Fig.1-2). For a layer under compressive strain, the heavy-hole band edge (defined along $k_\perp$) is higher in energy than the light hole band edge. Even with the subbands occurring at the same energies from their respected band edges, the splitting between the hh1 and lh1 subbands increases, Fig.2-4 (left). Similar reasoning can be applied when the well layer is under tensile strain; although, in this case the light-hole band edge is higher in energy, Fig.2-4 (right). Depending on the magnitude of tensile strain (i.e. the splitting) and the well width (energy of lh1 from its band edge), it is possible to to make the lowest energy transition in the structure, that between e1 and lh1 (see e.g. Gershoni *et al* 1989).

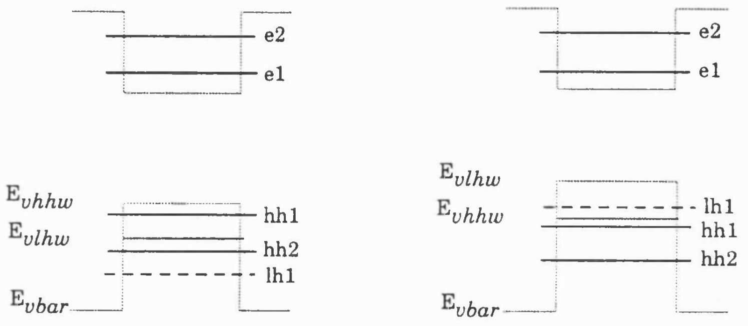

compressive strain tensile strain

Figure 2-4. *A schematic illustrating confined band edge positions and confined states in a quantum well where the well material is experiences biaxial strain. [cf. Fig. 1-2. for the unstrained case].*

In some cases, the shifts in the band edges can change the nature of the quantum well structure, for example, it is possible to have a combination of type I and type II line-ups in relation to the valence band states. This situation is thought to arise in the compressive strained $In_xGa_{1-x}As/GaAs$ system, where the electron and heavy hole potentials are type I but the electron and light hole potentials are type II (Marzin *et al* 1985).

Through accommodating strain in quantum well structures (QW), an additional flexibility in subband design becomes available. Specifically, compressive strain works in the same way as the effect of confinement, i.e. to increase the energy separation between the highest heavy- and light-hole subbands, (E_{hh1}-E_{lh1} with $E_{hh1}>E_{lh1}$). Tensile strain acts in an opposite manner to confinement, reducing E_{hh1}-E_{lh1} and in some cases giving $E_{lh1}>E_{hh1}$. In this sense it is possible to independently vary the splitting of the two highest heavy-hole states (E_{hh1}-E_{hh2}) mainly through the well width, and the splitting E_{hh1}-E_{lh1} through the strain (E.P O'Reilly 1989). The separation of these higher valence band states plays an important role in relation to the electronic and optical properties of the quantum well material.

For an unstrained QW, the in-plane valence band dispersions, $E_n(k_{||})$ where n is the band index, are highly non-parabolic, Fig.2-5. This is a result of in-plane mixing between the states, essentially each band taking on a mixed heavy and light hole character for $k_{||} \neq 0$ (see e.g. Bastard and Brum 1986). Neglecting mixing, the highest valence band state (hh1) is comparatively light in the plane of the well, a situation similar to that illustrated in figure 2-3c. (E.P O'Reilly 1989, see also Bastard and Brum 1986 *vis-á-vis* the diagonal approximation). Typically for the highest valence band state, the effect of mixing is to increase its effective mass near the band edge over that found when mixing is neglected. From **k.p** theory, the strength of the mixing, relating to the increase in band edge mass, is governed by the proximity of the other valence band states, particularly lh1 (E.P O'Reilly 1989). With this last sentence the tailoring of the in-plane mass in the valence band through strain and confinement can be appreciated.

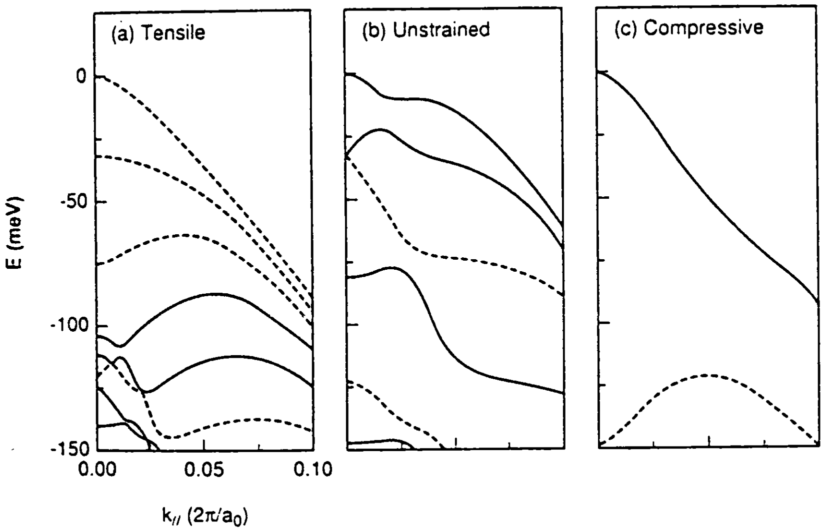

Figure 2-5. *Calculated valence band sub band structure of* $In_xGa_{1-x}As/InGaAsP$ *QW for (a) tensile strain* ($e_{||}$~1.5%, l_w=160Å), *(b) unstrained* (l_w=80Å) *and (c) compressive strain* ($e_{||}$~-1.2%, l_w=25Å). *The well widths were chosen to provide a band gap around 1.5 μm [further details can be found in Krijn et al 1992].*

For compressive strain, axial splitting and confinement increases E_{hh1}-E_{lh1} thereby greatly reducing the strength of the hh1 and lh1 mixing and subsequently the in-plane effective mass. This is demonstrated in figure 2-5, the reduction of the in-plane effective mass is implicit by the sharper curvature of the hh1 dispersion, cf. (1.1). Nonparabolicity is greatly reduced and the dispersion resembles a simple parabolic form. It is not immediately obvious that a similar result also occurs with tensile strain. However, calculations show that providing the effect of confinement can be minimised by choosing a wide well width. The highest valence band state (which is lh1) can also exhibit an lower in-plane mass over the unstrained case, (cf Fig. 2-5 taken from Krijn *et al* 1992). Structures with a low in-plane mass for the valence band yield significant advantages in transport and emitter technologies (E.P O'Reilly 1989).

§2.3 Use of Strain in QW Technology.

The accommodation of strain in heterostructures, such as quantum wells (QW), has proved valuable for many reasons. Overlooking the modifications to the band structure, the ability to accommodate strain can allow new material combinations to be considered. In one sense operating ranges for a particular technology can be increased. For example, multi-quantum well (MQW) structures based on GaAs substrates are routinely designed to operate beyond the GaAs band gap (~870 nm) at wavelengths up to 1.1 μm using compressively strained $In_xGa_{1-x}As$ (see e.g. Woodward *et al* 1990, J.J Coleman 1993). In another respect, at certain operating wavelengths, the poor properties of existing lattice matched structures may be replaced by opting for a strained material combination that exhibits a better all round performance. Such improvements may not necessarily arise from any band structure modifications, but simply through the quality of the sample in terms of growth and the homogeneity of one material over another, e.g. $InAs_zP_{1-z}$ in relation to $In_xGa_{1-x}As_yP_{1-y}$ (see e.g. Woodward *et al* 1992, and Chapter 5 for further details). The increased scope of materials are by no means restricted to heterostructures comprising III-V materials. Wide band gap II-VI heterostructures, such as $ZnSe/Zn_{1-x}Cd_xSe$, utilizing strain accommodation and the related band structure modifications are attracting great interest as visible emitters (see recent review by Nurmikko and Gunshor 1994). Furthermore, structures based on the *traditional* semiconductor materials, i.e. Silicon and Germanium, are expected to benefit with the introduction of strain (see e.g. People and Jackson 1990 and references therein). The alloy Si_xGe_{1-x} will be strained in a particular fashion depending on the substrate, i.e. the strain in the alloy layer can be either compressive (on Si) or tensile (on Ge) (see e.g. Hinckley and Singh 1990).

Quite apart from extending material choice or tailoring the band structure (discussed later), the realization of pseudomorphic growth has seen the development of structures with internally generated piezoelectric fields. The fields arise when stress (in this case arising from the lattice mismatch) is applied, typically, to a (111) plane of a semiconductor lacking inversion symmetry, i.e. III-V or II-VI (Mailhiot and Smith 1989). In a similar way to conventional (100) growth, heterostructures may be constructed *but* with the additional effect of the piezoelectric field in the strained layer. The strength of the piezoeffect is proportional to the shear component of strain, e_{ij} $(i \neq j)$, caused by the lattice mismatch of the layer (Moise *et al* 1993). MQW p-i-n devices, have been demonstrated with most of the work appearing so far using the InGaAs/GaAs system on (111) GaAs (e.g. Goossen *et al* 1990, Pabla *et al* 1993). Applying an electric field in the *opposite* direction to the piezoelectric field across the wells, reveals a *blue* shift of the n=1hh exciton and a corresponding increase in exciton absorption. Essentially the pre-biased state of the structure, from the internal field, has been cancelled through an opposing applied field. More recent work on a range of samples has highlighted additional design issues relating to the strength of the pre-biased state in (111) MQW p-i-n structures (Pabla *et al* 1993). Later in Chapter 6, a (100) based structure is presented based on the inducing-then-opposing field principle and is expected to show similar electro-absorption properties, i.e. a blue shift etc. Further discussions relating to the use of electro-absorption blue shift devices are also noted.

The novel effects are by no means restricted to electroabsorption type devices. Work studying the optical nonlinearities has demonstrated the involvement of the piezoelectric field (Cartwright *et al* 1993). In addition electronic devices, similar to MODFET's, utilizing the piezoelectric field have recently been reported (Lu and Huang 1994).

While accommodation of strain allows both new material systems and new technologies (cf. (111)) to be explored, it is largely the dramatic improvements to existing devices *through* band structure modifications that have captured the headlines. As demonstrated in figure 2-5, strain splitting and confinement can be used to tailor a much lighter hole mass in the highest valence band. Since these modifications occur in the valence band, devices relying on hole properties have reaped the benefits.

Considering optical devices, well documented improvements in the performance of quantum well lasers are testament to this *band structure* engineering (see recent review by O'Reilly and Adams 1994). A lighter hole mass leads to a reduction in the valence band density of states, which provides further improvements in the threshold current densities and differential gain obtained in QW lasers (see e.g. Krijn *et al* 1992, Corzine *et al* 1993). [note: recall the initial improvements realised in going from bulk to QW lasers (§1.3.2)]. Other advantages include increasing the polarization selective gain and a *tailored* reduction in many of the loss mechanisms, such as Auger and intervalence band absorption (IVBA), (see O'Reilly and Adams 1994 and references therein for further information).

Valence band engineering has also featured in modulator type devices. The effect of tensile strain in the well layer can offset the splitting of the heavy- and light-hole states caused by confinement. Thus in principle a properly chosen tensile strain can reinstate the degeneracy of the heavy-and light-hole subbands in QW structures that exists in bulk materials (see e.g. J. Singh 1993, Baliga *et al* 1994). Several device implications are immediate, the merging of heavy- and light-hole excitonic transitions can lead to marked improvements electro-absorption characteristics at low fields (Gomatam and

Anderson 1992). More importantly for devices in a waveguide configuration, the polarization sensitivity can be avoided, thereby providing electro-absorption/refraction operation regardless of whether the incident light is TE or TM polarized (cf. Weisbuch and Vinter 1991, p65-69 for polarization selection rules, also presented in §4.4.3). Ravikumar and co-workers (1993) studied a range of structures with increasing tensile strain and found for tensile strain of about ~0.3% in 120Å $In_xGa_{1-x}As/InP$ QW's ($x<0.53$) the peak absorption change for both TE and TM modes occurred at the same wavelength. However, this has not been the only approach to result in polarization *in*sensitive structures. Another method involves the use of separate compressive and tensile strained QW's in a MQW active region (see e.g. Thijs *et al* 1994 and references therein). The initial motivation behind this work was to obtain a semiconductor laser amplifier (SLA) (at 1.3μm). Light emerging from an optical fibre is randomly polarized, and for an unstrained MQW-SLA, light in the TE mode is amplified more than light in the TM mode (cf. selection rules governing the electron-heavy hole transitions §4.4.3). However with the active region containing *both* compressive (tensile) strain QW favouring TE (TM) polarization, and for each case tailoring the band gaps to be equal through composition and well width, equal gain can be provided to both polarization modes. Experimental investigations demonstrated polarization-insensitive operation with less than 1 dB difference in gain between the two polarization modes at 1.3 μm ±30 nm (Thijs *et al* 1994).

The latter approach provides an excellent example to the flexibility of device engineering that can be achieved through the use of strained layers, and from band structure design.

Electrical conduction devices, such as MODFET's, have also benefited through the use of strained layers. With the modifications in the valence band, the lighter hole mass attainable in either compressive or tensile strained layers suggests fast hole based (p-type channel) devices (e.g. Ruden *et al* 1989). However, improvements in n-type devices have also been recorded. For example, using compressively strained InGaAs (on GaAs) as the channel, the lower band gap (w.r.t GaAs) allows more charge to be transferred from the doped AlGaAs region which leads to higher output powers (see e.g. Ketterson *et al* 1986). In this sense, the improvements have come about through being able to *accommodate* a smaller band gap lattice-mismatched material rather than the modifications to the band structure.

Although this is only a brief summary, the impact that strained layer growth has had on heterostructure technology can be appreciated. As mentioned in the previous chapter, the devices investigated in the present work are transverse electroabsorption, comprising

MQW's in the active region. However, while reasonable levels of strain may be accommodated in structures containing single or a few QW's, e.g. as in QW lasers, in transverse electroabsorption devices considerably more periods of *strained* QW's are required for operation (cf. §1.3.3). It is therefore appropiate to draw attention to the question of relaxation, and indeed the mechanism by which this occurs, as the *cumulative* strain energy increases in such structures. This is the topic of the following section.

§2.4 Strain Coherence to Partial Relaxation.

In the study of strained layer epitaxy, several theories have been proposed to explain the breakdown of coherence at lattice mismatched interfaces via dislocations (Matthews and Blakeslee 1974, Hull *et al* 1986, People 1986, Jesser and Fox 1990). An early review of the various critical thickness models, and experimental results, is given by People and Jackson (1990). The model of Matthews and Blakeslee (MB) has so far proved to be the most useful in predicting the equilibrium critical thickness, h_c, for a mismatched epitaxial layer (see for e.g. Andersson *et al* 1987, Houghton *et al* 1990, Wang *et al* 1993). However, the subject is a highly contested one, with several workers reporting growth of coherently strained layers exceeding h_c found from the MB model (see for e.g. Bean *et al* 1984, Orders and Usher 1987). Large variations in measured critical thickness values are often explained by the particular sensitivity of the measurement process (Gourley *et al* 1988, Houghton *et al* 1990). For example, values of h_c for single QWs of InGaAs/GaAs have been determined using both low temperature photoluminescence (PL) and Hall measurements (Fritz *et al* 1987), and X-ray diffraction (Orders and Usher 1987). From these early studies, it was concluded that the optical spectroscopy, ie PL, is more sensitive to dislocation detection than X-ray diffraction. By measuring the optical properties of InGaAs/GaAs QW's, h_c was found to be consistent with the MB values, while results from X-ray diffraction indicated h_c values at least twice as large as those predicted from the MB model (see Gourley *et al* 1988 for further discussion). However, it should be noted that current X-ray mapping techniques comonly adopted are significantly more sensitive to lattice relaxation (cf. Fewster 1993, and §5.2.4). Recent studies, solely concerned with critical layer thickness measurements, tend to use several characterization techniques to support their conclusions (Houghton *et al* 1990, Wang *et al* 1993). In both these works, MQW structures were investigated and it was found that the MB model, with minor modifications, is also applicable. The question of MQW critical thickness and subsequent relaxation is relevant for the work in Chapter 5.

§2.4.1 Strain relaxation in (M)QW structures.

Proir to presenting the relevant MB equations, it is useful to graphically illustrate how strain relaxation via dislocations is thought to occur in strained layer structures (Houghton *et al* 1990). Two 'pure' mechanisms for elastic strain relaxation in strained layer MQW are illustrated (Fig.2-6). The initial structure is made up of material layers, A and B, which are grown on a thick substrate, which is also A (or at least has the same lattice constant as A). [The structure is similar to the InAsP/InP MQW samples grown on InP, which are experimentally investigated in Chapter 5.] Initially, the B layers are assumed to be coherently strained to fit the A substrate, i.e. $a_{||}^{MQW} = a_A$. The B layer is taken to have a larger bulk lattice parameter than the substrate so in the coherent picture, the compressive strain accommodated in the B layer is given by $e_{||}^{B} = (a_A - a_B)/a_B$ (upper diagram in Fig.2-6). For the first relaxation example, Fig.(2-6a), misfit dislocations are introduced at the first B/A interface, i.e. the beginning (base) of the MQW region. This is the most energetically favorable location for single misfit dislocations since here they reduce strain through the entire MQW (Hull *et al* 1986, Houghton *et al* 1990). As the mechanism proceeds, the MQW will tend to its 'free standing' in-plane lattice constant, $a_{||}^{MQW,fs}$, such that the strain is shared between both A and B layers (lower diagram of Fig.2-6a). In the second mechanism, (Fig.2-6b), misfit strain is relieved throughout the MQW region, for example, by paired dislocations or loops (Matthews and Blakeslee 1974). Each layer of the MQW tends towards its unstrained lattice parameter, so for this example, the strain in layer B will tend to zero while no strain occurs in layer A. Herein lies the principal difference between the two mechanisms. Upon completion, relaxation at the base of the MQW, Fig.(2-6a), has *shared* the strain, initially in the B layer, with the A layer.

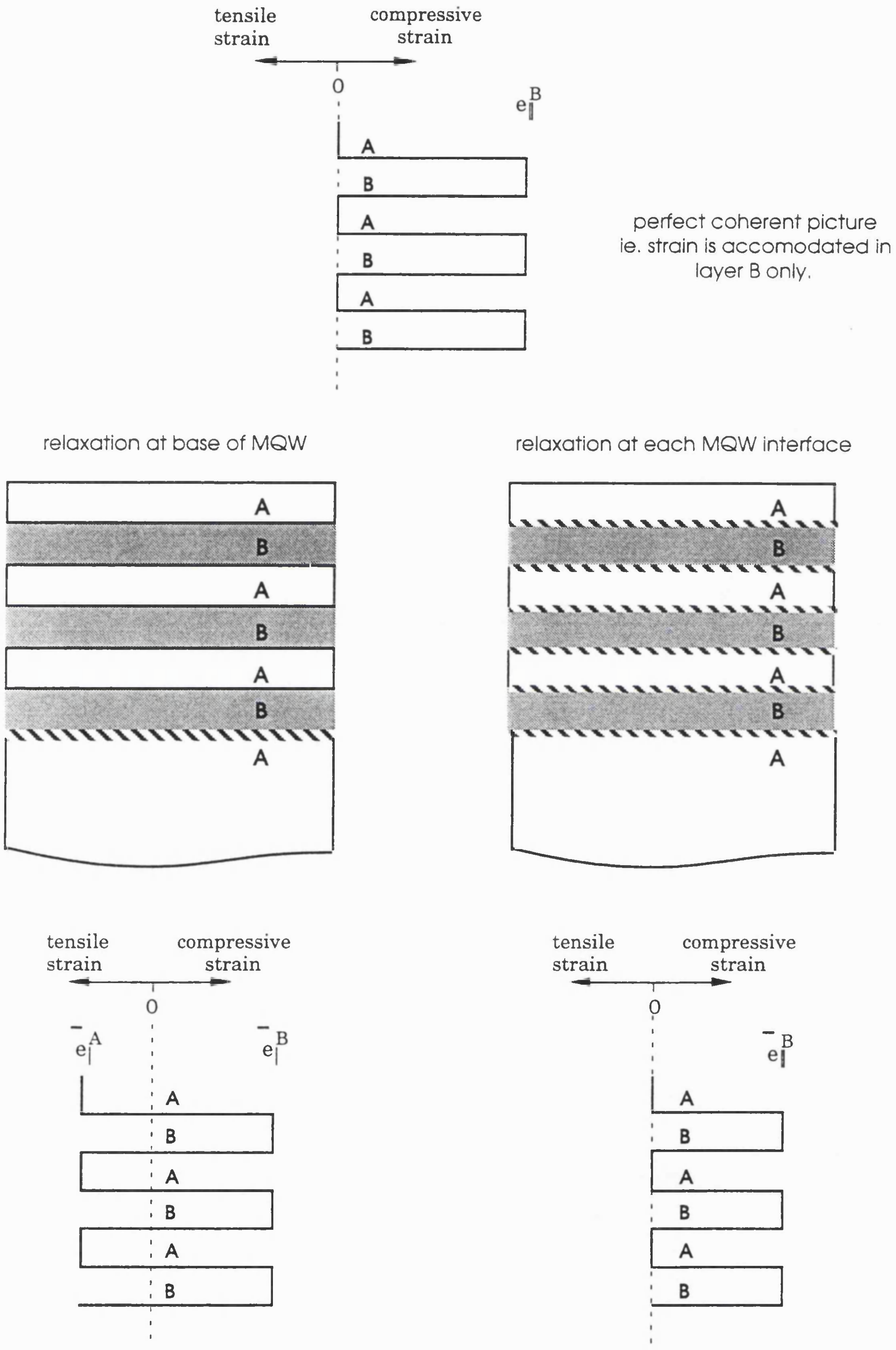

(a) (b)

Figure 2-6. *A schematic illustrating two possible mechanisms of strain relaxation in MQW structures (see text for further details).*

Coherence at the MQW interfaces is maintained in Fig.2-6a such that the in-plane lattice constant of the MQW is the same throughout the MQW region, tending towards the 'free standing' value. A more detailed discussion on the two mechanisms, aided with experimental investigations, is given by Houghton and co-workers (1990).

As to which of the two mechanisms will dominate in a structure, depends largely on the individual dimensions of the layers. For MQW regions with constituent layers thicker than their individual critical thickness, the process illustrated in Fig.2-6b is more likely to dominate. While in structures with layers less than their critical thickness, the integrated strain throughout the structure is thought to cause the MQW region to relax through the generation of misfit dislocations at the base of the MQW (Hull *et al* 1986, Houghton *et al* 1990). The possibility that the two mechanisms may co-exist in certain structures is thought to be unlikely, since the two relaxation mechanisms are competitive. Once some strain is relieved at the base, further relaxation at individual interfaces is energetically inefficient for MQWs with many periods (Houghton *et al* 1990).

§2.4.2 Critical thickness calculations.

For two semiconductor layers with unstrained lattice constants, a_o^A and a_o^B, the 'free standing' in-plane lattice constant of the two layers is given as (Matthews and Blakeslee 1976):

$$a_{\|}^{A/B,fs} = \frac{a_o^A G_A l_A + a_o^B G_B l_B}{G_A l_A + G_B l_B} \tag{2.4}$$

where $G_{A[B]} = 2\left(C_{11} + C_{12} - 2C_{12}^2/C_{11}\right)^{A[B]}$ are the shear moduli, and l_A and l_B are the thickness of the layers. For this equilibrium condition, the strains in the layers are written as:

$$e_{\|}^A = \frac{f_o G_B l_B}{G_A l_A + G_B l_B} \quad \text{and} \quad e_{\|}^B = -\frac{f_o G_A l_A}{G_A l_A + G_B l_B} \tag{2.5}$$

assuming $a_o^B > a_o^A$, with $f_o = \left(a_o^B - a_o^A\right)/a_o^A$ as the misfit between the layers . For equal shear parameters and lengths, the in-plane lattice constant is seen to lie halfway between the two unstrained values and the strain is equally shared between the two layers, i.e. $f_o/2$.

Growth of multilayers on a thick substrate, with lattice constant, a_0^s, such that $a_0^s \neq a_\parallel^{A/B,fs}$ changes the distribution of strain between the layers. The individual layer strains are now dominated by the mismatch with the substrate with the strain description in each layer given by (2.2) and (2.3). In their original work, Matthews and Blakeslee (1974), proposed two expressions to calculate the critical thickness of a layer in the presence of threading dislocations. The expressions were derived by balancing the forces arising from the dislocation line and the misfit strain, hence the model is often referred to as a force balance method. In the case when a dislocation is generated at lower interface of a strained layer, the critical thickness of the layer is a solution of:

$$h_c = \frac{b}{e_\parallel}\frac{\left(1 - \nu/4\right)}{4\pi(1+\nu)}\left[ln\left(\frac{h_c}{b}\right) + 1\right] \tag{2.6}$$

where b is the magnitude of the Burgers vector, taken as $b = a_0^i/\sqrt{2}$ for the strained layer (People and Jackson 1990), and ν is Poisson's ratio for the layer. The in-plane strain, $e_\parallel$, of the layer is obtained from (2.3). [note: the expression here assumes growth is on or near (100) surfaces, which is the case for all the structures investigated in this thesis.] Another mode of dislocation formation, generates dislocations at *each* interface of a buried strained layer. The critical thickness is given by:

$$h_c = \frac{b}{e_\parallel}\frac{\left(1 - \nu/4\right)}{2\pi(1+\nu)}\left[ln\left(\frac{h_c}{b}\right) + 1\right] \tag{2.7}$$

The components of (2.7) have the same meanings as before, so for a given strain the values of h_c predicted by (2.7) are twice as big as those found from (2.6), cf. Fig.2-7a. This is because with two interfaces to consider, twice the force of the dislocation line needs to be balanced (Matthews and Blakeslee 1974). It should be noted that in their original work, Matthews and Blakeslee (1974), mentioned the value calculated from the two interface model was *four* times larger than from the single interface model. The additional factor of two arises by assuming the half the strain in the layer was shared by an adjacent layer. In effect they calculated the critical thickness of a layer which formed part of a free standing superlattice.

In principle, to estimate the critical thickness of a single layer forming a MQW region, expression (2.7) should be used. Although, if the dislocations are formed during growth, then it appears sensible to use (2.6), since growth is by a single layer at a time. In practise, I have used (2.6), which can be viewed as a conservative estimate for the critical thickness of a single layer (cf. Fig.2-7a). It should also be noted, most of the critical thickness models, like the Matthews and Blakeslee model, are based on equilibrium considerations while it is apparent that kinetic forces, e.g. via substrate temperature or deposition rates, are known to effect the relaxation mechanism (see for e.g. Houghton 1991).

To determine a multilayer critical thickness, a method proposed by Hull *et al* (1986) and People (1986) treats the strained MQW region as a single strained layer. In these models, one assumes the growth of coherent multilayers on a substrate for which $a_o^s \neq a_{||}^{A/B,fs}$. The individual layers forming the MQW are assumed to be less than the single layer critical thickness for the given strain $e_{||}^{i}$. Since $a_o^s \neq a_{||}^{A/B,fs}$, the MQW as a whole experiences an additional in-plane strain, $e_{||}^{MQW}$, which is expressed in terms of the misfit between the free standing MQW and the substrate. Explicitly,

$$e_{||}^{MQW} = \frac{a_{||}^{A/B,fs} - a_o^s}{a_o^s} \tag{2.8}$$

The MQW/substrate mismatch, $e_{||}^{MQW}$, is simply the spatial average of the strain in a single period of the MQW. This misfit can be used to calculate the critical thickness of the MQW layer via (2.6). The reasoning behind using the single interface MB model, is that exceeding the multilayer critical thickness implies dislocations generated at the interface of the substrate and MQW as a whole, with the 'internal' interfaces of the MQW remaining coherent. Experimental studies by Hull and co-workers (1986), on Ge_xSi_{1-x}/Si strained-layer MQWs, demonstrated relaxation of a MQW structure in this manner.

Observing the onset of multilayer relaxation, has been reported by Wang and co-workers (1993) in a series of InGaAs/GaAs on GaAs MQWs with varying barrier widths. For the calculations, the authors used the average Indium composition in InGaAs/GaAs structures to construct an equivalent cubic layer. The critical thickness for this layer (w.r.t the GaAs substrate) was then determined using both the single and double interface models, (2.6) and (2.7) respectively. These values were then divided by the well width to give the number of periods that may be grown without relaxation. Performing X-ray diffraction and Normaski microscopy on the samples, the experimental results suggested the single layer model, (2.6), best described multilayer relaxation if the barrier width was the same, or greater, than the well width.

Undertaking a closer examination of their method (i.e. using the average composition in the structure), it is straightforward to show that in the case where one of the constituent layers in the MQW, (say A), is the same as the substrate, e.g. InAsP/InP MQW grown on InP. The free standing lattice constant, $a_{||}^{A/B,fs}$ of the MQW is equivalent to the cubic value determined from the average composition in the MQW. [note: this assumes the shear moduli are the same in both materials which is quite reasonable when the compositions are low.] The calculated critical thickness therefore corresponds to same values as if (2.8) were used. Therefore up to this stage, the authors were essentially following the method proposed by Hull *et al* (1986) and People (1986). An interesting point raised by their work, was the use of the average composition in the sample. Later on in the thesis, (Chapter 5), it is seen how the average composition of a structure is one of the parameters that can be accurately determined using X-ray diffraction. The role of the barrier width has also been noted in the work by David *et al* (1993), using plan view TEM with a series of partially relaxed InGaAs/GaAs MQW structures. For all samples with larger barrier widths than well widths no threading dislocations in the MQW region were observed, with the relaxation occurring in a manner similar to figure 2-6a. In a sample where the barrier width is smaller than the well width, threading dislocations in the MQW region were found. [note: the authors also noted the presence of dislocations at the MQW/capping layer interface].

One other effect that should be noted, comes from the recent experimental studies by Griffiths and co-workers (1993) in which a depth dependence of the relaxation mechanism was suggested. By probing, GaAs based InGaAs/GaAs MQW samples, with different laser wavelengths (which give different penetration depths), the authors examined the low temperature photoluminescence coming from various positions in the samples. Their results indicated that strain relaxation progresses gradually from the substrate, and that the QW nearest the surface exhibits the least strain. However, a closer inspection of the devices studied, reveals no capping layer was deposited, which would not be the case if the structure were a p-i(MQW)-n diode. Calculations of stresses in InGaAs/InP MQW structures (on InP) without capping layers, do predict a gradual redistribution of strain from the well to barrier layers with increasing distance from the base of the MQW. For the same structures with a capping layer, the strain in the well layers remains fixed throughout the structure (Nakajima 1992). In this respect, another explanation could account for the results obtained by Griffiths and co-workers, or quite possibily aid in a depth dependent relaxation process.

Single layer and multi-layer critical thickness calculations, are shown below. To make the results general, values of b=4Å and $\nu = 1/3$, typical for most III-V's have been used throughout. For the multilayer calculations, several well/barrier dimensions are chosen. In this case I have assumed structures with the form, $A_xB_{1-x}C$/BC grown on BC, i.e. the barriers are assumed to be unstrained and the misfit between $A_xB_{1-x}C$ and BC (plotted along x-axis) is accommodated in the well region.

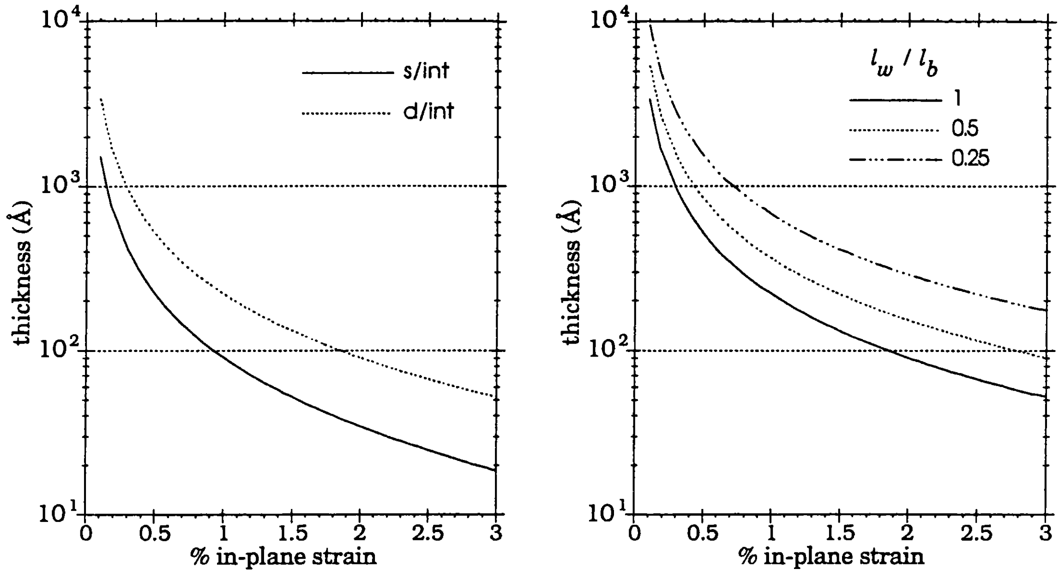

(a) (b)

Figure 2-7. *Calculated critical thickness values for varying in-plane strain ($e_{||}$). (a) using (2.6) single interface model and (2.7) double interface models. (b) a MQW critical thickness is calculated using (2.6) with $e_{||}$ determined from (2.4) and (2.8) for different well/barrier ratios. [note: the x-axis refers to the strain in the well region with the barriers assumed to be unstrained (see text for further details)].*

The results in figure 2-7b, show that for a given strain in the well layer, increasing the barrier thickness increases the predicted MQW critical thickness. This is to be expected, since for the types of structure chosen, increasing the barrier width reduces the average strain in one period and subsequently the integrated strain throughout the structure. This is verified by treating the A layer as the barrier material; with growth on an 'A' substrate, equation (2.8) reduces to:

$$e_{||}^{MQW} = f_0\left(\frac{G_B l_B}{G_A l_A + G_B l_B}\right) \qquad (2.9)$$

where $f_0 = \left(a_0^B - a_0^A\right)/a_0^A$ is the misfit between the layers.

For the MQW structures investigated in this work (Chapter 5), the strain to be accommodated in the well layer is always *less* than 1%. From the single layer critical thickness calculations, Fig.2-7a, this should allow well widths of up to ~100Å to be grown without causing individual layer relaxation. The calculation of multilayer critical thickness, suggest that for the number of periods we realistically need to consider (typically 30 upwards for a transverse geometry) the structure may relax by the mechanism illustrated in Fig.2-6a. It turns out, the structures in Chapter 5 do exhibit some degree of relaxation (deduced from high resolution X-ray diffraction), although it is noted both the optical and electrical properties are reasonably good.

This raises a rather obvious question regarding what effect the presence of dislocations have on the performance of prospective devices. Both the nature of the device and the relaxation mechanism (i.e. where the dislocations are) should to be specified. It is generally accepted that dislocations in the active region severely degrade the optical and electronic properties of the structure (J Singh 1993, chp.18). For example, dislocations are known to act as non-radiative recombination centers (E.P O'Reilly 1989), therefore the presence of dislocations in or near the active region of a QW laser, which relies on a radiative process, can serve to reduce efficiencies and the life of the laser (J Singh 1993, p738). However in MQW devices, relaxation by the mechanism in figure 2-6a, implies the active region is still relatively coherent, though with potentially a lot of dislocations at the MQW/buffer interface. Experimental results on strained InGaAs/GaAs MQW p-i-n structures, suggest some correlation between the dislocation density and the average strain, thickness of the MQW and thickness of the capping layer (David *et al* 1993). As already noted, most of the structures suggested a relaxation mechanism similar to figure 2-6a. With increasing dislocation density, the authors found the measured leakage currents in the devices got progressively higher. Bender and co-workers (1993) investigated high speed photodetectors from partially relaxed InGaAs/GaAs MQW samples, and found quantum efficiencies of unity for all the devices. In this sense the authors concluded that strain relaxation is not necessarily detrimental for fast photodetectors. Recently the optical properties of partially relaxed MQW modulators have been investigated (Ghisoni *et al* 1994). Although the QCSE was demonstrated for all the devices, it was found that for decreasing relaxation, the sharper defined exciton that results improves both the insertion loss and contrast ratio.

While it seems clear that partially relaxed structures are capable of demonstrating many of the properties associated with lattice matched structures, the long term stability of such MQW structures has yet to be adequately addressed (to my knowledge). This is particularly important in partially relaxed MQW structures which may be in some metastable state, and thereby degrade further through sustained operation, e.g. through heating effects. Similar doubts were initially feared in strained layer QW lasers, but on-going life-time testing has demonstrated that in some cases the strained QW lasers actually degrade less than lattice matched QW lasers (see O'Reilly and Adams 1994 and references therein). Further discussions concerning strain relaxation in MQW devices are presented in Chapter 5.

§2.5 Concluding Remarks.

The basic approach to strained layers and the modifications to heterostructrures has been presented. With regard to the work in this thesis, the use of strained layers in the active region, not only increases the constituent material choice but brings a further degree of flexibility in the design. This is demonstrated in Chapter 5 using theoretical and experimental investigations into $InAs_{1-x}P_x/InP$ (on InP) structures. In Chapter 6, a composite QW structure is proposed that is expected to exhibit electro-absorption characteristics *opposite* to that expected from conventional QW devices, i.e. a *blue* shift and corresponding *increase* in exciton strength with applied electric field. This structure comprises separate layers of InP, $In_zGa_{1-z}As$ and $InAs_{1-x}P_x$ and so to a large extent, is developed out of the ability to accommodate strained layers. As noted in §2.2.2 the strain induced modifications to the bulk layers, in particular band gaps and valence band splitting, have a direct bearing on the spectral positions of the excitonic transitions. Therefore any speculative investigation via modelling should at the very least include these effects. In the following two chapters, details of the modelling used for the present work are presented, taking into account the effects of strain. This is in addition to the more general calculations of the QCSE in heterostructures, i.e. subbands and exciton properties in an applied field.

References.

Andersson T.J, Chen Z.G, Kulakovski V.D, Uddin A, and Vallin J.T, *"Variation of the Critcal Thickness with In Content in Strained $In_xGa_{1-x}As$-GaAs Quantum Wells Grown by Molecular Beam Epitaxy"*, Appl. Phys. Lett., **51**, (1987), pp 752-754.

Baliga A, Trivedi D, and Anderson N.G, *"Tensile-Strain Effects in Quantum Well and Superlattice Band Structures"*, Phys. Rev., **B 49**, (1994), pp 10402-10416.

Bastard G, and Brum J.A, *"Electronic States in Semiconductor Heterostructures"* IEEE J. Quantum Electron., **QE-22**, (1986) pp 1625-1644.

Bean J.C, Feldman L.C, Fiory A.T, Nakahara S, and Robinson I.K, *"Ge_xSi_{1-x}/Si Strained-Layer Superlattice Grown by Molecular-Beam Epitaxy"*, J. Vac. Sci. Technol., **A2**, (1984), pp 436-440.

Bender G, Larkins E.C, Schneider H, Ralston J.D, Koidl, *"Strain Relaxation in High-Speed p-i-n Photodetectors with $In_{0.2}Ga_{0.8}As/GaAs$ Multiple Quantum Wells"*, Appl. Phys. Lett., **63**, pp 2920-2922.

Cartwright A.N, McCallum D.S, Boggess T.F, Smirl A.L, Moise T.S, Guido L.J, Barker R.C, Wherrett B.S, *"Magnitude, Origin, and Evolution of Piezoelectric Optical Nonlinearities in Strained [111]B InGaAs/GaAs Quantum Wells"*, J. Appl. Phys., **73**, (1993), pp 7767-7774.

Coleman J.J, in *Quantum Well Lasers*, Chapter 8, ed. P.S Zory, Academic Press, New York, (1993), pp 367-413.

Corzine S.W, Yan R.H, and Coldren L.A, in *Quantum Well Lasers*, Chapter 1, ed. P.S Zory, Academic Press, New York, (1993), pp 17-96.

David J.P.R, Kightley P, Chen Y.H, Goh T.S, Grey R, Hill G, and Robson P.N, *"Leakage Current Mechanisms in Strained InGaAs/GaAs MQW Structures"*, presented at GaAs and related Compounds Conference, Freiburg, Aug-Sept. (1993), pp 373-378.

Fewster P.F, *"X-ray Diffraction From Low-Dimensional Structures"*, Semicon, Sci. Technol. **8**, (1993), pp 1915-1934.

Feynman R.P, Leighton R.B, and Sands M, *The Feynman Lectures on Physics,* Vol. II, Addison-Wesley, Reading, (1964).

Fritz I.J, Gourley P.L, and Dawson L.R, *"Critical Layer Thickness in* $In_{0.2}Ga_{0.8}As/GaAs$ *Single Strained Quantum Well Structures"*, Appl. Phys. Lett., **51**, (1987), pp 1004-1006.

Gershoni D, Temkin H, Panish M.B, and Hamm R.A, *"Excitonic Transitions in Strained-Layer* $In_xGa_{1-x}As/InP$ *Quantum Wells"*, Phys. Rev., **B 39**, (1989), pp 5531-5534.

Ghisoni M, Parry G, Hart L, Roberts C, Marinopoulou A, and Stavrinou P.N, *"Effect of Well/Barrier Ratio on the Performance of Strained InGaAs/GaAs Quantum Well Modulators"*, Electron. Lett., **30**, (1994), pp 2067-2068.

Gomatam B.N, and Anderson N.G, *"Electroabsorption Enhancement in Tensile Strained Quantum-Wells via Absorption-Edge Merging"*, IEEE J. Quantum Electron., **QE-28**, (1992) pp 1496-1507.

Gourley P.L, Fritz I.J, and Dawson L.R, *"Controversy of Critical Layer Thickness for InGaAs/GaAs Strained-Layer Epitaxy"*, Appl. Phys. Lett., **52**, (1988), pp 377-379.

Goossen K.W, Caridi E.A, Chang T.Y, Stark J.B, and Miller D.A.B, *"Observation of Room Temperature Blue Shift and Bistability in a Strained InGaAs-GaAs <111> Self-*

Electro-Optic Effect Device", Appl. Phys. Lett., **56**, (1990), pp 715-717.

Hinckley J.M, and Singh J, "*Influence of Substrate Composition and Crystallographic Orientation on the Band Structure of Pseudomorphic Si-Ge alloy Films*", Phys. Rev., **B 42**, (1990), pp 3546-3566.

Houghton D.C, Perovic D.D, Baribeau J.M, and Weatherly G.C, "*Misfit Strain Relaxation in* Ge_xSi_{1-x}/Si *Heterostructures: The Structural Stability of Buried Strained Layers and Strained-Layer Superlattices*", J. Appl. Phys., **67**, (1990), pp 1850-1862.

Houghton D.C, "*Strain Relaxation Kinetics in* $Si_{1-x}Ge_x/Si$ *Heterostructures*", J. Appl. Phys., **70**, (1991), pp 2136-2151.

Hull R, Bean J.C, Cerdeira F, Fiory A.T, and Gibson J.M, "*Stability of Semiconductor Strained-Layer Superlattices*", Appl. Phys. Lett., **48**, (1986), pp 56-58.

Jesser W.A, and Fox B.A, "*On the Generation of Misfit Dislocations*", J. Elec. Mat., **19**, (1990), pp 1289-1297.

Ketterson A.A, Masselink W.T, Gedymin J.S, Klem J, Peng C-K, Kopp W.F, Morkoç H, and Gleason K.R, "*Characterisation of InGaAs/AlGaAs Pseudomorphic Modulation-Doped Field-Effect Transistors*", IEEE Trans. on Electron Devices, **33**, (1986), pp 565-571.

Krijn M.P.C.M, 't Hooft G.W, Boermans M.J.B, Thijs P.J.A, van Dongen T, Binsma J.J.M, Tiemeijer L.F, and van der Poel C.J, "*Improved Performance of Compressively as well as Tensile Strained Quantum Well Lasers*", Appl. Phys. Lett., **61**, (1992), pp 1772-1774.

Landolt-Börnstein, edited by Madelung, New Series, Group 3, Vol. 17a, (Springer, Berlin 1982) , pp 281-289; Vol. 22a, (Springer, Berlin 1989) pp 107-116.

Lu S.S, and Huang C.L, "*Piezoelectric Field Effect Transistor (PEFET) using* $In_{0.2}Ga_{0.8}As/Al_{0.35}Ga_{0.65}As/In_{0.2}Ga_{0.8}As/GaAs$ *Strained Layer Structure on (111)B GaAs Substrate*", Electron. Lett., **30**, (1994), pp 823-825.

Mailhiot C, and Smith D.L, "*Modulation of Internal Piezoelectric Fields in Strained-Layer Superlattices Grown along the [111] Orientation*", J. Vac. Sci., **A 7**, (1989), pp 609-615.

Marzin J.Y, Charasse M.N, and Sermage B, "*Optical Investigation of a New Type of Valence Band Configuration in* $In_xGa_{1-x}As$-*GaAs Superlattices*", Phys. Rev., **B 31**, (1985), pp 8298-8301.

Matthews J.W, and Blakeslee A.E, *"Defects in Epitaxial Multilayers: I. Misfit Dislocations"*, J. Cryst. Growth, **27**, (1974), pp 118-125.

Matthews J.W, and Blakeslee A.E, *"Defects in Epitaxial Multilayers: III. Preparation of Almost Perfect Multilayers"*, J. Cryst. Growth, **32**, (1976), pp 265-273.

Moise T.S, Guido L.J, and Barker R.C, *"Magnitude of the Piezoelectric Field in (111)B $In_yGa_{1-y}As$ Strained-Layer Quantum Wells"*, J. Appl. Phys., **74**, (1993), pp 4681-4684.

Nakajima K, *"Calculations of Stresses in $In_xGa_{1-x}As/InP$ Strained Multilayer Heterostructures"*, J. Appl. Phys., **72**, (1992), pp 5213-5219.

Nurmikko A.V, and Gunshor R.L, *"Blue-Green Emitters in Wide-Gap II-VI Quantum-Confined Structures"*, IEEE J. Quantum Electron., **QE-30**, (1994) pp 619-630.

Nye J.F, *Physical Properties of Crystals: Their Representation by Tensors and Matrices*, Oxford, Clarendon, (1957).

O'Reilly E.P, *"Valence Band Engineering in Strained-Layer Structures"*, Semicon. Sci. Technol., **4**, (1989), pp 121-137.

O'Reilly E.P, and Adams A.R, *"Bandstructure Engineering in Strained Semiconductor Lasers"*, IEEE J. Quantum Electron., **QE-30**, (1994) pp 366-379.

Osbourn G.C, *"Strained-Layer Superlattices from Lattice Mismatched Materials"*, J. Appl. Phys., **53**, (1982), pp 1586-1589.

Orders P.J, and Usher B.F, *"Determination of Critical Layer Thickness in $In_xGa_{1-x}As/GaAs$ Heterostructures by X-Ray Diffraction"*, Appl. Phys. Lett., **50**, (1987), pp 980-982.

Pabla A.S, Sanchez-Rojas J.L, Woodhead J, Grey R, David J.P.R, Rees G.J, Hill G, Pate M.A, Robson P.N, Hogg R.A, Fisher T.A, Willcox A.R.K, Whittaker D.M, Skolnick M.S, and Mowbray D.J, *"Tailoring of Internal Fields in InGaAs/GaAs Multiwell Structures Grown on (111)B GaAs"*, Appl. Phys. Lett., **63**, (1993), pp 752-754.

Pearsall T.P, (volume editor), *Semiconductors and Semimetals, Vol. 32 : Strained-Layer Superlattices:Physics*, Academic Press, New York, (1990)

People R, *"Correspondence between Coherently Strained Multilayers and a Single Coherently Strained Layer on Lattice Mismatch Substrate"*, J. Appl. Phys. **59**, (1986), pp 3296-3298.

People R, and Jackson S.A, in *Semiconductors and Semimetals, Vol. 32 : Strained-Layer Superlattices:Physics*, Chapter 4, vol.ed T.P Pearsall, Academic Press, New

York, (1990), pp 119-174.

Ravikumar K.G, Aizawa T, and Yamauchi R, *"Polarisation-Independent Field-Induced Absorption-Coefficient Variation Spectrum in an InGaAs/InP Tensile-Strained Quantum Well"*, IEEE Photon. Technol. Lett., **5**, (1993), pp 310-312.

Ruden P.P, Shur M, Arch D.K, Daniels R.R, Grider D.E, and Nohava T.E, *"Quantum-Well p-Channel AlGaAs/InGaAs/GaAs Heterostructure Insulated-Gate Field-Effect Transistors"*, IEEE Trans. on Electron Devices, **36**, (1989), pp 2371-2379.

Singh J, *Physics of Semiconductors and their Heterostructures*, McGraw-Hill, (1993).

Thijs P.J.A, Tiemeijer L.F, Binsma J.J.M, and van Dongen T, *"Progress in Long-Wavelength Strained-Layer InGaAs(P) Quantum-Well Semiconductor Lasers and Amplifiers"*, IEEE J. Quantum Electron., **QE-30**, (1994) pp 477-499.

Wang C.A, Groves S.H, Reinold J.H, and Calawa D.R, I, *"Critical Layer Thickness of Strained-Layer InGaAs/GaAs Multiple Quantum Wells Determined by Double-Crystal X-Ray Diffraction"*, J. Elec. Mat., **22**, (1993), pp 1365-1368.

Woodward T.K, Sizer II T, Sivco D.L, and Cho A.Y, *"$In_xGa_{1-x}As/GaAs$ Multiple Quantum Well Optical Modulators for the 1.02-1.07 μm Wavelength Range"*, Appl. Phys. Lett., **57**, (1990), pp 548-550.

Woodward T.K, Chiu T-H. and Sizer II T, *"Multiple Quantum Well Light Modulators for the 1.06 μm Range on InP Substrates: $In_yGa_{1-y}As_xP_{1-x}/InP$, $InAs_xP_{1-x}/InP$ and Coherently Strained $InAs_xP_{1-x}/In_yGa_{1-y}P$"*, Appl. Phys. Lett., **60**, (1992), pp 2846-2848.

Chapter 3: Stress, Strain and the k.p Theory: descriptions of constituent layers for heterostructures.

This chapter outlines a **k.p** model that aims to provide an accurate and simple description of bulk (un)strained semiconductor layers. Various levels of approximation are highlighted leading towards a description that is carried through to the following chapter which deals with heterostructure calculations. Several closed form expressions are presented which describe the band edge properties of semiconductors under the effects of strain.

§3.1 Introduction.

k.p theory is fundamentally a perturbation theory for exploring the properties of energy bands in the vicinity of some point in **k**-space. It is therefore well suited to semiconductors where the carriers of interest are situated near the Γ-point. A major advantage of the theory is that only a small number of parameters are required in order to produce an accurate description near the Γ-point (E.O Kane 1957). The parameters themselves can be determined accurately from various experiments involving optical absorption and cyclotron resonance (eg. Dresselhaus *et al* 1955). Its use for heterostructures was first established through the work by Bastard (1981, 1982), working within the envelope function approximation. Subsequently, the large amount of related work suggests it is the most widely used method for computing heterostructure properties in a variety of situations; see early review by Altarelli (1985), or specifically, Schuurmans and 't Hooft (1985), Eppenga *et al* (1987), for confined states and gain properties and Ekenberg and Altarelli (1984), Ram-Mohan *et al* (1988), Warburton *et al* (1991) for interpreting magneto-optic experiments. Comparisons with other methods of band structure calculations were encouraging. Schuurmans and 't Hooft compared energy-wavevector dispersions and confined states of GaAs/$Al_{1-x}Ga_xAs$ quantum wells with those produced using a tight binding description (Schulman and Chang 1985). Furthermore, Eppenga and co-workers computed the in-plane band structure of a GaAs/$Al_{0.25}Ga_{0.75}As$ quantum well with a **k.p** technique and compared the results to the same tight binding calculation. Excellent agreement between the two models was achieved.

The **k.p** method itself is subject to certain levels of approximation, many of the models mentioned so far (eg. Eppenga *et al* 1987) are based on a *full* 8 band **k.p** treatment (including spin). The description here includes the three highest valence bands and the lowest conduction band which are allowed to interact strongly with one another, their interactions with other remote bands are treated using perturbation theory. A similar set of bands were also considered by Smith and Mailhiot (1986) but here the bulk **k.p** parameters are calculated utilizing a pseudopotential calculation. This method avoids the assumption that the Bloch functions are the same throughout the heterostructure (cf. §4.1). Finally, one other approach is to neglect the interaction with remote bands that occurs in the *full* model (Bastard and Brum 1986, Marzin 1986, Johnson *et al* 1987). In this situation, known as the Kane model, closed form expressions of energy-wave vector relations can be obtained for each layer. The level of computing required is therefore substantially reduced. A useful comparison between this later approach with that of Smith and Mailhiot was presented for HgTe/CdTe superlattices (Johnson *et al* 1988). The energy levels, wave functions, effective masses and oscillator strengths were found to agree within 10%.

For the present work, the calculation of confined states in heterostructures is the main concern. Therefore only descriptions along the confinement (growth) axis will be considered (ie. k_z with $k_x = k_y = 0$). The *full* 8 band Hamiltonian becomes block diagonal and the problem reduces to a 4 band Hamiltonian (Schuurmans and 't Hooft 1985). The effects of strain are included and calculations of the energy-wavevector, $E(k_z)$, dispersion are obtained. Two Kane descriptions are also investigated, one of which is used for the subsequent heterostructure calculations (Chapter 4). As noted earlier, the main advantage of the Kane model is the substantial reduction in the level of computations required, though at the expense of a more complete description. Results are presented throughout the chapter, in particular, a comparison between the *full* and Kane **k.p** descriptions for various InP based materials, (§3.4). Also included is a further examination of the Kane approach leading to useful closed form expressions being derived (§3.5), which describe the effects of strain on the material parameters near the band edge.

§3.2 The k.p Method.

§3.2.1 Introduction to k.p theory.

The principles of **k.p** theory are briefly discussed. Extensive reviews on the subject can be found elsewhere, in particular, on the general description of semiconductors (E.O Kane 1966), and, on its application in heterostructures (G Bastard 1988).

Band structure basics

The wavefunctions in the conduction and valence band in a crystal are found by solving the time independent Schrödinger equation. This is written as

$$H_o\psi_{n\mathbf{k}}(\mathbf{r}) = \left[\frac{\hat{\mathbf{p}}^2}{2m_o} + V(\mathbf{r})\right]\psi_{n\mathbf{k}}(\mathbf{r}) = E_n\psi_{n\mathbf{k}}(\mathbf{r}) \tag{3.1}$$

where $\hat{\mathbf{p}}$ is the momentum operator, m_0 is the free electron mass, $V(\mathbf{r})$ is the periodic potential determined by the lattice, $\mathbf{r}$ is the position vector and n is the band index. With the periodicity of $V(\mathbf{r})$, the solutions of (3.1) have the form

$$\psi_{n\mathbf{k}}(\mathbf{r}) = e^{i\mathbf{k}\cdot\mathbf{r}} u_{n\mathbf{k}}(\mathbf{r}) \tag{3.2}$$

where $u_{n\mathbf{k}}(\mathbf{r})$ is a Bloch function that is periodic with V($\mathbf{r}$) and repeats itself in each unit cell of the crystal, **k** is the wavevector of the particle restricted to the first Brillouin zone. In heterostructures, an external slowly varying (over a unit cell) potential is also considered with the interest involving localised solutions of (3.1). Using an arbitrary set of expansion coefficients, A($\mathbf{k}$), a spatially localised wavefunction is expressed as

$$\begin{aligned} \psi_n(\mathbf{r}) &= \int A(\mathbf{k})\, e^{i\mathbf{k}\cdot\mathbf{r}} u_{n\mathbf{k}}(\mathbf{r})\, d\mathbf{k} \\ &\approx \left(\int A(\mathbf{k})\, e^{i\mathbf{k}\cdot\mathbf{r}}\, d\mathbf{k}\right) u_{no}(\mathbf{r}) \\ &= f_n(\mathbf{r}) u_{no}(\mathbf{r}) \end{aligned} \tag{3.3}$$

To arrive at the final form of (3.3), the main assumptions are that for a given energy band, the Bloch function is not dependent on **k** and can be represented by the band edge (**k**=0) Bloch function, $u_{no}(\mathbf{r})$. This is reasonable when we are interested in solutions near the band edge (see Altarelli 1985 for further discussion). The use of $u_{no}(\mathbf{r})$ removes it from the expansion which then defines an envelope function, $f_n(\mathbf{r})$, whose Fourier spectrum contains the plane wave components of the solutions in (3.2). This approach is known as the envelope function approximation (Luttinger and Kohn 1955) where the wavefunction consists of two components: the $u_{no}(\mathbf{r})$ functions which change rapidly on the atomic scale and the envelope functions, $f_n(\mathbf{r})$, which are slowly varying, changing on a scale that is much larger than the atomic spacing. In the following section, we are interested in obtaining a set of coupled equations for the envelope functions. Some properties of the $u_{no}(\mathbf{r})$'s are required although the Bloch functions themselves will not appear explicitly in the final equations.

*The **k.p** description*

The Hamiltonian of an electron in a solid is

$$H = \left[\frac{\hat{\mathbf{p}}^2}{2m_0} + V(\mathbf{r}) - e\phi(\mathbf{r})\right] \tag{3.4}$$

where V($\mathbf{r}$) is the potential of the solid, m_0 is the free electron mass, $\hat{\mathbf{p}}$ is the momentum operator and $-e\phi(\mathbf{r})$ is the potential of any applied electric field or potential due to a quantum well. The first step of **k.p** theory is to develop the wave function for the above Hamiltonian in the vicinity of some high symmetry point (usually the Γ-point) in terms of the band edge Bloch functions, $u_{io}(\mathbf{r})$, at that point, where i labels the band.

$$\psi(\mathbf{r}) = \sum_i f_i(\mathbf{r}) u_{io}(\mathbf{r}) \tag{3.5}$$

The band edge functions $u_{io}(\mathbf{r})$ have energies E_i according to

$$H_o u_{io}(\mathbf{r}) = E_i u_{io}(\mathbf{r}) \tag{3.6}$$

where H_o is the unperturbed Hamiltonian, similar to (3.1). The $u_{io}(\mathbf{r})$ can be labelled according to their symmetry properties (E.O Kane 1957), ie. for the lowest conduction band, S is used corresponding to an s-orbital, whereas, for the three highest valence bands, X, Y, Z are used corresponding to p-orbitals. To proceed, we apply H in equation (3.4) to a wavefunction of the form (3.5) and integrate over a unit cell. Since the envelope functions are slowly varying they are assumed constant over a unit cell and can be taken out of the integral. We find

$$\sum_j H_{ij} f_j = E f_i \tag{3.7}$$

with

$$H_{ij} = \left(E_j + \frac{\hat{\mathbf{p}}^2}{2m_o} - e\phi(\mathbf{r}) \right) \delta_{ij} + \frac{\hat{\mathbf{p}}}{m_o} \mathbf{P}_{ij} \tag{3.8}$$

where E_j is given by equation (3.6) and

$$\mathbf{P}_{ij} = \int_{\text{unit cell}} u_{io}^*(\mathbf{r}) \hat{\mathbf{p}} u_{jo}(\mathbf{r}) d\mathbf{r} \tag{3.9}$$

The index i runs, in principle, over all the energy bands of the crystal so as it stands equation (3.7), would provide a realistic description of the band structure. However, for practical calculations, a limited (*near*) set of bands are usually chosen which cover the energy range of interest. The bands in this near set are allowed to interact strongly with one another whereas interactions with the other bands (*far set*) are accommodated through a perturbation theory described by Löwdin (1951). The final set of equations (3.7) are for the near states but (3.8) is modified to contain the influence of the far set (see eg. G Bastard 1988 p50). Explicitly, (3.8) becomes:

$$U_{ij}^n = \left(E_j + \frac{\hat{\mathbf{p}}^2}{2m_o} - e\phi(\mathbf{r}) \right) \delta_{ij} + \frac{\hat{\mathbf{p}}}{m_o} \mathbf{P}_{ij} + \frac{\hat{\mathbf{p}}^2}{m_o^2} \sum_q^f \frac{\mathbf{P}_{iq} \mathbf{P}_{qj}}{E_j - E_q} \tag{3.10}$$

or

$$U^{n}_{ij} = (E_j - e\phi(\mathbf{r}))\delta_{ij} + \frac{\hat{\mathbf{p}}}{m_o}\mathbf{P}_{ij} + \frac{1}{2}\sum_{\alpha\beta} D^{\alpha\beta}_{ij}\,\hat{\mathbf{p}}_\alpha\,\hat{\mathbf{p}}_\beta \tag{3.11}$$

with α,β = x, y, z and

$$D^{\alpha\beta}_{ij} = \frac{1}{m_o}\delta_{ij}\delta_{\alpha\beta} + \frac{2}{m_o^2}\sum_{q}^{f}\frac{\mathbf{P}^{\alpha}_{iq}\,\mathbf{P}^{\beta}_{qj}}{E_j - E_q} \tag{3.12}$$

Here U^{n}_{ij} is the modified H_{ij} where i, j run over the near set (n) and q is over the far set (f). The structure of equation (3.11) shows the effective mass tensor $D^{\alpha\beta}_{ij}$ (Luttinger and Kohn 1955) and the linear term (in momentum) responsible for coupling between the s-like conduction band and the p-like valence bands in the near set through the Kane matrix element, $\mathbf{P}_{ij}$ (E.O Kane 1966).

In (3.1) and (3.4), the spin-orbit operator which accounts for the spin-orbit interaction (see eg. E.O Kane 1966) was neglected. When included, it is usually made diagonal by using linear combinations of Bloch p functions (ie. $X\uparrow, X\downarrow, Y\uparrow, Y\downarrow, Z\uparrow, Z\downarrow$) as a basis in the expansion of equation (3.5). With the new basis, known as the angular momentum representation $|J, m_j\rangle$ (Luttinger and Kohn 1955, E.O Kane 1956), the spin-orbit coupling is diagonal at **k**=0 and is therefore included in the values of E_i from (3.6) . If the interaction were not considered, the three highest valence bands would appear degenerate at **k**=0. As it is, the interaction partially removes the degeneracy, leaving the degenerate heavy -and light-hole bands higher in energy than the spin-orbit split-off band (Fig.3-1)

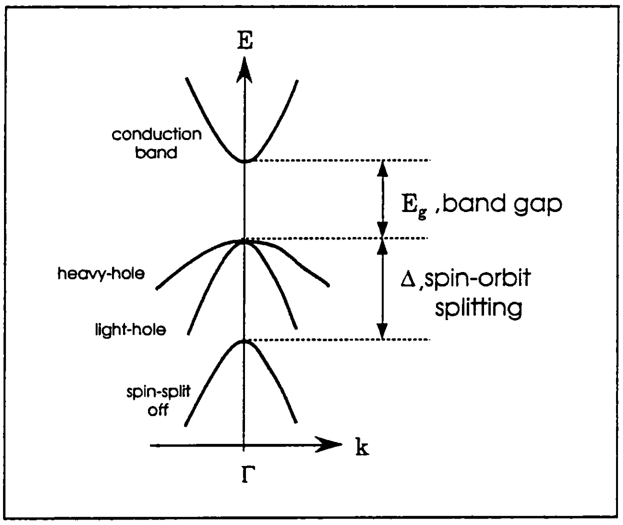

Figure 3-1. *A Schematic of the band structure of a direct gap III-V semiconductor near the Γ-point.*

Finally, this set of basis functions are used to evaluate the elements of the Hamiltonian (U^n_{ij}) which then operates on the envelope functions f_i.

$$\sum_j U^n_{ij} f_j = E f_i \tag{3.13}$$

Using the angular momentum basis states given by E.O Kane (1966), the elements of U^n_{ij} were calculated by Schuurmans and 't Hooft (1985). The bands they included in the near set were the lowest conduction band, heavy- and light-hole band and spin-orbit split-off band in a 4 band Hamiltonian in k_z (ie. $k_x=k_y=0$). These basis states and Hamiltonian are used in the present work. For completeness, this is presented in the following section.

§3.2.2 Four band k.p description.

The $\left|J, m_j\right\rangle$ basis functions used by E.O Kane (1966) to diagonalize the spin-orbit interaction are written as

$$u_{el} = \left|\tfrac{1}{2},\tfrac{1}{2}\right\rangle = \left|S\uparrow\right\rangle \qquad [Eg] \tag{3.14a}$$

$$u_{hh} = \left|\tfrac{3}{2},\tfrac{3}{2}\right\rangle = \frac{1}{\sqrt{2}}\left|X\uparrow\right\rangle + \frac{1}{\sqrt{2}}\left|iY\uparrow\right\rangle \qquad [\ 0\ ] \tag{3.14b}$$

$$u_{lh} = \left|\tfrac{3}{2},\tfrac{1}{2}\right\rangle = \frac{1}{\sqrt{6}}\left|X\downarrow\right\rangle + \frac{1}{\sqrt{6}}\left|iY\downarrow\right\rangle - \sqrt{\frac{2}{3}}\left|Z\uparrow\right\rangle \qquad [\ 0\ ] \tag{3.14c}$$

$$u_{so} = \left|\tfrac{1}{2},\tfrac{1}{2}\right\rangle = \frac{1}{\sqrt{3}}\left|X\downarrow\right\rangle + \frac{1}{\sqrt{3}}\left|iY\downarrow\right\rangle + \frac{1}{\sqrt{3}}\left|Z\uparrow\right\rangle \qquad [-\Delta] \tag{3.14d}$$

where the energies at the Γ-point ($\mathbf{k}=0$) are listed alongside in square brackets. There is another set corresponding to opposite spin of the bands ie. m_j->$-m_j$. However by neglecting inversion asymmetry and disregarding the k-dependent spin-orbit coupling (E.O Kane 1966), the eigenvalues will occur in degenerate pairs (Schuurmans and 't Hooft 1985). Essentially the 8 band problem (including spin) is reduced to 4 bands (neglecting spin) for $k_x=k_y=0$ ($k_{||}=0$). For $k_{||}=0$, the wave function is written as:

$$\psi^l = \sum_j f^l_j(z) u^l_{jo}(\mathbf{r}) \tag{3.15}$$

where $f^l_j(z)$ is the slowly varying envelope of the wave function and $u^l_{jo}(\mathbf{r})$ is the rapidly varying band edge Bloch part. Anticipating the later work with heterostructures, it will be useful to present all the following equations with the superscript designations, l, where ($l = w, b$) referring to either the well or barrier material. The label j runs over the states from the near set in (3.14) and also over the far set of Γ-point states. Coupling between near and far states are treated by perturbation theory, (§3.2.1). Writing the time-independent Schrödinger equation for the heterostructure problem, in matrix form:

$$\left\{\mathbf{U}^l - \delta E_v^l \mathbf{I}\right\}\mathbf{F}^l = \{E\mathbf{I}\}\mathbf{F}^l \tag{3.16}$$

where $\mathbf{F}^l$ is column vector of $\left(f_{el}^l, f_{hh}^l, f_{lh}^l, f_{so}^l\right)$, $\mathbf{I}$ is the unit matrix and $\mathbf{U}^l$ is the matrix operator of (3.11) written as:

$$\begin{array}{cc} & \begin{array}{cccc} el & hh & lh & so \end{array} \\ \mathbf{U}^l = & \left[\begin{array}{cccc} E_g^l + s^l\hat{\varepsilon} & 0 & -i\sqrt{\frac{2}{3}}\mathbf{P}^l\hat{k}_z & i\sqrt{\frac{1}{3}}\mathbf{P}^l\hat{k}_z \\ 0 & -(\gamma_1^l - 2\gamma_2^l)\hat{\varepsilon} & 0 & 0 \\ i\sqrt{\frac{2}{3}}\mathbf{P}^l\hat{k}_z & 0 & -(\gamma_1^l + 2\gamma_2^l)\hat{\varepsilon} & 2\sqrt{2}\gamma_2^l\hat{\varepsilon} \\ -i\sqrt{\frac{1}{3}}\mathbf{P}^l\hat{k}_z & 0 & 2\sqrt{2}\gamma_2^l\hat{\varepsilon} & -\Delta^l - \gamma_1^l\hat{\varepsilon} \end{array}\right] \end{array} \tag{3.17}$$

with the operator $\hat{\varepsilon} = \frac{\hbar^2\hat{k}_z^2}{2m_o}$ and $\hat{k}_z \to -i\frac{\partial}{\partial z}$. E_g^l is the bulk band gap at the Γ-point and is the spin-orbit splitting in the valence band. The zero of energy is taken at the top of the valence band as is evident from (3.14). The coupling between the light states ($m_j = ½$) is described by the Kane matrix element, $\mathbf{P}^l$, which is given by

$$\mathbf{P}^l = -i\frac{\hbar}{m_0}\int_{\text{unit cell}} u_s^l(\mathbf{r})\hat{p}_z u_z^l(\mathbf{r})\,d\mathbf{r} \tag{3.18}$$

The parameters s^l, γ_1^l and γ_2^l describe the combined effect of the free electron term and the interaction with bands in the far set for the s state (s^l) and p states (γ_1^l and γ_2^l). The parameters for the p states are *similar* to those first used by Luttinger (1956) only now they neglect the interaction of the s state, since in the present case, this is included in the near set. They are related to the usual Luttinger parameters ($\gamma_{1,L}^l$ and $\gamma_{2,L}^l$) by the equations (Schuurmans and 't Hooft 1985)

$$\gamma_1^l = \gamma_{1,L}^l - \frac{E_P^l}{3E_g^l} \tag{3.19}$$

$$\gamma_2^l = \gamma_{2,L}^l - \frac{E_P^l}{6E_g^l} \tag{3.20}$$

where, $E_P^l = \dfrac{2m_o\left(\mathbf{P}^l\right)^2}{\hbar^2}$ and has units of energy.

The term δE_v^l is the energy offset of the valence band between the well and barrier material (cf. §1.2.2), formally written as

$$\delta E_v^l = \begin{cases} 0 \text{ for } l = w \\ Q_v\left(E_g^b - E_g^w\right) \text{ for } l = b \end{cases} \tag{3.21}$$

where Q_V is the valence band offset parameter specifying how much of the difference in the band gaps (ie. total confinement energy) is shared in favour of the valence band. For type I structures, the $E(k_z)$ relations obtained from (3.16) will put the valence band edge of the barrier material an energy δE_v^l lower than the valence band edge of the well material.

In choosing bulk wavefunctions for the envelopes f_j^l and solving (3.16), we obtain the energy relation, $E(k_z)$, for each material in the heterostructure. The effects of strain are still to be considered for the structures here, but as it stands (3.17) can be used for any lattice matched heterostructures eg. GaAs/$Al_xGa_{1-x}As$ (Schuurmans and 't Hooft 1985). One useful point to note is that the heavy hole states ($m_j = 3/2$) do not couple to the light states ($m_j = 1/2$) in (3.17). Later, it is seen how this feature further simplifies the calculations in that the heavy hole envelope functions can be treated separately from the light states. The next section shows how the effects of strain can be incorporated in the theory.

§3.3 Stress, Strain and the k.p Theory.

In §2.1, it was shown that the nature of stress and strain on a crystal lattice can be described using tensors. The stress tensor components, σ_{ij}, describe the force (or stress) acting on the crystal while the strain tensor components, e_{ij}, describe the lattice distortion arising from the stress. In this section, the involvement of strain in the **k.p** approach is briefly reviewed. As with the previous section, I will note what I believe are the main points involved with the emphasis on the modelling requirements set out at the beginning of this chapter. Further comprehensive details can be obtained from the published literature concerning the effects of strain on the band structure of diamond and zinc-blende semiconductors (eg. Pikus and Bir 1959 & 1974, T. Bahder 1990), and in particular, Volume 32 of Semiconductors and Semimetals (ed Pearsall 1990) which is dedicated to strained layer superlattices.

Considering a heterostructure made from two materials (well *w* and barrier *b*) with unstrained lattice constants a_o^w and a_o^b. Recall for pseudomorphic strained layer growth (along z axis) the in-plane lattice constant $a_{||}$ (in x, y planes) will be the same throughout the structure (cf. §2.2). Since growth is on a thick substrate (typ.~ 300μm), this will be the dominant lattice constant in the structure (a_o^s). The substrate then imposes its lattice constant on the well and barrier material to satisfy the condition $a_{||}$ is constant.

For the case when $a_o^w \neq a_o^s$ (ie. the situation investigated the present work), the well material will deform to take on the in-plane lattice constant (ie. that of the substrate). The in-plane components of the strain tensor are given as:

$$e_{||}^w = \frac{a_o^s - a_o^w}{a_o^w} \tag{3.22}$$

and

$$e_{zz}^w = -\frac{2C_{12}^w}{C_{11}^w} e_{||}^w \tag{3.23}$$

where the C_{ij} parameters are the bulk elastic coefficients for the material. With a knowledge of the strain tensors e_{ij}, the effects of strain can be treated as an additional perturbation to the Hamiltonian in equation (3.4). In their original work, Pikus and Bir (1959) realised that due to the deformation of the lattice, a transformation of coordinates is required so when the wavefunctions of the perturbed Hamiltonian (3.4) are expanded in terms of the wavefunctions of the unperturbed Hamiltonian *both* functions will have the same periodicity. Applying this transformation, the perturbed wavefunctions have the periodicity of the unstrained lattice and the expansion can proceed in a similar manner to that described in §3.2. In their work, Pikus and Bir (1959), neglected terms of $O(e^2)$ and $O(ek^2)$ and strain interactions between the far set were not included. The final Hamiltonian reduced to the sum of two matrices:

$$\mathbf{H}_{total} = \mathbf{H}(\mathbf{k}) + \mathbf{H}(\mathbf{e}) \tag{3.24}$$

The basis states chosen (near set) were the valence band states (X, Y, Z) so the strain independent matrix **H(k)** is just that given by Luttinger and Kohn (1955) while **H(e)** contained strain terms of O(e). The strain terms are energy corrections to the respective band edges of the material. Following the approach of Pikus and Bir, an 8 band **k.p** model for strained zinc-blende crystals was presented by Bahder (1990). The inclusion of the conduction band in the near set (S, X, Y, Z) meant that for his work **H(k)** was identical to the interaction matrix from Kane (1966). The strain dependent matrix now contained the coupling of the conduction band to the hydrostatic deformations and additional terms that couple the conduction and valence band. In transforming this matrix to the angular momentum representation, the strain dependent spin-orbit interactions are small and can be ignored (Bahder 1990) so the basis states given by Kane (1966) will suffice. Terms that arise due to the inversion asymmetry of zinc-blende structures can also be neglected (keeping on equal footing with the Schuurmans and 't Hooft Hamiltonian §3.2.2). Although, since these terms couple the conduction and valence bands through e_{ij} where $i \neq j$ (Bahder 1990), they would be zero for the structures in this work anyway.

For the angular momentum basis states in equations (3.14);

$$\mathbf{H}^{l}_{total} = \mathbf{U}^{l} + \mathbf{D}^{l}_{o} \tag{3.25}$$

where $\mathbf{U}^{l}$ is the Hamiltonian of Schuurmans and 't Hooft (3.17), and $\mathbf{D}^{l}_{o}$ is the strain dependent Hamiltonian.

In matrix form with $k_{\|}=0$, the strain contribution is :

$$\begin{array}{cc} & \begin{array}{cccc} \quad el \quad & \quad hh \quad & \quad lh \quad & \quad so \quad \end{array} \\ \mathbf{D}^{l}_{o} = & \begin{bmatrix} \delta E_{h}^{(c)l} & 0 & i\sqrt{\frac{2}{3}} e^{l}_{zz} \mathbf{P}^{l} \hat{k}_{z} & -i\sqrt{\frac{1}{3}} e^{l}_{zz} \mathbf{P}^{l} \hat{k}_{z} \\ 0 & \delta E_{h}^{(v)l} - \frac{1}{2}\delta E_{s}^{l} & 0 & 0 \\ -i\sqrt{\frac{2}{3}} e^{l}_{zz} \mathbf{P}^{l} \hat{k}_{z} & 0 & \delta E_{h}^{(v)l} + \frac{1}{2}\delta E_{s}^{l} & -\sqrt{\frac{1}{2}}\delta E_{s}^{l} \\ i\sqrt{\frac{1}{3}} e^{l}_{zz} \mathbf{P}^{l} \hat{k}_{z} & 0 & -\sqrt{\frac{1}{2}}\delta E_{s}^{l} & \delta E_{h}^{(v)l} \end{bmatrix} \end{array} \tag{3.26}$$

where $\mathbf{P}^{l}$ is defined in (3.18) and as before, $\hat{k}_{z} \rightarrow -i\frac{\partial}{\partial z}$. The structure of $\mathbf{D}^{l}_{o}$ can be written as,

$$\mathbf{D}^{l}_{o} = \mathbf{D}^{l}_{o}(\mathbf{e}) + \mathbf{D}^{l}_{o}(\mathbf{e}\hat{k}_{z}) \tag{3.27}$$

where the main contribution of strain comes from the first matrix $\mathbf{D}^{l}_{o}(\mathbf{e})$ which determines the energy shifts of the band edges in the presence of strain.

The elements are defined as :

$$\delta E_h^{(c)l} = a_c^l(2e_{||}^l + e_{zz}^l) \qquad (3.28)$$

$$\delta E_h^{(v)l} = a_v^l(2e_{||}^l + e_{zz}^l) \qquad (3.29)$$

$$\delta E_s^l = 2b^l(e_{zz}^l - e_{||}^l) \qquad (3.30)$$

The hydrostatic shifts of the conduction and valence band, $\delta E_h^{(c)l}$ and $\delta E_h^{(v)l}$ respectively, are determined by the proportional change in volume, $(2e_{||}^l + e_{zz}^l)$. a_c^l and a_v^l are the hydrostatic deformation potentials of the conduction and valence band edges respectively (E.P O'Reilly 1989). The uniaxial strain, which lifts the degeneracy of the valence band, enters as $(e_{zz}^l - e_{||}^l)$ with b^l as the shear deformation potential. The coupling between the light hole and the spin-orbit split-off band, (off diagonal terms in $\mathbf{D}_0^l(\mathbf{e})$), causes the splitting of the heavy and light hole band edges to be nonlinear with strain; although, when $\Delta^l >> |b^l(e_{zz}^l - e_{||}^l)|$ the coupling has little effect and the heavy - to light- hole splitting is $\approx 2b^l(e_{zz}^l - e_{||}^l)$ (Marzin *et al* 1990).

The second matrix in (3.27) arises from Bahder's re-examination of a **k.p** description for strained materials, (Bahder 1990), and describes the strain coupling between the conduction and valence bands away from the band edge $(k_z \neq 0)$. Previous work had often overlooked $\mathbf{D}_0^l(\mathbf{e}\hat{k}_z)$ despite including the conduction band in the near set (eg. Jogai and Yu 1990, F.H Pollak 1990, Marzin *et al* 1990, People and Sputz 1990), although more recently, Gershoni *et al* (1993) have included it in their study. The importance of the term has (to my knowledge) yet to be established in heterostructure calculations; although by inspection, the effect of $\mathbf{D}_0^l(\mathbf{e}\hat{k}_z)$ is seen to be small in comparison to the equivalent matrix element appearing in the unstrained Hamiltonian, (3.17). [note: typical values of the strain tensor are $|e_{zz}| \leq 0.02$, actually less than 1% for the work in Chapter 5]. Neglecting this term therefore appears to be quite a reasonable approximation.

§3.4 Band Structure Calculations.

The total Hamiltonian, $\mathbf{H}_{total}^l$, for region l in a structure can be constructed by using the two matrices $\mathbf{U}^l$ in (3.17) and $\mathbf{D}_0^l$ in (3.26). With $\mathbf{H}_{total}^l$ in place of $\mathbf{U}^l$ in (3.16) and choosing bulk solutions for the envelope functions, the E(k_z) dispersion can be obtained for each layer in the structure. However, the term δE_v^l in (3.16) corresponds to the *unstrained* valence band discontinuity, so the zero of energy would indicate the top of the valence band in the *unstrained* well material ($l = w$). I have found when dealing with heterostructures it is often convenient to treat the band discontinuity as a variable parameter. Particularly when looking at material combinations that have not been widely studied and have unfamiliar band discontinuities. Turning to a structure where one of the materials is strained, the term *valence band discontinuity* is ambiguous because of the non-degenerate valence band. In view of this, I decided to take the valence band discontinuity, δE^{l}_{vhh}, as being with respect to the heavy hole band edges, and furthermore to keep the zero of energy coinciding with the heavy hole band edge of the well material. Formally, this requires a simple matrix calculation on the strain Hamiltonian (3.26) written as:

$$\mathbf{D}^{l} = \mathbf{D}^{l}_{o} + \mathbf{D}^{l}_{shift} \tag{3.31}$$

where $\mathbf{D}^{l}_{o}$ is given in (3.26) and $\mathbf{D}^{l}_{shift}$ is simply,

$$\mathbf{D}^{l}_{shift} = \left(-\delta E^{(v)l}_{h} + \frac{1}{2}\,\delta E^{l}_{s} \right)\mathbf{I} \tag{3.32}$$

The final strain Hamiltonian, $\mathbf{D}^{l}$, has the diagonal elements defined with respect to the heavy hole diagonal element (now set to zero). With δE^{l}_{vhh} in place of δE^{l}_{v} in equation (3.16) the $E(k_z)$ dispersions for all the layers have the zero of energy coinciding with the heavy hole band edge of the well material. A useful consequence of applying (3.31) is that the hydrostatic shift of the conduction band relative to the valence bands can be described by one term, $\delta E^{(gap)l}_{h}$, given as:

$$\begin{aligned} \delta E^{(gap)l}_{h} &= \delta E^{(c)l}_{h} - \delta E^{(v)l}_{h} \\ &= \left(a^{l}_{c} - a^{l}_{v} \right)\left(2e^{l}_{\|} + e^{l}_{zz} \right) \\ &= a^{l}_{gap}\left(2e^{l}_{\|} + e^{l}_{zz} \right) \end{aligned} \tag{3.33}$$

Here, a^{l}_{gap} is the deformation potential of the band gap and is a parameter that is often measured experimentally (see Appendix A).

§3.4.1 Using full k.p theory.

This section describes the calculation of the bulk band structure, $E(k_z)$, for a material using a *full* **k.p** description. For the purpose of the work in this thesis, *full* is taken to mean the level of description involved in obtaining the Schuurman and 't Hooft Hamiltonian (3.17). The following section (§3.4.2) deals with a simpler form of (3.17), hence the need to distinguish between the two for later discussion.

The bulk envelope functions are taken as $f^l_j \propto e^{ik_z z}$, then the operator goes $\hat{k}_z \rightarrow k_z$. The energy-dispersion relation $E(k_z)$ can be found from,

$$\left\{\mathbf{H}^l_{total} - \delta E^l_{vhh}\mathbf{I}\right\}\mathbf{F}^l = \{E\mathbf{I}\}\mathbf{F}^l \tag{3.34}$$

where the total Hamiltonian for each layer in the heterostructure is,

$$\mathbf{H}^l_{total} = \mathbf{U}^l\left(\hat{k}_z \rightarrow k_z\right) + \mathbf{D}^l\left(\hat{k}_z \rightarrow k_z\right) \tag{3.35}$$

$\mathbf{U}^l$ and $\mathbf{D}^l$ are given in equations (3.17) and (3.31) respectively. The heavy hole valence band discontinuity is in this case:

$$\delta E^l_{vhh} = \begin{cases} 0 \text{ for } l = w \\ Q_v\left(E^b_{gs} - E^w_{gs}\right) \text{ for } l = b \end{cases} \tag{3.36}$$

with Q_v as the heavy hole valence band offset parameter and E^l_{gs} defined later (3.54) as the strained conduction to heavy hole band gap. [note: for unstrained materials E^l_{gs} reduces to E^l_g]

The far band terms in $\mathbf{U}^l$, namely γ^l_1, γ^l_2 and s^l along with the matrix element $\mathbf{P}^l$ are determined from knowledge of the four band edge effective masses m^l_{el}, m^l_{hh}, m^l_{lh} and m^l_{so} and energy gaps (E^l_g, Δ^l) at the Γ-point of each unstrained bulk material. We find in (3.17) for small k_z, the dispersions of all the bands are parabolic with effective masses (Schuurmans and 't Hooft 1985):

$$\frac{m_o}{m^l_{el}} = s^l + \frac{2E^l_P}{3E^l_g}\left(1 + \frac{1}{2}\frac{E^l_g}{E^l_g + \Delta^l}\right) \tag{3.37a}$$

$$\frac{m_o}{m^l_{hh}} = \gamma^l_1 - 2\gamma^l_2 \tag{3.37b}$$

$$\frac{m_o}{m^l_{lh}} = \gamma^l_1 + 2\gamma^l_2 + \frac{2E^l_P}{3E^l_g} \tag{3.37c}$$

$$\frac{m_o}{m^l_{so}} = \gamma^l_1 + \frac{1}{2}\left(\frac{2E^l_P}{3E^l_g}\right)\frac{E^l_g}{E^l_g + \Delta^l} \tag{3.37d}$$

where

$$E_P^l = \frac{2m_0\left(P^l\right)^2}{\hbar^2}\ \text{(eV)} \tag{3.38}$$

Experimentally determined masses and energy gaps for most binary III-V semiconductors are well reported (eg. Landolt-Börnstein 1982, 1989). In the case of ternary materials ($A_xB_{1-x}C$) only a few have been adequately studied. A common way around this problem is to interpolate between the two constituent binary materials in accordance with the virtual crystal approximation (eg. Loehr and Manasreh 1993). Here the total crystal potential $V_{A_xB_{1-x}C}(\mathbf{r})$ is assumed to be the average potential $xV_{AC}(\mathbf{r}) + (1-x)V_{BC}(\mathbf{r})$. Considering the case of the Luttinger parameters ($\gamma_{1,L}$ and $\gamma_{2,L}$) these are directly related to matrix elements of the crystal potential so ,

$$\gamma_{n,L}^{A_xB_{1-x}C} = x\gamma_{n,L}^{AC} + (1-x)\gamma_{n,L}^{BC} \quad , \ n = 1,2 \tag{3.39}$$

will give the Luttinger parameters for the ternary material (Loehr and Manasreh 1993). It is therefore appropriate in this case to use equations (3.19) and (3.20) to obtain the modified Luttinger parameters used in (3.17).

With the elements of $\mathbf{H}_{total}^l$ and the offset δE_{vhh}^l known the energy dispersion relation can be found from the characteristic equation:

$$\left\| \mathbf{H}_{total}^l - \left(\delta E_{vhh}^l + E\right)\mathbf{I} \right\| = 0 \tag{3.40}$$

which, at given energy, E, requires the solution of a polynomial of degree 4 in $(k_z^l)^2$ giving eight k_z^l solutions. The same result is obtained if (3.34) is recast into an eigenvalue problem for k_z^l, so for a given energy, E, the eigenvalues k_z^l can be determined (Chang and Schulman 1982, Smith and Mailhiot 1986, Warburton 1991). Displaying the k_z dependence of $\mathbf{H}_{total}^l$ explicitly,

$$\mathbf{H}_{total}^l = \mathbf{H}_2^l (k_z^l)^2 + \mathbf{H}_1^l (k_z^l) + \mathbf{H}_0^l \tag{3.41}$$

then from (3.34),

$$\left\{ \left(\mathbf{H}_2^l\right)^{-1} \left(\mathbf{H}_0^l - \left(\delta E_{vhh}^l + E\right)\mathbf{I}\right) + \left(\mathbf{H}_2^l\right)^{-1} \mathbf{H}_1^l (k_z^l) + (k_z^l)^2 \right\} \mathbf{A}^l = 0 \tag{3.42}$$

and finally expressed as an eigenvalue problem:

$$\begin{pmatrix} 0 & \mathbf{I} \\ -\left(\mathbf{H}_2^l\right)^{-1}\left(\mathbf{H}_0^l - \left(\delta E_{\mathrm{vhh}}^l + E\right)\mathbf{I}\right) & -\left(\mathbf{H}_2^l\right)^{-1}\mathbf{H}_1^l \end{pmatrix}\begin{pmatrix} \mathbf{A}^l \\ k_z^l\mathbf{A}^l \end{pmatrix} = k_z^l\begin{pmatrix} \mathbf{A}^l \\ k_z^l\mathbf{A}^l \end{pmatrix} \qquad (3.43)$$

The matrices making up $\mathbf{H}_{total}^l$ all have dimensions 4×4, so it follows that the matrix on the left in (3.43) has dimensions 8×8 and therefore 8 eigenvalues, k_z^l. These occur in groups of two, $k_z$and $-k_z$ and can take on either real (corresponding to propagating solutions) or imaginary (decaying solutions). Therefore choosing an energy and calculating the eigenvalues of (3.43), the bulk $E(k_z)$ dispersion is constructed for a particular layer in the heterostructure. In (3.42) and (3.43) the wave function is left as a linear combination of Bloch solutions, similar to (3.2), with the A's as expansion coefficients in (3.3) (Chang and Schulman 1982). The main objective in this work, with regards to calculating the $E(k_z)$ dispersion from a *full* **k.p** model is so that comparisons with the reduced **k.p** models (eventually used in heterostructure calculations) can be carried out. In view of this, only the eigenvalues need to be found, although it is noted a complete treatment of heterostructure calculations using the above method has been given by Warburton (1991)

Using the eigenvalue method (3.43), the calculated complex band structure of GaAs using (3.40) is shown in (Fig.3-2). Each line in Fig.3-2 corresponds to two solutions. The effective masses and energy gaps used were taken from Schuurmans and 't Hooft (1985) so Fig.3-2 can be compared with their calculation (Fig.1). From Fig.3-2, it is clear that six solutions all lie within the first Brilloiun zone, $|k_z| < \left(2\pi/a_0\right)$, and correspond to physically realistic solutions (Schuurmans and 't Hooft 1985). The electron and light hole bands are coupled across the band gap by an imaginary band, and become real above their respective band edges. The other two bands (heavy -hole and spin-orbit split-off), proceed as one would expect, with some interaction between the latter and the light hole band being evident. Two solutions in Fig.3-2, lie outside the first Brilloiun zone. These are often referred to as 'spurious' solutions and are physically unrealistic, cf. (3.2). Several comments regarding spurious solutions appear in the literature (Schuurmans and 't Hooft 1985, G Bastard 1988, p86), where they are described as remnants of a remote band which arise due to limited set of basis functions used in the **k.p** approach.

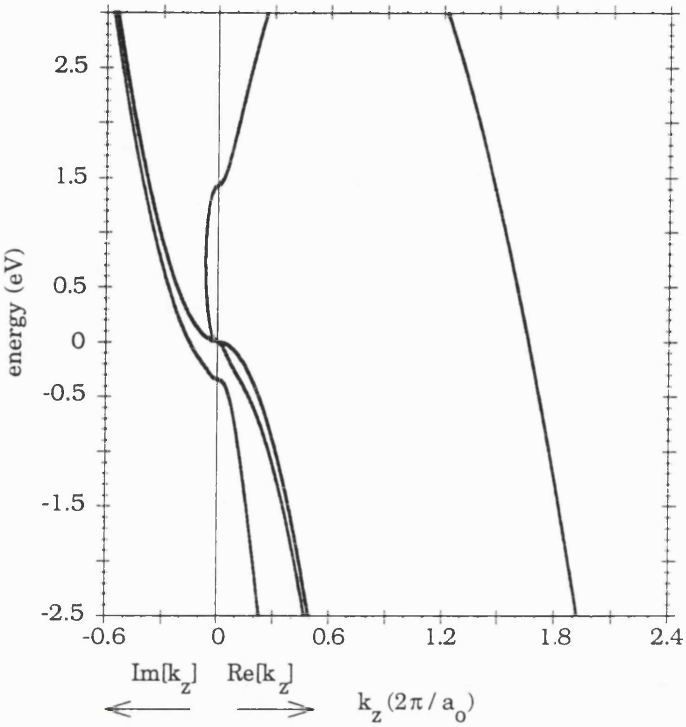

Figure 3-2. *Calculated complex band structure of GaAs. Real values of k_z are plotted on the positive x-axis and Imaginary values are plotted on the negative x-axis.*

In adopting a *full* **k.p** model for heterostructure problems, the involvement of large k valued spurious solutions can prove numerically troublesome since the total wavefunction must be expanded in each layer (eg. Schuurmans and 't Hooft 1985). To get round these problems, several numerical schemes have been proposed which appear to give satisfactory results (Schuurmans and 't Hooft 1985, Ram-Mohan *et al* 1988, Warburton 1991). However, as Bastard has pointed out (see Bastard 1988, p87), another approach is to avoid the inclusion of the remote bands altogether, and use a *reduced* **k.p** description for energies close to the band edge. This compromised description is the topic of the following section.

§3.4.2 Using reduced k.p theory: the Kane model.

The main difference between a *full* and reduced (or Kane) **k.p** model lies in the degree of interaction affecting the bands considered in the near set. Reiterating the results of §3.2.1, the *full* model treated a set of four closely spaced bands (near set) which were allowed to couple strongly to one another, while the coupling between these and the remote bands (much further away in energy) is treated by second order perturbation theory.

Another method, originating from the work of Kane (1956, 1957), only considers the strong coupling between the four closely spaced bands and neglects coupling from the remote bands. Calculating the band structure for InSb using both models, Kane showed that the effects from the remote bands have a negligible contribution close to the band edges of the near set. As the dispersion extended further away (in k space), the coupling from remote bands became more significant.. This reduced **k.p** method, commonly referred to as the Kane method, has subsequently been widely adopted (cf. §3.1), offering an accurate description of materials near the band edge while providing analytic $E(k_z)$ expressions which are easily handled numerically.

The Hamiltonian representing the Kane model can be obtained from the *full* **k.p** Hamiltonian by dropping the terms of $O(k^2)$ that describe the combined effect of the free electron term with the coupling to remote bands. The difference between the two models can be viewed as;

$$\text{full } \mathbf{k.p} \quad \mathbf{H}^{l}_{total} = \mathbf{H}^{l}_{2}(k^{l}_{z})^{2} + \mathbf{H}^{l}_{1}(k^{l}_{z}) + \mathbf{H}^{l}_{0} \tag{3.50}$$

$$\text{Kane } \mathbf{k.p} \quad \mathbf{H}^{l}_{total} = \mathbf{H}^{l}_{1}(k^{l}_{z}) + \mathbf{H}^{l}_{0} \tag{3.51}$$

where for both cases, $\mathbf{H}^{l}_{total}$ can represent either heavy or light states.

Earlier, in (§3.2.2) it was noted that the heavy states ($m_j = \pm \frac{3}{2}$) in the bulk Hamiltonian, $\mathbf{U}^{l}$ in (3.17) do not couple at all to the light states ($m_j = \pm \frac{1}{2}$). Similar comments also apply to $\mathbf{D}^{l}$ in (3.26). So regardless of whether the *full* **k.p** or the Kane **k.p** model is used, the heavy hole states can be treated separately thereby reducing the level of computation required. [note: this decoupling is valid because (3.17) is derived assuming $k_{||}=0$. In the case where $k_{||}\neq 0$ there can be strong mixing of the heavy and light states (eg. Eppenga *et al* 1987)]. It seems appropriate to draw attention to this now since in the Kane method (described in this section) it will become clear that the level of approximation used for the description of light and heavy states is not the same.

For the heavy hole case, removing the terms of $O(k^2)$ leaves it dispersionless since it is seen in (3.17) to interact only with the far states. To overcome this problem the interactions with the far states are reinstated leaving the description for heavy hole states the same as in the *full* **k.p** method, (3.17).

Explicitly,

$$\mathbf{H}^l_{total_{hh}} = -\frac{\hbar^2\hat{k}_z^2}{2m_o}(\gamma^l_{1,L} - 2\gamma^l_{2,L}) = -\frac{\hbar^2\hat{k}_z^2}{2m^l_{hh}} \tag{3.52}$$

noticing that the usual Luttinger parameters can be used to define the heavy hole effective mass in a particular layer.

Considering just the light particle states ($m_j = \pm \frac{1}{2}$), the three band (el, lh & so) Hamiltonian is,

$$\mathbf{H}^l_{total_{3B}} = \begin{array}{c} \begin{array}{ccc} \quad el \quad & \quad lh \quad & \quad so \quad \end{array} \\ \begin{bmatrix} E^l_{gs} & -i\sqrt{\frac{2}{3}}\mathbf{P}^l_K\hat{k}_z & i\sqrt{\frac{1}{3}}\mathbf{P}^l_K\hat{k}_z \\ i\sqrt{\frac{2}{3}}\mathbf{P}^l_K\hat{k}_z & \delta E^l_s & -\sqrt{\frac{1}{2}}\delta E^l_s \\ -i\sqrt{\frac{1}{3}}\mathbf{P}^l_K\hat{k}_z & -\sqrt{\frac{1}{2}}\delta E^l_s & E^l_{so} \end{bmatrix} \end{array} \tag{3.53}$$

where,

$$E^l_{gs} = E^l_g + \delta E^{(gap)l}_h + \frac{1}{2}\,\delta E^l_s \tag{3.54}$$

$$E^l_{so} = -\Delta^l + \frac{1}{2}\,\delta E^l_s \tag{3.55}$$

The terms $\delta E^{(gap)l}_h$ and δE^l_s are given by (3.33) and (3.30) respectively. The heavy hole band edge in $\mathbf{H}^l_{total}$ for all layers is set to zero, therefore E^l_{gs} can be regarded as the strained band gap between the conduction and heavy hole band edge. It is clear from (3.54) that if a layer has zero strain then this reduces to the bulk unstrained value, ie. $E^l_{gs}(e^l_{||} \rightarrow 0) = E^l_g$. The subscript 'K' on the Kane matrix element, $\mathbf{P}^l_K$, is to indicate that this will now be found within the equations obtained from the Kane model. This is achieved in a similar manner as that carried out for $\mathbf{P}^l$ in the *full* model (3.37). Further discussion on this subject and the corresponding equations appears in §3.5. For now it is sufficient to realise that $\mathbf{P}^l_K$ is fitted to reproduce the bulk unstrained effective masses at the Γ-point.

For bulk envelope functions taken as $f^l_j \propto e^{ik_z z}$, the operator is $\hat{k}_z \rightarrow k_z$. The energy-dispersion relation $E(k_z)$ is found from,

$$\left\{\mathbf{H}^l_{total} - \delta E^l_{vhh}\mathbf{I}\right\}\mathbf{F}^l = \{E\mathbf{I}\}\mathbf{F}^l \tag{3.56}$$

$$\left\{\mathbf{H}^{l}_{total} - \delta \mathrm{E}^{l}_{\mathrm{vhh}}\mathbf{I}\right\}\mathbf{F}^{l} = \{\mathbf{EI}\}\mathbf{F}^{l} \tag{3.56}$$

where $\mathbf{H}^{l}_{total}$ is (3.53) and $\mathbf{F}^{l}$ is $\left(f^{l}_{\mathrm{el}}, f^{l}_{\mathrm{lh}}, f^{l}_{\mathrm{so}}\right)$ for the light states, and $\mathbf{H}^{l}_{total}$ is (3.52) and $\mathbf{F}^{l}$ is f^{l}_{hh} for the heavy states. The energy offset $\delta \mathrm{E}^{l}_{\mathrm{vhh}}$ is used for both heavy and light states and is given by (3.36). The analytic $\mathrm{E}(\mathrm{k}_z)$ dispersion is found from the characteristic equation:

$$\left\| \mathbf{H}^{l}_{total} - \left(\delta \mathrm{E}^{l}_{\mathrm{vhh}} + \mathrm{E}\right)\mathbf{I} \right\| = 0 \tag{3.57}$$

Considering (3.57) for the well material (dropping the superscript), we find for the heavy hole states,

$$\mathrm{k}_z^2 = -\frac{2\,\mathrm{m}_{\mathrm{hh}}}{\hbar^2}\,\mathrm{E} \tag{3.58}$$

and for the light states,

$$\mathrm{k}_z^2 = \frac{3}{\mathbf{P}_{\mathrm{K}}^2}\,\frac{\left(\mathrm{E}-\mathrm{E}_{\mathrm{gs}}\right)\left[(\mathrm{E}-\delta\mathrm{E}_{\mathrm{s}})(\mathrm{E}-\mathrm{E}_{\mathrm{so}}) - \frac{1}{2}\delta\mathrm{E}_{\mathrm{s}}^2\right]}{\left(3\mathrm{E}+\delta\mathrm{E}_{\mathrm{s}}-2\mathrm{E}_{\mathrm{so}}\right)} \tag{3.59}$$

The relations for the barrier material have the same form and can be obtained with the substitution $\mathrm{E} \rightarrow (\mathrm{E} + \delta\mathrm{E}^{b}_{\mathrm{vhh}})$ in equations (3.58) and (3.59). Examination of the above relations show the heavy hole dispersion is parabolic (ie. $\mathrm{k}_z^2 \propto \mathrm{E}$) with an effective mass of m_{hh}. However the light states, described from (3.59), are clearly not and instead have some higher order relationship with energy. This situation is called band non-parabolicity and is responsible for an energy dependence of the effective mass in a given band (eg. G Bastard 1988, p46). In fact, equation (3.59) can be written for the conduction band as,

$$\frac{\hbar^2 \mathrm{k}_z^2}{2\,\mathrm{m}_{\mathrm{el}}(\mathrm{E})} = \left(\mathrm{E} - \mathrm{E}_{\mathrm{gs}}\right) \tag{3.60}$$

with

$$\mathrm{m}_{\mathrm{el}}(\mathrm{E}) = \frac{3\mathrm{m}_{\mathrm{o}}}{\mathrm{E}_{\mathrm{P}_{\mathrm{K}}}}\,\frac{\left[(\mathrm{E}-\delta\mathrm{E}_{\mathrm{s}})(\mathrm{E}-\mathrm{E}_{\mathrm{so}}) - \frac{1}{2}\delta\mathrm{E}_{\mathrm{s}}^2\right]}{\left(3\mathrm{E}+\delta\mathrm{E}_{\mathrm{s}}-2\mathrm{E}_{\mathrm{so}}\right)} \tag{3.61}$$

clearly showing energy dependence of the electron effective mass. Non-parabolicity occurs in the **k.p** description due to the coupling of the bands considered in the model, and hence can be anticipated by noting any off-diagonal terms (dependent on k_z) appearing in $\mathbf{H}^{l}_{total}$.

Although the Kane approach has significant numerical advantages, the accuracy of the method is clearly an issue. In the later heterostructure calculations, the energy range of interest is typically within 60 meV of the band edges (for the lowest energy transitions). Although rarely quantified, presumably due to the dependence on the material, previous studies (§3.1) have suggested similar limits in which the Kane approach can be used as an effective description. Using the two **k.p** approaches detailed here, ie. *full* and Kane, calculated band structures can be compared. Inevitably limits exist in the *full* model, however it is reasonable to suppose the effective energy range is larger than in the Kane approach through accounting for interactions from remote bands. Previously, the Kane approach compared favorably to a tight binding method for GaAs and AlAs for energies near the band edge, particularly for the conduction band (G Bastard 1988, p48). Other comparisons have already been noted (cf. Johnson *et al* 1988, 1990) but little work has been published concerning Phosphorus based strained layers. Examples are shown for $In_xGa_{1-x}As$ material (Fig. 3-2, 3-3), which apart from the technological importance (covering wavelength range 1-1.6μm) can also be made to experience a tensile strain (for x<0.53) or compressive strain (x>0.53) with growth on an InP substrate. [note: the material is also regularly grown on GaAs substrates where it experiences compressive strain for all values of x]. In figure (3-2), the strained $E(k_z)$ dispersion is calculated from both approaches (for x=0.39 corresponding to ~1% tensile strain). Only the light particle states, ($m_j = \pm \frac{1}{2}$), are displayed since the heavy hole descriptions are exactly the same in both models. Since the layer is under tensile strain, the light hole band edge is correctly seen to lie above the heavy hole band edge (cf. §2.2.2). Calculated band edge positions (ie. at $k_z=0$) are identical for both approaches, which can be expected since the terms that are neglected in the Kane approach are $O(k_z^2)$. Hence the important strain-induced energy shifts of the band edges, eg. band gap modification, heavy-light hole separation, are accounted for. For small k_z, ie. energies close to the band edge, the Kane description compares very well; the conduction band dispersion compares very well up to energies ~200 meV from the band edge (with a maximum deviation of less than 0.2 meV). The accuracy of the light hole dispersion is slightly less, ie. ~150 meV from Fig. 3-3a for a similar deviation. A further point to note, is the wave vector expressed in units of $(2\pi/a_{0,z})$. Here $a_{0,z}$ is the distorted lattice constant in the growth direction, (cf. Fig. 2-1).

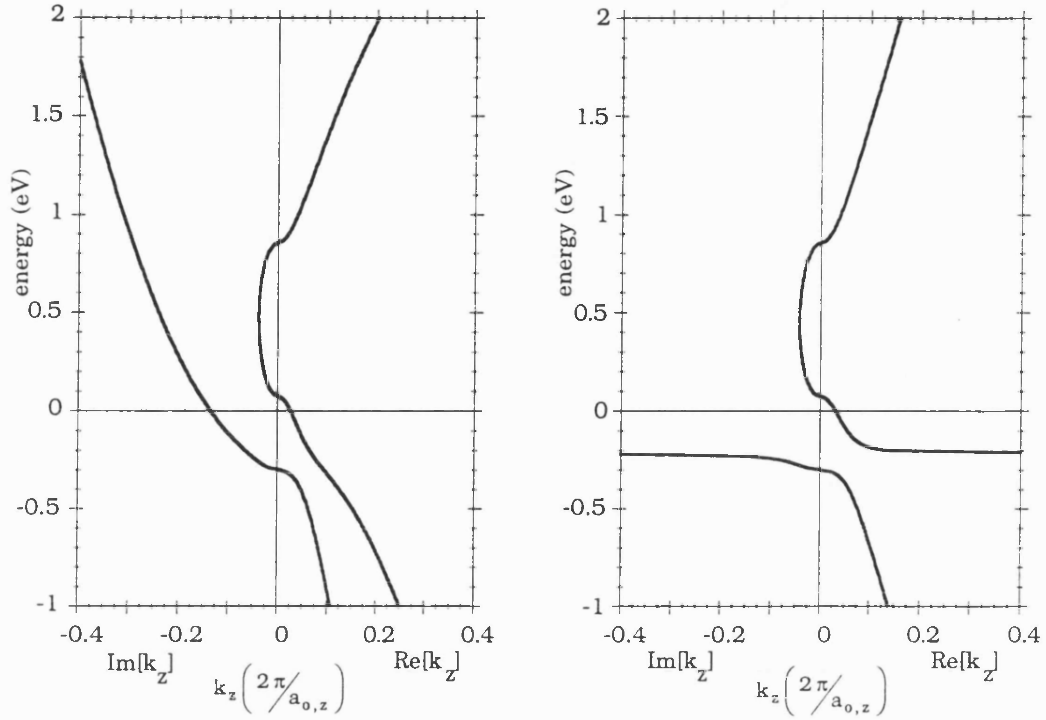

(a) (b)

Figure 3-2. *Comparison of calculated band structures for* $In_{0.39}Ga_{0.61}As$ *on InP corresponding to ~1% tensile strain in the InGaAs layer. (a) full description. (b) Kane description.*

The restricted accuracy of the light hole dispersion is mainly due to the divergence that occurs in the Kane model (Schuurmans and 't Hooft 1985). Further examination of the description for the three light bands (el, lh & so), shows (3.59) diverges when the denominator is zero (cf. asymtope in Fig. 3-2b above). Making use of (3.55), the asymptote can be seen to occur at an energy $E \approx -2\Delta/3$ from the heavy hole band edge which is always zero (for a well material). However, the energy *separation* between the light hole band edge and the asymptote *is* strain dependent, which actually arises from the strain induced separation of the light- and heavy-hole band edges (Fig.3-3). Therefore care must be taken to define the energy range where the $k_{||}=0$ light hole states can be accurately obtained using the Kane model. It can be appreciated that in addition to value of the spin-orbit splitting for a material, the strength and nature of the strain is clearly a factor, (see Fig.3-3 below).

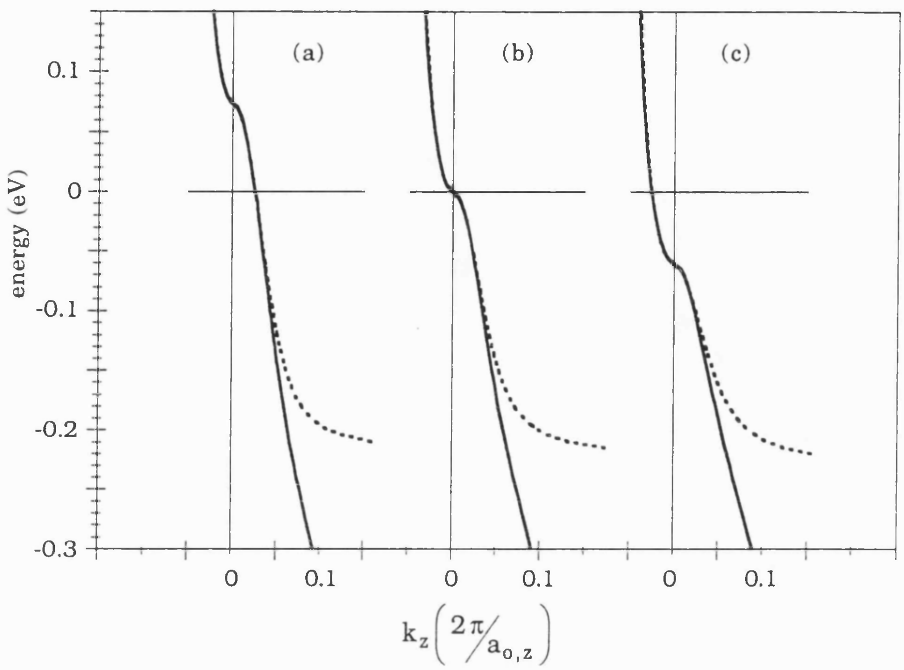

Figure 3-3. *Comparison of the light hole dispersion near the band edge between full description (solid) and Kane description (dotted). Three cases are shown corresponding to (a)* $In_{0.39}Ga_{0.61}As$ *on InP (~1 % tensile strain) (b)* $In_{0.53}Ga_{0.47}As$ *on InP (lattice matched) (c)* $In_{0.67}Ga_{0.33}As$ *on InP (~1 % compressive strain).*

In Fig.3-3, three situations (tensile, lattice matched and compressive) are considered. In all cases the heavy hole band edge is indicated (at zero energy). As expected, the position of the light hole band edge moves from higher to lower energy (w.r.t heavy hole band edge) as the strain in the layer goes from tensile to compressive, (cf. §2.2.2). The results show the effective range of the Kane approach (for describing light hole states) is progressively more limited with increasing compressive strain. The light hole band edge moves further towards the asymptote (further away from the heavy-hole band edge) for increasing compressive strain. In actual fact, the asymptote for each case occurs at a slightly different energy since the bulk value of Δ changes with composition. However, from the above figure it is clear the dominant effect is the strain induced splitting which restricts the effective energy range. For moderate strains (say $|e_{||}| \leq 0.015$ which allows reasonably wide strained QW layers to be confidently grown, cf. Fig. 2-7), the Kane description for $In_xGa_{1-x}As$, on either InP or GaAs, is effective for 60 meV away from the band edges. This is a sufficient range for the calculations of ground states in quantum well and related structures. Turning to the $InAs_{1-x}P_x$ system (on InP) studied in Chapter 5, calculations indicate the effective energy limits for the Kane description are somewhat lower (w.r.t the band edges); ~80 meV for conduction band, ~30 meV for the light hole band. These are easily explained by both a smaller spin-orbit splitting (for x>0.8 cf. Appendix A) and the fact that the layer is under compressive strain. For heterostructure calculations, the conduction band range adequately covers the energy of the lowest confined state for the material forming the well region. Unfortunately, the same cannot be said for light hole states, where the model is only effective for larger well widths, ie. structures with the light hole state less than 30 meV from the band edge.

From the above results and having looked at other systems, I typically find the Kane approach describes the light hole dispersion down to energies~ $-\Delta^l/3$. That is, if the strain induced splitting causes the light hole band edge to lie at energies comparable to or greater (ie. lower in energy) than $-\Delta^l/3$, then the light hole dispersion from the Kane model is not accurate.

§3.5 Further Investigation into the Kane Model.

The last section introduced the Kane approach and demonstrated the resulting closed form $E(k_z)$ relationship describing the electronic structure of a material near its band edge. The point was made that the value of the matrix element, $\mathbf{P}_K$, is required to reproduce the band edge effective masses at the Γ-point. The latter part of this section (§3.5.2) details the method and relations used in the present work to determine this. Before this, further investigation into the Kane approach is undertaken which serves to highlight some of the assumptions and consequences involved. In addition, closed form expressions providing information on the strained layer (ie. masses, band gaps etc..) are derived (§3.5.1).

Two levels of description in the Kane model are used in the current section. Both neglect any coupling of the *near* set with the remote bands (the *far* set); as before the near set includes the conduction, light hole and spin-orbit split-off bands. The differences between the Kane descriptions are due to either including the free electron term, $\hbar^2\hat{k}_z^2/2m_0$, or neglecting it (ie. §3.4.2). To distinguish between the two I will call the former the 'free electron' Kane model, while the latter will be referred to as the Kane model. [note: It is the Kane model in §3.4.2 that is used in the heterostructure calculations, Chapter 4]. The 'free electron' Kane model is seen to be consistent with the development outlined in §3.2.1, and is essentially given by (3.8). The Kane Hamiltonian of (3.52) neglects all terms of $O(k^2)$ *including* the free electron term, the assumption being that the free electron term is much smaller than the energy of interest, ie. $E - \hbar^2\hat{k}_z^2/2m_0 \approx E$. For energies close to the band edge this is a reasonable approximation (B. R. Nag 1980).

§3.5.1 Analytic expressions.

In this section closed form expressions describing band edge effective masses, band non-parabolicity and band edge energy positions for strained bulk semiconductor layers are presented. The results are particularly useful for existing single band heterostructure models. They produce the input parameters typically required in most heterostructure calculations (ie. band edge mass, band gaps and non-parabolicity) and can therefore extend the models to adequately account for strained layers.

The derivation is based on the approach by People and Sputz (1990), although differences occur in the choice of Hamiltonian. In their work, People and Sputz derived the expressions obtained from two cases of **k.p** description. In one case, the conduction band was explicitly included which in some respects is similar to the Hamiltonian in (3.35). In the other case, only the valence bands are included and so the Hamiltonian is similar to (3.24). It should be made clear that for both cases, coupling with the remote bands is included so in our nomenclature their descriptions can be regarded as *full* descriptions. A further point worth mentioning is that People and Sputz used the basis functions prescribed by Luttinger and Kohn (1955) whereas I have used Kane's set (3.14). This results in some elements of the strain Hamiltonian differing in sign and phase.

The analysis by People and Sputz (1990) starts by expressing the $E(k_z)$ dispersion for a particular band up to $O(k_z^4)$, ie.

$$E_j(k_z) = \frac{\hbar^2 k_z^2}{2m_j^*} - \gamma^{(j)} \frac{\hbar^2 k_z^4}{2m_j^*} \tag{3.62}$$

where E_j and m_j^* are the energy and effective mass in the z-direction (confinement direction for heterostructures). The subscript j is the band index (eg. conduction band) and $\gamma^{(j)}$ is the non-parabolicity parameter for the jth band. Equation (3.62) assumes jth band edge at the Γ-point is at zero energy. It can be written more generally as,

$$E_j(k_z) = E_0^{(j)} + E_1^{(j)} k_z^2 + E_2^{(j)} k_z^4 \tag{3.63}$$

here $E_0^{(j)}$ is the band edge energy at the Γ-point, $E_1^{(j)}$ and $E_2^{(j)}$ are k_z independent terms related to the effective mass and non-parabolicity,

$$E_1^{(j)} \equiv \frac{\hbar^2}{2m_j^*} = \frac{1}{2}\left[\frac{1}{k_z}\frac{\partial E(k_z)}{\partial k_z}\right]\Bigg|_{k_z=0,\,E=E_0^{(j)}} \tag{3.64}$$

and

$$E_2^{(j)} \equiv -\gamma^{(j)}\frac{\hbar^2}{2m_j^*} = \frac{1}{4\,!}\left[\frac{1}{k_z}\frac{\partial^3 E(k_z)}{\partial k_z^3}\right]\Bigg|_{k_z=0,\,E=E_0^{(j)}} \tag{3.65}$$

where $E(k_z)$ is the general characteristic relation between the energy and the wave vector obtained using a **k.p** description.

General expressions.

The characteristic relation used in (3.64) and (3.65) is from the 'free electron' Kane Hamiltonian (ie. including the free electron term). It can be obtained from (3.53) by adding $\hbar^2\hat{k}_z^2/2m_o$ to each element on the leading diagonal and following the same method in §3.4.2 or equivalently, from (3.59), by substituting $E \rightarrow E - \hbar^2\hat{k}_z^2/2m_o$. The characteristic relation up to $O(k_z^4)$ for the well material is (dropping the superscript),

$$(E - E_{gs})\left((E - E_{lh})(E - E_{so}) - \frac{1}{2}\,\delta E_s^2\right) = Q + R \tag{3.66}$$

where,

$$Q = \frac{\hbar^2 k_z^2}{2m_o}\left[3E^2 - 2E(\breve{x}) + (\breve{y}) + \frac{2m_o P_{K,m_o}^2}{3\hbar^2}\left(3E + 2\delta E_s - 2E_{so} - E_{lh}\right)\right]$$

and

$$R = -\frac{\hbar^2 k_z^4}{2m_o}\left[\frac{\hbar^2}{2m_o}\left(3E - (\breve{x}) + \frac{2m_o P_{K,m_o}^2}{3\hbar^2}\right)\right]$$

with

$$\breve{x} = (E_{gs} + E_{lh} + E_{so})$$

$$\breve{y} = (E_{gs}E_{lh} + E_{gs}E_{so} + E_{lh}E_{so} - \frac{1}{2}\,\delta E_s^2)$$

All the terms have been defined previously with the exception of E_{lh} ($= \delta E_s$) which refers to the light hole diagonal element in (3.53). The subscripts on the matrix element, **P**, indicate it is the coupling element within the 'free electron' Kane Hamiltonian. To keep the final expressions general, implicit differentiation is applied to both sides of (3.66) and the relevant substitutions given in (3.64) and (3.65) are used.

After some work, the following general expressions for the effective mass,

$$\frac{m_o}{m_j^*} = 1 + \frac{2m_oP_{K,m_o}^2}{3\hbar^2}\left(\frac{(3E_0^{(j)} + 2\delta E_s - 2E_{so} - E_{lh})}{(3(E_0^{(j)})^2 - 2E_0^{(j)}(\breve{x}) + (\breve{y}))}\right) \tag{3.67}$$

and non-parabolicity are found,

$$-\gamma^{(j)}\frac{\hbar^2}{2m_j^*}\left(3(E_0^{(j)})^2 - 2E_0^{(j)}(\breve{x}) + (\breve{y})\right) = \frac{\hbar^2}{4m_0^2}[T - U] \tag{3.68}$$

where

$$T = \left(1 - \frac{m_o}{m_j^*}\right)\left(3E_0^{(j)} - (\breve{x}) + \frac{2m_oP_{K,m_o}^2}{3\hbar^2}\right)$$

$$U = -\left(\frac{m_o}{m_j^*}\right)\left[\left(1 - \frac{m_o}{m_j^*}\right)\left(3E_0^{(j)} - (\breve{x})\right)\right]$$

As noted earlier, the term $E_0^{(j)}$ is the energy of the *j*th band at the Γ-point (ie. k_z=0). The index *j* refers to the light particle states (ie. conduction, light-hole or spin-orbit split-off bands). The band edge energies, $E_0^{(j)}$'s are simply solutions of

$$(E - E_{gs})\left((E - E_{lh})(E - E_{so}) - \frac{1}{2}\delta E_s^2\right) = 0 \tag{3.69}$$

which written out in full are,

$$E_0^{el} = E_{gs} \tag{3.70a}$$

$$E_0^{lh} = \frac{(E_{lh} + E_{so})}{2} + \frac{1}{2}\sqrt{E_{lh}^2 - 2E_{lh}E_{so} + 2\delta E_s^2 + E_{so}^2} \tag{3.70b}$$

$$E_0^{so} = \frac{(E_{lh} + E_{so})}{2} - \frac{1}{2}\sqrt{E_{lh}^2 - 2E_{lh}E_{so} + 2\delta E_s^2 + E_{so}^2} \tag{3.70c}$$

The above expressions for the band edge energies of the light states are defined with respect to the heavy hole band edge of the well material (taken as zero in this thesis (§3.4)). It is worth noting, that these solutions are the same for both the *full* model (3.40) and the Kane model (3.57). On their own, equations (3.70) provide valuable information about the changes in band gaps and valence band splitting induced by lattice mismatch strain. For example, (3.70a) and (3.54), provide the band gap (band gap between conduction and heavy hole valence band) of a material under strain, while (3.70b) gives the valence band splitting of the heavy- and light-hole band edges. This is illustrated in figure. 3-4 where these changes are calculated for the $In_xGa_{1-x}As$ on InP system. For the same material system, with equations (3.67) and (3.68), the effective mass and non-parabolicity values for a given band can be found, Fig.3-5 and Fig.3-6 respectively.

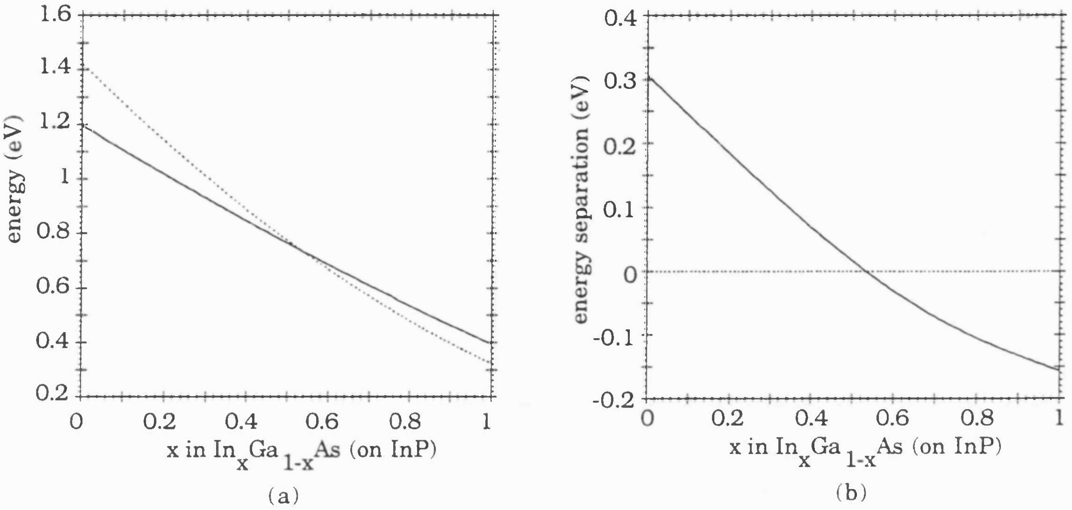

Figure 3-4. *Calculated band edge energies for $In_xGa_{1-x}As$ on InP, solid lines include the effects of strain while dotted are the unstrained bulk values. (a) strained band gap, E_{gs}. (b) separation of the light and heavy hole band edges.*

The results from figures 3-4 ,3-5 and 3-6 compare well with the data presented by People and Sputz (1990). The conduction band results are in almost perfect agreement despite not including remote bands. Discrepancies start to arise with the light hole results. The calculated mass (Fig.3-4(b)) appears heavier (for compressive strain (x>0.53)) compared to the value which includes remote bands (cf. Fig.2. in People and Sputz (1990)). Although the overall effects of strain (ie. the shape of the results across the range) are the same for both models. The calculated non-parabolicity does exhibit a different shape across the range in Fig.3-6(b) compared to Fig.10 from People and Sputz 1990, although the actual values are reasonably close to each other. The 'turn over' visible in Fig.3-6(b) is not present in the People and Sputz results, instead their value increases slowly across the composition range.

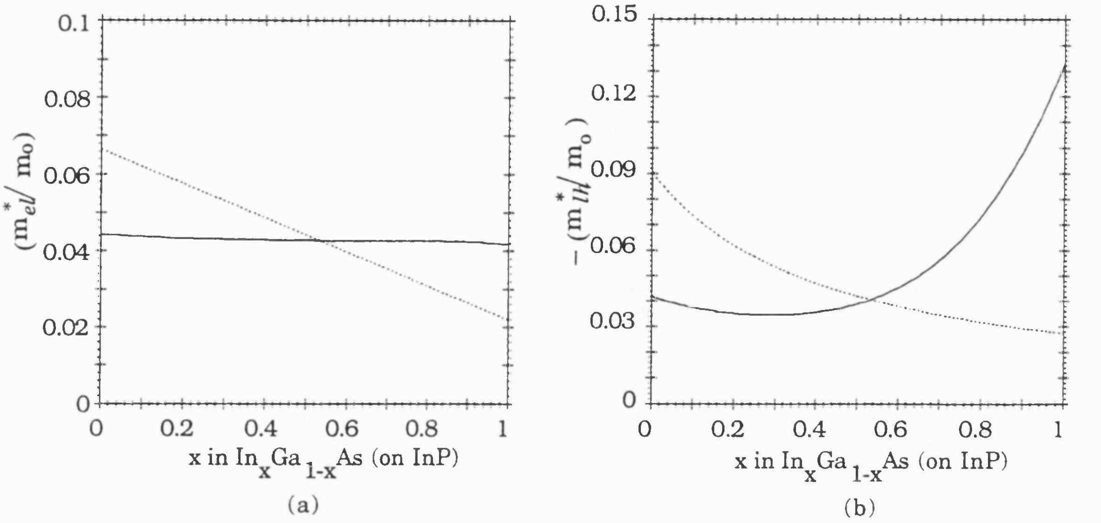

Figure 3-5. *Effective masses at the band edge for $In_xGa_{1-x}As$ on InP, solid lines include the effects of strain while dotted are the unstrained bulk values. (a) conduction band. (b) light hole band.*

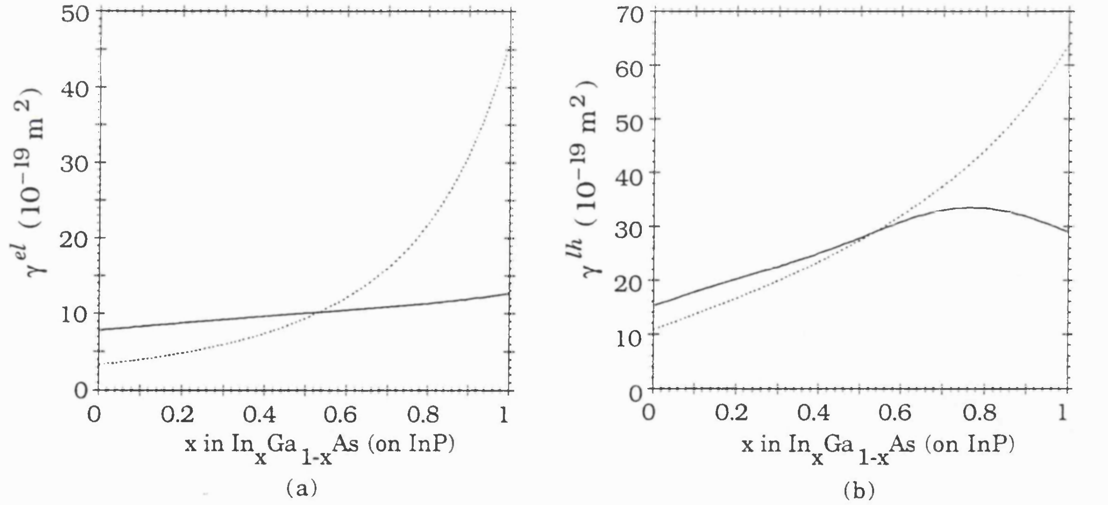

Figure 3-6. *Non-parabolicity at the band edge for $In_xGa_{1-x}As$ on InP, solid lines include the effects of strain while dotted are the unstrained bulk values. (a) conduction band. (b) light hole band.*

Equations (3.66) to (3.70) have the same form for the barrier material.

Unstrained expressions.

When there is no strain in the layer, ie. $e_{\|}^{l} = 0$, the relations for the band edge energies reduce to,

$$E_0^{el} = E_g \tag{3.71a}$$

$$E_0^{lh} = 0 \tag{3.71b}$$

$$E_0^{so} = -\Delta \tag{3.71c}$$

As expected, these correspond exactly to those given in (3.14) for **k**=0. Using the above values in (3.67) produces,

$$\frac{m_0}{m_{el}^*} = 1 + \frac{2m_0\mathbf{P}_{K,m_0}^2}{3\hbar^2}\left(\frac{1}{E_g + \Delta} + \frac{2}{E_g}\right) \tag{3.72a}$$

$$\frac{m_0}{m_{lh}^*} = 1 - \frac{2m_0\mathbf{P}_{K,m_0}^2}{3\hbar^2}\left(\frac{2}{E_g}\right) \tag{3.72b}$$

$$\frac{m_0}{m_{so}^*} = 1 - \frac{2m_0\mathbf{P}_{K,m_0}^2}{3\hbar^2}\left(\frac{1}{E_g + \Delta}\right) \tag{3.72c}$$

which agree exactly with those given by G Bastard (1988), p46. The above equations are essentially the 'free electron' Kane equivalent of those listed for the *full* model in (3.37). Then following a similar method, the matrix element, $\mathbf{P}_{K,m_0}$, is determined using the above equations. As before, a knowledge of the bulk unstrained effective masses and energy gaps at the Γ-point for the material is required. Apart from the obvious lack of remote terms in (3.72), there are important differences between the two methods. In the present case, the value of $\mathbf{P}_{K,m_0}$ must be different for each band in order to reproduce the correct band edge mass. Furthermore, consideration of the valence band masses (3.72b,c) indicates these take on negative values (G Bastard 1988, p46). The former comment about changing the matrix element depending on the band, may seem unsatisfactory from a theoretical point of view but is simply a consequence of using a Kane description (Schuurmans and 't Hooft 1985). The essential point is that the *a priori* bulk unstrained masses are reproduced at the band edge.

§3.5.2 The matrix element in the Kane model.

The first step towards evaluating the matrix element in (3.52) is to find the general expression for the band edge effective masses in the Kane model. As in the previous section, use is made of (3.64) but now the $E(k_z)$ dispersion is given by (3.59). This results in the following general expression giving the band edge effective mass,

$$\frac{1}{m_j^*} = \frac{2P_K^2}{3\hbar^2}\left(\frac{(3E_0^{(j)} + 2\delta E_s - 2E_{so} - E_{lh})}{(3(E_0^{(j)})^2 - 2E_0^{(j)}(\breve{x}) + (\breve{y}))}\right) \tag{3.73}$$

multiplying both sides by the free electron mass, m_0, and making the substitution,

$$E_{P_K} = \frac{2m_0P_K^2}{\hbar^2} \tag{3.74}$$

which has units of energy, then (3.73) can be rewritten as,

$$\frac{m_0}{m_j^*} = \frac{E_{P_K^j}}{3}\left(\frac{(3E_0^{(j)} + 2\delta E_s - 2E_{so} - E_{lh})}{(3(E_0^{(j)})^2 - 2E_0^{(j)}(\breve{x}) + (\breve{y}))}\right) \tag{3.75}$$

In view of the previous section, it is sensible to indicate that the matrix element term is dependent on the band index *j*. The band edge energies, $E_0^{(j)}$, as noted earlier, are the same for all the **k.p** descriptions considered in this chapter (ie. *full*, free electron Kane and Kane models) and can be found from the relations in (3.70). With an equivalent substitution of, (3.74), in (3.67), similarities between (3.67) and (3.75) are hardly surprising and become more obvious when comparing the unstrained relations for the effective masses. For (3.75) these are,

$$\frac{m_0}{m_{el}^*} = \frac{E_{P_K^{el}}}{3}\left(\frac{1}{E_g + \Delta} + \frac{2}{E_g}\right) \tag{3.76a}$$

$$\frac{m_0}{m_{lh}^*} = \frac{E_{P_K^{lh}}}{3}\left(-\frac{2}{E_g}\right) \tag{3.76b}$$

$$\frac{m_0}{m_{so}^*} = \frac{E_{P_K^{so}}}{3}\left(-\frac{1}{E_g + \Delta}\right) \tag{3.76c}$$

where we have used the unstrained band edge energies given in (3.71). The above relations are then used to determine the matrix element, $E_{P_K^j}$, for each band knowing the unstrained bulk effective masses and energies at the Γ-point. For a given band, the matrix element determined by (3.76) is used in the heterostructure calculations (Chapter 4), and the band edge effective mass will be that given by (3.75). In the case of unstrained layers the band edge mass would already be known in order to calculate $E_{P_K^j}$, then (3.75) would just reduce to the relations in (3.76). However, $E_{P_K^j}$, would still need to be evaluated so that the non-parabolicity (ie. the energy dependence of the mass) could be accounted for.

Similar points raised in discussing the equations from the free electron Kane model (3.70) will also apply here. It should be clear from comparing (3.70) and (3.76) that for the same bulk unstrained effective masses, the matrix element for the Kane model will be slightly higher (lower) for the conduction (valence) band. Furthermore, there are small differences in the strained band edge effective masses calculated using (3.67) and (3.73) with the respective matrix elements. The same would also occur if the results from the *full* model of People and Sputz (1990) are compared. This must be the case since the level of approximation between each model is different. In going from the *full* model to the Kane model the description of a semiconductor is compromised. However, as will become clear in the following chapter, calculations employing a Kane description require the same level computation that is needed in particle-in-box type calculations. Given that calculating heterostructure properties requires further calculations, which themselves are fairly involved. I felt that by using the Kane approach, an intermediate consistent treatment of strain in heterostructures can be obtained while keeping the computing effort to a minimum.

References.

Alterelli M, "*Band Structure, Impurities and Excitons in Superlattices*" in *Heterojunctions and Semiconductor Superlattices,* edited by Allan G, Bastard G, Boccara N, Lannoo M, and Voos M, Springer-Verlag, Berlin, (1986), pp 12-37.

Bahder T.H, "*Eight Band **k.p** Model of Strained Zinc-Blende Crystals*" Phys. Rev. **B 41**, (1990), pp 11992-12001: Errata: Phys. Rev. **B 46**, (1992), pp 9913.

Bastard G, "*Superlattice Band Structure in the Envelope-Function Approximation*" Phys. Rev. **B 24**, (1981), pp 5693-5697.

Bastard G, "*Theoretical Investigations of Superlattice Band Structure in the Envelope-*

Function Approximation" Phys. Rev. **B 25**, (1982), pp 7584-7597.

Bastard G, and Brum J.A, "*Electronic States in Semiconductor Heterostructures*" IEEE J. Quant. Elect. JQE-**22** , (1986), pp 1625-1644.

Bastard G, *Wave Mechanics Applied to Semiconductor Heterostructures,* Les Editions de Physique, Paris, (1988), chapters 2 &3.

Chang Y.C, and Schulman J.N, "*Complex band structures of crystalline solids: An eigenvalue method* " Phys. Rev. **B 25**, (1982), pp 3975-3986.

Dresselhaus G, Kip A.F, and Kittel C, "*Cyclotron Resonance of Electrons and Holes in Silicon and Germanium Crystals*" Phys. Rev. **98**, (1955), pp 368-384.

Eppenga R, Schuurmans M.F.H, and Colak S, "*New **k.p** Theory for* $GaAs/Ga_{1-x}Al_xAs$ *type Quantum Wells*" Phys. Rev. **B 36**, (1987), pp 1554-1564.

Gershoni D, Henry C.H, and Baraff G.A, "*Calculating the Optical Properties of Multidimensional Heterostructures: Application to the Modelling of Quaternary Quantum Well Lasers*", IEEE J. Quantum Electron., **QE-29**, (1993) pp 2433-2450.

Jogai B, and Yu P.W, "*Energy Levels of Strained* $In_xGa_{1-x}As$-*GaAs Superlattices*" Phys. Rev. **B 41**, (1990), pp 12650-12658.

Johnson N.F, Ehrenreich H, Hass K.C, and McGill T.C, "*f-Sum Rule and Effective Masses in Superlattices*" Phys. Rev. Lett. **59**, (1987), pp 2352-2355.

Johnson N.F, Ehrenreich H, Wu G.Y, and McGill T.C, "*Superlattice **k.p** Models for Calculating Electronic Structure*" Phys. Rev. **B 38**, (1988), pp 13095-13098.

Johnson N.F, Ehrenreich H, Hui P.M, and Young P.M, "*Electronic and Optical Properties of III-V and II-VI Semiconductor Superlattices*" Phys. Rev. **B 41**, (1990), pp 3655-3669.

Kane E.O, "*Energy Band Structure in p-type Germanium and Silicon*" J. Phys. Chem. Solids **1**, (1956), pp 82-99.

Kane E.O, "*Band Structure of Indium Antimonide*" J. Phys. Chem. Solids **1**, (1957), pp 249-261.

Kane E.O, "*The **k.p** Method*" in *Physics of III-V Compounds*, Vol.1 of *Semiconductors and Semimetals*, edited by R.K.Willardson and A.C.Beer, Academic Press, New York, (1966), pp 75-100.

Landolt-Börnstein, *Numerical Data and Functional Relationships in Science and Technology*, edited by Madelung, New Series, Group 3, Vol. 17a, (Springer, Berlin 1982) , pp 281-289; Vol. 22a, (Springer, Berlin 1989) pp 107-116.

Löwdin P.O, "*A Note on the Quantum Mechanical Perturbation Theory*" J. Chem. Phys. **19**, (1951), pp 1396-1401.

Loehr J.P, and Manasreh M.O, in "*Semiconductor Quantum Wells and Superlattices for Long-Wavelength Infrared Detectors*" edited by M.O. Manasreh, Artech House, (1993) , chapter 3, pp 55-106.

Luttinger J.M, "*Quantum Theory of Cyclotron Resonance in Semiconductors: General Theory*" Phys. Rev. **102**, (1956), pp 1030-1041.

Luttinger J.M, and Kohn W, "*Motion of Electrons and Holes in Perturbed Periodic Fields*" Phys. Rev. **97**, (1955), pp 869-883.

Marzin J.Y, "*Strained Superlattices*" in *Heterojunctions and Semiconductor Superlattices,* edited by Allan G, Bastard G, Boccara N, Lannoo M, and Voos M, Springer-Verlag, Berlin, (1986), pp 161-176.

Marzin J.Y, Gérard J.M, Voisin P and Brum J.A, in *Semiconductors and Semimetals, Vol. 32 : Strained-Layer Superlattices:Physics*, Chapter 3, vol.ed T.P Pearsall, Academic Press, New York, (1990), pp 55-118.

Nag. B.R, *Electron Transport in Compound Semiconductors*, Springer-Verlag, Berlin, (1980).

Nye J.F, *Physical Properties of Crystals: Their Representation by Tensors and Matrices*, Oxford, Clarendon, (1957).

O'Reilly E.P, "*Valence Band Engineering in Strained-Layer Structures*", Semicon. Sci. Technol., **4**, (1989), pp 121-137.

Pearsall T.P, (volume editor), *Strained Layer Superlattices: Physics*, Vol. 32 of *Semiconductor and Semimetals*, eds. R.K.Willardson and A.C.Beer,Academic Press, New York, (1990)

People R, and Sputz S.K, "*Band Nonparabolicities in Lattice-Mismatch-Strained Bulk Semiconductor Layers*" Phys. Rev. **B 41**, (1990), pp 8431-8439.

Pikus G.E, and Bir G.L, "*Effect of Deformation on the Hole Energy Spectrum of Germanium and Silicon*" Fiz. Tverd. Tela (Leningrad) 1, (1959) pp 1642-1658
[Sov. Phys. Solid State **1**, (1960), pp 1502-1517]

Pikus G.E, and Bir G.L, *Symmetry and Strain Induced Effects in Semiconductors*, Wiley, New York, (1974), chapter 5.

Pollak F.H, in *Semiconductors and Semimetals, Vol. 32 : Strained-Layer Superlattices:Physics*, Chapter 2, vol. ed T.P Pearsall, Academic Press, New York, (1990), pp 17-53.

Ram-Mohan L.R, Yoo K.H, and Aggarwal R.L, "*Transfer-matrix Algorithm for the Calculation of the Band Structure of Semiconductor Superlattices*" Phys. Rev. **B 38**, (1988), pp 6151-6159.

Schulman J.N, and Chang Y.C, "*Band Mixing in Semiconductor Superlattices*" Phys. Rev. **B 31**, (1985), pp 8041-8048.

Schuurmans M.F.H, and 't Hooft G.W, "*Simple Calculations of Confinement States in a Quantum Well*" Phys. Rev. **B 31**, (1985), pp 8041-8048.

Smith D.L, and Mailhiot C, "***k.p*** *Theory of Semiconductor Superlattice Electronic Structure. I. Formal Results.*" Phys. Rev. **B 33**, (1986), pp 8345-8359.

Warburton R.J, "*High Magnetic Field Studies of Strained Layer Superlattices*" D. Phil. Thesis, University of Oxford (1991).

Warburton R.J, Nicholas R.J, Howard L.K, and Emeny M.T, "*Intraband and Interband Magneto-optics of p-type* $In_{0.18}Ga_{0.82}As/GaAs$ *Quantum Wells*" Phys. Rev. **B 43**, (1991), pp 14124-14133.

Chapter 4. **Calculations for Heterostructures: electronic and optical Properties.**

The following chapter details the methods used for calculating various properties of heterostructures. Specifically, the emphasis is on obtaining electronic and optical descriptions of a given structure under the effects of an applied electric field. In the present work, the electronic description amounts to a calculation of the confined states in either quantum wells (QW) or superlattices (SL). If the heterostructure as a whole can be considered as an artificial material, then the confined states will represent its band structure. In considering optical properties, the accent has been placed on calculating the absorption spectrum close to the heterostructure band edge. Particular attention is paid to the absorption due to excitons which provide heterostructures with their remarkable electro-absorption properties, namely the quantum confined Stark effect (Miller *et al* 1984, 1985).

§4.1 Introduction: electronic properties.

The following two sections (§4.2 and §4.3), present the methods used for calculating confined states in heterostructures. The first section concentrates on superlattices and single quantum wells in the 'flat band' condition ie. zero field solutions. While in §4.3, the method adopted for calculating states under the influence of a perpendicularly applied electric field is detailed. It should be emphasised that the model accounting for applied fields is equally capable of investigating zero field situations. However, by separating the methods in this way it serves to highlight not only their qualitative differences, but also present a 'suite' of models that may be used in heterostructure device design. Further discussion is saved for the relevant sections, although some justification for the use of different models is briefly summarized below.

A heterostructure with a uniform applied electric field allows the possibility of tunnelling, so strictly speaking, there are no bound states in the problem (see eg. Schmitt-Rink *et al* 1989). Despite this, there have been many ways to approach theoretical field calculations, (cf. §4.3), although the computation techniques are generally lengthy and quite involved. This can still be the case if a particular method is consistently used for zero applied field. Particularly when realistic descriptions are employed (ie. finite barrier heights and widths) and further calculations are required, eg. optical properties. In contrast, zero field methods (at least in a simple envelope function approximation) are computationally no more demanding than the classic 'particle-in-a-box' problem found in any introductory text on Quantum Mechanics. Therefore such calculations can be carried out much more efficiently. For example, consider investigating the quaternary system $(Al_xGa_{1-x})_yIn_{1-y}As/(Al_uGa_{1-u})_vIn_{1-v}As$ for structures to operate around 1.55μm. It turns out that a wide range of suitable designs exist differing in well width and composition (P.Guy, private communication). Clearly the ability to perform wide range efficient calculations with these parameters is beneficial in device design. In practice, once an initial group of structures has been isolated, one can proceed to investigate more thoroughly the merits of each design depending on the proposed application. This type of design procedure was utilized for the work appearing in chapter 5.

The correspondence with the 'particle-in-a-box' problem is evident from considering the real space potential profile of a typical structure (cf Fig.1-2). Essentially, the difference lies with the description of the constituent layers making up the structure. Working within the envelope function approximation (EFA), (Bastard 1981,1982), enables each layer to be described in terms of an 'effective mass'. This embodies all the information about the microscopic details of the layer, such as the periodic potential arising from the crystal lattice. The resulting 'macroscopic' view means that for the simplest case (a one band model), the band edge effective mass of the particle in the layer replaces the free electron mass in the text book problem. A quantum well, constructed by *joining* three materials with different band gaps (barrier/well/barrier), can now be viewed as a 'particle-in-a-box' problem with the envelope function replacing the wavefunction. The time independent Schrödinger equation must be satisfied in each layer and solutions have a well-known form. Application of the boundary conditions produces a transcendental function with zeros corresponding to the bound states (eigenvalues) of the problem. This function is specified by the solutions to the auxiliary equations in each layer which are simply the energy-wave vector relationships (for a one band description this is parabolic in nature). Of course adopting a more sophisticated band structure description in each layer, eg. the eight band **k.p** description of Smith and Mailhiot (1986), results in the computations becoming significantly more involved. For the present work, a reduced **k.p** model (Kane) is used to describe each layer. This was shown in the last chapter (§3.4.2) to adequately describe the bulk layer band structure near the band edge, including the effects of strain on band edges and effective masses, while still providing a simple closed form expression for the energy-wave vector relationship. Computations for a range of structures (superlattices or single quantum wells) at zero applied field can be efficiently performed, (§4.2). The Kane description is also used for the field calculations presented in §4.3.

Boundary conditions with the Kane model.

The present section is concerned with presenting the Kane model (3.4.2) in a form that is used throughout the rest of this work. The boundary conditions required for heterostructure calculations are seen to appear quite naturally, although it should be stressed that these refer only to the situation where the Kane model is used (Taylor and Burt 1987). As to the general subject of boundary conditions for heterostructures, this is an area which has and still continues to attract considerable interest (Morrow and Brownstein 1984, Altarelli 1986, Smith and Mailhiot 1986, Taylor and Burt 1987, Pötz and Ferry 1987, Burt 1988, Ando *et al* 1989, Einevoll *et al* 1990, Laikhtman 1992, Elçi 1994). A good discussion on the subject is given by Burt (1992).

For the initial problem of calculating the confined states, we are only interested in motion along the confinement (z) direction. In the Kane model, the wavefunction for the light states in each material is written as (Taylor and Burt 1987),

$$\psi^{l}(z) = f^{l}_{el}(z)u_{el} + f^{l}_{lh}(z)u_{lh} + f^{l}_{so}(z)u_{so} \tag{4.1}$$

where $f^{l}_{el}(z), f^{l}_{lh}(z)$ and $f^{l}_{so}(z)$ are the conduction, light hole and spin-orbit split-off envelope functions in material l. The basis functions, u_{el}, u_{lh} and u_{so}, are the band edge Bloch functions listed in (3.14), these are generally assumed to be the same in each material (Bastard 1981). Since only the confinement motion is considered, the heavy hole state does not couple to the *near* bands and is separately described, (cf. §3.4.2).

The Hamiltonian operating on the envelope functions for the light states is written as:

$$\mathbf{H}^{l}_{total_{3B}} = \begin{array}{c} \begin{array}{ccc} el & \qquad lh & \qquad so \end{array} \\ \begin{bmatrix} E^{l}_{gs} & -i\sqrt{\frac{2}{3}}\mathbf{P}_{K}\hat{k}_{z} & i\sqrt{\frac{1}{3}}\mathbf{P}_{K}\hat{k}_{z} \\ i\sqrt{\frac{2}{3}}\mathbf{P}_{K}\hat{k}_{z} & E^{l}_{lh}\ (=\delta E^{l}_{s}) & -\sqrt{\frac{1}{2}}\delta E^{l}_{s} \\ -i\sqrt{\frac{1}{3}}\mathbf{P}_{K}\hat{k}_{z} & -\sqrt{\frac{1}{2}}\delta E^{l}_{s} & E^{l}_{so} \end{bmatrix} \end{array} \tag{4.2}$$

which is similar to that presented in (§3.4.2). The difference here is that the strain terms coupling conduction and valence band states have been neglected. Comments have already been made about neglecting these terms (§3.4.2). The matrix element, $\mathbf{P}_{K}$, should in principle be layer dependent (Bastard 1982). Although it is found in practice that most III-V materials take on a similar values (see for eg. Hermann and Weisbuch 1977) and so generally the matrix element is assumed to be the same throughout the structure (Bastard 1982). It was also suggested the similar matrix elements in bulk materials demonstrated the similarities between the Bloch functions, thereby justifying the underlying assumption in the envelope function approximation (Bastard 1982). Work appearing in the literature has since demonstrated the assumption is a reasonable one, and the majority of **k.p** calculations involving both strained and unstrained structures tend to adopt this approximation, (cf. §3.1). Notable exceptions include Smith and Maihoit (1986) and Pötz *et al* (1985), with further comments about the latter work appearing at the end of this section.

In each layer the Schrödinger equation, (3.34), must be satisfied. For the light states, three coupled differential equations for the three envelope functions are written as,

$$(\mathrm{E}^l_{\mathrm{gs}} - \delta\mathrm{E}^l_{\mathrm{vhh}} - \mathrm{E})f^l_{el} - i\sqrt{\frac{2}{3}}\mathrm{P_K}\hat{\mathrm{k}}_{\mathrm{z}} f^l_{lh} + i\sqrt{\frac{1}{3}}\mathrm{P_K}\hat{\mathrm{k}}_{\mathrm{z}} f^l_{so} = 0 \tag{4.3a}$$

$$i\sqrt{\frac{2}{3}}\mathrm{P_K}\hat{\mathrm{k}}_{\mathrm{z}} f^l_{el} + (\mathrm{E}^l_{\mathrm{lh}} - \delta\mathrm{E}^l_{\mathrm{vhh}} - \mathrm{E})f^l_{lh} - \sqrt{\frac{1}{2}}\delta\mathrm{E}^l_{\mathrm{s}} f^l_{so} = 0 \tag{4.3b}$$

$$-i\sqrt{\frac{1}{3}}\mathrm{P_K}\hat{\mathrm{k}}_{\mathrm{z}} f^l_{el} - \sqrt{\frac{1}{2}}\delta\mathrm{E}^l_{\mathrm{s}} f^l_{lh} + (\mathrm{E}^l_{\mathrm{so}} - \delta\mathrm{E}^l_{\mathrm{vhh}} - \mathrm{E})f^l_{so} = 0 \tag{4.3c}$$

The problem can be simplified by rewriting the equations in terms of one envelope function (Bastard 1981, Taylor and Burt 1987, Johnson *et al* 1990). It is worth noting that these works are all concerned with zero strain structures, hence there is no light hole to spin orbit coupling which somewhat simplifies the reduction method. The coupled differential equations (4.3) are rewritten into a differential equation ($\hat{\mathrm{k}}_{\mathrm{z}} = -i\,{}^{\mathrm{d}}\!/_{\mathrm{dz}}$) that is non-linear in energy, ie.

$$\left[-\frac{\mathrm{d}}{\mathrm{dz}}\mathrm{B}^l_n(\mathrm{E})\frac{\mathrm{d}}{\mathrm{dz}}\mathrm{A}^l_n(\mathrm{E}) + \mathrm{V}^l_n\right]f^l_n = \mathrm{E}f^l_n \tag{4.4}$$

The coefficients, $\mathrm{B}^l_n(\mathrm{E})$ and $\mathrm{A}^l_n(\mathrm{E})$, are energy and position dependent (throughout the structure) while V^l_n is the position dependent band edge for the *n*th band. For the bands considered in this thesis, expressions for the coefficients are listed in Table 4-1. Only those for the electron and light hole bands are presented for the light states, along with the coefficient values for the heavy hole band.

[note: In Table 4-1, $\mathrm{E}^l_{\mathrm{gs}}$, $\mathrm{E}^l_{\mathrm{lhkz}}$ and $\mathrm{E}^l_{\mathrm{sokz}}$ are the strained conduction, light hole and spin-orbit split-off band edges of a layer. They are energy solutions of the general $\mathrm{E(k_z)}$ relation in each layer when $\mathrm{k_z}$=0 , see for example §3.5.1 and (3.70)]

Table 4-1. *Coefficients which appear in the differential equations for the envelope functions (equation 4.4)*

conduction band (*n=el*)

$B^l_n(E)$:
$$\frac{P^2_{K,n}}{3}\left(\frac{3E + 3\delta E^l_{vhh} + 2\delta E^l_s - 2E^l_{so} - E^l_{lh}}{(E + \delta E^l_{vhh} - E^l_{lhkz})\ (E + \delta E^l_{vhh} - E^l_{sokz})}\right)$$

$A^l_n(E)$:
$$1$$

V^l_n:
$$\left(E^l_{gs} - \delta E^l_{vhh}\right)$$

heavy hole band (*n=hh*)

$B^l_n(E)$:
$$-\frac{\hbar^2}{2m^l_{hh}}$$

$A^l_n(E)$:
$$1$$

V^l_n:
$$-\delta E^l_{vhh}$$

light hole band (*n=lh*)

$B^l_n(E)$:
$$\frac{P^2_{K,n}}{3}\left(\frac{(E + \delta E^l_{vhh} - E^l_{so}) + {}^{\delta E^l_s}\!/_2}{(E + \delta E^l_{vhh} - E^l_{gs})(E + \delta E^l_{vhh} - E^l_{sokz})}\right)$$

$A^l_n(E)$:
$$\left(\frac{3E + 3\delta E^l_{vhh} + 2\delta E^l_s - 2E^l_{so} - E^l_{lh}}{(E + \delta E^l_{vhh} - E^l_{so}) + {}^{\delta E^l_s}\!/_2}\right)$$

V^l_n:
$$\left(E^l_{lhkz} - \delta E^l_{vhh}\right)$$

The boundary conditions on the envelope functions can be obtained by integrating (4.4) across an interface (Johnson *et al* 1990). These can be stated as requiring the continuity of

$$\mathrm{B}_n^l(\mathrm{E})\frac{\mathrm{d}}{\mathrm{dz}}\mathrm{A}_n^l(\mathrm{E})f_n^l \tag{4.5}$$

and

$$\mathrm{A}_n^l(\mathrm{E})f_n^l \tag{4.6}$$

across a heterostructure interface. Under the appropriate conditions, the coefficients in Table (4-1) reduce to the unstrained expressions appearing in the literature (Bastard 1981, Taylor and Burt 1987, Johnson *et al* 1990). The work by Bastard (1981,1982) first suggested the relations (4.5) and (4.6) for Kane models to be consistent with the continuity of cell averaged current . For energies near the nth band edge, equation (4.5) for electrons and heavy holes generalises the BenDaniel and Duke (1966) condition which states that

$$\frac{1}{\mathrm{m}^{*l}}\frac{\mathrm{d}}{\mathrm{dz}}f_n^l \quad \text{is continuous at the interface}$$

The second condition for electrons and heavy holes is the expected continuity of the envelope function (Bastard 1981). However, for the light hole bands (and spin-orbit split-off bands), the coefficient, $\mathrm{A}_n^l(\mathrm{E})$ is discontinuous at the interface (unless the materials are the same). Since the product, $\mathrm{A}_n^l(\mathrm{E})f_n^l$ is continuous, the light hole envelope is necessarily discontinuous. This loss of continuity for the light hole (and spin-orbit split-off) envelope function is a result of neglecting terms of $O(\mathrm{k}^2)$ in the Kane approach (Taylor and Burt 1987, Burt 1992).

As they stand, the conditions (4.5) and (4.6) are the boundary conditions that need to be applied if the Kane model is used. They differ from those previously published (eg. Johnson *et al* 1990) in that additional terms due to strain are included. The coefficient, $\mathrm{B}_n^l(\mathrm{E})$, contains the matrix element which, in Bastard's approach (Bastard 1981, 1982), is treated as a constant throughout the structure. However, work by Pötz and Ferry (1985) on unstrained structures allowed the matrix element to be layer dependent. [note: their **k.p** model included coupling terms accounting for the far band interaction which were also allowed to be layer dependent]. To account for this in the present situation, the Hamiltonian needs to be modified to keep it Hermitian (Pötz and Ferry 1985). This has been another area of much debate since there appears no unique way to do this (see for eg. von Roos 1983, Morrow and Brownstein 1984, Einevoll *et al* 1990). If a position dependent matrix element is to be used in (4.2), then, to keep $\mathbf{H}_{total}^l$ Hermitian, the off-diagonal conduction-valence band terms can be replaced by (Pötz and Ferry 1985),

$$\mathbf{P}_{\mathrm{K}}^{l}\hat{\mathrm{k}}_{\mathrm{z}} \rightarrow \frac{1}{2}\left(\mathbf{P}_{\mathrm{K}}^{l}\hat{\mathrm{k}}_{\mathrm{z}} + \hat{\mathrm{k}}_{\mathrm{z}}\mathbf{P}_{\mathrm{K}}^{l}\right) \tag{4.7}$$

Following a similar procedure to that above, we obtain the boundary conditions:

$$\left(\mathbf{P}_{\mathrm{K},n}^{l}\right)^{2}\widehat{\mathrm{B}}_{n}^{l}(\mathrm{E})\frac{\mathrm{d}}{\mathrm{dz}}\mathrm{A}_{n}^{l}(\mathrm{E})f_{n}^{l} \tag{4.8}$$

and

$$\mathrm{A}_{n}^{l}(\mathrm{E})f_{n}^{l} \tag{4.9}$$

where the new coefficient is related to the appearing in Table 4-1, ie. $\widehat{\mathrm{B}}_{n}^{l}(\mathrm{E}) = {}^{\mathrm{B}_{n}^{l}(\mathrm{E})}\!\big/_{\mathbf{P}_{\mathrm{K},n}^{2}}$.

Pötz and Ferry's justification for using position dependent parameters such as the matrix element, is that the boundary conditions refer to the unit cell averaged quantities either side of an interface. They recognized this as being consistent with the envelope function approach which only allows descriptions on a macroscopic scale. Instead of requiring the Bloch functions to be identical throughout the structure, their approach only calls for a one-to-one relationship between the Bloch functions in each layer (Pötz and Ferry 1987).

§4.2 Subband Calculations: zero applied field.

Generally, the practical structures considered in this thesis are all Multi-Quantum Well (MQW) structures (chapter 5). For these structures it is assumed the width of the barrier material is sufficient to minimise coupling between the wells (cf. §1.3). In this case, the electronic properties of the MQW can be determined from those found in a single isolated well. Obtaining the value for a 'sufficient' barrier width is very much system dependent, relying on a number of parameters such as band offset (ie. well depth) and effective masses (ie. penetration length into the barrier). Because of this, I felt it would be useful to construct a model that could indicate the degree of coupling present in MQW structures. The aim was not to give it a central role in the overall project, but rather 'a walk on part' that would be useful in the initial stages of investigating material systems. For this reason, a zero field superlattice (SL) model was chosen which was nothing more than a EFA version of the classic Kronig-Penney analysis of electrons moving in a periodic lattice (Bastard 1981, 1982). Exactly how many wells constitute a superlattice analysis would again be system dependent. However, an early review on GaAs/AlGaAs structures by Kolbas and Holonyak (1984) indicated that between 6 to 10 wells making up a MQW region is enough to warrant the use of a superlattice calculations. The type of structures investigated here (Chapter 5) have at least 30 wells making up the MQW region.

The following sections initially develop the expressions in terms of *three* layer structures (or four in quantum well), in relation to the structures investigated in Chapter 6.

§4.2.1 Superlattice solutions: three layer basis.

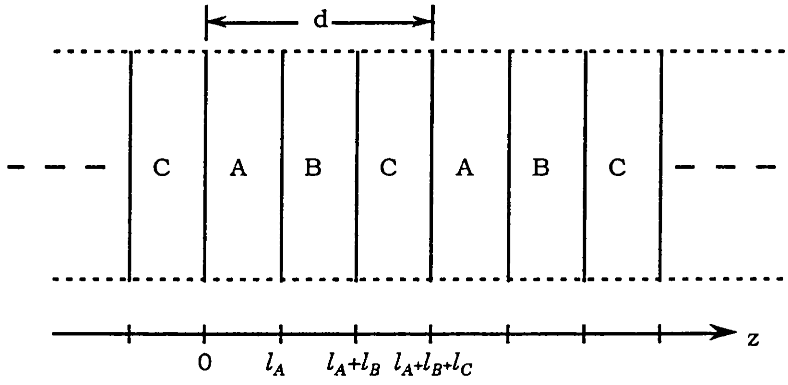

Figure 4-1. *Schematic representation of a structure with a three layer basis.*

For the structure in Fig.4-1, the layers A, B and C make up one period of the superlattice (ie. the superlattice has a three layer basis). In addition to the boundary conditions on the envelopes at each interface, the Bloch condition must be employed to give the required translational symmetry of the problem (Bastard 1981, 1982),

$$f_n(z+d) = \exp[iqd]f_n(z) \tag{4.10}$$

The superlattice wavevector, q, is directed in the growth direction and d is the length of one period in the structure, ie. the superlattice unit cell (Bastard 1982). The energy-wavevector dispersion for the superlattice, E(q) will be restricted to the first Brillouin zone of the superlattice, ie. $-\pi/d \le q \le \pi/d$.

For a given energy, the envelope function in each layer can be written as a sum of forward and backward travelling plane waves:

$$f_n(z) = \alpha_A \exp[ik_A z] + \beta_A \exp[-ik_A z] \qquad \text{for } 0 \le z \le l_A \tag{4.11}$$

$$f_n(z) = \alpha_B \exp[ik_B(z - l_A)] + \beta_B \exp[-ik_B(z - l_A)] \qquad \text{for } l_A \le z \le l_A + l_B \tag{4.12}$$

$$f_n(z) = \alpha_C \exp[ik_C(z - l_A - l_B)] + \beta_C \exp[-ik_C(z - l_A - l_B)] \qquad \text{for } l_A + l_B \le z \le l_A + l_B + l_C \tag{4.13}$$

where the wavevector, k_l, is given by the auxiliary equation of (4.4) for each layer and is expressed as,

$$k_l^2 = \frac{\left(E - V_n^l\right)}{B_n^l(E) A_n^l(E)} \tag{4.14}$$

In the case of $n{=}el$ or lh, this is simply the $E(k_z)$ dispersion from the Kane model (3.59), or a parabolic description (3.58) when $n{=}hh$. Note that the energy dependence of k_l and the coefficients, α_l and β_l, are not explicitly written in the above relations. It should also be noted that a choice of reference level in the structure is required to properly define V_n^l; consequently (3.36) should also be modified to include the third layer.

Initially, the derivation that follows regards $k_l^2 > 0$; in other words, the considered energy range is such that the wave vectors in each layer, k_l, are real. For energies close to the band edge of the well layer this is typically not the case and is addressed later in the section.

Applying the boundary conditions (4.5) and (4.6) at the A-B and B-C interfaces, transfer matrices, $T_{l\to l'}$, relating the coefficients in each layer may be found, ie.

$$\begin{bmatrix} \alpha_B \\ \beta_B \end{bmatrix} = T_{A\to B} \begin{bmatrix} \alpha_A \\ \beta_A \end{bmatrix} \quad \text{and} \quad \begin{bmatrix} \alpha_C \\ \beta_C \end{bmatrix} = T_{B\to C} \begin{bmatrix} \alpha_B \\ \beta_B \end{bmatrix}, \tag{4.15}$$

The general form of a transfer matrix at an interface between layer l and l' can be written as,

$$T_{l\to l'} = \begin{bmatrix} \left(A_n^{l,l'} + \zeta_n^{l,l'}\right)\exp[ik_l l_l] & \left(A_n^{l,l'} - \zeta_n^{l,l'}\right)\exp[-ik_l l_l] \\ \left(A_n^{l,l'} - \zeta_n^{l,l'}\right)\exp[ik_l l_l] & \left(A_n^{l,l'} + \zeta_n^{l,l'}\right)\exp[-ik_l l_l] \end{bmatrix} \tag{4.16}$$

where

$$A_n^{l,l'} = \frac{A_n^l(E)}{A_n^{l'}(E)} \tag{4.17}$$

and

$$\zeta_n^{l,l'} = \frac{B_n^l(E)\ A_n^l(E) ik_l}{B_n^{l'}(E)\ A_n^{l'}(E) ik_{l'}} \tag{4.18}$$

The Bloch condition enters as,

$$\begin{bmatrix}\alpha_A \\ \beta_A\end{bmatrix}\exp[i\mathrm{q}\mathrm{d}] = \mathrm{T}_{C\to A}\begin{bmatrix}\alpha_C \\ \beta_C\end{bmatrix} \tag{4.19}$$

Substituting (4.15) into (4.19), the problem reduces to an eigenvalue equation of the combined transfer matrices, with eigenvalues, $\exp[i\mathrm{qd}]$, and eigenvectors α_A and β_A. Explicitly,

$$\mathrm{T}_{SL}\begin{bmatrix}\alpha_A \\ \beta_A\end{bmatrix} = \exp[i\mathrm{qd}]\begin{bmatrix}\alpha_A \\ \beta_A\end{bmatrix} \tag{4.20}$$

where,

$$\mathrm{T}_{SL} = \mathrm{T}_{C\to A}\mathrm{T}_{B\to C}\mathrm{T}_{A\to B}$$

Non-trivial solutions of (4.20) exist when $|\mathrm{T}_{SL} - \exp[i\mathrm{qd}]| = 0$, which can be expanded as,

$$\exp[2i\mathrm{qd}] - \exp[i\mathrm{qd}](\tau_{11} + \tau_{12}) + (\tau_{11}\tau_{22} - \tau_{12}\tau_{21}) = 0 \tag{4.21}$$

Here the τ's represent the matrix elements of T_{SL}. For solutions of (4.21) with either real or imaginary q (corresponding to propagating or decaying states) the determinant of T_{SL} must equal one (Sai-Halasz *et al* 1978). Both types of solution give for the superlattice dispersion, q, the relation (Sai-Halasz *et al* 1978, Bastard 1982),

$$\cos(\mathrm{qd}) = \frac{1}{2}(\tau_{11} + \tau_{12}) \tag{4.22}$$

Substituting the relevant elements into (4.22), the dispersion relation for propagating states in each layer, ie. $\mathrm{k}_l^2 > 0$ is:

$$\begin{aligned}\cos(\mathrm{qd}) = {}& \cos(\mathrm{k}_A l_A)\cos(\mathrm{k}_B l_B)\cos(\mathrm{k}_C l_C) \\ & - \frac{1}{2}\{\Omega_{BC}\cos(\mathrm{k}_A l_A)\sin(\mathrm{k}_B l_B)\sin(\mathrm{k}_C l_C) + \Omega_{CA}\sin(\mathrm{k}_A l_A)\cos(\mathrm{k}_B l_B)\sin(\mathrm{k}_C l_C) \\ & + \Omega_{AB}\sin(\mathrm{k}_A l_A)\sin(\mathrm{k}_B l_B)\cos(\mathrm{k}_C l_C)\}\end{aligned} \tag{4.23}$$

where $\Omega_{l,l'}$ is a real variable,

$$\Omega_{l,l'} = \mathrm{A}_n^{l',l}\zeta_n^{l,l'} + \mathrm{A}_n^{l,l'}\zeta_n^{l',l} \tag{4.24}$$

and use is made of the following identities,

$$\mathrm{A}_n^{l,l'}\mathrm{A}_n^{l'',l} = \mathrm{A}_n^{l'',l'}$$

and

$$\zeta_n^{l,l'}\zeta_n^{l'',l} = \zeta_n^{l'',l'} \tag{4.25}$$

For unstrained layers and taking the zero of energy to be the conduction band edge of the A layer, (4.23) for electrons reduces to the dispersion given by Bastard (1982) [Equation 51].

It has already been noted that (4.23) describes the case when the wavevector is real in each layer, therefore it is only valid for energies that lie above all the band edges in the structure, Fig.4-2. In the present work, the important energy range is near the band edge of the well layer where it is likely that in one (or two) of the layers solutions are decaying, ie. $\mathrm{k}_l^2 < 0$ in (4.14). For this case the layer is regarded as a barrier and $\mathrm{k}_l \rightarrow i\kappa_l$ such that the envelopes, (4.11)-(4.13), become exponentially decaying. However, the derivation procedure need not be repeated. With the appropriate substitution of $\mathrm{k}_l \rightarrow i\kappa_l$ into (4.23), the dispersion relation for q can be found for the structure in the particular energy range (Fig.4-2). It can be shown that for energies such that:

$i\kappa_\mathrm{A}$, $\mathrm{k_B}$ and $\mathrm{k_C}$:

$$\begin{aligned}\cos(\mathrm{qd}) = {} & \cosh(\kappa_\mathrm{A} l_A)\cos(\mathrm{k_B} l_B)\cos(\mathrm{k_C} l_C) \\ & -\frac{1}{2}\Big\{\Omega_\mathrm{BC}\cosh(\kappa_\mathrm{A} l_A)\sin(\mathrm{k_B} l_B)\sin(\mathrm{k_C} l_C) + \overline{\Omega}_\mathrm{CA}\sinh(\kappa_\mathrm{A} l_A)\cos(\mathrm{k_B} l_B)\sin(\mathrm{k_C} l_C) \\ & \qquad -\overline{\Omega}_\mathrm{AB}\sinh(\kappa_\mathrm{A} l_A)\sin(\mathrm{k_B} l_B)\cos(\mathrm{k_C} l_C)\Big\}\end{aligned} \tag{4.26}$$

$i\kappa_\mathrm{A}$, $\mathrm{k_B}$ and $i\kappa_\mathrm{C}$:

$$\begin{aligned}\cos(\mathrm{qd}) = {} & \cosh(\kappa_\mathrm{A} l_A)\cos(\mathrm{k_B} l_B)\cosh(\kappa_\mathrm{C} l_C) \\ & -\frac{1}{2}\Big\{\overline{\Omega}_\mathrm{BC}\cosh(\kappa_\mathrm{A} l_A)\sin(\mathrm{k_B} l_B)\sinh(\kappa_\mathrm{C} l_C) - \Omega_\mathrm{CA}\sinh(\kappa_\mathrm{A} l_A)\cos(\mathrm{k_B} l_B)\sinh(\kappa_\mathrm{C} l_C) \\ & \qquad -\overline{\Omega}_\mathrm{AB}\sinh(\kappa_\mathrm{A} l_A)\sin(\mathrm{k_B} l_B)\cosh(\kappa_\mathrm{C} l_C)\Big\}\end{aligned} \tag{4.27}$$

$i\kappa_\mathrm{A}$, $i\kappa_\mathrm{B}$ and $\mathrm{k_C}$:

$$\begin{aligned}\cos(\mathrm{qd}) = {} & \cosh(\kappa_\mathrm{A} l_A)\cosh(\kappa_\mathrm{B} l_B)\cos(\mathrm{k_C} l_C) \\ & -\frac{1}{2}\Big\{-\overline{\Omega}_\mathrm{BC}\cosh(\kappa_\mathrm{A} l_A)\sinh(\kappa_\mathrm{B} l_B)\sin(\mathrm{k_C} l_C) + \overline{\Omega}_\mathrm{CA}\sinh(\kappa_\mathrm{A} l_A)\cosh(\kappa_\mathrm{B} l_B)\sin(\mathrm{k_C} l_C) \\ & \qquad -\Omega_\mathrm{AB}\sinh(\kappa_\mathrm{A} l_A)\sinh(\kappa_\mathrm{B} l_B)\cos(\mathrm{k_C} l_C)\Big\}\end{aligned} \tag{4.28}$$

where,

$$\overline{\Omega}_{l,l'} = \mathrm{A}_n^{l',l}\zeta_n^{l,l'} - \mathrm{A}_n^{l,l'}\zeta_n^{l',l} \tag{4.29}$$

and κ_l is the imaginary solution of (4.14). Note, (4.29) or (4.24) with $k_l \rightarrow i\kappa_l$ implies an imaginary value. However it turns out that the product of this and the hyperbolic function ($\sin(i\kappa_l l_l) \rightarrow i\sinh(\kappa_l l_l)$) is real. Hence (4.29) and (4.26) are always considered real valued.

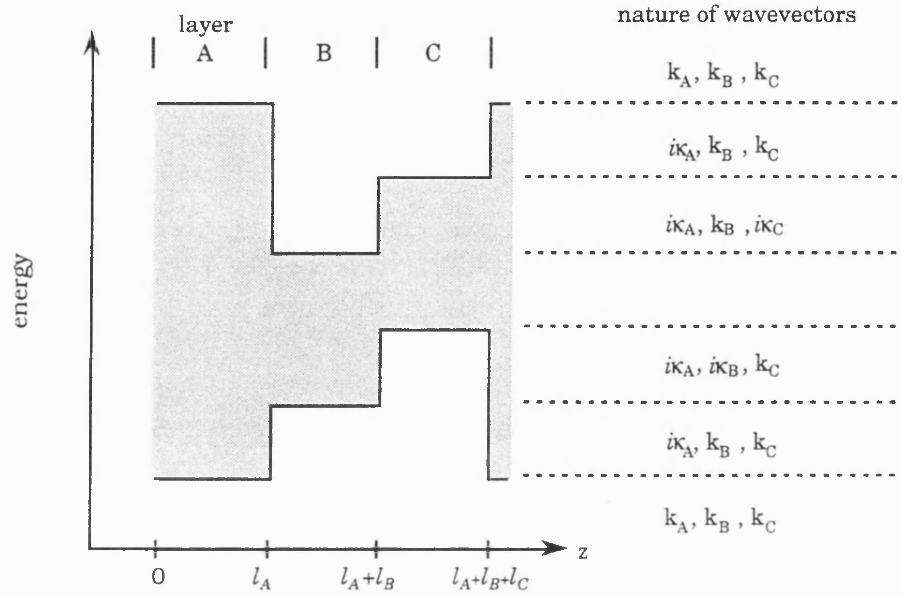

Figure 4-2. *Potential energy profile of a three layer structure similar to those considered in chapter 6. The energy dependent nature of the wave vectors in each layer is indicated.*

Allowed superlattice states are found from the above relations when $|\text{RHS}| \leq 1$. For a given value of q the relations then admit an infinite number of solutions. Although, for the present work, it is typically the lowest energy subband corresponding to either the conduction or valence band of the superlattice that is of interest. This subband occurs for $q = 0$ to $q = |\pi/d|$ (Fig.4-3a) corresponding to the bottom and top (respectively) of the miniband.

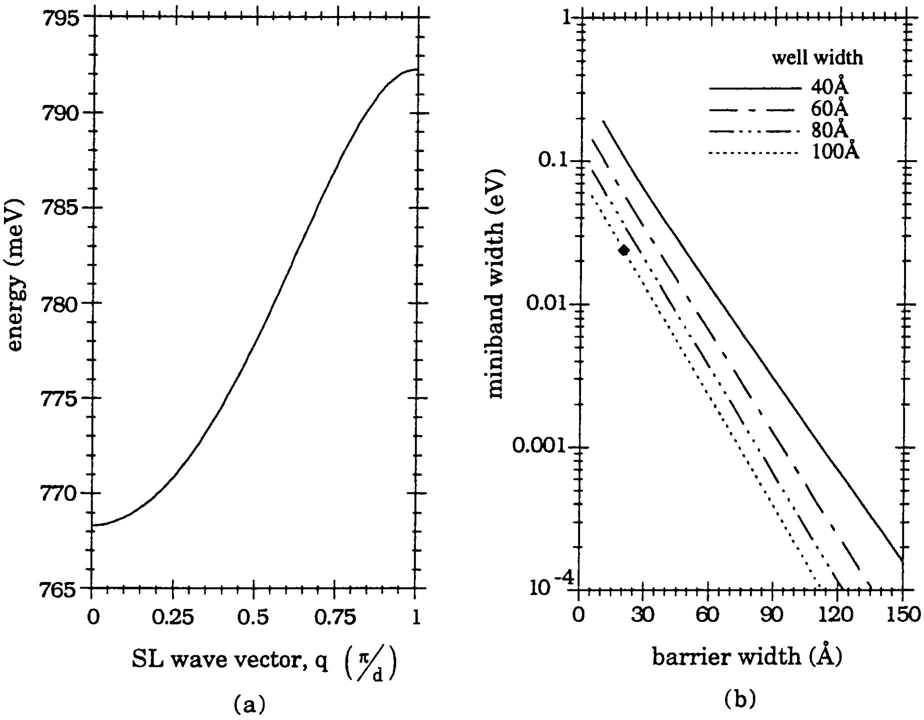

Figure 4-3. *Superlattice calculations for $In_{0.53}Ga_{0.47}As/InP$ structures.(a) The E(q) dispersion of the lowest conduction band for a 100Å(well)/20Å(barrier) structure. (note: the zero of energy is at the bulk heavy hole band edge of the well layer). (b) The miniband width of the lowest conduction band for several well widths plotted as a function of barrier width. (note. the result from (a) is indicated in (b)).*

The well width dependence of the miniband width in Fig.4-3b can be explained by considering the lowest conduction band state of a single well. As the well width narrows, the state lies further away from the band edge of the well layer and the potential barrier it experiences reduces. The penetration of the envelope function into the barrier material increases and subsequently induces coupling if adjacent wells are present. Therefore the degree of coupling in a system depends not only on the barrier width but also the height of the potential barrier (Bastard 1988, chp.1&3 discusses these points further).

Reduction to two layer basis.

Using the three basis relation (4.23), the more recognizable two basis relation can be recovered by employing either one of two conditions:

(i) setting one of the layer widths to zero, (for example l_C = 0), then (4.23) becomes:

$$\cos(qd) = \cos(k_A l_A)\cos(k_B l_B) - \frac{1}{2}\Omega_{AB}\sin(k_A l_A)\sin(k_B l_B) \qquad (4.30)$$

All the terms retain the same definition and meaning, only now $d = l_A + l_B$.

(ii) treating two layers as being identical materials, but not necessarily equal lengths, for example $B = C$ (therefore $k_B = k_C$) then (4.23) becomes:

$$\cos(qd) = \cos(k_A l_A)\cos\big(k_B(l_B + l_C)\big) - \frac{1}{2}\Omega_{AB}\sin(k_A l_A)\sin\big(k_B(l_B + l_C)\big) \qquad (4.31)$$

Strictly speaking, (4.31) is still a three basis description since $d = l_A + l_B + l_C$. Of course if $l_B + l_C = l_D$ is considered then it can be thought of in terms of two layers, A and D. Finally, for the relations (4.30) and (4.31) the wavevectors are taken to be real, but as before, other cases are obtained with the substitution $k_l \rightarrow i\kappa_l$ when required.

Since the two basis descriptions are contained in those required for a basis of three, the program used for superlattice calculations is written for a three layer superlattice. When conventional two layer structures are investigated (Chapter 5), I have employed condition (ii) in the calculations.

Superlattice or multi-quantum well?

Generally, it is the SL relations (4.26)-(4.28) that are relevant for the structures investigated in this work. Layer A is always treated as the barrier material (ie. InP) while layers B and C will either form a composite well material (Chapter 6) or single well material (Chapter 5). For these structures, the utility of SL calculations lie in the quantitative measure of coupling between the wells, given as the energy band or 'miniband' of the SL. Thus the calculations can demonstrate the connection and distinction between MQW's and SL's. The distinction depends on the relative magnitude of the barrier width (l_A) and of the wave function penetration depth in the barrier, κ_A^{-1} (Chemla and Miller 1985). In MQW's, $\kappa_A l_A >> 1$ so the electronic and optical properties are those of a series of uncoupled wells. Conversely, for SL's, $\kappa_A l_A < 1$ and the coupling of energy levels among the wells gives rise to subbands or minibands for the superlattice (Fig.4-4).

Typically, SL calculations are used to find a barrier width that gives $\sim 10^{-4}$ eV miniband for the ground states. This figure is arbitrary and quite possibily an over cautious target since the SL calculation is carried out assuming no field exists across the structure. It should be remembered that the practical devices in this thesis are p-i-n diodes with the MQW forming the intrinsic region. The built in field would, to some extent, reduce the alignment of states in adjacent wells and therefore reduce the coupling.

Once a minimum barrier is found the MQW structure is investigated as a single QW. Hence the rest of the theory (eg. effects of electric field, optical properties) is based on single QW calculations.

§4.2.2 Quantum well solutions: composite wells.

Single quantum well solutions with two layers making up a composite well region can be derived in a similar manner using a transfer matrix approach. Instead of the Bloch condition (4.10), the assumption,

$$f_n(z) \to 0 \quad \text{as} \quad z \to \pm\infty \tag{4.32}$$

is used which implies that the envelope function is bound. Therefore the two layers making up the well region are enclosed by the barrier material (A layer) whose width is sufficient to satisfy (4.32). It follows that the energy range is restricted so exponentially decaying solutions exist in the barrier regions, ie. $k_A^2 < 0$ so $k_A \to i\kappa_A$.

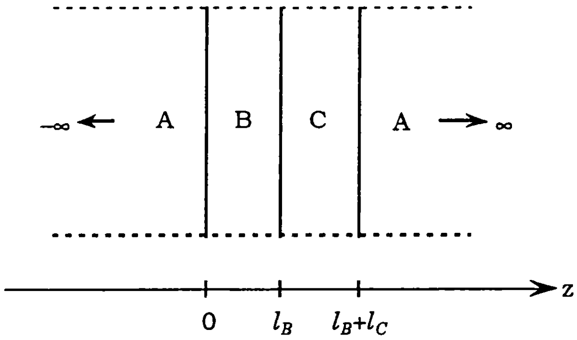

Figure 4-4. *Schematic representation for a single quantum well structure.*
[note the change of labelling on the z a-axis from the superlattice case (cf. Fig.4-1)]

A transfer matrix can be found for the structure:

$$\begin{pmatrix} \alpha_A \\ \beta_A \end{pmatrix}_{\text{at } z=0} = T_{SQW} \begin{pmatrix} \alpha_A \\ \beta_A \end{pmatrix}_{\text{at } z=l_B+l_C} \tag{4.33}$$

with,

$$T_{SQW} = T_{A\to B} T_{B\to C} T_{C\to A}$$

The individual transfer matrices relate the envelope coefficients between adjacent layers at the interface, although it should be noted they do not take the same form as those presented in the previous section.

In the QW structure (Fig.4-4), the envelopes in the two encompassing A layers are written as:

$$
\begin{aligned}
f_n(z) &= \alpha_A \exp\left[-\kappa_A z\right] + \beta_A \exp\left[\kappa_A z\right] && \text{for } z \le 0 \\
f_n(z) &= \alpha_A \exp\left[-\kappa_A\left(z - l_B - l_C\right)\right] + \beta_A \exp\left[\kappa_A\left(z - l_B - l_C\right)\right] && \text{for } z \ge l_B + l_C
\end{aligned}
$$

For a bound solution (4.33) must be satisfied, this requires that $\alpha_A\big|_{z=0} = \beta_A\big|_{z=l_B+l_C} = 0$. Consequently, for this to be true, the energy dependent matrix element, τ_{11}, of T_{SQW} must be zero. Therefore the problem of finding the QW energy solutions is expressed as finding the zeros of the transcendental function, $\tau_{11}(E) = 0$. As with the superlattice dispersion, the form of the transcendental equation depends on the nature of the wavevectors at the given energy (cf. Fig.4-2).

$\underline{i\kappa_A,\ k_B \text{ and } k_C}$:

$$
\begin{aligned}
&\cos\left(k_B l_B\right)\cos\left(k_C l_C\right) \\
&\qquad -\frac{1}{2}\left\{\Omega_{BC}\sin\left(k_B l_B\right)\sin\left(k_C l_C\right) + \overline{\Omega}_{CA}\cos\left(k_B l_B\right)\sin\left(k_C l_C\right)\right. \\
&\qquad\quad \left. -\overline{\Omega}_{AB}\sin\left(k_B l_B\right)\cos\left(k_C l_C\right)\right\} = 0
\end{aligned}
\tag{4.34}
$$

$\underline{i\kappa_A,\ k_B \text{ and } i\kappa_C}$:

$$
\begin{aligned}
&\cos\left(k_B l_B\right)\cosh\left(\kappa_C l_C\right) \\
&\qquad -\frac{1}{2}\left\{\overline{\Omega}_{BC}\sin\left(k_B l_B\right)\sinh\left(\kappa_C l_C\right) - \Omega_{CA}\cos\left(k_B l_B\right)\sinh\left(\kappa_C l_C\right)\right. \\
&\qquad\quad \left. -\overline{\Omega}_{AB}\sin\left(k_B l_B\right)\cosh\left(\kappa_C l_C\right)\right\} = 0
\end{aligned}
\tag{4.35}
$$

$\underline{i\kappa_A,\ i\kappa_B \text{ and } k_C}$:

$$
\begin{aligned}
&\cosh\left(\kappa_B l_B\right)\cos\left(k_C l_C\right) \\
&\qquad -\frac{1}{2}\left\{-\overline{\Omega}_{BC}\cosh\left(\kappa_B l_B\right)\sin\left(k_C l_C\right) + \overline{\Omega}_{CA}\cosh\left(\kappa_B l_B\right)\sin\left(k_C l_C\right)\right. \\
&\qquad \left. -\Omega_{AB}\sinh\left(\kappa_B l_B\right)\cos\left(k_C l_C\right)\right\} = 0
\end{aligned}
\tag{4.36}
$$

The same results can be obtained by considering the equivalent superlattice relations (Bastard 1988). In the limit of infinitely thick barriers (ie. $\kappa_A l_A >> 1$), the right hand side of equations (4.26)-(4.28) diverges like $\exp\left[\kappa_A l_A\right]$, unless the coefficients in front of them are equal to zero. Thus the above equations may also be reproduced in this way.

In situations where only the zero field energy solutions are required, computing the superlattice dispersion when $\kappa_A l_A >> 1$ achieves the same result. [note: A feature which was useful in testing the two programs]. However for calculations concerning optical properties, the envelope functions at the solutions are needed. In this case, the direct transfer matrix method (above) was the preferred choice. In a straight forward manner the coefficients at each interface can be evaluated once the energy is known and the envelope function constructed.

Reduction to a single well layer.

The same conditions applied to the superlattice relations can be equivalently used for (4.34)-(4.36).

(i) setting $l_C = 0$, then (4.34) or (4.35) both reduce to

$$\cos\left(k_B l_B\right) + \frac{1}{2}\,\overline{\Omega}_{AB}\sin\left(k_B l_B\right) = 0 \tag{4.37}$$

A similar equation is found for (4.36) if $l_B = 0$ and C is treated as the well material.

(ii) assuming the well layers B and C are the same material but not necessary equal lengths, then (4.34) or (4.35) can be written as,

$$\cos\left(k_B\left(l_B + l_C\right)\right) + \frac{1}{2}\,\overline{\Omega}_{AB}\sin\left(k_B\left(l_B + l_C\right)\right) = 0 \tag{4.38}$$

§4.3 Calculating Subbands in an Electric Field.

Calculating the field induced energy shifts of electron and hole subbands in heterostructures has been treated by many authors using a variety of methods. A brief review of some of these works is discussed before presenting the method adopted in this thesis.

§4.3.1 Previous methods appearing in the literature.

Early work by Bastard *et al* (1983) used a variational method to describe ground state energy shifts in a QW under an applied electric field, F. Both infinite and finite quantum well descriptions (of width L) were considered. For weak applied fields, the energy shift was seen to be proportional to F^2L^4, while for larger fields, deviations from this quadratic field dependence were found (Bastard *et al* 1983). In addition to this, the results were compared with solutions from a perturbation method, good agreement between both approaches was found. However, despite providing a useful insight into the parameters that determine the size of the shift, as with all variational methods, considerable insight is required to choose the form of the starting wave function. Extending the relatively simple ground state forms (Bastard *et al* 1983) to higher energy states or composite well structures (Chapter 6) would become increasingly complicated.

Exact numerical calculations for an applied electric field can be performed if the Schrödinger equation for the problem is recast such that the solutions are Airy functions (Austin and Jaros 1985, Miller *et al* 1985). As with the variational method, calculations have been performed based on infinite QW descriptions (Miller *et al* 1985, Matsuura and Kamizato 1986) and finite QW descriptions (Austin and Jaros 1985, Ghatak *et al* 1990). In the latter descriptions, the Airy function solution in each layer requires straight forward matching conditions at each well/barrier interface (Austin and Jaros 1985). In this way the method can be extended to describe multiple layer structures exhibiting interwell coupling of electronic states (McIlroy 1986, Brennan and Summers 1987, Atkinson *et al* 1990).

Another technique is based on approximating the sloping potential arising from the applied field in a 'piecewise-constant' manner (Miller *et al* 1985, Harwit *et al* 1988, Stevens *et al* 1988, Ghatak *et al* 1988). Calculating the particle transmission through the structure as a function of energy, the quasi-bound states of the structure can be found from the local maxima. This so called 'tunnelling resonance method' or TRM, is computationally simple to implement with the solutions in each piecewise layer comprising forward and backward propagating plane waves. Its suitability for multiple layer structures was demonstrated by Ghatak *et al* 1988, with calculations of energy states in a coupled quantum well system under an applied field. In addition, by its piecewise nature, any arbitrary potential profile can be handled, a feature typified by the work of Ghisoni *et al* 1993 in which a four well diffused structure (eight layers) is investigated using a TRM method.

In keeping with a piecewise potential, a recent method that has a strong analogy with optical waveguide theory is due to Anemogiannis *et al* (1993). The boundary conditions outside the structure are similar to those used for leaky waves in waveguide theory (see for eg. Tamir and Kou 1986). This allows a complex transcendental equation to be formulated whose complex roots refer to the energy solution and lifetime of the state. The versatility of the method (referred to as APM by the authors) is at the same level as the TRM method (ie. multilayers, arbitrary profile).

Finally, some other techniques which should be noted are Monte-Carlo methods (see eg. Singh 1986), Finite Element Methods (Nakamura *et al* 1989) and a perturbation expansion involving the zero field bound states (Lengyel *et al* 1990)

Numerical comparisons between several methods have been reported in the literature (see for eg. Bastard *et al* 1983, Miller *et al* 1985, Brennan and Summers 1987, Jonsson and Eng 1990, Anemogiannis *et al* 1993). An interesting result due to Miller and co-workers is the good agreement found between a finite well TRM approach, and both the infinite well Airy function and variational methods *providing* the infinite well models use 'effective well widths'. This effective well width is chosen such that an infinite QW model reproduces the zero field energy states found in a finite QW model (Miller *et al* 1985). Other comparisons involving an Airy function method (finite QW), a Finite Element Method and a piecewise potential method indicated no significant differences in the calculated energy states of the multilayer structures investigated. In fact, it was emphasised that accounting for any differences in the effective masses between the layers, produces much more variation in energy levels than the particular chosen algorithm (Jonsson and Eng 1990).

It should be remembered, that calculations of subbands in electric fields were to be part of an overall model that would describe the electro-absorption properties of QW structures. Previous work at U.C.L had successfully employed either the TRM (Stevens *et al* 1988) or the finite well Airy function approach (Atkinson *et al* 1990) for investigating these effects in various GaAs/$Al_xGa_{1-x}As$ structures. Consulting the literature at the time there appeared no other reason not to consider either one of these two approaches as both of them could realistically describe the range structures in this thesis.

Initially, I had hoped to extend the range of these 'available' models to account for InP based strain layer structures. In both of these works (and with all those mentioned above) a one band model is used to describe each layer (Stevens *et al* 1988, Atkinson *et al* 1990). Using the expressions from the previous chapter (§3.5.1), values of well depths (knowing an offset) and band edge effective masses could be calculated for a (un)strained system and used in place of the 'host' GaAs/$Al_xGa_{1-x}As$ values. Furthermore, non-parabolicity (for electrons and light holes) could also be included since both of the existing models had provisions for this. A modified version of Dr. Stevens model was completed and appeared to give sensible results. Comparisons at zero field with the three band description in (§4.2.2) for single QWs gave energy levels typically within 1-2 meV of each other. It is fair to suggest similar results could have been expected with the Airy function method since the two methods had compared favorably for the GaAs/$Al_xGa_{1-x}As$ system (D.Atkinson, private communication). Moreover, this model allows for up to ten layers to be examined and would be useful if strained layer coupled structures were to be investigated.

It was the advent of the composite well structures (chapter 6) that prompted the development of a TRM model using a three band description throughout. Although, that is not to say the available models could not adequately describe these structures. However, in addition to some minor practical reasons behind the decision, the prospect of further investigating these and other structures with a unified approach was appealing. In the rest of this section the TRM approach is described in greater detail and specifically for the case when a three band **k.p** model is used to describe the layers.

§4.3.2 The tunnelling resonance method.

To account for the presence of an applied electric field along the z direction, an extra term eFz is added to the diagonal terms of $\mathbf{H}^{l}_{total}$ (4.2), where F represents the applied field and e is the charge of an electron. As before, the problem can be recast into the form,

$$\left[-\frac{d}{dz}B^{l}_{n}(E,F,z)\frac{d}{dz}A^{l}_{n}(E,F,z)+V^{l}_{n}(F,z)\right]f_{n}(z)=Ef_{n}(z) \qquad (4.39)$$

Modified coefficients for the electron, heavy- and light-hole envelopes are given in Table 4-2. Note the explicit z dependence of the coefficients which arises because of the applied field. In addition to this it is useful keep the layer dependence label (l) which is also z dependent but on a much larger scale.

Table 4-2. *Coefficients which appear in the electric field dependent differential equations for the envelope functions (equation 4.39)*

	conduction band (*n=el*)
$B_n^l(E,F,z)$:	$\frac{P_{K,n}^2}{3}\left(\frac{3E + 3\delta E_{vhh}^l - 3eFz + 2\delta E_s^l - 2E_{so}^l - E_{lh}^l}{(E + \delta E_{vhh}^l - eFz - E_{lhkz}^l)\,(E + \delta E_{vhh}^l - eFz - E_{sokz}^l)}\right)$
$A_n^l(E,F,z)$:	1
$V_n^l(F,z)$:	$\left(E_{gs}^l - \delta E_{vhh}^l + eFz\right)$
	heavy hole band (*n=hh*)
$B_n^l(E,F,z)$:	$-\frac{\hbar^2}{2m_{hh}^l}$
$A_n^l(E,F,z)$:	1
$V_n^l(F,z)$:	$-\delta E_{vhh}^l$
	light hole band (*n=lh*)
$B_n^l(E,F,z)$:	$\frac{P_{K,n}^2}{3}\left(\frac{(E + \delta E_{vhh}^l - eFz - E_{so}^l) + \delta E_s^l/2}{(E + \delta E_{vhh}^l - eFz - E_{gs}^l)(E + \delta E_{vhh}^l - eFz - E_{sokz}^l)}\right)$
$A_n^l(E,F,z)$:	$\left(\frac{3E + 3\delta E_{vhh}^l - 3eFz + 2\delta E_s^l - 2E_{so}^l - E_{lh}^l}{(E + \delta E_{vhh}^l - eFz - E_{so}^l) + \delta E_s^l/2}\right)$
$V_n^l(F,z)$:	$\left(E_{lhkz}^l - \delta E_{vhh}^l + eFz\right)$

The effect of an applied electric field on a composite well structure is shown schematically below.

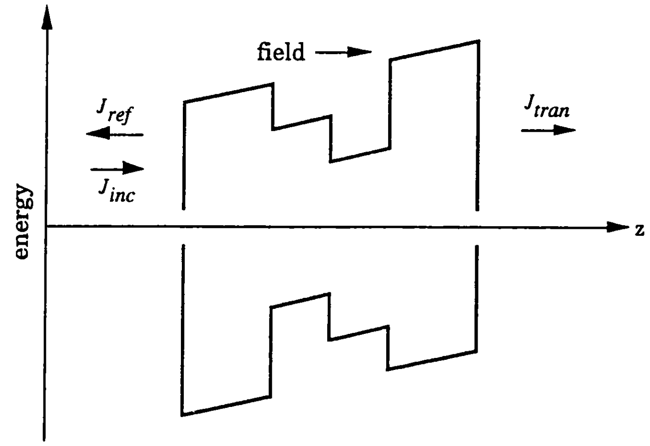

Figure 4-5. *Schematic of the potential profile of a composite well structure with an electric field applied perpendicularly to the layers. Only the conduction and heavy hole bands are illustrated.*

In the above picture, there exist regions outside the well that have a lower potential energy than inside. A particle inside the well region will have a finite probability of tunnelling through the barrier to these regions and consequently its lifetime in the well is finite. Hence no true bound states can exist (equation (4.32) cannot be satisfied). However, if the particle has a long lifetime it can be regarded as quasi-bound. The aim of the TRM is to find the energy states with a long lifetime, ie. the quasi-bound states.

Before the TRM is presented, its worth noting that with the above picture, (Fig.4-5), quasi-bound states are found at zero applied field due to the use of finite barrier widths. Herein lies a qualitative difference between this method and that of the previous section which employed infinite barrier widths to support bound states; although for an applied electric field, a picture employing infinite barrier widths would still not have true bounds states for the same reasons given above (Ghatak *et al* 1988). [note: numerically they both predict the same energy levels at zero applied field].

Considering Fig.4-5, a particle at a given energy incident on the barrier from the left has a finite probability of tunnelling through the structure and reaching the right hand side. Expressed in terms of probability current densities, J, a transmission coefficient for the structure, T, can be defined as the ratio of the transmitted and incident probability current density, J_t/J_i (see for eg. Messiah 1970, chp. 3). The quasi-bound states are determined by calculating T as a function of energy and finding the local maxima in T(E). The corresponding lifetime can be determined from ΔE (the half width half maximum of the peaks in $T(E)$) using the Heisenberg uncertainty relation $\tau \approx \hbar/\Delta E$ (Miller *et al* 1985)

Numerical procedure

The numerical procedure consists of describing the structure in a piecewise manner, hence the potential energy profile is divided into N sub-layers (Fig.4-6). For a given energy and electric field, the *i*th sub-layer has constant values of $B_n^{l,i}$, $A_n^{l,i}$ and $V_n^{l,i}$ in the interval $z_i \rightarrow z_{i+1}$.

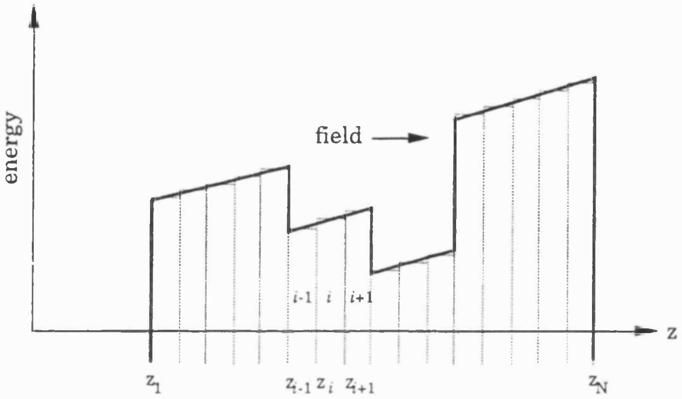

Figure 4-6. *Schematic of the conduction band potential profile for a composite well structure with an electric field applied perpendicularly to the layers. The overall potential is approximated in a piecewise manner.*

In an effective mass description (ie. the EFA), the tunnelling probability can be expressed solely in terms of the envelope functions rather than using the full wave functions (Ben Daniel and Duke 1966). For each sub-layer the envelope function is written as the sum of forward and backward travelling waves:

$$f_n^i(z) = \alpha_i \exp[i k_i z] + \beta_i \exp[-i k_i z] \qquad (4.40)$$

where α_i and β_i are constant coefficients in each sub-layer and the wave vector for the layer is given by:

$$k_i^2 = \frac{\left(E - V_n^{l,i}(F)\right)}{B_n^{l,i}(E,F)\,A_n^{l,i}(E,F)} \qquad (4.41)$$

As discussed earlier (§4.2), for propagating states, $k_i^2 > 0$ and the envelope function takes the form of (4.40). However for $k_i^2 < 0$, corresponding to evanescent states, the wave vector becomes imaginary, $k_i \rightarrow i\kappa_i$ and the counterpart of (4.40) is written as:

$$f_n^i(z) = \alpha_i \exp[-\kappa_i z] + \beta_i \exp[\kappa_i z] \tag{4.42}$$

Outside the structure $(z > z_N)$, $k_i^2 > 0$ and there can be no backward travelling wave, in which case:

$$f_n^N(z) = \alpha_N \exp[ik_N z] \tag{4.43}$$

The current density must be conserved throughout the potential structure. Conditions at each sub-layer interface take the same form as those presented earlier (4.5) and (4.6). For the present case, the following two conditions must be satisfied at a given interface (say $z = z_{i+1}$):

$$A_n^{l,i}(E,F) f_n^i(z_{i+1}) = A_n^{l,i+1}(E,F) f_n^{i+1}(z_{i+1}) \tag{4.44a}$$

$$B_n^{l,i}(E,F)\frac{d}{dz}A_n^{l,i}(E,F)f_n^i(z)\Big|_{z=z_{i+1}} = B_n^{l,i+1}(E,F)\frac{d}{dz}A_n^{l,i+1}(E,F)f_n^{i+1}(z)\Big|_{z=z_{i+1}} \tag{4.44b}$$

As with the earlier sections of this chapter, use is made of a transfer matrix technique to propagate these conditions throughout the structure. To illustrate this, consider a section comprised of three sub-layers, $i-1$, i and $i+1$. The aim is to find a transfer matrix which conserves the probability current density between the sub-layers $i-1$ and $i+1$ across layer i. At the first interface, $(z = z_i)$, we can write

$$\begin{pmatrix} A_n^{l,i-1}(E,F) f_n^{i-1}(z) \\ B_n^{l,i-1}(E,F)\frac{d}{dz}A_n^{l,i-1}(E,F)f_n^{i-1}(z) \end{pmatrix}_{\text{at } z=z_i} = T_i(E,F,z_i)\begin{pmatrix} \alpha_i \\ \beta_i \end{pmatrix} \tag{4.45}$$

For the RHS of (4.45), $T_i(z_i)$ is a (2x2) matrix containing terms associated with the coefficients α_i and β_i. The terms can be found from direct application of the continuity conditions at $z = z_i$ on the envelope function in layer i.

Similarly for the second interface at $z = z_{i+1}$,

$$T_i(E,F,z_{i+1})\begin{pmatrix} \alpha_i \\ \beta_i \end{pmatrix} = \begin{pmatrix} A_n^{l,i+1}(E,F) f_n^{i+1}(z) \\ B_n^{l,i+1}(E,F)\frac{d}{dz}A_n^{l,i+1}(E,F)f_n^{i+1}(z) \end{pmatrix}_{\text{at } z=z_{i+1}} \tag{4.46}$$

Making use of (4.45) and (4.46), the relationship between the sub-layers $i-1$ and $i+1$ can be expressed as:

$$T_i(E,F,\Delta z_i)\begin{pmatrix} A_n^{l,i-1}(E,F)f_n^{i-1}(z) \\ B_n^{l,i-1}(E,F)\frac{d}{dz}A_n^{l,i-1}(E,F)f_n^{i-1}(z) \end{pmatrix}_{\text{at } z=z_i} = \begin{pmatrix} A_n^{l,i+1}(E,F)f_n^{i+1}(z) \\ B_n^{l,i+1}(E,F)\frac{d}{dz}A_n^{l,i+1}(E,F)f_n^{i+1}(z) \end{pmatrix}_{\text{at } z=z_{i+1}} \tag{4.47}$$

where

$$T_i(E,F,\Delta z_i) = T_i(E,F,z_{i+1})T_i^{-1}(E,F,z_i)$$

For propagating states in sub-layer i, such that the envelope function is given by (4.40) and $k_i^2 > 0$ in (4.41), the transfer matrix is:

$$T_i(E,F,\Delta z_i) = \begin{pmatrix} \cos(k_i\Delta z_i) & \frac{\sin(k_i\Delta z_i)}{B_n^{l,i}(E,F)k_i} \\ -B_n^{l,i}(E,F)k_i\sin(k_i\Delta z_i) & \cos(k_i\Delta z_i) \end{pmatrix} \tag{4.48}$$

While for the case of evanescent states with imaginary solutions $k_i \rightarrow i\kappa_i$ in (4.40), the transfer matrix is given as:

$$T_i(E,F,\Delta z_i) = \begin{pmatrix} \cosh(\kappa_i\Delta z_i) & \frac{\sinh(\kappa_i\Delta z_i)}{B_n^{l,i}(E,F)\kappa_i} \\ B_n^{l,i}(E,F)\kappa_i\sinh(\kappa_i\Delta z_i) & \cosh(\kappa_i\Delta z_i) \end{pmatrix} \tag{4.49}$$

For either of the above transfer matrices, Δz_i represents the width of the ith sub-layer.

Working with equation (4.47) the envelope function can be evaluated throughout the structure. The tunnelling transmission coefficient as a function of energy can be written as:

$$T(E,F) = \frac{\left(f_n^*(z)B_n^N(E,F)\frac{d}{dz}A_n^N(E,F)f_n(z) - f_n(z)B_n^N(E,F)\frac{d}{dz}A_n^N(E,F)f_n^*(z) \right)\Big|_{z=z_N}}{\left(f_n^*(z)B_n^0(E,F)\frac{d}{dz}A_n^0(E,F)f_n(z) - f_n(z)B_n^0(E,F)\frac{d}{dz}A_n^0(E,F)f_n^*(z) \right)\Big|_{z=z_1}}$$

If the outer regions (N and 0) for the problem are considered to be the same then $T(\mathrm{E},\mathrm{F})$ reduces to:

$$T(\mathrm{E},\mathrm{F}) = \frac{\left(f_n^*(z)\,\dfrac{\mathrm{d}f_n(z)}{\mathrm{d}z} - f_n(z)\,\dfrac{\mathrm{d}f_n^*(z)}{\mathrm{d}z} \right)\Bigg|_{z=z_N}}{\left(f_n^*(z)\,\dfrac{\mathrm{d}f_n(z)}{\mathrm{d}z} - f_n(z)\,\dfrac{\mathrm{d}f_n^*(z)}{\mathrm{d}z} \right)\Bigg|_{z=z_1}} \tag{4.50}$$

§4.3.3 Comments on all subband calculations.

Software testing was carried out throughout the development of the various subband programs. The programs were comprised of units, which individually could be tested with known inputs, and thus helped in the debugging and testing of the routines. Moreover, some units were common to both zero and applied field calculations and thus could be used in a such a manner, eg. the layout of structure, material files. Initially, routines were developed for the particle-in-a-box type calculations. The calculated subbands, including electric field effects, could be easily checked with existing models (eg. Stevens *et al* 1988).

Useful investigations into several **k.p** type model are available in the literature (eg. Yoo *et al* 1989, P. von Allmen 1992), although mainly for GaAs/AlGaAs based QW's. Yoo and co-workers considered zero applied field QW structures, and included in their study a Kane type model (which they referred to as a 'three band Bastard' model). Using the same material parameters, excellent agreement was found when comparing the values of confined state energies from the present model; this is expected since the models are essentially the same. In comparison with their *full* 8 band model, the Kane model routinely underestimated the e1 and lh1 states by <2 meV across a range of well widths 5Å to 200Å. Interestingly, the comparison by von Allmen, using a *full* 14 band and various other models, including a *full* 8 band, showed the 8 band model overestimated the e1 subband by ~1 meV. Using his input values, I found the Kane model underestimated the e1 state by 0.7 meV (in comparison with the 14 band model). To my knowledge, similar comparisons have not been carried out for strained systems. However, several authors have listed calculated values of subbands from various models (eg. Jogai and Yu 1990, list InGaAs/GaAs calculated transitions using *full* **k.p** model). Using the same input parameters, I found the transitions predicted were typically within 2 meV of Jogai and Yu's results.

Example calculations in figure 4-7 show the lowest energy subbands for an $In_{0.53}Ga_{0.47}As/InP$ (lattice matched) QW. At zero applied field, the well width dependence on the e1-hh1 subband separation (ie. the 'bandgap' of the structure) is shown (Fig.4-7a,c). For a well width of 70Å, the effects of an applied electric field on the e1-hh1 separation is shown in the adjacent graphs (Fig.4-7b,d). The decrease of e1-hh1 separation with field is the dominant contribution to the overall decrease of the exciton transition energy.

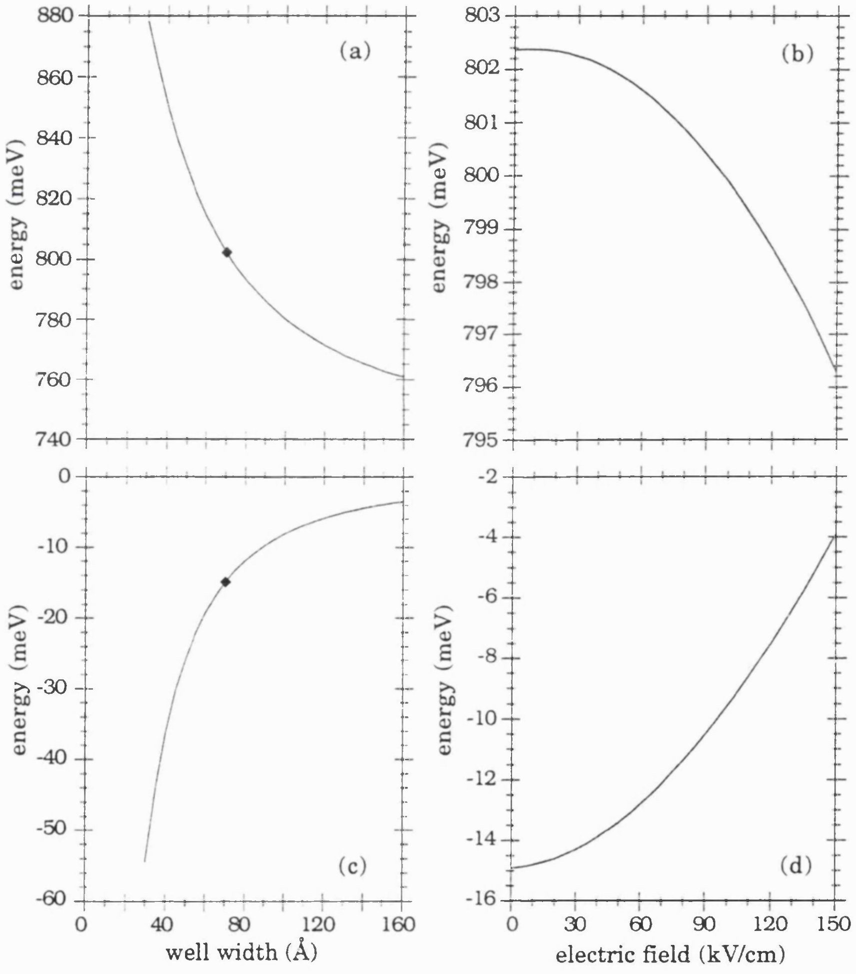

Figure 4-7. *Calculations for $In_{0.53}Ga_{0.47}As/InP$ quantum wells. (a) and (c) show zero field subbands e1 and hh1 respectively as a function of well width. (b) and (d) show the effects of an applied electric field on the e1 and hh1 subbands in a 70Å $In_{0.53}Ga_{0.47}As$ well (marked in (a) and (c)). The zero of energy in all cases is taken to be the heavy hole band edge of the bulk $In_{0.53}Ga_{0.47}As$.*

§4.4 Optical Properties near the Band edge.

A principle feature of low dimensional structures, such as quantum wells (QW), is the clear observation of excitonic transitions even at room temperature (cf. Fig.1-3). Determining the transition energies and their strengths represents the last installment to the model detailed in this thesis. These calculations are based on a variational approach (§4.4.2) which calculates the binding energies associated with the excitonic transitions. The envelope function that describes the exciton is then used in calculations of the absorption spectra near the band edge (§4.4.3).

While an accomplished account of excitons in these structures is beyond the scope of the present work, it is useful to summarise some of the key points and assumptions relating to the method of calculation. This is combined with a summary of previous work appearing in the literature.

§4.4.1 The exciton problem.

The theory of excitons in bulk semiconductors (i.e. 3D) is extremely well documented (Elliott 1957, Knox 1963, Dimmock 1967). The case of semiconductors where motion is in two dimensions only (2D) has also been studied (Shinada and Sugano 1966). For both environments the electron-hole (e-h) interaction produces peaks in the absorption spectrum at energies of the exciton states. The usual interpretation is that the absorption is enhanced by the e-h interaction in proportion to the increased probability of creating an electron and a hole at the same position (Shinada and Sugano 1966). Our interest lies in the dominant, lowest energy peak which can be determined by solving a hydrogenic type Schrödinger equation corresponding to the 1s exciton state. The absorption coefficient at the energy of the 1s state (E_{1s}) is proportional to $|\phi_{1s}(\mathbf{r} = 0)|^2$ where $\phi_{1s}(\mathbf{r})$ is the e-h envelope function for the exciton (Shinada and Sugano 1966). As with most two-body problems, a transformation to center of mass and relative coordinates, ($\mathbf{r}$), is often employed which greatly simplifies the problem (see e.g. Schiff 1968 p108).

The main difference between the two environments are for 2D, where $E_{1s} = E_g - 4|R|$ whereas for 3D, $E_{1s} = E_g - |R|$. The energy term $|R|$ is the bulk (3D) Rydberg commonly referred to as the bulk binding energy of the e-h pair. It is noted that in the ideal 2D case the binding energy of the e-h pair is 4 times larger than in 3D structures due to the confinement, and consequently the excitonic enhancement is greater. Other differences relating to higher exciton states and the coupling to the continuum (ie. energies $>E_g$) have been noted by Shinada and Sugano (1966).

Concerning excitons in actual quantum wells, it is well known that, for lower energy states, the system is somewhere between a 2D and 3D case (Schmitt-Rink *et al* 1989). The enhanced binding energy of the lowest exciton state, ie. n=1hh, for GaAs/AlGaAs QW was first observed by Dingle *et al* (1974). The exciton binding energy for a well width, L_W, of ~200Å was estimated to be ≈7 meV, which is approximately twice that found in bulk GaAs (≈4 meV). Further evidence came from the work by Miller and co-workers (1981) who used photoluminescence excitation to study a range of GaAs/AlGaAs samples with well widths $42Å \leq L_W \leq 145Å$. Comparing the experimental splitting of the 1s state with the onset of the continuum (interpreted as the 2s state), they deduced 1s exciton binding energies in the range 8-12 meV for both heavy and light hole transitions. The binding energies increased with decreasing well width, and were found to be larger for the light hole exciton.

At the 2D and 3D limits, the exciton problem can be solved analytically (Shinada and Sugano 1966). However, in the case of actual structures with finite well widths, the problem is complicated mainly by the Coulomb term governing the e-h interaction (Schmitt-Rink *et al.* 1989). Several approximations can be made to ease the calculations, for example in the 'strong confinement approximation', where the confinement energies of the electron and hole states are large compared to the Coloumb energy, the total wavefunction can be separated into the two directions of the system. In this regime, the motion of the particles along the *growth* direction is governed by the confinement while the Coulomb interaction mainly affects the motion *in the plane* of the layers (Schmitt-Rink *et al.* 1989). A further consequence is that a transformation to center of mass and relative coordinates can still be made in the plane of the layers, since the crystal is assumed to be infinite in this direction. Thus an envelope function can be used to describe the relative motion of the exciton in the plane of the layer. Most of the theoretical calculations for exciton binding energies in quantum wells use a variational method, which relies on a good choice of trial wavefunction to minimise the excitonic transition energy (eg. Miller *et al.* 1981, Bastard *et al.* 1982, Shinozuka and Matsuura 1983, Greene and Bajaj 1983, Greene *et al.* 1984, Miller *et al.* 1985). The trial wave function is written as:

$$\Phi_{ex} = f_{el}(z_e) f_h(z_h) \phi(\rho, \mathbf{z}) \tag{4.51}$$

where $f_{el}(z_e)$ and $f_h(z_h)$ are the electron and hole wave functions in the confinement direction, $\phi(\rho, \mathbf{z})$is an envelope function for the exciton which is assumed to depend only on the relative electron-hole coordinates in the cylindrical coordinate system (eg. $\rho^2 = (x_e - x_h)^2 + (y_e - y_h)^2$). This function can be based on the 1s envelope functions used in either the 2D or 3D limit which have the form:

$$\text{2D:} \quad \phi_{1s}(\rho) \approx \exp[-\alpha\rho] \tag{4.52}$$

$$\text{3D:} \quad \phi_{1s}(\rho, z) \approx \exp\left[-\alpha\sqrt{\rho^2 + z^2}\right] \tag{4.53}$$

In both cases α is the single variational parameter. Using the 2D function, the trial wave function (4.51) is seen to be separable in z and ρ. Calculations comparing the two functions and assuming an infinite well depth have been done by Bastard *et al* (1982). For well widths, $L_W<(1.4a_b)$ where a_b is the bulk Bohr radius (approx. 150Å for GaAs), both functions give almost identical binding energies for the exciton. For well widths $L_W>(1.4a_b)$ the separable wave function was found to give binding energies *less* than the bulk value, and for very large L_w the calculated binding energy tended to zero. This unphysical result clearly indicated the breakdown of the strong confinement approximation, with the confinement energies (varying as L_W^{-2}) becoming comparable to the Coulomb energy in the z direction (Schmitt-Rink *et al* 1989). In contrast, the non-separable wave function, (4.53), resulted in a smooth variation in binding energy from 4R to R as L_W went from 0 to ∞.

Further calculations employing finite well depths provided a more realistic physical picture of actual QW structures (Greene and Bajaj 1983, Priester *et al.* 1984, Grundman and Bimberg 1988). It was found that the penetration of the electron and hole wave functions into the barrier material increases as $L_W \rightarrow 0$, so for very thin well widths the exciton should tend towards the 3D exciton of the barrier material. Correspondingly, the binding energy would then reduce and tend towards the bulk value of the barrier. Although a significant enhancement of the binding energy was still expected for an intermediate range of well widths. This effect of barrier penetration has been experimentally observed in InGaAs/GaAs strained QW structures. Moore *et al* (1990) measured a decrease in the heavy hole binding energy as the well width was reduced below ~50Å in agreement with their calculations.

The form of the trial wave function has also adopted a more elaborate approach. Some authors have suggested using trial wave functions with *two* variational parameters (Shinozuka and Matsuura 1983, Greene and Bajaj 1983, Grundman and Bimberg 1988). In the wave function proposed by Gruudman and Bimberg, the additional parameter was defined as a measure of exciton dimensionality. This could continuously interpolate between the 3D limits for zero and infinite well width, and the 2D limits for infinite barriers. In a similar notation as (4.52) and (4.53), the exciton envelope can be written as:

$$\phi_{1s}(\rho, z) \approx \exp\left[-\alpha\sqrt{\rho^2 + \lambda^2 z^2}\right] \tag{4.54}$$

where now α and λ are varying parameters, the latter being the measure of dimensionality. Calculations were performed for both the GaAs/$Al_{0.4}Ga_{0.6}As$ and lattice matched InGaAs/InP systems, with finite well depths. For $L_W \rightarrow 0$ and $L_W \rightarrow \infty$, λ approached unity implying 3D excitons. In the range 10Å<L_W<~200Å, the variational parameter, λ, was close to zero demonstrating a quasi- 2D nature for the lowest energy exciton.

The effect of an applied electric field on excitonic properties in a QW was initially investigated by Miller *et al.* (1984, 1985) and Brum and Bastard (1985). Both works employed a separable trial wavefunction (essentially (4.51) and (4.52), and accounted for finite well depths. Despite the differences in their methods for the subband calculations, they arrived at similar conclusions for fields applied perpendicularly to the layers. The free particle electron and hole states are polarized by the field to opposite ends of the well. The Coulomb interaction between the pair reduces resulting in a reduction in the binding energy. Near the band edge of a structure, the enhanced absorption of the n=1hh excitonic transition decreases and the excitonic transition energy reduces ie. red shifts to longer wavelengths, (cf. the §1.2 and the QCSE). In fact, most of the energy shift of the n=1hh transition is due to the e1 and hh1 subbands shifting with field (cf. Fig.4-7b,d). These theoretical results were able to explain the experimental observations made by Miller and co-workers (1984, 1985).

All of the above studies were based on single band descriptions of the electron and hole making up the exciton. The effect of coupling between subband states (in particular the valence band mixing of the hole states) on exciton calculations has since been investigated (Sanders and Chang 1985, Ekenberg and Alterelli 1987, Sanders and Bajaj 1987, Zhu and Huang 1987, Bauer and Ando 1988, Hiroshima 1988, Andreani and Pasquarello 1990). The differences between these works is typically related to the method of calculation and, in some cases, consideration of external perturbations, ie. magnetic field, electric field, pressure. (The work of Bauer and Ando (1988) considers these differences in more detail.) However, the general agreement is that valence band mixing slightly increases the binding energy of ground state excitons (n=1hh and n=1lh) but has considerably more affect on the binding energies involving higher subbands (see e.g. Ekenberg and Alterelli 1987). Additional coupling between bound and continuum excitons through the Coulomb potential was considered by Zhu and Huang (1987) and Andreani and Pasquarello (1990).

The purpose of this section was to highlight some of the assumptions often employed in exciton calculations, and attempt to summarise the development of exciton calculations from the ideal infinite well depth models (e.g. Miller 1981) to the realistic 'state of the art' calculations proposed by Andreani and Pasquarello (1990). All the theories of excitons in quantum well structures can be divided (rather crudely) according to whether they neglect coupling or include it. Numerical comparisons show that when coupling is included the calculated binding energies are larger by 1-$1^{1}/_{2}$ meV for n=1hh excitons and 1-3 meV for n=1lh excitons compared to the uncoupled models[1]. Given the overall aim of the present work, I felt these differences would be acceptable and decided against explicitly including any coupling. Furthermore, the computing requirements for single band (uncoupled) calculations are relatively straightforward and could be easily extended to account for a variety of structures (for e.g. those considered in Chapter 6).

The level of calculation in the following section, in some respects, is equivalent to the work of Preister *et al.* (1984) and Miller *et al.* (1984, 1985). However, before presenting the methods used for the optical calculations, it is useful to clarify some approximations that will be used.

Normalization of envelope functions.

The envelope functions obtained from either §4.2.2 or §4.3, are used throughout optical calculations, for example, to evaluate the overlap integral for an optical transition (see e.g. Bastard 1988, chp.7). To correctly normalise them requires,

$$f_n = \frac{f_n'}{\sqrt{\mathrm{N}_n}} \ , \text{ where } \ \mathrm{N}_{el,lh} = \int_{-\infty}^{\infty} \left(1 + \mathrm{X}^2 + \mathrm{Y}^2\right) \left| f_n' \right|^2 \mathrm{dz} \qquad (4.55a)$$

$$\mathrm{N}_{hh} = \int_{-\infty}^{\infty} \left| f_n' \right|^2 \mathrm{dz} \qquad (4.55b)$$

where f_n' is the unnormalized envelope function. For the electron or light hole, the additional terms, X and Y, are due to the mixing from the other two bands. For example, in the case of the first conduction band state, e1, then X and Y indicate the admixture of the light hole and spin orbit split-off band (which are written in terms of the conduction band envelope). Explicit expressions can be obtained directly from the equations (4.3), or

---

[1] It should be noted that most calculations appearing in the literature are for the GaAs/$\mathrm{Al_xGa_{1-x}As}$ system. It is assumed that differences in other material systems would be of a similar magnitude.

more generally, the method used by Kane (1957) which deals in terms of admixture between S and P states. The work by Kane (1957) demonstrated that, even in the case of a narrow gap material (InSb), for electron states close to the band edge the degree of mixing is very small. Furthermore, I investigated the contribution of these terms to the e1 state for $InAs_xP_{1-x}$ QW structures (x<30% and well widths 50Å-200Å), and found no significant change to the normalized envelope function using either (4.55a) or the one band model, (4.55b). Similar conclusions have recently been made by Sirtori and co-workers (1994). For the rest of the work, the envelope functions obtained from either §4.2.2 or §4.3 are normalized according to (4.55b).

In-plane dispersions

To describe the in-plane dispersion of the states in the quantum well (ie. $k_{||} \neq 0$), a simple parabolic description is used. This is often referred to as the 'diagonal approximation' (Bastard and Brum 1986), since it ignores any off-diagonal components that arise in a multi-band **k.p** approach (see for eg. Eppenga *et al* 1987). In the diagonal approximation, a mass reversal of the bands occurs, ie. the heavy hole bands perpendicular to the layers become light in the plane and similarly, the light hole band becomes heavy, (cf. §2.3.2). When mixing is included, the situation becomes complicated and the bands in the plane cannot be described as either heavy or light but must be treated as a combination of both (Bastard and Brum 1986). In the case of the lowest heavy hole state, hh1, the general effect of mixing is an increase in its effective mass from that given by the diagonal approximation (Bastard 1988, chp.3). It is difficult to quantify this without performing the necessary calculations, although some approximate methods exist in the literature (see for eg. Ridley 1990). Furthermore, the effects of mixing are very much system dependent (ie. well width, strain etc.) since the strength of mixing depends mainly on the relative positions of the energy states at $k_{||} = 0$. Considering the effect on hh1, a significant contribution comes from the first light hole state, lh1. In compressively strained systems, the separation between hh1 and lh1 increases due to lifting of the degenerate band edges in the bulk layer. Therefore the effect of lh1 on the hh1 band in the plane is reduced (see eg. O'Reilly 1989), and the diagonal approximation becomes more reasonable. It is worth noting that the opposite is expected to happen if the well layer is under tensile strain (Andreani *et al* 1987).

The energy wave vector in-plane dispersion for a subband in the diagonal approximation is written as:

$$E_n(k_{||}) = E_n(k_{||}^0) + \frac{\hbar^2 k_{||}}{2m_{||,n}^*} \tag{4.56}$$

where $E_n(k_{||}^0)$ is the energy solution of either (4.4) or (4.39) for the nth band at $k_{||} = 0$. For the valence band in the diagonal approximation, the in-plane effective masses can be related to the band edge masses perpendicular to the layers (Stevens *et al* 1988):

$$m_{||,hh}^* = \frac{4m_{hh}^* m_{lh}^*}{m_{lh}^* + 3m_{hh}^*} \quad \text{and} \quad m_{||,lh}^* = \frac{4m_{hh}^* m_{lh}^*}{3m_{lh}^* + m_{hh}^*} \tag{4.57}$$

where m_{hh}^* and m_{lh}^* are given by (3.52) and (3.75) respectively. In the conduction band, I take $m_{||,el}^* = m_{el}^*$, with m_{el}^* given by (3.75). The reduced mass of an exciton is given by

$$\frac{1}{\mu} = \frac{m_{||,el}^* m_{||,m}^*}{m_{||,el}^* + m_{||,m}^*} \tag{4.58}$$

where m denotes either heavy hole or light hole in-plane mass. For the the actual calculations, the effects of different masses in the layers is taken into account by calculating an 'effective' value for the reduced mass. Equation (4.58) is averaged over a two dimensional configuration space (z_e, z_h) weighted by the envelope functions.

§4.4.2 Calculating excitonic transitions.

The excitonic transition energy in a quantum well structure (with or without an applied electric field) is written:

$$E_{ex} = E_{el}(k_{||}^0) - E_h(k_{||}^0) + E_B \tag{4.59}$$

Here, $E_{el}(k_{||}^0)$ and $E_h(k_{||}^0)$ are the confined electron and hole states (for $k_{||} = 0$) states calculated from (4.4) (or (4.39) for an applied electric field) with respective envelope functions, $f_{el}(z_e)$ and $f_h(z_h)$. [note: $E_{el}(k_{||}^0) - E_h(k_{||}^0)$ is the energy separation of the states ie. for the ground states (e1 and hh1) this is essentially the band edge of the heterostructure]. The binding energy of the pair is represented by E_B, which takes a negative value in (4.59). Hence the excitonic transition energy occurs at a lower energy than the separation $E_{el}(k_{||}^0) - E_h(k_{||}^0)$. In writing (4.59), the 'strong confinement approximation' is invoked (Schmitt-Rink *et al.* 1989), ie. the Coulomb interaction does not effect the confined states. This approximation is valid providing the confinement energy in the conduction and valence bands is larger than $|E_B|$ which is the case for the n=1hh transition in the structures considered here. In systems where this is not the case (eg. in extremely shallow wells or some of the II-VI systems) the effect of the Coulomb potential can significantly alter the bound states of the system (Wu and Nurmikko 1988).

A variational method (see for eg. Schiff 1968) is used to find the maximum (negative) value of E_B, ie.

$$E_B = \underset{\alpha}{max}...\langle H_{e\text{-}h}\rangle = \iiint_{R_{z\rho\phi}} \Phi^*_{ex}(z_e, z_h, \rho) H_{e\text{-}h} \Phi_{ex}(z_e, z_h, \rho) \qquad (4.60)$$

where α is the variational parameter in the excitonic wave function $\Phi_{ex}(z_e, z_h, \rho)$. $H_{e\text{-}h}$ describes the electron-hole interaction in the plane of the layers which in cylindrical coordinates (Priester *et al* 1984) is written as,

$$H_{e\text{-}h} = -\frac{\hbar^2}{2\mu_{||}}\left(\frac{1}{\rho}\frac{\partial}{\partial\rho}\rho\frac{\partial}{\partial\rho} + \frac{1}{\rho^2}\frac{\partial^2}{\partial\varphi^2}\right) + \frac{-e^2}{4\pi\varepsilon\sqrt{(\rho^2 + z^2)}} \qquad (4.61)$$

The first term is the kinetic energy operator of the relative motion of the electron-hole system, travelling in the plane of the well with a reduced mass, $\mu_{||}$. The second term represents the Coulomb potential energy between the electron and hole, ε is the static dielectric constant and e is the charge of an electron. The excitonic binding energy is found by allowing $H_{e\text{-}h}$ to operate on the separable wave function,

$$\Phi_{ex}(z_e, z_h, \rho) = f_{el}(z_e) f_h(z_h) \phi(\rho) \qquad (4.62)$$

where $f_{el}(z_e)$ and $f_h(z_h)$ are the *normalized* electron and hole envelope functions. A simple *normalized* 2D form is used to describe the in-plane relative motion (Miller *et al* 1985), written as

$$\phi(\rho) = \alpha\sqrt{\frac{2}{\pi}}\exp[-\alpha\rho] \qquad (4.63)$$

with α as a variational parameter in units of m^{-1}. The variational term is often related to the radius of the exciton in the plane of the layers, , (ie. $1/\alpha$ cf. Miller *et al* 1985). It is worth remembering that with the variational approach (see for eg. Schiff 1968 p255), the result for E_B will always be less than or equal to the eigenvalue of H_{e-h}. Hence the excitonic transition energy obtained from (4.59) will always be overestimated.

Equation (4.60) can be expanded further and presented as maximizing negative values of the variational function, $E_B(\alpha)$, :

$$E_B(\alpha) = E_{KE}(\alpha) + E_{PE}(\alpha) \tag{4.64}$$

where,

$$E_{KE}(\alpha) = \frac{\hbar^2\alpha^2}{2\mu^*} \tag{4.65}$$

$$E_{PE}(\alpha) = -\frac{e^2\alpha}{2\pi\varepsilon^*}\iint |f_{el}(z_e)|^2 |f_h(z_h)|^2 G(|z_e - z_h|)dz_e dz_h \tag{4.66}$$

The evaluation of $E_{PE}(\alpha)$ over ρ is represented by the function $G(|z_e - z_h|)$ (Miller *et al* 1985), written in full as,

$$G(|z_e - z_h|) = (2\alpha|z_e - z_h|)\left[\left(\frac{\pi}{2}\right)\left[H_1(2\alpha|z_e - z_h|) - N_1(2\alpha|z_e - z_h|)\right] - 1\right]$$

where $H_1(x)$ and $N_1(x)$ are the first order Struve and Neumann functions (see eg. Abramowitz and Stegun 1964). In equations (4.65) and (4.66), averaged values of $\mu_{||}$, the exciton mass in the plane, and ε, the static dielectric constant are used (Susa 1993).

$$\frac{1}{\mu^*} = \iint |f_{el}(z_e)|^2 |f_h(z_h)|^2 \frac{m_{e||}(z_e)m_{h||}(z_h)}{m_{e||}(z_e) + m_{h||}(z_h)} dz_e dz_h \tag{4.67}$$

$$\varepsilon^* = \frac{1}{|z_e - z_h|}\int_{z_h}^{z_e} \varepsilon(z)dz \tag{4.68}$$

§4.4.3 Calculating absorption near the band edge.

The absorption spectra near the band edge of a semiconductor may be viewed as the sum of excitonic absorption and band to band absorption. The methods for calculating absorption spectra near the band edge of semiconductors are well documented (see eg. Elliot 1957, Bassani *et al* 1975 chp 5 & 6). The theory has been extended to quantum well structures (see eg. Bastard 1988 chp.7), essentially requiring the QW properties (ie. band gap, excitonic transition energy, broadening etc.) to be used in place of the equivalent bulk properties. Of course obtaining the quantum well properties can, in some cases, involve quite demanding calculations depending on the level of description that is used (eg. multi-band models including mixing of states). For the present work, the approach has been to keep such calculations to a minimum. This is continued for the absorption calculations where the main concern is with the lowest energy excitonic absorption in a quantum well structure. To produce a realistic picture, band to band absorption is also considered but it should be remembered that at higher energies, the present description (ie. in-plane dispersion) is unlikely to be suitable since it neglects in-plane mixing. The possible short comings of the present description are discussed in §4.4.4.

Excitonic absorption

The absorption coefficient for an exciton formed between a conduction band state (*el*) and a valence band state (*m=hh,lh*) can be written as (see eg. Sanders and Bajaj 1987) :

$$\alpha_{\mathrm{ex}}^{el,m}(\hbar\omega) = \frac{\pi e^2 \hbar}{\varepsilon_0 \mathrm{m}_0 c n L} \, \mathrm{f}_{el,m} \, \mathrm{B}\left(\hbar\omega - \mathrm{E}_{\mathrm{ex}}^{el,m}\right) \qquad (4.69)$$

where c is the velocity of light, n is the refractive index of the material, e is the electronic charge , m_0 is the free electron mass and $\varepsilon_0$is the permittivity of a vacuum. L is commonly taken as the well width (or well and barrier width) in the structure and $\mathrm{B}(\hbar\omega - \mathrm{E}_{\mathrm{ex}}^{el,m})$ is a line shape function describing the broadening of the exciton peak centered at $\mathrm{E}_{\mathrm{ex}}^{el,m}$ (Sanders and Bajaj 1987, Sugawara *et al* 1990). The term, $\mathrm{f}_{el,m}$, is known as the exciton oscillator strength per unit area and is expressed as:

$$\mathrm{f}_{el,m} = \frac{2}{\mathrm{m}_0 \mathrm{E}_{\mathrm{ex}}^{el,m}} \left| \int \mathrm{A}(\mathrm{k}_{||}) \, \mathbf{P}_{el,m}(\mathrm{k}_{||}) \, \mathrm{dk}_{||} \right|^2 \qquad (4.70)$$

The exciton state is formed by a linear combination of the product of electron and hole states. $\mathrm{A}(\mathrm{k}_{||})$ is the expansion coefficient which is seen to rapidly decrease as the in-plane wave vectors increase, indicating that the exciton is made up from states near the band edges (Sugawara *et al* 1990). As a result the optical matrix element, $\mathbf{P}_{el,m}(k_{\|})$, is often approximated to the band edge value, $\mathbf{P}_{el,m}(0)$ and can be taken outside the integral. The expansion coefficient is determined by the Fourier transform of the exciton envelope function (Sugawara *et al* 1990). Thus the envelope function is written as,

$$\phi(\rho) = \int A(k_{\|})\exp[ik_{\|}\rho]\,dk_{\|} \tag{4.71}$$

Since absorption due to the exciton is proportional to finding the electron and hole at the same position (Shinada and Sugano 1966), the integration over $k_{\|}$ is found from:

$$\phi(0) = \int A(k_{\|})\,dk_{\|} \tag{4.72}$$

where $\phi(0)$ is given by the normalizing coefficient in (4.63). The optical matrix element for a transition between a valence band state, *m*, and a conduction band state, *el*, can be written as (see eg. Bassani *et al* 1975 chp.5, Bastard 1988 chp.7)

$$\mathbf{P}_{el,m}(0) = \langle\psi_{el}|\hat{\mathbf{e}}\cdot\hat{\mathbf{p}}|\psi_m\rangle = \int \psi_{el}^*\hat{\mathbf{e}}\cdot\hat{\mathbf{p}}\psi_m\,d\mathbf{r} \tag{4.73}$$

where $\hat{\mathbf{e}}$ is the unit polarization vector and $\hat{\mathbf{p}}$ is a momentum operator. The wave functions for the initial and final states have the form $\psi_n = F_n(\mathbf{r})u_{n,o}(\mathbf{r})$ ie. single band descriptions. Furthermore, $F_n(\mathbf{r}) = \exp[ik_{\|,n}\cdot r_{\|}]f_n(z)$, for the case of quantum wells where $f_n(z)$ is the envelope function for the state describing the z motion whereas $\exp[ik_{\|,n}\cdot r_{\|}]$ describes the motion in the plane of the layers. Substituting in the wave functions, the optical matrix element for the interband transition can be written,

$$\mathbf{P}_{el,m}(0) = \int_{crystal} F_{el}^*(\mathbf{r})F_m(\mathbf{r})\,d\mathbf{r}\int_{cell} u_{el,o}^*(\mathbf{r})\hat{\mathbf{e}}\cdot\hat{\mathbf{p}}u_{m,o}(\mathbf{r})\,d\mathbf{r} \tag{4.74}$$

where since the envelope functions, $F_n(\mathbf{r})$, are slowly varying on the scale of the unit cell, the integral has been split into an integral over the unit cell involving the periodic functions, $u_{n,o}(\mathbf{r})$, and an integral over the crystal involving the $F_n(\mathbf{r})$'s (see eg. Bastard 1988 chp.7). The first integral is further simplified by assuming the dipole approximation is valid (see eg. Bassani *et al* 1975 chp.5), ie. $k_{\|,el} = k_{\|,m}$. In other words, momentum in the plane is conserved by only allowing vertical transitions between the subbands, a condition known as the k-selection rule. The integral over the crystal volume then reduces to an integral along the z direction involving the quantum well envelope functions:

$$\int_{crystal} F_{el}^{*}(\mathbf{r})F_{m}(\mathbf{r})d\mathbf{r} \approx \int f_{el}^{*}(z)f_{m}(z)dz \tag{4.75}$$

This part of the optical matrix element highlights selection rules on the subband indices. Neglecting the polarization selection rules, an optical transition will only take place when (4.75) is non-zero. At zero field (ie. flat-band condition) in a symmetric QW, a good approximation to use is $\Delta n = 0$, where n is the subband index. Hence transitions (both excitonic and band to band) are expected between e1-hh1, e1-lh1, e2-hh2 etc.

The second part of (4.74), ie. the integral over the unit cell, gives rise to the selection rules on the polarization of the incident light wave. To express these, the valence band periodic functions used up till now, ie. $u_{m,o}(\mathbf{r})$ or specifically, $u_{hh,o}(\mathbf{r})$ and $u_{lh,o}(\mathbf{r})$, are written in terms of the Bloch p functions (cf. 3.14). The polarization selection rules can then be presented in terms of the Kane matrix element (3.18) (see eg. Sanders and Bajaj 1987). A good discussion regarding polarization selection rules in heterostructures is given by Corzine *et al* (1993). In this work, the authors demonstrated a method to express the polarization matrix element in terms of the angle, θ, between the incident electric field vector and the electron wave vector. Following their method,

$$\left|\int u_{el,o}^{*}(\mathbf{r})\hat{\mathbf{e}}\cdot\hat{\mathbf{p}}u_{hh,o}(\mathbf{r})d\mathbf{r}\right|^{2} = \frac{m_oE_P}{4}\left(1 - \cos^{2}\theta\right) \quad hh\text{ - }el \text{ transitions} \tag{4.76a}$$

$$\left|\int u_{el,o}^{*}(\mathbf{r})\hat{\mathbf{e}}\cdot\hat{\mathbf{p}}u_{lh,o}(\mathbf{r})d\mathbf{r}\right|^{2} = \frac{m_oE_P}{4}\left(\frac{1}{3} + \cos^{2}\theta\right) \quad lh\text{ - }el \text{ transitions} \tag{4.76b}$$

Note that spin degeneracy is already accounted for in (4.70) by the factor of 2 and was therefore not included in obtaining the above relations. The expressions are written in terms of E_P which has units of energy and is related to the Kane matrix element (cf. §3.4). Moreover since we are interested in energies close to the sub band edge, the electron wave vector, can be taken to lie parallel with the confinement axis, ie. close to the (sub) band edge the in-plane components are negligible (Corzine *et al* 1993). So for incident light with the electric field vector parallel (perpendicular) to the the confinement axis, ie. TM (TE) modes, we find (w.r.t $^{m_oE_P}/_4$):

$$\text{TE} \rightarrow 1, \quad \text{TM} \rightarrow 0 \quad hh\text{ - }el \text{ transitions}$$
$$\text{TE} \rightarrow {}^{1}\!/_{3}, \quad \text{TM} \rightarrow {}^{4}\!/_{3} \quad lh\text{ - }el \text{ transitions}$$

The configuration used for the experimental results presented in Chapter 5, has the incident light normal to the layers. The electric field vector is perpendicular to the confinement axis (ie. parallel to the layers) which implies TE selection rules (cf. Fig.1-5).

Making use of (4.72), (4.74) and (4.75), the oscillator strength per unit area (4.70) is written as:

$$\mathrm{f}_{el,m} = \frac{2}{\mathrm{m_o E_{ex}^{\mathit{el,m}}}} \left|\phi_{el,m}(0)\right|^2 \left|\int u_{el,o}^*(\mathbf{r})\hat{\mathbf{e}}\cdot\hat{\mathbf{p}}u_{lh,o}(\mathbf{r})\mathrm{d}\mathbf{r}\right|^2 \left|\int f_{el}^*(\mathrm{z})f_m(\mathrm{z})\mathrm{dz}\right|^2 \qquad (4.77)$$

To calculate the excitonic absorption spectra from (4.69) the broadening function, B(x), needs to be determined. In theory, B(x) in (4.69) should be a delta function at the excitonic transition energy. However, in actual QW structures the exciton resonance is broadened and is simulated through the use of a broadening function. Further discussion on broadening is presented in the next section. For now, it is enough to state that a normalized Lorentzian function is used to describe the excitonic resonance at room temperature, ie.

$$\mathrm{B}\left(\hbar\omega - \mathrm{E_{ex}^{\mathit{el,m}}}\right) = \frac{\Gamma}{2\pi\left(\left(\hbar\omega - \mathrm{E_{ex}^{\mathit{el,m}}}\right)^2 + \frac{\Gamma^2}{4}\right)} \qquad (4.78)$$

which is centered on the exciton peak energy, $\mathrm{E_{ex}^{\mathit{el,m}}}$, and has a full width half maximum (FWHM) in energy determined by Γ.

Band to band absorption

At slightly higher energies (ie. the binding energy) from the exciton, transitions from the valence band to the conduction band take place. For a QW these are transitions between the bound states (ie. el-hh1, el-lh1 etc.). The absorption between subbands can be written as (see eg. Bastard)

$$\alpha_{\mathrm{b\text{-}b}}^{el,m}(\hbar\omega) = \frac{\pi e^2\hbar}{\varepsilon_0 \mathrm{m_o^2} cn\hbar\omega}\left|\mathbf{P}_{el,m}(\mathrm{k}_{||})\right|^2 \rho_{el,m}\left(\hbar\omega - \left[\mathrm{E}_{el}(\mathrm{k}_{||}^0) - \mathrm{E}_m(\mathrm{k}_{||}^0)\right]\right) \qquad (4.79)$$

As with the exciton absorption, $\left|\mathbf{P}_{el,m}(\mathrm{k}_{||})\right|^2$, is the optical matrix element which for simplicity is taken to be the value at the band edge, $\mathbf{P}_{el,m}(0)$ (see equations (4.73-4.76). The reduced density of states function between the subbands, $\rho_{el,m}(\mathrm{x})$, can be analytically written because of the simple in-plane parabolic dispersions used, cf. (4.56).

We find (including spin),

$$\rho_{el,m}\left(\hbar\omega - \left[E_{el}(k_{\|}^{0}) - E_{m}(k_{\|}^{0})\right]\right) = \frac{\mu_{el,m}^{*}}{\pi\hbar^{2}}\left(\frac{1}{l_{w}}\right)\Theta\left(\hbar\omega - \left[E_{el}(k_{\|}^{0}) - E_{m}(k_{\|}^{0})\right]\right) \quad (4.80)$$

where $\mu_{el,m}^{*}$ is given by (4.67) and l_w is taken as the well width (or composite width). $\Theta(x)$ is a step function with a unity value for energies larger than the energy separation of the subbands at $k_{\|} = 0$. To account for broadening, the step function may be replaced by (Chemla *et al* 1984, Stevens *et al* 1988),

$$\Theta\left(\hbar\omega - \left[E_{el}(k_{\|}^{0}) - E_{m}(k_{\|}^{0})\right]\right) \rightarrow \frac{1}{1 + \exp\left[\dfrac{E_{el}(k_{\|}^{0}) - E_{m}(k_{\|}^{0}) - \hbar\omega}{\hbar\Gamma_{b-b}}\right]} \quad (4.81)$$

where Γ_{b-b} is a broadening parameter with units of energy. In addition to (4.80) and (4.81), a Sommerfeld factor may also be included to account for the effect of Coloumb interaction above the band edge (Shinada and Sugano 1966, Chemla *et al* 1984, Stevens *et al* 1988). [note: All the calculated spectra in this thesis do not include the Sommerfeld factor].

§4.4.4 Comments on exciton calculations.

Remarks concerning the diagonal approximation have already been made in §4.4. In the following section, using example structures, I have attempted to highlight how this compromised description affects the various parameters relevant to the exciton calculations (ie. binding energies, absorption etc.). In addition comments about other important parameters, such as broadening functions, are discussed.

Zero field calculations-binding energy.

Calculations of the lowest energy exciton (e1hh1) were carried out for $In_{0.05}Ga_{0.95}As$/GaAs QW's across a range of well widths, Fig.4-7(a). This is a strained system and was chosen because of the availability of experimental data (Joyce *et al* 1991, Joyce 1992). Since growth is on a GaAs substrate the well layers ($In_{0.05}Ga_{0.95}As$) are under compressive strain. Further details concerning the growth and characterization are given in the aforementioned works by Joyce and co-workers.

are given in the aforementioned works by Joyce and co-workers.

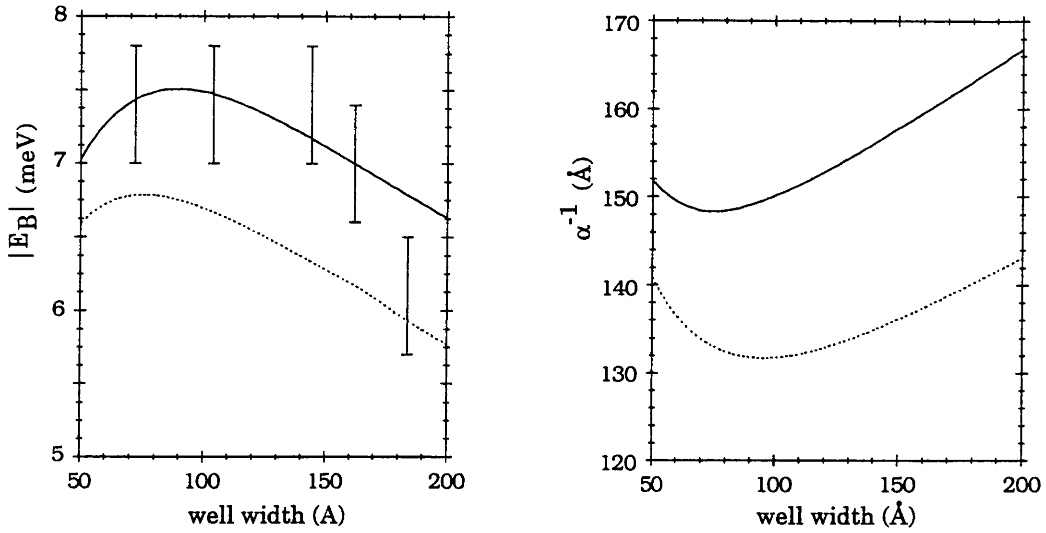

(a) (b)

Figure 4-8. *Calculated parameters of the e1hh1 exciton in $In_{0.05}Ga_{0.95}As$ / GaAs quantum wells as a function of well width. (a) Calculated binding energy* $|E_B|$ *using two different values for the in-plane heavy hole mass. Using* $m^*_{||,hh}$ *obtained within the diagonal approximation (dotted) and using* $2m^*_{||,hh}$ *(solid). The error bars indicate the experimentally determined binding energies from Joyce (1992). (b) The calculated in-plane radius of the exciton using* $m^*_{||,hh}$ *(dotted), using* $2m^*_{||,hh}$ *(solid).*

Recall that working within the diagonal approximation, coupling with other bands is neglected and the in-plane heavy hole mass, $m^*_{||,hh}$, obtained for hh1 will always be underestimated (see *in-plane dispersions* in §4.4). In other words, when mixing is included this tends to increase the predicted in-plane mass. For a larger $m^*_{||,hh}$, the reduced mass of the exciton increases, (cf. 4.58), which increases the calculated binding energy (solid line in Fig.4-8(a)). The choice of using $2m^*_{||,hh} \approx 0.22m_0$ in the calculations was somewhat arbitrary. Although it is worth noting that magneto optical measurements on $In_{0.12}Ga_{0.88}As$/GaAs samples have indicated in-plane heavy hole mass values $0.17m_0 \rightarrow 0.22m_0$ for well widths of 50Å → 200Å(Moore *et al* 1990). The program allows the in-plane mass to be input directly if values are available (either from theory or experiment). Otherwise, values obtained from the diagonal approximation are used, (4.57). It is worth noting according to figure 4-8, the discrepancies incurred by using the diagonal approximation appear to be within the limits suggested in §4.4.1.

Another useful parameter to display is the inverse of the variational parameter (i.e. $1/\alpha$) as a function of well width. Commonly referred to as the exciton radius, this is seen to increase with increasing well width (Fig.4-8b) which in turn reduces the binding a smaller in-plane radius (solid line in Fig.4-8b).

Effect of an applied electric field-binding energy.

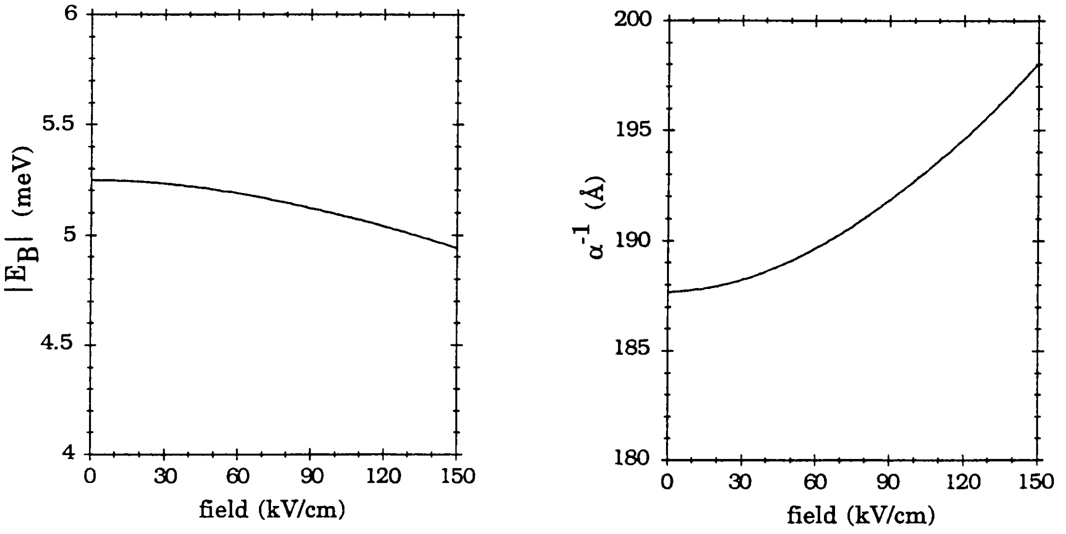

(a) (b)

Figure 4-9. *Calculated parameters of the e1hh1 exciton in InGaAs/InP quantum wells as a function of applied electric field. (a) Calculated binding energy* $|E_B|$ *using* $m^*_{||,hh}$ *obtained within the diagonal approximation. (b) The calculated in-plane radius of the exciton using* $m^*_{||,hh}$

Taking as an example a 70Å InGaAs/InP (lattice matched) quantum well. Upon application of an electric field, the calculated binding energy decreases, Fig.4-9a. Associated with this, the in-plane radius increases from its value at zero field (Fig.4-9b), which again highlights the inverse relationship between the binding energy of the exciton and its radius. Although the calculations were carried out assuming the diagonal approximation, its fair to suggest that the results when mixing is included would follow a similar pattern, ie. the binding energy (radius) decreases (increases) from its zero field value. It is also noted that with respect to the exciton transition energy, the decrease in binding energy is small, hence the dominant mechanism behind the decrease in excitonic transition energy comes from the decrease in the subband separation (cf. Fig.4-7b,d)

Before the absorption calculations are discussed, it is worth summarizing the consequences of using the diagonal approximation on the binding energy calculations. For the lowest energy exciton (e1hh1), the binding energy will generally be underestimated. This is due to underestimating the reduced mass of the exciton and subsequently overestimating the in-plane radius. Considering these exciton parameters will be useful for the following discussion on the absorption calculations.

The calculated absorption spectra.

Accurately predicting the absorption spectra for a structure not only depends on the type of band structure description used but also on describing the broadening mechanisms present in the structure. Comments on the former appear later, but first it is useful to highlight the effects of broadening on the final spectra. In particular, on the excitonic peak absorption.

The broadening mechanisms can be classed into inhomogenous (eg. interface roughness, alloy fluctuations, well width fluctuations in MQW's) and homogenous fluctuations (eg. phonon scattering and other mechanisms affecting exciton lifetime) and are further discussed by Schmitt-Rink *et al* (1989). All of the broadening mechanisms in some way contribute to the overall line width (and shape) of the excitonic resonance. It is not the aim here to further discuss the mechanisms or propose how one might account for them. Several authors have already addressed these problems (see eg. Stevens *et al* 1988, J Singh 1993, Lin *et al* 1994). In the present work, a Lorentzian function (4.78) is used to describe the shape of the exciton resonance at room temperature (Stevens *et al* 1988). The dependence of the exciton absorption peak value on the line width can be appreciated by considering (4.78) when $\hbar\omega = E_{ex}^{el,m}$, then $B(0) = 2/\pi\Gamma$ where Γ represents the FWHM of the resonance. Therefore, the peak absorption is inversely dependent on the line width. Given that the resonance line width is extremely important, it is also interesting to note the use of a different line *shape* can effect the predicted peak absorption value. For example, some authors use a Gaussian shape to account for the exciton resonance at room temperature (eg. Shim and Lee 1993). In terms of line width (the half width half maximum), this can be written as

$$B_G\left(\hbar\omega - E_{ex}^{el,m}\right) = \frac{1}{\sqrt{1.44\pi}\,\sigma}\exp\left(\frac{-\left(E_{ex}^{el,m} - \hbar\omega\right)^2}{1.44\sigma^2}\right) \qquad (4.82)$$

where σ represents the half width half maximum (HWHM) of the exciton resonance. For the same line width value, ie. $\Gamma = 2\sigma$, the peak absorption predicted using a Lorentzian line shape is $\sim 2/3$ of that found if a Gaussian shape is used. Typically, the operating temperature usually determines which shape best fits experimental data and at room temperature, a Lorentzian function is more representative of the exciton resonance (cf.

Sugawara *et al* 1990 for experimental fits to InGaAs/InP exciton resonances).

The line width dependence on the absorption peak is a contributing factor to the smaller peak absorption found in InP based structures compared to GaAs based structures. MQW's on InP, eg. comprising InGaAs/InP, typically have line widths of twice those found in GaAs/AlGaAs. The increased line widths are often attributed to alloy broadening since the well materials for InP structures are ternary (or quaternary) compounds see eg. J Singh 1993). However, it is slightly misleading to attribute the poorer absorption characteristics of long wavelength devices solely on the line width. A method often employed in experimental investigations is to measure the integrated area of the exciton resonance; with this technique the dependence on the line width is removed (Masumoto *et al* 1985, Masselink *et al* 1985, Sugawara *et al* 1990). From (4.69) the area is defined as,

$$A_{\text{ex}}^{el,m} = \int_{\hbar\omega_1}^{\hbar\omega_2} \alpha_{\text{ex}}^{el,m}(\hbar\omega)\, d\hbar\omega = \frac{\pi e^2 \hbar}{\varepsilon_0 m_0 c n L} f_{el,m} \qquad (4.82)$$

$A_{\text{ex}}^{el,m}$ is then the area of the exciton peak in units of eV/cm and is seen to be proportional to the oscillator strength, with the limits $\hbar\omega_1$ and $\hbar\omega_2$ chosen to cover the absorption peak. Comparisons between GaAs/AlGaAs samples (from Masselink *et al* 1985) and InGaAs/InP samples, Sugawara and co-workers (1990) found the integrated area of InGaAs QW's to be ~70% smaller than that for GaAs. They argued that the decrease in area for InGaAs QW's is due to the larger exciton radius in the plane of the wells, which originates from the lighter exciton reduced mass found in lower gap materials such as InGaAs.

The dependence on the exciton radius (and hence reduced mass) enters through the evaluation of the oscillator strength (4.77) with (4.72). The oscillator strength is inversely proportional to the in-plane radius (ie. $\propto \alpha^2$), which in turn has an inverse dependence with the reduced mass of the exciton, (cf. Fig.4-9 which demonstrates a larger in-plane radius for a smaller reduced mass). The calculated in-plane radius using the diagonal approximation will be typically overestimated, and in fact represents an upper limit since the reduced mass in this decoupled picture represents a lower limit. In relation to the calculated oscillator strength (or excitonic area) it follows that using this upper limit of the in-plane radius will typically underestimate the oscillator strength.

References.

Abramowitz M, and Stegun I.A, *Handbook of Mathmatical Functions.* Dover Publications (1964).

Alterelli M, "*Band Structure, Impurities and Excitons in Superlattices*" in *Heterojunctions and Semiconductor Superlattices,* edited by Allan G, Bastard G, Boccara N, Lannoo M, and Voos M, Springer-Verlag, Berlin, (1986), pp 12-37.

Ando T, Wakahara S, and Akera H, "*Connection of Envelope Functions at Semiconductor Heterointerfaces. I. Interface matrix calculated in Simplest Models*", Phys. Rev. **B 40**, (1989), pp 11609-11618.

Andreani L.C, Pasquarello A, and Bassani F, "*Hole Subbands in Strained GaAs-$Ga_{1-x}Al_xAs$ Quantum Wells: Exact Solution of the Effective Mass Equation*", Phys. Rev. **B 36**, (1987), pp 5887-5894.

Andreani L.C, and Pasquarello A, "*Accurate Theory of Excitons in GaAs-$Ga_{1-x}Al_xAs$ Quantum Wells*", Phys. Rev. **B 42**, (1990), pp 8928-8938.

Anemogiannis E, Glytsis E.N, Gaylord T.K, "*Bound and Quasibound State Calculations for Biased/Unbiased Semiconductor Quantum Heterostructures*", IEEE J. Quantum Electron., **QE-29**, (1993) pp 2731-2740.

Atkinson D, Parry G, Rivers A, and Roberts J.S, "*Modelling of Low Voltage Electroabsorption in Coupled Quantum Wells with Applications to Low-Voltage Optical Modulation*", Semicond. Sci. Technol. **5**, (1990), pp 516-524.

Austin E.J, and Jaros M, "*Electronic Structure of an Isolated GaAs-AlGaAs Quantum Well in a Strong Electric Field*", Phys. Rev. **B 31**, (1985), pp 5569-5572.

Bassani F, and Pastori Parravicini, G in *Electronic States and Optical Transitions in Solids* edited by R.A. Ballinger, Pergamon Press, (1975).

Bastard G, "*Superlattice Band Structure in the Envelope-Function Approximation*", Phys. Rev. **B 24**, (1981), pp 5693-5697.

Bastard G, "*Theoretical Investigations of Superlattice Band Structure in the Envelope-Function Approximation*", Phys. Rev. **B 25**, (1982), pp 7584-7597.

Bastard G, Mendez E.E, Chang L.L, and Esaki L, "*Exciton Binding Energy in Quantum Wells*", Phys. Rev. **B 26**, (1982), pp1974-1979.

Bastard G, Mendez E.E, Chang L.L, and Esaki L, *"Variational Calculations on a Quantum Well in an Electric Field"*, Phys. Rev. **B 28**, (1983), pp 3241-3245.

Bastard G, and Brum J.A, *"Electronic States in Semiconductor Heterostructures"*, IEEE J. Quantum Electron., **QE-22**, (1986) pp 1625-1644.

Bastard G, *Wave Mechanics Applied to Semiconductor Heterostructures,* Les Editions de Physique, Paris, (1988).

Bauer G.E.W, and Ando T, *"Exciton Mixing in Quantum Wells"*, Phys. Rev. **B 38**, (1988), pp 6015-6030.

BenDaniel D.J, and Duke C.B, *"Space-Charge Effects on Electron Tunneling"*, Phys. Rev. **152**, (1966), pp 683-692.

Brennan K.F, and Summers C.J, *"Theory of Resonant Tunnelling in a Variably Spaced Multiquantum Well Structure: An Airy Function Approach"*, J. Appl. Phys. **61**, (1987), pp 614-623.

Brum J.A, and Bastard G, *"Electric Field Induced Dissociation of Excitons in Semiconductor Quantum Wells"*, Phys. Rev. **B 31**, (1985), pp 3893-3898.

Burt M.G, *"An Exact Formulation of the Envelope Function Method for the Determination of Electronic States in Semiconductor Microstrutucres"*, Semicon. Sci. Technol. **3**, (1988), pp 739-753.

Burt M.G, *"The Justification for Applying the Effective Mass Approximation to Microstructures"*, J. Phys. Condens. Matter **4** , (1992), pp 6651-6690.

Chemla D.S, Miller D.A.B, Smith P.W, Gossard A.C, and Wiegmann W, *"Room Temperature Excitonic Nonlinear Absorption and Refraction in GaAs/AlGaAs Multiple Quantum Well Structures"*, IEEE J. Quantum Electron. vol. JQE-20, (1984) pp 265-275.

Chemla D.S, and Miller D.A.B, *"Room-Temperature Excitonic Nonlinear-Optical Effects in Semiconductor Quantum-Well Structures"*, J. Opt. Soc. Am. B **2**, (1985), pp 1155-1173.

Corzine S.W, Yan R.H, and Coldren L.A, in *Quantum Well Lasers*, Chapter 1, ed. P.S Zory, Academic Press, New York, (1993), pp 17-96.

Dimmock J.O, Vol.3 of *Semiconductor and Semimetals*, eds. R.K.Willardson and A.C.Beer,Academic Press, New York, (1967), p 259.

Dingle R, Wiegmann W, and Henry C.H, *"Quantum States of Confined Carriers in Very Thin* $Al_xGa_{1-x}As$*-GaAs-*$Al_xGa_{1-x}As$ *Heterostructures"*, Phys. Rev. Lett. **33**,

(1974), pp 827-830.

Ekenberg U, and Altarelli M, "*Exciton Binding Energy in a Quantum Well with Inclusion of Valence Coupling and Nonparabolicity*", Phys. Rev. **B 35**, (1987), pp 7585-7595.

Elliot R.J, "*Intensity of Optical Absorption by Excitons*", Phys. Rev. **108**, (1957), pp 1384-1389.

Elçi A, "*Effective Band Hamiltonian in Semiconductor Quantum Wells*", Phys.Rev. **B 49**, (1994), pp 7432-7442.

Einevoll G.T, Hemmer P.C, and Thomsen J, "*Operator Ordering in Effective Mass Theory for Heterostructures. I. Comparison with Exact Results for Superlattices, Quantum Wells and Localized Potentials* ", Phys. Rev. **B 42**, (1990), pp 3485-3496.

Eppenga R, Schuurmans M.F.H, and Colak S, "*New **k.p** Theory for* $GaAs/Ga_{1-x}Al_xAs$ *type Quantum Wells*", Phys. Rev. **B 36**, (1987), pp 1554-1564.

Ghatak A.K, Thyagarajan K, and Shenoy M.R, "*A Novel Numerical Technique for Solving the One Dimensional Schrödinger Equation Using Matrix Approach-Application to Quantum Well Structures*", IEEE J. Quantum Electron. vol. JQE-24, (1988) pp 1524-1531.

Ghatak A.K, Goyal I.C, and Gallawa R.L, "*Mean Lifetime Calculations of Quantum Well Structures: A Rigorous Analysis*", IEEE J. Quantum Electron. vol. JQE-26, (1990) pp 305-310.

Ghisoni M, Murray R, Rivers A.W, Pate M, Hill G, Woodbridge K, and Parry G, "*An Optical Study of Encapsulant Thickness Controlled Interdiffusion of Asymmetric GaAs Quantum Well Material*", Semicon. Sci. Technol. **8**, (1993), pp 1791-1796.

Greene R.J, and Bajaj K.K, "*Binding Energies of Wannier Excitons in* $GaAs$-$Ga_{1-x}Al_xAs$ *Quantum Well Structures*", Solid State Commun. **45** , (1983), pp 831-835.

Greene R.J, Bajaj K.K, and Phelps D.E, "*Energy Levels of Wannier Excitons in* $GaAs$-$Ga_{1-x}Al_xAs$ *Quantum Well Structures*", Phys. Rev. **B 29**, (1984), pp 1807-1812.

Grundmann M, and Bimberg D, "*Anisotropy Effects on Excitonic Properties in Realistic Quantum Wells*", Phys. Rev. **B 38**, (1988), pp 13486-13489.

Harwit A, Harris, Jr. J.S, and Kapitutnik A, "*Calculated Quasi-Eigenstates and Quasi-Eigenenergies of Quantum Well Superlattices in an Applied Electric Field*", J. Appl. Phys. **60**, (1986), pp 3211-3212.

Hermann C, and Weisbuch C, “*k.p* *perturbation theory in III-V compounds and alloys: a reexamination*”, Phys. Rev. **B 15**, (1977), pp 823-833.

Hiroshima T, "*Exciton States in Strained Quantum Wells*", Phys. Rev. **B 36**, (1987), pp 4518-4521

McIlroy P.W.A, “*Effect of an Electric Field on Electron and Hole Wave Functions in a Multiquantum Well Structure*”, J. Appl. Phys. **59**, (1986), pp 3532-3536.

Johnson N.F, Ehrenreich H, Hui P.M, and Young P.M, “*Electronic and Optical Properties of III-V and II-VI Semiconductor Superlattices*”, Phys. Rev. **B 41**, (1990), pp 3655-3669.

Jonsson B, and Eng S.T, “*Solving the Schrödinger Equation in Arbitrary Quantum Well Potential Profiles Using the Transfer Matrix Method*”, IEEE J. Quantum Electron. vol. JQE-26, (1990), pp 2025-2035.

Joyce M.J, Xu Z.Y, and Gal M, “*Photoluminescence Excitation Spectroscopy of As-Grown and Chemically Released* $In_{0.05}Ga_{0.95}As/GaAs$ *Quantum Wells*”, Phys. Rev. **B 44**, (1991), pp 3144-3149.

Joyce M.J, “*Excited Subband Excitons in InGaAs/GaAs Quantum Wells: Comparison of Theory and Experiment*”, Superlattices and Microstructures, **12**, (1992), pp 293-296.

Kane E.O, "*Band Structure of Indium Antimonide*", J. Phys. Chem. Solids **1**, (1957), pp 249-261.

Knox R.S, *Theory of Excitons,* Solid State Physics, Academic Press, (1963), Suppl.5.

Kolbas R.M, and Holonyak, Jr. N, “*Man-Made Quantum Wells: A New Perspective on the Finite Square-Well Problem*”, Am. J. Phys. **52**, (1984), pp 431-437.

Laikhtman B, “*Boundary Conditions for Envelope Functions in Heterostructures*”, Phys. Rev. **B 46**, (1992), pp 4769-4774.

Lengyel G, Jelley K.W, and Engelmann R.W.H, “*A Semi-Empirical Model for Electroabsorption GaAs/AlGaAs Multiple Quantum Well Modulator Structures*”, IEEE J. Quantum Electron. vol. JQE-26, (1990), pp 296-304.

Lin C.H, Meese J.M, and Chang Y.C, “*Optical Propoerties of* $GaAs/Al_xGa_{1-x}As$ *Multiple Quantum Well Versus Electric Field Including Exciotn Transition Broadening Effects in Optical Modulators*”, J. Appl. Phys. **75**, (1994), pp 2618-2627.

Mathieu H, Lefebvre P, and Christol P, "*Simple Analytical Method for Calculating Exciton Binding Energies in Semiconductor Quantum Wells*", Phys. Rev. **B 46**,

(1992), pp 4092-4101.

Masselink W.T, Pearah P.J, Klem J, Peng C.K, Morkoç, H, Sanders G.D, and Chang Y.C, *"Absorption Coefficients and Exciotn Oscillator Strengths in AlGaAs-GaAs Superlattices"*, Phys. Rev. **B 32**, (1985), pp 8027-8033.

Masumoto Y, Matsuura M, Tarucha S, and Okamoto H, *"Direct Experimental Observation of the Two-Dimensional Shrinkage of the Exciton Wave Function in Quatum Wells"*, Phys. Rev. **B 32**, (1985), pp 4275-4278.

Matsuura M, and Kamizato T, *"Subbands and Excitons in a Quantum Well in an Electric Field"*, Phys. Rev. **B 33**, (1986), pp 8385-8389.

Messiah A, *Quantum Mechanics*, Vol. 1, 6th Edition, North-Holland Publishing Company, Amsterdam, (1970).

Miller D.A.B, Chemla D.S, Damen T.C, Gossard A.C, Wiegmann W, Wood T.H, and Burrus C.A, *"Band Edge Electroabsorption in Quantum Well Structures: The Quantum Confined Stark Effect"*, Phys. Rev. Lett. **53**, (1984), pp 2173-2176.

Miller D.A.B, Chemla D.S, Damen T.C, Gossard A.C, Wiegmann W, Wood T.H, and Burrus C.A, *"Electric Field Dependence of Optical Absorption Near the Band Gap of Quantum Well Structures"*, Phys. Rev. **B 32**, (1985), pp 1043-1060.

Miller R.C, Kleinman D.A, Tsang W.T, and Gossard A.C, *"Observation of the Excited Level of Excitons Binding Energy in GaAs Quantum Wells"*, Phys. Rev. **B 24**, (1981), pp1134-1136.

Moore K.J, Duggan G, Woodbridge K, and Roberts C, *"Observations and Calculations of the Exciton Binding Energy in (InGa)As/GaAs Strained Quantum Well Heterostructures"*, Phys. Rev. **B 41**, (1990), pp 1090-1094.

Morrow R.A, and Brownstein K.R, *"Model Effective-Mass Hamiltonians for Abrupt Heterojunctions and the Associated Wave-Function Matching Conditions"*, Phys. Rev. **B 30**, (1984), pp 678-680.

Nakamura K, Shimizu A, Koshiba M, and Hayata K, *"Finite-Elements Analysis of Quatum Wells of Arbitrary Semiconductors with Arbitrary Potential Profiles"*, IEEE J. Quantum Electron., JQE-25, (1989), pp 889-895.

Pötz W, Porod W, and Ferry D.K, *"Theoretical Study of Subband Levels in Semiconductor Heterostructures"*, Phys. Rev. **B 32**, (1985), pp 3868-3875.

Pötz W, and Ferry D.K, *"On the Boundary Conditions for Envelope-Function Approaches for Heterostructures"*, Superlattices and Microstructures, 3, (1987), pp 57-61.

Priester C, Allan G, Lannoo M, "*Wannier Excitons in GaAs-*$Ga_{1-x}Al_xAs$ *Quantum Well Structures: Influence of the Effective Mass Mismatch*", Phys. Rev. **B 30**, (1984), pp 7302-7304.

Ridley B.K, *"The In-Plane Effective Mass in Strained Layer Quantum Wells"*, J. Appl. Phys. **68**, (1990), pp 4667-4673.

Sai-Halasz G.A, Esaki L, and Harrison W.A, *"InAs-GaSb Superlattice Energy Structure and its Semiconductor-Semimetal Transition"*, Phys. Rev. **B 18**, (1978), pp 2812-2818.

Sanders G.D, and Chang Y.C, *"Effect of Band Hybridation on Exciton States in GaAs-*$Al_xGa_{1-x}As$ *Quantum Wells"*, Phys. Rev. **B 32**, (1985), pp 5517-5520

Sanders G.D, and Bajaj K.K, "*Electronic Properties and Optical Absorption Spectra of Graded Gap GaAs-*$Al_xGa_{1-x}As$ *Quantum Wells*", Phys. Rev. **B 36**, (1987), pp 4849-4857.

Schiff L.I, *Quantum Mechanics*, 3^{rd} edition, McGraw -Hill, New York, (1968), p 88.

Schmitt-Rink S, Chemla D.S, and Miller D.A.B, "*Linear and Nonlinear Optical Properties of Semiconductor Quantum Wells*", Advances in Physics, Vol.38, (1989) pp89-188.

Shinada M, and Sugano S, "*Interband Optical Transitions in Extremely Anisotropic Semiconductors. I. Bound and Unbound Exciton Absorption*", J. Phys. Soc. Jpn, **21**, (1966), pp 1936-1946.

Shinozuka Y, and Matsuura M, "*Wannier Exciton in Quantum Wells*", Phys. Rev. **B 28** , (1983), pp4878-4881. Erratum: Phys. Rev. **B 29**, (1984), pp 3717-3718.

Singh J, *"A New Method for Solving the Ground State Problem in Arbitrary Quantum Wells: Application to Electron-Hole Quasi-bound Levels in Quantum Wells under High Electric Field"*, Appl. Phys. Lett. **48**, (1986), pp 434-436.

Sirtori C, Capasso F, Faist J, and Scandolo S, *"Nonparabolicity and a Sum Rule Associated with Bound-to-Bound and Bound-to-Continuum Intersubband Transitions in Quantum Wells"*, Phys. Rev., **B 50**, (1994), pp 8663-8674.

Smith D.L, and Mailhiot C, "***k.p*** *Theory of Semiconductor Superlattice Electronic Structure. I. Formal Results.*", Phys. Rev. **B 33**, (1986), pp 8345-8359.

Stevens P.J.S, Whitehead M, Parry G, and Woodbridge K, *"Computer Modelling of the*

Field Dependent Absorption Spectrum of Multiple Quantum Well Material", IEEE J. Quantum Electron. vol. JQE-24, (1988), pp 2007-2014.

Sugawara M, Fujii T, Yamazaki S, and Nakajima K, *"Theoretical and Experimental Study of the Optical-Absorption Spectrum of Exciton Resonance in* $In_{0.53}Ga_{0.47}As/InP$ *Quantum Wells"*, Phys. Rev. **B 42**, (1990), pp 9587-9597.

Susa N, *"Improvement in Electroabsorption and the Effects of Parameter Variations in the Three-Step Asymmetric Coupled Quantum Well"*, J. Appl. Phys. **73**, (1993), pp 932-942.

Tamir T, and Kou F.Y, *"Varieties of Leaky Waves and Their Excitation Along Multilayered Structures"*, IEEE J. Quantum Electron. vol. JQE-22, (1986), pp 544-551.

Taylor R.I, and Burt M.G, *"Continuity Conditions for Envelope Functions at Semiconductor Interfaces Derived from the Bastard Model"*, Semicond. Sci. Technol. **2**, (1987), pp 485-490.

von Allmen P, *"Conduction Subbands in* $GaAs/Al_xGa_{1-x}As$ *Quantum Well: Comparing Different* ***k.p*** *Models"*, Phys. Rev., **B 46**, (1992), pp 15382-15386.

von Roos O, *"Position-Dependent Effective Masses in Semiconductor Theory"*, Phys. Rev. **27**, (1983), pp 7547-7552.

Wu J.W, and Nurmikko A.V, *"Wannier Excitons in Semiconductor Quantum Wells with Small Valence Band Offsets: A Generalized Variational Approach"*, Phys. Rev. **B 38**, (1988), pp 1504-1507.

Yoo K.H, Ram-Mohan L.R, and Nelson D.F, *"Effect of nonparabolicity in* $GaAs/Ga_{1-x}Al_xAs$ *Semiconductor Quantum Wells"*, Phys. Rev., **B 39**, (1989), pp 12808-12813.

Young P.M, and Ehrenreich H, *"Evidence for Quantum Well Asymmetry in Optical Absorption"*, Appl. Phys. Lett. **61**, (1992), pp 1069-1071.

Chapter 5. Investigating $InAs_xP_{1-x}$ Multiple Quantum Wells.

The present chapter is devoted to further investigating $InAs_xP_{1-x}$ /InP MQW structures both from an experimental and theoretical viewpoint. Before this is undertaken, a brief review of the limited published work is given along with further comparisons with other material systems.

§5.1 Introduction.

The quaternary system, $In_vGa_{1-v}As_xP_{1-x}$, has long provided suitable material combinations for use in quantum well (QW) long wavelength emitter and detector structures. In the quaternary form it can be latticed matched to InP and provide an operating range from ~1μm to 1.6μm (eg. T.P Pearsall 1982). A common ternary subset is the $In_vGa_{1-v}As$/InP QW system, where the group III compositions can be chosen for either lattice matched (ie. v=0.53) or strained structures (ie. v>0.53 for compressive or v<0.53 for tensile) (see for eg. Gershoni *et al* 1988, Gershoni *et al* 1989). Another ternary combination for a QW system is $InAs_xP_{1-x}$ /InP, which until recently had received little attention (Woodward *et al* 1991). In this system, $InAs_xP_{1-x}$, is the well material which is under compressive strain with respect to InP. The large difference in band gap between InAs and InP for a relatively small change of lattice constant enables the $InAs_xP_{1-x}$ system to access optoelectronic devices over the range from ~1μm to 1.6μm (Woodward *et al* 1991, Schneider and Wessels 1991, Hou and Tu 1992).

As a strained system, the utility of $InAs_xP_{1-x}$ /InP, in comparison to $In_xGa_{1-x}As$/InP and $In_xGa_{1-x}As$/GaAs is demonstrated in Fig.5-1. For example, devices operating around 1.06μm would require less than 1% compressive strain to be accommodated in the $InAs_xP_{1-x}$ layer. In contrast, GaAs based structures, ie. $In_xGa_{1-x}As$/GaAs, require about 2% of compressive strain to be accommodated which often proves troublesome, because of relaxation in multi-quantum well structures (Woodward *et al* 1990). Of course similar considerations would apply if $InAs_xP_{1-x}$ /InP MQW devices operating around 1.55μm were attempted. However, at these wavelengths, devices using only a few $InAs_xP_{1-x}$ /InP QW's may be beneficial in laser design, where the ~2% compressive strain could be used to significantly reduce the carrier injection levels required for lasing (eg. see Corzine *et al* 1993 for further information).

$InAs_xP_{1-x}$ /InP devices, grown by Chemical Beam Epitaxy (CBE), operating around 1μm have been demonstrated by Woodward and co-workers (1991). [This and related work is discussed in more detail later on.] Using Gas -Source Molecular Beam Epitaxy (GS-MBE) Hou and Tu (1992) investigated MQW, structures, (30 period), with arsenic compositions varying from 15% to 75%. Room temperature absorption spectra showed clear excitonic transitions from three samples with the lowest energy heavy hole transition, (n=1hh), at 1.06, 1.3 and 1.55 μm. Recently the same group have reported good electroabsorption characteristics from a 10 period $InAs_{0.41}P_{0.59}$/InP MQW (Hou *et al*

1993). Operating close to 1.3μm, clear demonstration of the quantum confined Stark effect (QCSE) (Miller *et al* 1985) could be seen. In comparison with the InGaAsP/InP and InGaAlAs/InAlAs structures, commonly used at these wavelengths, a larger Stark shift of the n=1hh exciton was found (Hou *et al* 1993). This larger shift, for a given applied field, was attributed to a smaller valence band discontinuity in the $InAs_{0.41}P_{0.59}$/InP device.

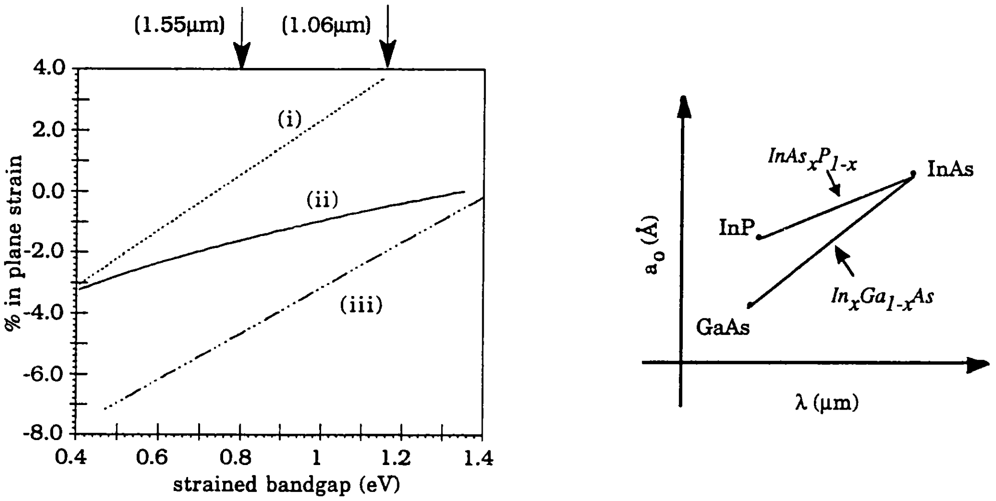

(a) (b)

Figure 5-1. *(a) Calculated in-plane strain against strained bulk band gap for: (i)* $In_xGa_{1-x}As$ *on InP. (ii)* $InAs_xP_{1-x}$ *on InP. (iii)* $In_xGa_{1-x}As$ *on GaAs. (in all cases x is varied from 0 to 1). (b) Schematic showing the lattice constants with wavelength range for the materials studied here.*

The question of band offsets in this system was first addressed by Schneider and Wessels (1991). Low temperature optical emission was investigated from single QW samples grown by Metal Organic Chemical Vapour Deposition (MOCVD). The arsenic composition was kept nominally at 67% as the well width varied from ~2 monolayers to 80Å (Schneider and Wessels 1989). Using a parabolic model and including strain induced band edge shifts, band offset parameters of 75:25 were found to best fit the experimental results. Further evidence for a large conduction band offset has recently come from experimental studies on MOCVD grown buried heterostructure laser diodes, employing $InAs_{0.43}P_{0.57}$ as the active medium (Yamamoto *et al* 1994). The structures, designed to emit around 1.3μm, showed a remarkable high temperature performance. Continuous wave (CW) lasing was confirmed up to 132°C with a threshold current of 22.8 mA. The authors suggested the high temperature characteristics were a result of the large conduction band offset in the system, reducing the carrier overflow at high operating temperatures.

Despite the relative immaturity of the system, the limited body of work using $InAs_xP_{1-x}$ QW structures has already made a considerable impact. The main aim of the present work was to investigate $InAs_xP_{1-x}$ /InP MQW devices operating around 1μm. Beginning the project, it was apparent that growth of such structures had not been attempted by conventional (solid source) Molecular Beam Epitaxy (MBE). Since the structures contained phosphorus, it was suggested that growth by conventional MBE would be difficult, while GS-MBE, CBE and MOCVD could all grow this material (Woodward *et al* 1991). Working in collaboration with Sheffield University, we were able to demonstrate, for the first time, growth of InAsP/InP MQWs by conventional MBE (David *et al* 1993, David *et al* 1995). In addition, although an InAsP/InP device operating around 1μm had been experimentally demonstrated (Woodward *et al* 1991), there had been few theoretical studies on the system around 1μm.

Before these results are presented, it will be useful to briefly summarise work appearing in the literature concerning MQW devices operating around 1μm.

§5.1.1 Operation around 1.06 μm.

Optoelectronic devices operating around this wavelength are desirable because of the increasing availability of compact and efficient neodymium based solid state lasers, (eg. Nd:YLF, Nd:YAG). Proposed applications have ranged from constructing digital photonic logic planes for use in parallel optical processing (Woodward *et al* 1991, Goodhill *et al* 1994), to producing short mode-locked pulses for electro-optic spectroscopy applications (see eg. Loh *et al* 1993). Previously, MQW modulators operating around this wavelength have been demonstrated in GaAs-based $In_xGa_{1-x}As$/GaAs (Woodward *et al* 1990), and InP-based $InAs_xP_{1-x}$/InP, $InAs_xP_{1-x}$/$In_vGa_{1-v}P$ and $In_vGa_{1-v}As_xP_{1-x}$/InP (Woodward *et al* 1992). With the exception of the latter quaternary case, all the other structures have one (or two) of the constituent layers strained with respect to the substrate. Considering the GaAs-based system, as already noted, when growth is directly on GaAs, the degree of compressive strain in the well layer can reach ~2%. From a structural point of view, the maximum single layer thickness of the well material lies between 50-100Å (Matthews and Blakeslee 1974), above this relaxation occurs via dislocations. Turning to the $InAs_xP_{1-x}$/InP system, since the degree of strain is somewhat less (<1%), the single layer critical thickness is larger (cf. Fig.2-7a). In this sense, structures with well widths up to ~100Å may be envisaged, confident that the individual layers will remain largely coherent. For MQW structures in both systems the cumulative strain will be an issue, leading to some degree of relaxation (cf. §2.4); although it is reasonable to expect for a given number of periods, any detrimental effects of relaxation would be less in the InP based structure. This is supported from a straightforward comparison between similar 50 period $In_xGa_{1-x}As/GaAs$ (on GaAs) and $InAs_xP_{1-x}/InP$ (on InP) MQW structures (Woodward *et al* 1991). The InP based structure demonstrated a much sharper defined exciton with the peak absorption some 25% higher than the GaAs based device. The higher peak absorption is expected, given the strong dependence of peak absorption on exciton linewidth (cf. §4.4.3). [note: Strictly speaking, there may also be differences in the oscillator strengths (ie. excitonic area) between the structures]. The increase in broadening with relaxation is a feature that has been consistently observed in a number of publications, including the present work (eg. Woodward *et al* 1990, Ghisoni *et al* 1994). Comparing GaAs and InP based structures, Woodward and co-workers (1991), found that non-uniform strain relaxation was higher in the GaAs structure, and was therefore proposed as a significant broadening mechanism.

Attempts to improve GaAs-based structures have often employed a thick (relaxed) $In_vGa_{1-v}As$ buffer layer ($v<x$) before growing the p-i(MQW)-n epilayers. The constituent layers making up the MQW are strained with respect to the $In_vGa_{1-v}As$ buffer, ie. $In_xGa_{1-x}As$ (wells) are under compression while the GaAs (barriers) are under tension. By using the buffer layer not only is the strain in the well layers less than for growth directly on GaAs, but providing both the compositions and dimensions are correctly chosen (cf. (2.4)), the MQW structure can have a *net* zero strain. Structures with these characteristics are often referred to as strain balanced (see eg. Cunningham *et al* 1992, Woodward *et al* 1992). Recently, a device operating around 1.05μm, using this principle demonstrated a ~2.5 meV reduction in exciton linewidth over a structure not having a buffer layer (Goodwill *et al* 1994).

Strain balanced structures have also been demonstrated in InP-based structures operating around 1μm (Woodward *et al* 1992, Chiu *et al* 1993). The QW system is $InAs_xP_{1-x}/In_vGa_{1-v}P$ but, unlike the GaAs case, it does not require the growth of a buffer layer. The $InAs_xP_{1-x}$ (well) is under compressive strain with respect to InP while, the $In_vGa_{1-v}P$ (barrier) is under tension. Room temperature absorption spectra were presented along with comparisons of $InAs_xP_{1-x}/InP$ and $In_vGa_{1-v}As_xP_{1-x}/InP$ MQWs (Woodward *et al* 1992). Although the quaternary system was lattice matched, the authors found that both the ternary systems gave better overall performance in terms of exciton peak resolution. The room temperature half width half maximum (HWHM) of the quaternary structure was almost twice that of the strain-balanced structure (13 meV and 7 meV respectively). The InAsP/InP structure presented had a HWHM of 9 meV, although it was noted that previous samples grown by the authors had achieved HWHM of

6meV. Overall, the strain balanced sample produced the best electroabsorption characteristics, and demonstrated a clear QCSE on application of an electric field. However, it should also be noted that the InGaP material has a larger band gap than InP, which provides greater potential confinement, thereby aiding the retention of the exciton peak under an applied field (Pezeshki *et al* 1991).

The study made by Woodward and co-workers was interesting, and certainly suggested a natural direction in which the present work could go if MQW relaxation became an issue (§5.4). However, obtaining good quality InAsP/InP MQW structures by conventional MBE was our main concern.

§5.1.2 Modelling parameters: initial considerations.

Prior to theoretically investigating QW structures, bulk material parameters for the constituent layers must be found. The Landolt-Börnstein compilations generally provide a good source of bulk parameters for III-V semiconductors, including some alloy compounds (Landolt-Börnstein 1982, 1986). Unless otherwise stated, the parameters used for the present modelling (see Appendix A) were obtained from these sources. For most cases a simple linear interpolation between the two binary values was used for InAsP parameters. Notable exceptions were the bulk band gap and spin-orbit splitting where experimentally determined expressions were used (Nicholas *et al* 1979).

Initial investigations into the QW system, were often hampered by the lack of reliable experimental results. While structures were clearly being demonstrated, there was little detailed characterization of the samples which would help to 'fine tune' both bulk and QW parameters. For example, in the case of the band gap deformation parameter for InP (which describes the hydrostatic band gap shift, cf. 3.33), at least two values were listed (Landolt-Börnstein 1986). Furthermore, using experimental values for the band gap dependence with pressure (cf. Appendix A), yielded even more possible values. [note: InAs parameters were typically better characterized because of the large amount of published work on InGaAs QW structures. In addition I have had some involvement with well characterized InGaAs/AlGaAs strained QW structures (Ghisoni *et al* 1994, Hart *et al* 1995). The majority of InAs parameters used for InAsP modelling were established from this work.] The effect of different InP deformation gaps on the dominant subband energies at zero field, is illustrated in Fig.5-2. In addition, the dependence of the QW parameter, the heavy hole valence band offset, is shown (Fig.5-2a).

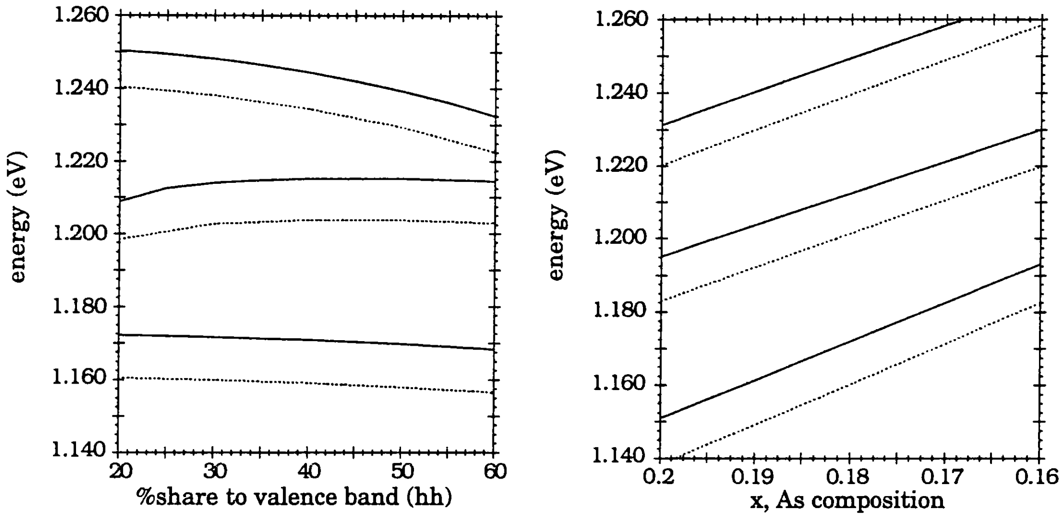

(a) (b)

Figure 5-2. *Calculated subband energies, e1hh1, e1lh1 and e2hh2 (increasing in energy) for an 100Å* $InAs_xP_{1-x}/InP$ *QW. (Solid) using InP* a_{gap}*=-8.6 eV. (Dotted) using InP* a_{gap}*=-5.68 eV. (a) structure with 18% arsenic for varying heavy hole valence band offset share of the total confinement energy. (b) subbands for a 100Å well width showing the effect of a ±2% variation in arsenic composition.*

The two deformation gaps used for Fig.5-2 represent the outer limits of the values obtained for InP (Landolt-Börnstein 1986). The lower transition energies predicted using a smaller deformation potential are consistent with the smaller strained bulk band gap that results (cf. 3.33). For all the above subbands, the difference is ~11 meV which corresponds to ~11 nm at these energies. The arsenic composition dependence can be appreciated by considering the difference between the bulk band gaps of InP and InAs, which is approximately 1 eV. To a first approximation, a linear interpolation between these values suggests a change in the ternary band gap of 10 meV for a 1% variation. This is approximately what is found from Fig. 5-2b. Just considering these two parameters, the deformation potential and the composition, it becomes clear how difficult it is to 'fine tune' a set of parameters from incomplete experimental results. For example, a transition from nominally a 100Å QW may be seen at 1.171 eV, which could be fitted with the larger deformation potential and 18% arsenic or assuming 17% arsenic with the smaller deformation potential. Even when higher transitions are visible, the situation is still not clear, although for a coherently accommodated strain, the lowest energy heavy and light hole splitting is a sensitive measure of arsenic composition (cf. §2.2.2).

At present, the parameters listed in Appendix A, represent our best 'calibrated' set.

They appear to give the best agreement with the available published results and our own structures. The relative insensitivity of the $\Delta n = 0$ transitions, in a symmetric QW, to the offset parameters is well known, particularly for the lowest energy transition (Kopf *et al* 1992). Recording the higher energy transitions can reduce the uncertainties, cf. energy transition of e2hh2 in Fig.5-2a. However given the variations in material parameters and recognizing the limitations of the present model for higher transition energies and binding energy values, accurately determining the offsets can still prove ambiguous in square QW structures. Throughout the following work, I have used the parameters 75:25 first suggested by Schneider and Wessels (1991).

§5.2 Preliminary Structures.

§5.2.1 Growth and Fabrication.

Samples were grown by Dr. Mark Hopkinson at Sheffield University in a conventional (solid source) MBE chamber. For photocurrent measurements, the p-i-n wafers were processed (by G.Hill and M.Pate, Sheffield University) into diode mesa structures. Additional processing for absorption measurements was carried out by A. Rivers, K. Lee and D. Prescott, University College London.

The MBE technique for growing epitaxial layers is briefly outlined here, more detailed discussions, particularly on the growth of QW structures, can be found in the literature (see for eg. Tsang 1984, Joyce 1985). With this method, the substrate is held in a high vacuum while molecular or atomic beams of the constituents fall upon its surface. The rates at which these atomic beams strike the surface can be closely controlled, allowing growth of very high quality layers. For the growth of InAsP layers, the In, As, and P components, along with the dopants, are stored and heated in separate cells. Abrupt changes in crystal composition (eg. the ratio of As in InAsP) can be obtained by controlling shutters in front of the cells. With typical growth rates of ~1μm/hr, the control of the shutters can allow compositional changes on the scale of the lattice constant. The conditions for the structures investigated here follow, further details are found in David *et al* (1993) (and David *et al* 1995). Growth was carried out in a VG V80H MBE system equipped with all solid sources. These included, Indium, Arsenic, Phosphorus, Beryllium (p-type dopant), Silicon (n-type dopant). Elemental arsenic and phosphorus (As_4, P_4) are cracked to As_2 and P_2 in a high temperature zone operating at 950°C. Conditions were typical of those for high quality InP growth, ie. substrate temperature ~480°C and P_2/In ratio ~5. Arsenic incorporation approached unity efficiency for mole fractions below 0.7. Hence the growth of $InAs_xP_{1-x}$/InP QW structures was carried out by simply opening and closing the arsenic shutter during InP growth. All of the devices were grown on (100) n^+ InP substrates and had the same basic p-i-n diode structure: 0.2µm n^+ ($1x10^{18}cm^{-3}$) InP buffer layer was followed by an undoped spacer of 0.05 or 0.1µm InP. Next the MQW active region was grown and then a 0.1µm undoped spacer before deposition of the p^+ ($5x10^{17}cm^{-3}$) contact layer, typically 0.5µm.

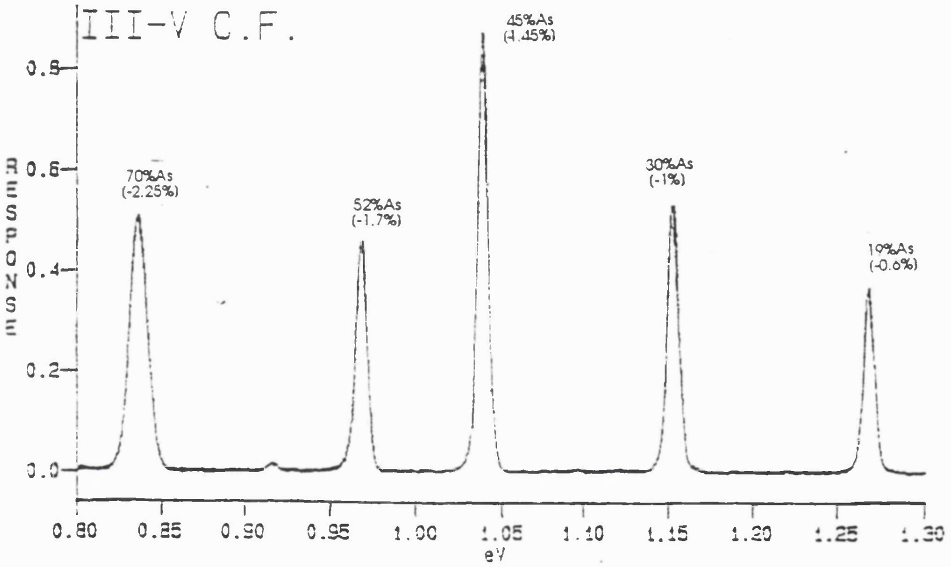

Figure 5-3. *Low temperature (10K) photoluminescence from a sample containing 5 single 40Å* $InAs_xP_{1-x}$*/InP QW. [Measurement by Dr. J.P.R David, S.E.R.C Facility at Sheffield University].*

For photocurrent and absorption measurements, the p-i-n samples were fabricated at Sheffield into circular mesa diodes of 100-400µm diameter by wet chemical etching. The bottom n^+ contact was InGe/Au with the samples held in place on a header by gold epoxy. The top p^+ contact of AuZn/Au was an annular ring to allow optical access to the devices, eg. the 400µm mesas often used provided an optical access of 200µm.

It should be noted that the structures presented here were obtained over a period of 2 years, consequently before each request, several calibration samples (not p-i-n) were often undertaken. One of these preliminary samples (M393) comprised five nominally 40Å thick $InAs_xP_{1-x}$ layers, each separated by 530Å of InP. The arsenic composition for each layer varied from 0.7 for the bottom QW (nearest the substrate) to 0.19 for the top QW.

Low temperature (10K) Photoluminescense carried out at Sheffield (by Dr. J.P.R David) demonstrates the wide range of wavelengths attainable in the system (Fig.5-3).

§5.2.2 Characterization.

Structural characterization.

High-resolution X-ray diffraction (HRXRD) was carried out on several of the p-i-n wafers. Dr. L. Hart, at the Interdisciplinary Research Centre for Semiconductor Materials (IRC-SM) based at Imperial College, was chiefly responsible for the measurements and interpretation. The HRXRD machine was a Philips HR1880 high resolution diffractometer which allowed both 004 and 115 rocking curve reflections to be obtained. For structures grown on (001) surfaces, interpreting these measurements provides information on the lattice parameters (perpendicular and parallel) in the structure. In addition to the HRXRD measurements, Transmission Electron Microscopy (TEM) images were obtained for selected samples, from Sheffield and by Dr. Xiao Mei Zhang at the IRC-SM. Direct imaging of the layers through TEM allowed the dimensions of the well and barrier to be found and observe any dislocations present in the MQW region (to a resolution of $\sim 10^7$ cm^{-2} (X.M. Zhang, private communication).

Electrical characterization.

Current-Voltage (I-V) measurements on unbonded p-i-n mesas were routinely made at Sheffield (by Dr. J.P.R. David). The same measurements were repeated at UCL on structures bonded to headers prior to photocurrent measurements. In general, I found no significant differences in the electrical characteristics between bonded or unbounded devices. The doping level in the intrinsic region of the diodes was calculated from Capacitance-Voltage (C-V) measurements carried out at Sheffield.

Optical characterization.

Photocurrent measurements on all the samples were carried out at UCL. The experimental apparatus essentially comprises of a 100W quartz halogen lamp as the source, which passes through a grating monochromator before being focused onto the device. A power supply unit provides the applied field across the device and a lock-in amplifier measures the photogenerated voltage across a 120kΩ resistor which is in series with the device. The whole system is computer controlled which allows photocurrent spectra at various applied fields to be taken quite routinely. Photocurrent spectra give a good indication to the absorption present in the device and can be related to the absorption coefficient (Whitehead *et al* 1988a, M. Whitehead 1990). For selected samples, transmission measurements at zero applied field were undertaken to extract the absorption coefficient. The measurement set up was similar to that used in photocurrent, with the lock-in now reading from a germanium detector which is used to measure the transmitted light through the sample. At least, two scans are carried out for each sample. One detecting the transmitted light through the epilayer and substrate (i.e. the wafer), and the other through just the substrate (i.e. the epilayer removed). The absorption coefficient for the epilayer can be expressed as (M. Whitehead, 1990)

$$\alpha = -\frac{1}{d} \ln\left(\frac{T_{total}}{T_{sub}}\right) \tag{5.1}$$

where d is the total absorbing length, T_{total} and T_{sub} are the transmission through the sample (i.e. epilayer+substrate) and substrate respectively.

§5.2.3 Initial p-i(MQW)-n results.

For the first attempted growth of $InAs_xP_{1-x}$/InP p-i-n MQW structures we decided on three structures. In each sample, the total absorbing length (i.e. the well/barrier widths and no. of periods) was designed to be the same, but the group V composition (and hence strain) in each sample would be varied. The nominal well/barrier widths were 100Å/150Å and were repeated 50 times making up the MQW region.

Table 5-1. *Optical results from the three $InAs_xP_{1-x}/InP$ structures. (photocurrent spectra subject to ±0.5nm)*

sample	%As in well	R.T n=1hh peak (μm)	R.T n=1hh HWHM (meV)	10K PL FWHM (meV)
M395	16.94[a]	1.060	6.5	6.8
M396	20[b]	1.092	9.2	7.6
M397	24.68[a]	1.137	9.5	8.5

[a] calculated assuming the TEM well/barrier ratio (see §5.2.4)
[b] estimated value from modelling, ±0.5%

The arsenic compositions were chosen from earlier calibration runs on SQW which would place the room temperature lowest energy e1hh1 exciton (n=1hh) for each sample around 1-1.1 μm. Calculations suggested that for structures operating around these wavelengths, the arsenic compositions should be less than 30%, with the well layers needing to accommodate less than 1% compressive strain. This was borne out by the results from HR-XRD performed on the samples (Table 5-1). Photocurrent spectra, at zero applied field, from the three samples is shown in Fig.5-4a. For each sample, a clear n=1hh transition is seen, which, as expected, increases in wavelength with increasing arsenic composition (Table 5-1).

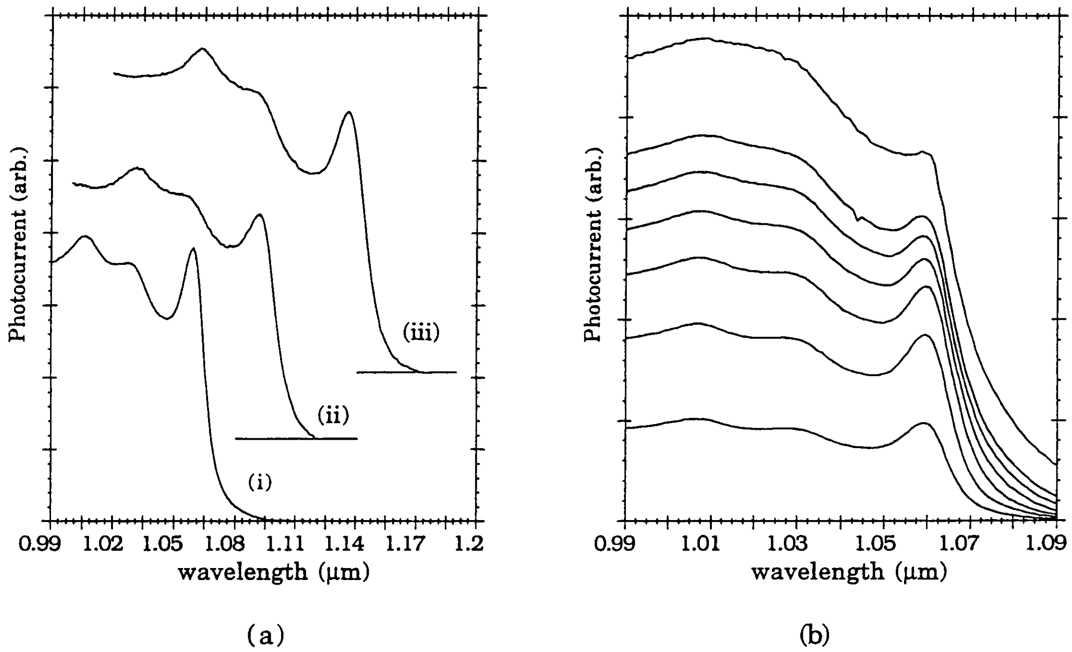

Figure 5-4. *Room temperature photocurrent from InAs$_x$ P$_{1-x}$/InP MQW samples grown by MBE. (a) zero applied field spectra of (i) M395 (ii) M396 and (iii) M397 samples. (b) Photocurrent response of M395 for applied reverse biases of 0,1,2,3,4,5 and 10 V (see text).*

Also evident is the corresponding increase in half-width half maximum (HWHM) of each peak (Table 5-1) as the arsenic increased. A similar trend was also observed in the emission from the 10K photoluminescence from the samples (David *et al* 1993). The full-width half maximum values (FWHM) are reproduced in Table 5-1. Similar observations have been noted for samples grown by CBE (Chiu *et al* 1993). We note that for their sample operating at ~1.13μm (similar to M397), the HWHM is 11 meV. In agreement with much of the previous work, the increase in broadening was attributed to an increasing density of misfit dislocations in samples with larger arsenic compositions.

In addition to the n=1hh transition, two higher transitions for each sample are present. The modelling of these structures (presented later §5.2.4), assigns these as e1lh1 (n=1lh) and e2hh2 (n=2hh), for decreasing (increasing) wavelengths (energies) from the n=1hh peak. It can be seen from Fig.5-4a, the light hole transition is not very pronounced. Given that the offsets are in favour of the conduction band, and the fact that compressive strain will shift the light hole band edge further towards the valence band edge of the barrier. A likely explanation is that the light hole is not strongly localised in the well region, due to the small potential confinement and the lighter mass.

The photocurrent spectra in Fig.5-4b, show the effect of an an increasing applied electric field. The carrier concentration in the intrinsic region of the diodes was estimated from C-V measurements to be 2~4 x10^{16} cm^{-3}. The effect of this rather high background doping can be appreciated by solving the usual diode equations, via Poisson's equation (see for eg. Sze 1981, chp.2). Assuming a built in field of 1.3V (approximately the band gap of InP) and 2 x10^{16} cm^{-3}, we find at zero applied field only around 13% of the nominal intrinsic region experiences an electric field. For increasing reverse bias, the electric field gradually extends across the intrinsic region, increasing the fraction of photogenerated carriers which reach the contacts (ie. increasing the diodes quantum efficiency). The spectra in Fig.5-4b, clearly demonstrate this, with the overall photocurrent increasing with increasing bias. The expected Stark shift of the n=1hh peak is not clear, and is mainly dominated by broadening, which can be attributed to the large electric field variation across the wells, due to the high carrier concentration.

Despite the poor diode characteristics from this early set, clear room temperature excitons had been observed. These preliminary results were the first reported attempt to grow this QW system by conventional MBE (David *et al* 1993, Stavrinou *et al* 1993). The high carrier concentration in the intrinsic region was put down to the use of an inferior Phosphorus source in the MBE kit (M.Hopkinson, private communication). This was eventually replaced, and with the new source, intrinsic region concentrations were typically an order of magnitude lower. Consequently, the later structures exhibited a much better photocurrent response with applied field (§5.3.2).

§5.2.4 Calculations based on HRXRD and TEM results.

Using both HRXRD and TEM carried out on the samples (M395, M397), allowed investigations into the structural nature of the devices. Knowledge of the arsenic composition was important both from a growth and modelling point of view. In addition, given the large number of periods in these samples the question of relaxation could also be addressed.

The use of HRXRD on QW and MQW structures is well documented (see for eg. Quillec *et al* 1984, Fewster 1993). Although the present section is not intended to be a detailed study into the use of HRXRD, it is useful to demonstrate the governing factors which determine the composition in the well material. This information can be valuable when considering published work dealing with strained layer MQW structures. It is shown that determining the arsenic composition in the well layers relies not only on good knowledge of the well/barrier width ratio, but also on the type of X-ray reflections used in the experiment. Calculations of the excitonic positions using the various well widths and composition values found are compared with experimental results.

The HRXRD results that are considered are distinguished by the types of reflections used in the experiment. In the first case, (I), compositions are derived from only considering 004 reflection curves, while for the second case, (II), both 004 and 115 reflections are considered. Depending on the reflections used, a value of the *average* arsenic composition throughout the structure can be found from the measurements. In the case of $InAs_xP_{1-x}/InP$ QWs, the percentage arsenic in the well material is determined by

$$x = x_{av}\left(\frac{l_w + l_b}{l_w}\right) \tag{5.2}$$

where l_w and l_b are the well and barrier width respectively, and x_{av} is the average arsenic composition (%) throughout the structure. In what follows the term in brackets will be referred to as the QW ratio and denoted by r_i, with i indicating either nominal ratio or measured (from TEM) ratio. A summary of the structure dimensions and corresponding ratios are listed in Table 5-2. Also included is the measured X-ray period of the structure (ie. l_w+l_b), determined from the 004 reflections.

Table 5-2. *Sample details on the dimensions of the three* $InAs_x\,P_{1-x}/InP$ *structures.*

sample	nominal l_w/l_b(Å)	TEM l_w/l_b(Å)	r_{nom}	r_{TEM}	HRXRD period (Å)
M395	100/150	107/141	2.50	2.32	273
M396	100/150	108/147	2.50	2.36	/
M397	100/150	105/146	2.50	2.39	270

Plan view TEM and corner cleaved cross-sections from the samples indicated no dislocations or defects present in the MQW layers with high contrast and sharp interfaces seen between the InAsP and InP layers. From HRXRD, the 004 reflections from both M395 and M397, showed well resolved satellite peaks, indicative of a good MQW structure. The interpretation of the peaks was aided by simulation spectra based on dynamical X-ray theory (see eg. Fewster and Curling 1987), The measured average arsenic compositions from the two structures (Tables 5-3, 5-4) were arrived at using this technique.

Comparing Cases I and II, it is seen that, for a given QW ratio, significant differences can be found for the measured average composition of a structure [note: the average composition is *measured* in that it is calculated from measured values of the lattice constants in the structure]. The cause of these variations can be put down to the fact that both structures appear to exhibit some degree of relaxation. That is, the measured in-plane lattice constant ($a_{\|}$) is not the same as the InP substrate (5.8696Å), which would be expected for coherent growth (cf. §2.2). From the two types of reflections considered, only those from the 115 direction can provide any information about the in-plane lattice constant. The average values measured from 004 reflections alone (Table 5-3), assume the structure to be coherent. In constructing an equivalent cubic layer to determine the composition, the in-plane dimensions are therefore taken to be InP. For a relaxed structure this is not true and compositions from 004 reflections alone will always provide a lower limit to the actual arsenic composition. However, if a structure is coherent, then the same average composition would be determined for either case I or II.

Often in the literature, only reflections from 004 are considered when authors quote structure details for strained MQW samples (Woodward *et al* 1991, Hou and Tu 1992, Yamamoto *et al* 1994).

Table 5-3. *Case I: Determination of arsenic composition from 004 reflections only*

sample	average % As	calc. % As (from r_{nom})	calc % As (from r_{TEM})
M395	5.965	14.91	13.84
M397	7.412	18.53	17.71

Table 5-4. *Case II: Determination of structural properties and arsenic composition using both 004 and 115 reflections.*

sample	measured a_z (Å)	measured $a_\parallel$ (Å)	average % As	calc. % As (from r_{nom})	calc. % As (from r_{TEM})
M395	5.8933	5.8742	7.309	18.28	16.94
M397	5.8990	5.8804	10.327	25.82	24.68

Since the TEM imaging showed no dislocations in the MQW region, the relaxation present in these samples is thought to arise from dislocations at the interface, between the start of the MQW region and the buffer region (cf. §2.4). With this description, the MQW region is itself coherent and has the same in-plane lattice constant throughout. The constituent layers are therefore strained with respect to one another, so the InP barriers are experiencing some tensile strain, while the InAsP layer is under compressive strain (Fig. 5-5). To include this in the modelling, I use the measured $a_\parallel$ from Table 5-4 as the lattice constant the QW layers deform to. The main effects of relaxation are reductions in both the strained band gap between the conduction-heavy hole band edges, and in the heavy-light hole band edge splitting for the well material. The slight reduction in band gap would cause the n=1hh transition to appear at lower energies (longer wavelengths) than if the structure was coherent, (cf. Fig.5-14). For M397, the reduction in strained band gap is ~5meV (~5 nm) although a slightly larger change occurs in the valence band edge splitting between the heavy- and light-hole, ie. ~7 meV (~7 nm). The experimental splitting of the n=1hh and n=1lh transitions would be larger than the band edge splitting, since quantum confinement effects are also present. However by considering the experimental splitting, n=1|hh-lh|, the dependence on the band gap (and related parameters) can be removed.

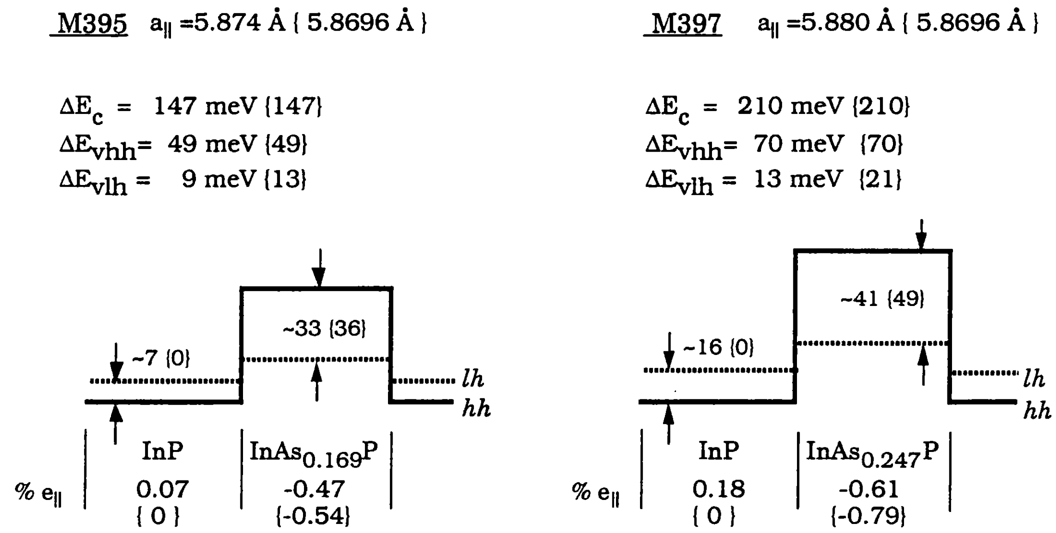

Figure 5-5. *Schematic of the potential energy profile from samples M395, and M396, solid (dotted) lines indicate the heavy- (light-) hole profiles. Unless indicated, all numbers are in meV, those in { } represent the values obtained in the coherent case. Arsenic compositions are taken from Table 5-4, and the offset parameters of 75:25 are used.*

It should be clear that, given the type of characterization performed on the samples, a number of possible compositions and well widths can be obtained. Determining the composition in the well material from (5.2) indicates another possible source for uncertainty. This time, for a given average composition, the two QW ratios used can produce up to a 1% discrepancy in composition. It would be useful to compare calculated excitonic transitions from these possibilities with those found experimentally. Those deduced from the case II data in Table 5-4, ie. 004 and 115 reflections, are expected to best represent the actual structure. However, the calculations will also consider those deduced from Table 5-3, ie. just 004 reflections. At the very least this highlights how comparing modelled and experimental transitions, from this limited data, can suggest relaxation has taken place.

Calculations of the excitonic transitions at zero applied field, are found out using the zero field model (§4.2.2). Strictly speaking, because of the built in field of the diode, some of the wells will experience an electric field. However due to the small confinement energy, the higher order transitions visible in the photocurrent spectra (Fig.5-4a), are expected to rapidly ionise for applied fields. As they are clearly visible, it is assumed that the majority of the photocurrent is from the wells experiencing little or no field. Moreover, no blue shift of the n=1hh exciton was observed from the recorded photocurrent spectra of M395 with +0.5V applied. The well widths used in the calculations are deduced from the measured HRXRD period using both the QW ratios given in Table 5-2. In addition the well widths measured directly from TEM are considered. For each case and sample, a structure is deduced using the following measurements:

(a) r_{nom} applied to average arsenic and HRXRD period.
(b) r_{TEM} applied to average arsenic and HRXRD period
(c) r_{TEM} applied to average arsenic and TEM period.

Finally, for case I, the in-plane lattice constant is taken to be that of InP while for case II, the measured value of $a_{\parallel}$ (Table 5-4) is used.

Table 5-5. *Calculations of excitonic transition energies and separations for the structures deduced from the case I results.*

sample	case	structure ($\%As/L_w$)	n=1hh (eV)	n=1|hh-lh| (meV)	n=2hh-1hh (meV)
M395	I(a)	14.90/109Å	1.1942	34.5	65.7
	I(b)	13.81/118Å	1.2031	32.5	57.0
	I(c)	13.81/107Å	1.2061	32.4	64.6
M397	I(a)	18.52/109Å	1.1555	40.5	69.4
	I(b)	17.73/113Å	1.1626	39.5	65.7
	I(c)	17.73/105Å	1.1652	39.4	72.4

Table 5-6. *Calculations of excitonic transition energies and separations for the structures deduced from the case II results. For each sample, the in-plane lattice constant of MQW is taken from Table. 5-4.*

sample	case	structure ($\%As/L_w$)	n=1hh (eV)	n=1|hh-lh| (meV)	n=2hh-1hh (meV)
M395	II(a)	18.28/109Å	1.1561	36.5	70.8
	II(b)	16.94/118Å	1.1673	34.1	61.3
	II(c)	16.94/107Å	1.1706	34.0	69.8
M397	II(a)	25.82/109Å	1.0751	44.3	79.7
	II(b)	24.82/113Å	1.0849	42.4	73.7
	II(c)	24.82/105Å	1.0879	42.3	81.7

In comparing the results, (Tables 5-5 and 5-6), it is clear that using the compositions from 004 reflections alone, significantly overestimates the predicted n=1hh transition (~30 meV for M395, ~70 meV for M397). With the benefit of the 115 reflections, this is seen to result from underestimating the arsenic composition in the structures. In contrast, the calculated n=1hh transitions in Table 5-6 show very good agreement with experimental positions. It is useful to compare the difference in predicted arsenic composition of M395 and M397, with the difference in n=1hh transitions. Experimentally, we find ~80meV separation between the n=1hh transitions, compared to ~4% difference (case I) and ~8% difference (case II) in the predicted arsenic compositions. Earlier considerations (§ 5.1.3) had suggested a change of 1% arsenic yields ~10 meV shift in energy, which is consistent with the findings here. In this respect, relaxation could have been suggested simply by considering the average arsenic values obtained from the 004 reflections.

Table 5-7. *Experimental transition energies and splitting for M395, M396 and M397.*

sample	n=1hh (eV) (±0.5 meV)	n=1|hh-lh| (meV)	n=2hh-1hh (meV)
M395	1.169	37.3±1.2	62.3±1.2
M396	1.135	39.9±1.8	66.5±1.2
M397	1.089	45.6±1.8	74.0±1.2

Staying with the results from Table 5-6, the predicted heavy- to light- hole transition separation is seen to be slightly less than is measured (Table 5-7). The discrepancy could certainly be accounted for in the calculated binding energies, considering the reasons already noted in §4.4. Another possible source of error is the breakdown of the strong confinement approximation (SCA), mainly in calculating the light hole transition. As illustrated in figure 5-5, the strain splitting in the valence band leaves the light hole potential well fairly shallow, and comparable with binding energy values; a situation which contravenes the SCA. With the SCA no longer valid, the result is the Coulomb potential significantly contributes to the confinement potential, effecting the confined states and binding energies. Wu and Nurmikko (1988), demonstrated that for shallow valence band confinement in II-VI systems, the Coulomb potential has a large contribution to the valence band states. The overall effect, increased the potential confinement for the state over that given by the 'bare' material potential difference. This resulted in an increase in binding energy and a decrease of the transition energy in comparison with calculations adopting the SCA. It would not be unreasonable to expect similar effects in the InAsP/InP system, given the band offset parameters and arsenic compositions used here. In this case, the measured splitting would be larger than that calculated, which is the situation found for all of the results in Table 5-6.

These points aside, the modelling using the structures deduced from the combined 004/115 reflections and TEM ratios gave the best agreement with experiment.

§5.3 Devices around 1.06 μm: Further Investigation.

The present section details further experimental and theoretical work on structures designed to operate around 1.06 μm. Although this had been the overall aim of the InAsP/InP work, the initial problems with background doping in p-i-n diodes had to be overcome. The cause of this, the original phosphorus cell was eventually replaced with a higher purity one. Several intermediate MQW samples were grown (not presented here), which showed considerably better applied field responses, although the arsenic compositions were generally >25% (estimated from modelling).

§5.3.1 Fixed wavelength design.

Varying both the width and arsenic composition in the $InAs_xP_{1-x}$ well material, a range of accessible wavelengths, covered by the zero field e1hh1 (n=1hh) excitonic transition, can be found (see Fig.5-6a). As expected, for a given well width, increasing the arsenic composition shifts the n=1hh peak to longer wavelengths, ie. the effective band gap of the QW structure decreases. In the adjacent plot, (Fig.5-6b), the same data is displayed in a different format. Here, the curves demonstrate how a fixed n=1hh peak wavelength may be achieved using different well width and arsenic composition (illustrated with wavelengths corresponding to Nd:YLF (1.047 μm) and Nd:YAG (1.064 μm) lasers). For the arsenic values displayed in Fig.5-6b, the in-plane strain (w.r.t InP) is less than 1%. Taking a conservative, 100Å% estimate for the single layer critical thickness (cf. Fig.2-7a), the range of well widths and compositions considered in Fig.5-6b are clearly within this condition. The multilayer critical thickness will be discussed in §5.3.4.

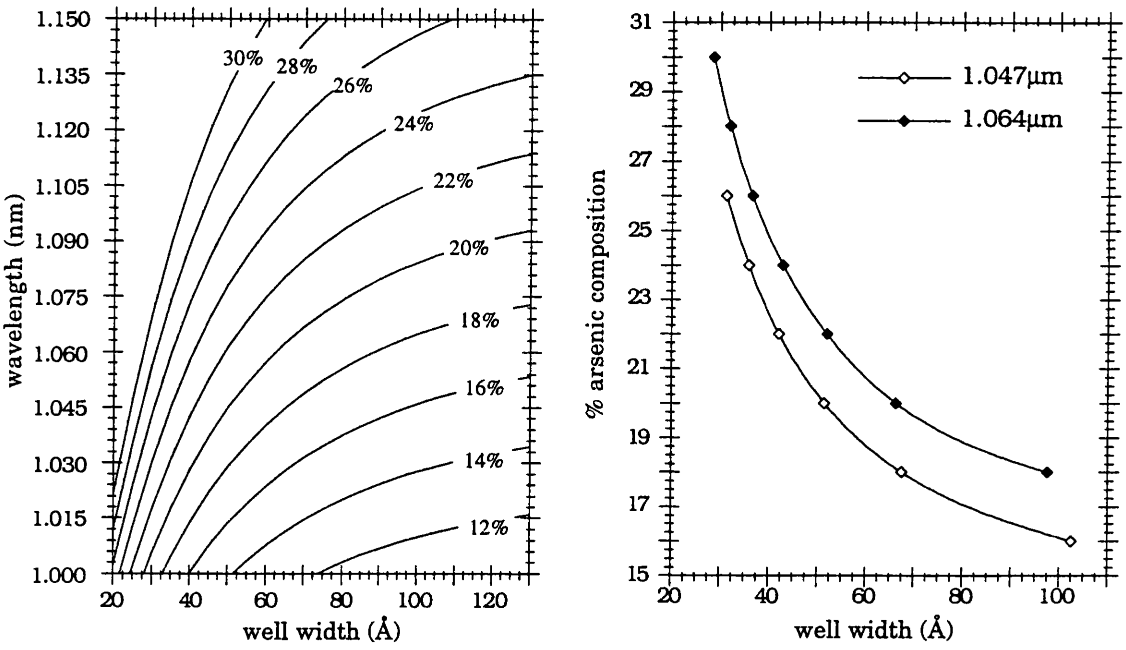

(a) (b)

Figure 5-6. *Calculations of the zero field e1hh1 excitonic transition (n=1hh), in $InAs_xP_{1-x}/InP$ QW structures. The band offset parameters 75:25 are used throughout.*

Previous theoretical and experimental work on GaAs/AlGaAs structures has demonstrated the well width significantly effects the QCSE in QW structures (see for eg. Bastard *et al* 1983, Brum and Bastard 1985, Whitehead *et al* 1988b). It should be emphasised, that in these works, the n=1hh peak occurred at different wavelengths, since GaAs was the well material. For the present strained case, I have carried out similar investigations *but* with the n=1hh peaks of the structures occurring at the same wavelength. For the following work, two device structures are chosen; [(i)] 98Å $InAs_{0.18}P_{0.82}$ and [(ii)] 58Å $InAs_{0.21}P_{0.79}$, with a zero field n=1hh peak wavelength at 1.064 μm.

Under the effects of an applied electric field, differences between the two structures are immediately evident (Fig.5-7). For the wide well structure, [(i)], the n=1hh transition shift per unit field is much larger than that for the narrow well (Fig.5-7a). Essentially, the lower lying states in the wider well are more strongly perturbed by the change in potential. A useful quantity to show is the calculated squared overlap integral for applied field between the ground electron and heavy hole state, which closely follows the change in excitonic peak absorption (cf. 4.77). For an applied field, the narrow QW is seen to retain a larger overlap than the wide QW, (Fig.5-7b); a feature due to the smaller induced spatial separation of the states in the well (Bastard *et al* 1983). Experimental studies have shown that the implied trends are observed (Whitehead *et al* 1988b). The exciton absorption peaks in narrow QW maintain their shape but shift slowly, while larger well width structures rapidly lose their peak heights as field is applied.

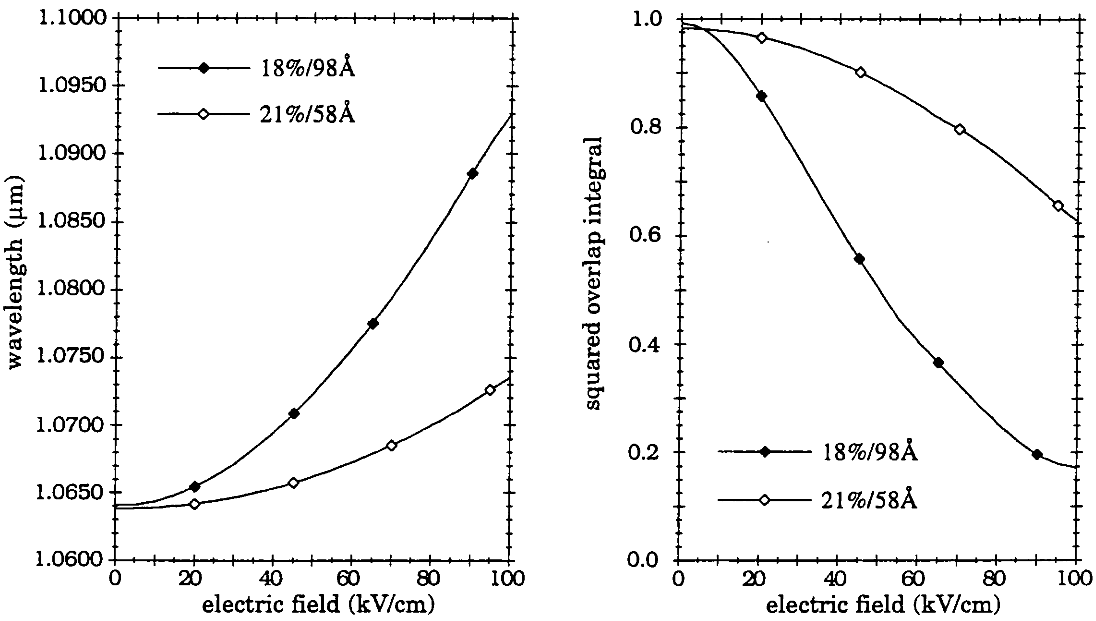

(a) (b)

Figure 5-7. *Applied electric field calculations for two* $InAs_xP_{1-x}/InP$ *QW structures. (a) The red shift in wavelength of the n=1hh exciton transition (b) The decrease in squared overlap integral between the e1 and hh1 states, representing the decrease in n=1hh peak absorption.*

The squared overlap integral calculations with field, (Fig.5-7b), show the relative peak decrease (relative to the zero field peak), but they fail to demonstrate how the structures are related to each other in terms of absolute absorption. However, calculating the area of the exciton peak, from (4.82), can lead towards absolute values of the peak absorption coefficients. In Fig.5-8a, the calculated areas covering the range of 1.064 μm structures are presented, along with a scaled $1/l_w$ plot. It should be remembered that for a given well width the arsenic composition is different (cf. Fig.5-6b). Despite this, the calculated areas are seen to follow the $1/l_w$ dependence, a relationship first suggested from experimental and theoretical studies on GaAs QWs (Masumoto *et al* 1985, Masselink *et al* 1985). The increase in calculated area for narrow wells is a result of the shrinkage of the exciton wavefunction (Masumoto *et al* 1985). The resulting smaller in-plane radius (and hence larger binding energy) implies a higher probability of finding the electron and hole in the same position (cf. 4.63, 4.72). Extracting the peak absorption coefficient for a given structure, is accomplished by multiplying the area by $2/\pi\Gamma$, where Γ is the FWHM of a Lorentzian function (cf. §4.4.3 and 4.78). In this case for a given linewidth, the peak absorption coefficient for the narrow well structure, [(ii)], will clearly be higher since the area is larger. In fact, assuming a $\frac{1}{l_w}$ dependence, then the ratio of the two peak absorption values is given by the inverse ratio of the respective well widths; although, in practice many of the broadening mechanisms also show a well width dependence (see for eg. G Bastard 1988 chp. 7, J Singh 1993 chp. 16).

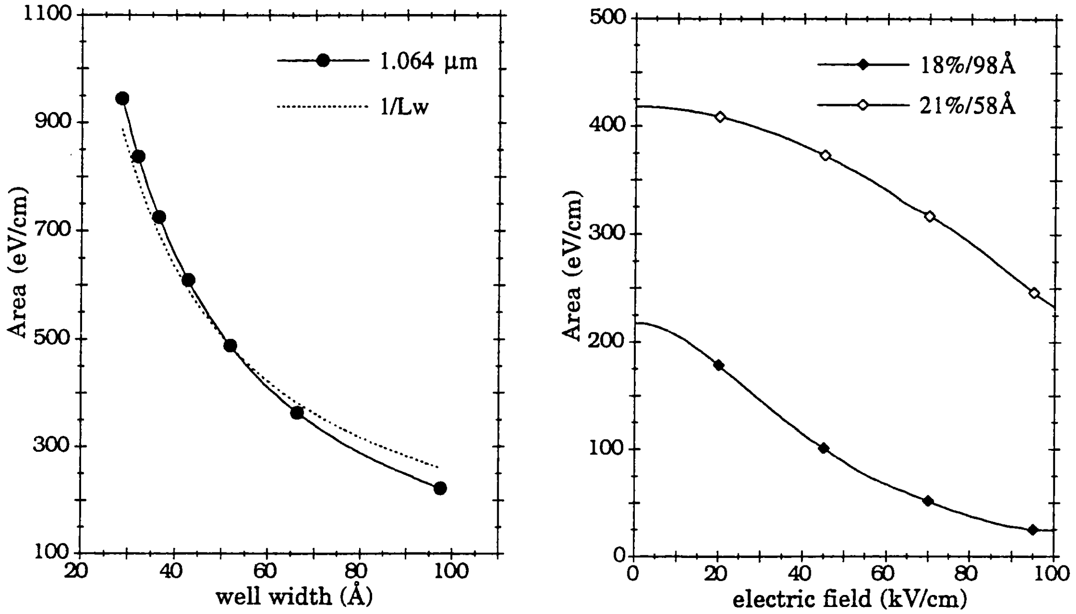

(a) (b)

Figure 5-8. *(a) The calculated integrated area of the n=1hh exciton for the fixed wavelength structures shown in Fig.5-5b. Also shown a scaled $1/l_w$ line. (b) The calculated reduction in n=1hh integrated area with field of two samples discussed in the text (cf. Fig. 5-7).*

The spectra are calculated up to applied fields of 85 kV/cm, beyond 100 kV/cm both the heavy and light hole states fluctuated in value, rather than following a smooth linear increase (cf. Fig.5-7). For these applied fields the linewidths from the TRM calculations (§4.3) were above 10^{-3} eV, which are at least an order of magnitude higher than values found in other systems (Miller *et al* 1985, P.J Stevens 1989). Presumably the states could no longer be considered as quasi-bound. The TRM linewidths, which are inversely related to the lifetime of the state, were seen to increase rapidly with applied field. This mainly concerned the valence band, and was to be expected given the small valence band potential confinement found using the offset parameters 75:25. Experimental studies by Woodward and co-workers (1990), found rapid broadening of the n=1hh exciton as field was applied, and above 100 kV/cm there was virtually no evidence of the exciton. They suggested that field ionization is a dominant cause of the broadening, noting the small confinement potential of the system would facilitate this. Similar arguments have been used to explain the electro-absorption spectra of shallow GaAs QW (Goossen *et al* 1990).

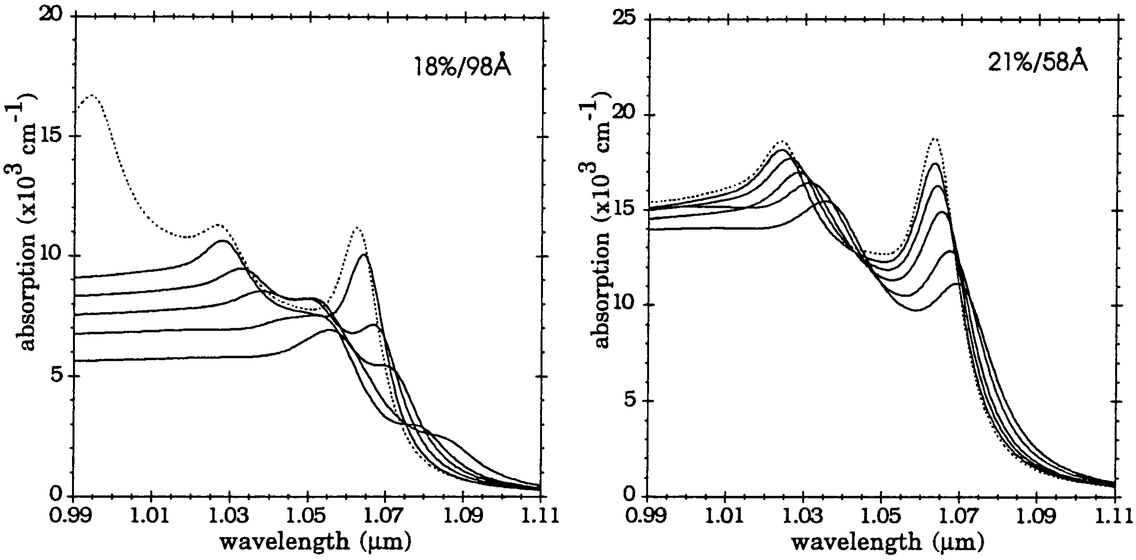

(a) (b)

Figure 5-9 *Calculated electroabsorption spectra for the two structures previously discussed. The dotted line corresponds to the zero field spectra, solid lines are for applied fields of 15, 35, 50, 75 and 85 kV/cm. (see text for further details on spectra).*

Some comments regarding the construction of the spectra are made in preparation for a later comparison with experiment.

(i) The linewidths (HWHM) used for the zero field spectra (dotted lines) are; 7.5 [8], 10 [10] and 10 [10] meV for n=1hh, n=1lh and n=2hh for (a)[(b)]. The n=1hh linewidths correspond to those measured for the real devices (in the next section). The others are arbitrarily chosen to produce realistic spectra, but are expected to be larger since the overlap (and hence confinement) of these states is smaller.

(ii) Electric field induced broadening of all the transitions was included. The linewidths from the TRM calculations were not used, since these are quite small for the fields considered. Furthermore there does not appear to be a consistent method in view of how to include them (Miller *et al* 1986). Broadening due to the background doping was included according to the method of Stevens *et al* (1988), which gives a non-uniform electric field across the MQW.

The line width of the resonance is given as $\Gamma^{el,m} = \Gamma^{el,m}(0) + \Gamma^{el,m}(F, l_w)$, with

$$\Gamma^{el,m}(F, l_w) = \frac{\partial E_{ex}^{el,m}(F, l_w)}{\partial F} \Delta F \tag{5.4}$$

where the excitonic transition energy at a given applied field is $E_{ex}^{el,m}(F, l_w)$, and $\Delta F = {}^{eN_i L_{MQW}}\!/_{\varepsilon}$ where N_i is the intrinsic region doping and L_{MQW} is the total MQW length. For both spectra, a field variation of 20 kV/cm was used which corresponds to a background doping level of 2×10^{15} cm^{-3} over 0.7 μm.

(iii) I found it necessary to include the transition e1hh2 (particularly for the wide well). The rapid decrease in the strength of the n=1hh transition is mostly transferred to the e1hh2 transition which subsequently increases with field. In Fig.5-9(a), this occurs just behind the zero field n=1hh transition and is responsible for the 'pinning' of the absorption at these wavelengths. The growth of forbidden transitions is well understood in relation to the electro-absorption sum rules given by Miller *et al* (1986).

§5.3.2 Experimental Results.

To investigate the results from the previous section, growth of the two *example* structures was requested. From the superlattice calculations, (§4.2.1), a barrier width of 100Å in both structures would keep the coupling of the first electron level <0.3meV. In the valence band, the heavy hole coupling was <0.05meV while for the light hole, the coupling was ~2-5 meV. This demonstrated that despite the small valence band offset, i.e. 25%, the barrier width chosen should be sufficient to treat the n=1hh transition as uncoupled, especially if the built-in field of the diode is considered. The nominal details appear in Table 5-8.

Table 5-8. *Nominal structure details of the two $InAs_x\,P_{1-x}/InP$ MQW p-i-n samples.*

sample	% As in well	well/barrier thickness (Å)	no. of periods	QW ratio (r_{nom})
M737	18.0	98/100	30	2.02
M738	21.0	58/100	30	2.72

Using double polished unprocessed parts of the wafers, the absorption spectra were measured. This typically involved taking an average of five scans to minimise noise in the spectra. The measured transition energies from the wafers used for absorption evaluation were compared to those found from the photocurrent measurements. Typically across the areas examined (10x15 mm), variations of ±2 nm were found in the variation in arsenic composition. The results presented in Figures 5-10 and 5-11, are converted photocurrent spectra using absorption spectra taken across the same range (Whitehead *et al* 1988b, M. Whitehead 1990).

Table 5-9. *Tabulated results from the absorption spectra shown Figure (5-10).*

sample	n=1hh (nm)	HWHM of n=1hh (meV)	peak absorption α_{well} (cm^{-1})	product $\alpha_{well}l_w$
M737	1.069	7.5	11105[a]	0.0117[b]
M738	1.056	8	18344[a]	0.0110[b]

[a] calculated assuming the nominal ratios in Table 5-8.

[b] the well width is found from the nominal ratios and measured X-ray period in Table 5-11.

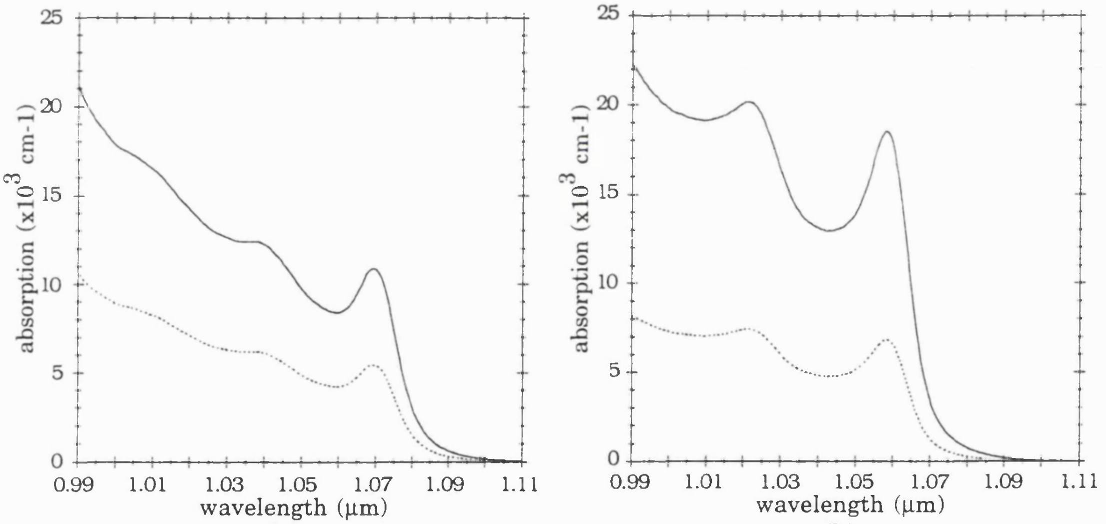

(a) (b)

Figure 5-10. *Zero applied field absorption spectra for (a) M737 (b) M738. Dotted lines indicate the absorption of the device (including the optically 'inert' barriers), Solid lines are extrapolated absorption in the well using the QW ratios in Table 5-8.*

Comparisons with the predicted spectra, (Fig.5-9), show qualitative agreement in terms of the number of transitions visible across the range of wavelengths. As expected, for approximately the same potential confinement, a wider well can support more bound states (G. Bastard 1988). The n=1hh transitions from each sample do not occur at the same wavelength, and are separated by some 13nm. In the following section (§5.3.3), it is demonstrated that the period and arsenic compositions in both samples are larger than requested, and a significant arsenic variation across the wafers is indicated.

The HWHM of the n=1hh peak in both samples is similar, and in this case it is interesting to note the product of the peak absorption and well width (Table.5-9). The oscillator strength calculations, leading to excitonic area, in the last section showed that despite the different compositions, the area approximately follows a $\frac{1}{l_w}$ dependence. Since the linewidths are similar, it follows that the product, $\alpha_{well} l_w$, is expected to be comparable in both samples.

Table 5-10. *Electrical characterization results. The intrinsic region doping is calculated from C-V measurements and the applied electric field values giving dark currents ~10nA were carried out on bonded devices at UCL (calculated assuming a 1V built-in field).*

sample	nominal i-region (μm)	i-region doping (cm^{-3})	measured i-region (μm)	electric field at 10nA (kV/cm)
M737	0.744	1-2 $\times 10^{15}$	~0.72	155
M738	0.624	4-5 $\times 10^{15}$	~0.59	190

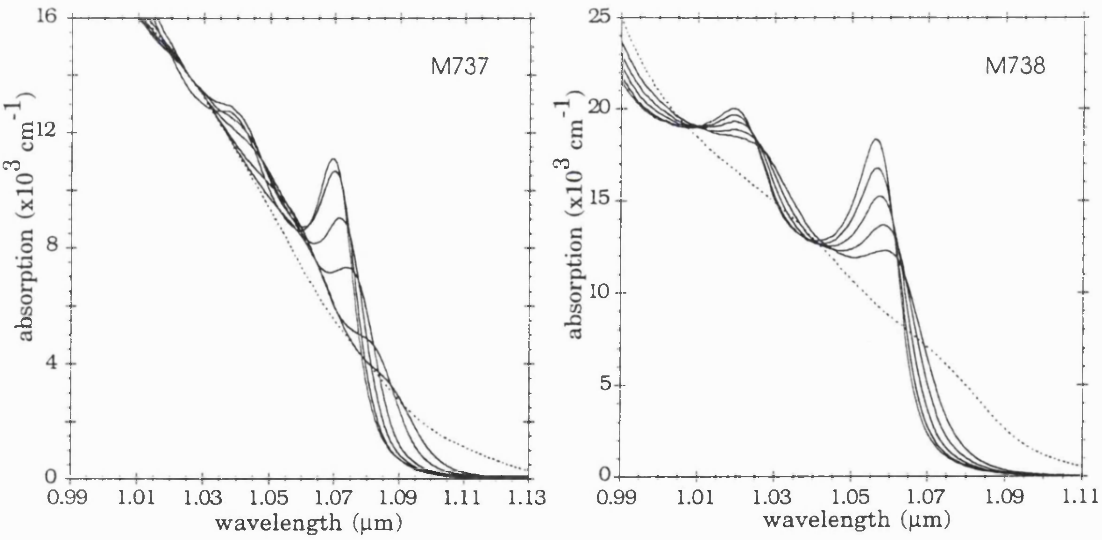

(a) (b)

Figure 5-11. *Observation of the QCSE for the samples (a) M737 (b) M738. The applied field is estimated assuming a 1V built in potential for each sample, the solid lines are fields of ~15 , 35, 50, 70 and 85 kV/cm (cf. Fig.5-9). The dotted line corresponds to 152 kV/cm in (a) and 186 kV/cm for (b). [note the 15 and 35 kV/cm were scaled very slightly to account for the lower quantum efficiency of the diode at low fields. The later photocurrent response curves (Fig.5-13) attest to the small scaling required]*

Since the background doping in the two structures was significantly better than the earlier samples (Table 5-10), the QCSE can be observed for both structures (Fig. 5-11).

The relative decrease in peak height agrees well with the theory; the wider well sample (M737) reducing very quickly with applied field while for M738 the collapse is less dramatic. For both samples, broadening of the exciton feature with applied field is observed and above applied fields of 100 kV/cm the exciton is not clearly visible, presumably due to field ionization (Woodward *et al* 1990). Additional broadening could be attributed to the non-uniform electric field across the wells (estimated from Table 5-10 as 20 kV/cm and 30 kV/cm for M737 and M738 respectively). These two could adequately explain the observed results, although later results (§5.4), suggest that broadening due to strain relaxation in the samples can also play an important role (cf. Fig.5-19).

M737 and M738 differ slightly in arsenic composition from the theoretical examples of §5.3.2. However a comparison between calculated and experimental absorption spectra is still useful, since it appears that it is well width rather than As composition which mainly governs the form of the electro-absorption spectra. The QCSE for both structures is fairly well predicted, the experimental results clearly demonstrate what was expected from theory. For a given field (<100 kV/cm), the narrow quantum well retains the shape and strength of the n=1hh exciton much better than the wider well (compare solid lines in Fig.5-8 and Fig.5-11). The calculated spectra are not as good at shorter wavelengths, in fact they are more representative of the photocurrent spectra in terms of relative height of the n=1hh transition. To some extent this could probably be improved, for example by including the Sommerfeld factor (see for eg. Chemla *et al* 1984, Stevens *et al* 1988). However, I believe the main cause of this discrepancy is the use of a simple in-plane description (ie. the diagonal approximation cf. §4.4.1), particular for the valence band (cf. §4.4.3).

Although by no means optimal structures, some indication as to the performance of the two devices can be undertaken. In figure 5-12, the change in absorption with respect to the zero applied field spectra is presented, ie. $\Delta\alpha(\lambda,F)=\alpha(\lambda,0)-\alpha(\lambda,F)$. The change in absorption is averaged over the measured period (cf. Table 5-11) and so includes the optically 'inert' barrier material. From a device point of view, it is this averaged absorption (or absorption change) that is important.

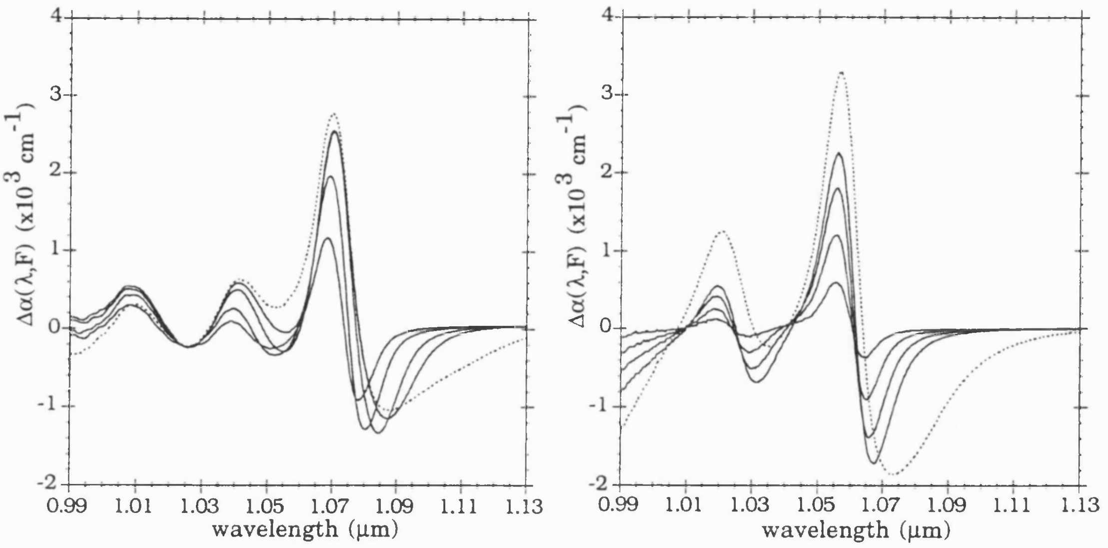

(a)

(b)

Figure 5-12. *Absorption change (including barrier width) with applied field, (a) M737 (b) M738. The solid lines correspond to 35,50,75 and 85 for both samples, dotted lines are for 152kV/cm for (a) and 186kV/cm for (b).*

In both samples, the largest change in absorption, $\Delta\alpha(\lambda,F)$, occurs at the zero field n=1hh peak wavelength. This represents a decrease in absorption as field is applied and so satisfies the requirement for SEED devices (see review by D.A.B Miller 1990). For low applied fields, ie. <100kV/cm, the wider well sample exhibits a slightly larger $\Delta\alpha(\lambda,F)$ at the zero field n=1hh peak (cf. solid lines in Fig.5-12). Moreover, the change at this wavelength does not increase significantly as the field is increased over 100kV/cm. In contrast, in the narrow well $\Delta\alpha(F)$ continues to increase substantially (approx. 50%) as the field increases up to ~180 kV/cm. [for fields >200 kV/cm, the photocurrent spectra for both samples became increasingly noisy]. Similar observations can be made concerning increasing absorption at wavelengths longer than the zero field n=1hh peak. The larger absorption change found in the narrow sample suggests this structure might be better suited to applications which require an increase in absorption at the operating wavelength, eg. in active mode-locking (eg. A.E Siegman 1986).

To my knowledge, the only other results demonstrating the QCSE in InAsP/InP devices around 1μm are the CBE samples of Woodward and co-workers (1990, 1991). The two reported samples contain 50 periods of 100Å/100Å and 90Å/90Å of well and barrier material (hereafter referred to as W1 and W2 respectively). The zero applied field n=1hh transitions are at 1.05 μm (W1) and 1.06 μm (W2). Interestingly, the n=1hh HWHM of these samples is 6 meV (W1) and 9 meV (W2) yet the measured peak absorption appears to be the same in both cases (~12000 cm^{-1}). Sample M737 (Fig.5-11a) with a HWHM of 7.5 meV, is almost identical in terms of the QCSE and peak absorption. This is particularly encouraging since the zero field n=1hh transition for M737 is at 1.07 μm and presumably the sample has more arsenic in the wells leading to a greater misfit/relaxation (cf. §5.4). Using the $\Delta\alpha(\lambda,F)$ results at the n=1hh peak, the projected contrast ratio for M737 (ie. $\exp[\Delta\alpha(F)d]$) for 1μm of material (same as W1), is 1.3 (at 70 kV/cm) and 1.32 (at 152 kV/cm). For 0.9 μm (same as W2), the contrast reduces to 1.26 (at 70 kV/cm) and 1.28 (at 152 kV/cm). These can be compared to the results from Woodward *et al*, which are 1.35 (at 60 kV/cm) and 1.4 (at 160 kV/cm) for W1 (Woodward *et al* 1990), and 1.27 (at 120 kV/cm). The lower values found in the present samples can be mainly attributed to the slightly lower zero applied field peak absorption (which is typically 500 cm^{-1}).

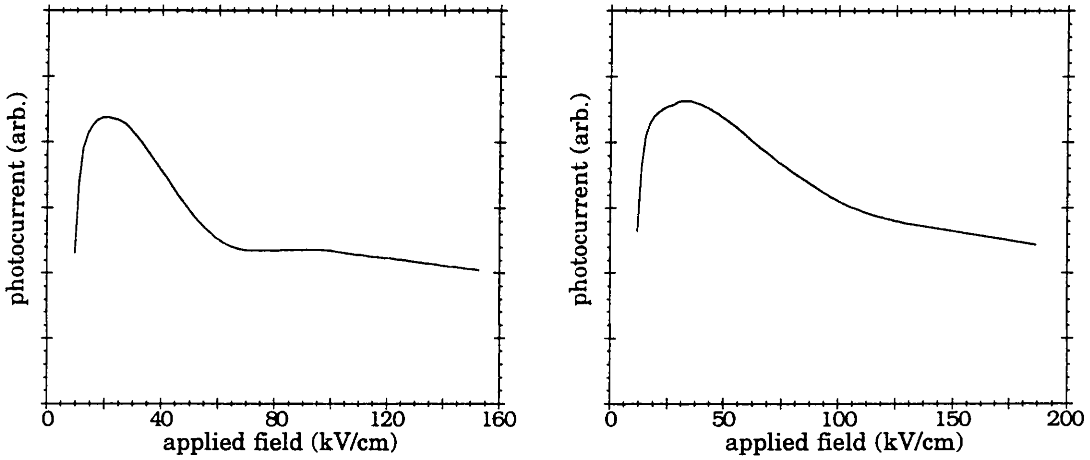

(a) (b)

Figure 5-13. *Photocurrent vs applied field for the two structures (a) M737 at 1.069 μm (b) M738 at 1.056 μm. In both cases the solid line corresponds to the zero applied field n=1hh exciton peak wavelength. These responses demonstrate the good quantum efficiency of the diodes.*

Finally, to illustrate the electrical quality of the diodes, in figure 5-13 the photocurrent against applied field is plotted for both samples at the wavelength of the zero applied field n=1hh transition. At the n=1hh exciton peak wavelength, the negative conductance observed in both samples is due to the QCSE and can therefore explain the difference in negative conductance between the samples (cf. §5.3.1); essentially the rapid reduction in peak height and larger shift with field for the wider well leads to a larger negative conductance.

§5.3.3 Calculations using HRXRD results.

To determine the compositions, HRXRD reflections were performed on parts of the unprocessed wafer from each sample. The fabricated devices were taken from around the centre of the wafer (G.Hill, private communication). For M737, a rectangular piece (~2 x 1 cm) was used in the X-ray study. However, due to the fragmented pieces that were received, it could not be established which part of the wafer this represented. For M738, approximately half of the wafer was still intact, and the X-ray reflections were taken along the side nearest the center, ie. close to the diameter (~5cm). In all, three positions of each wafer were examined along the longest side. For each position, a total of 4 reflections were taken, (004, $00\bar{4}$ and 115, $\bar{1}\,\bar{1}5$), to reduce any effects of tilt or growth misorientation (L.Hart, private communication). The results from the X-ray study are presented in Table 5-10, for each sample, the case (i) represents the results from the centre position of the particular wafer.

Table 5-10. *Summary of HRXRD measurements from M737 and M738.*

sample	measured a_z (Å)	measured $a_{\parallel}$ (Å)	equivalent a_{cubic} (Å)	average % As	measured period (Å)
M737(i)	5.9002	5.8812	5.8901	10.869	210
M737(ii)	5.8984	5.8775	5.8873	9.384	207
M737(iii)	5.8989	5.8786	5.8882	9.835	210
M738(i)	5.8954	5.8753	5.8848	8.029	162
M738(ii)	5.8933	5.8831	5.8879	9.685	164
M738(iii)	5.8953	5.8756	5.8849	8.056	164

The measured periods are slightly larger than those requested, which was also the case with the earlier samples (cf. Table 5-2); although in comparison, the increase is certainly a lot less, ie. typically 2-3 monolayers from the nominal values. The average arsenic composition is found from constructing an equivalent cubic layer from the two measured lattice constants ($a_{\parallel}$ and a_z). [This is listed here since it will be useful for the following discussions on relaxation]. Compared to the nominal average arsenic compositions, which are 8.91% and 7.71% for M737 and M738 respectively (cf. Table 5-8 and eqn.(5.2)), the values measured from the wafers are higher and vary depending on the position on the sample. In addition, measurements of the in-plane lattice constant show some relaxation has occurred in both samples, ie. $a_{||} \neq a_{InP}$ (5.8696Å). In most cases, the variation of $a_{||}$ appears to increase consistently with the increase in average arsenic found. The following section on relaxation, addresses this point in more detail.

In §5.2.4, the importance of the well and barrier widths, or more precisely the ratio (5.2), for determining the arsenic composition in the well layer was demonstrated. Shown in figure (5-13) are the results of the calculated n=1hh, n=1lh and n=2hh excitonic transitions, based on the three arsenic values found from each wafer. For each average arsenic value and period in Table 5-12, a structure is determined by varying the ratio and finding the corresponding well width and well composition using (5.2). As before, the measured in-plane lattice constant (from Table 5-10) defines the strained state for both well and barrier layers. Also for the calculations, I paid particular attention to *lowering* the nominal ratio since this had been suggested by the earlier results (cf. Table 5-2). Indeed for both samples, reducing the ratio does bring the calculated transitions into better agreement with those experimentally observed. The relative separation in transitions is well described although the absolute calculated values are somewhat lower than those observed. The discrepancy is most likely to come from using an incorrect arsenic value. The HRXRD results demonstrate an arsenic variation across the wafer, one possibility is that the actual devices used in the photocurrent measurements have a different composition from those used in the X-ray analysis. The variation in arsenic across the wafer was only brought to light with these samples. Until then it had been assumed that while some variation would be expected towards the edge of the samples, the center would be relatively uniform (M.Hopkinson, private communication). Even more alarming was the degree of variation, particularly for M737. Recalling that the piece used for X-ray was approximately half of the full 2 inch wafer, the reflections taken along the diameter revealed an asymmetric spread of over 4% arsenic (in the well). It was asymmetric in that most of the variation was localised between the center and one edge, ie. the variation from the center to the other edge amounted to ~0.5%.

Since these findings, it has been decided that future work on strained, MQW devices should pay particular attention to which parts of the wafers are being investigated, (cf. §7.1). Although, ironically, one valuable aspect of the arsenic variation across the samples is the increased range of information that has been obtained regarding relaxation in InAsP/InP MQW samples. Although on no account does this form a complete set, these preliminary results do bring to light some interesting features of relaxation in MQW samples.

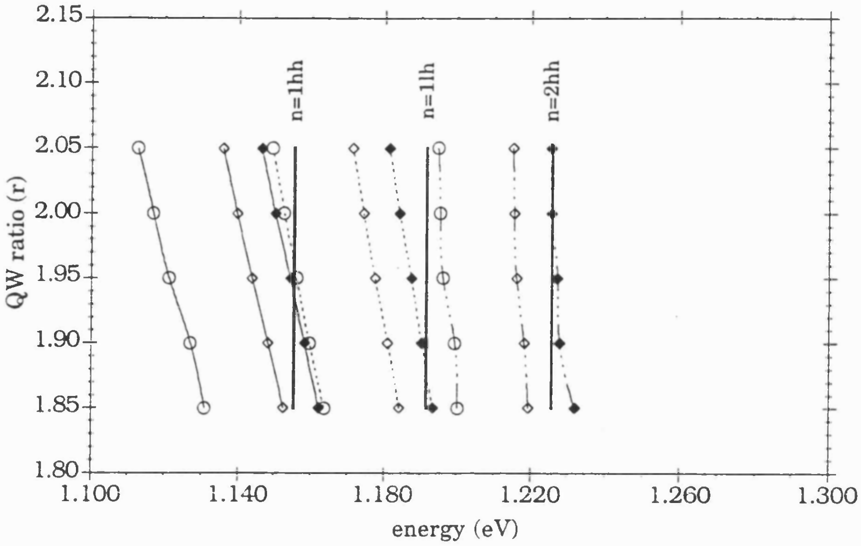

(a)

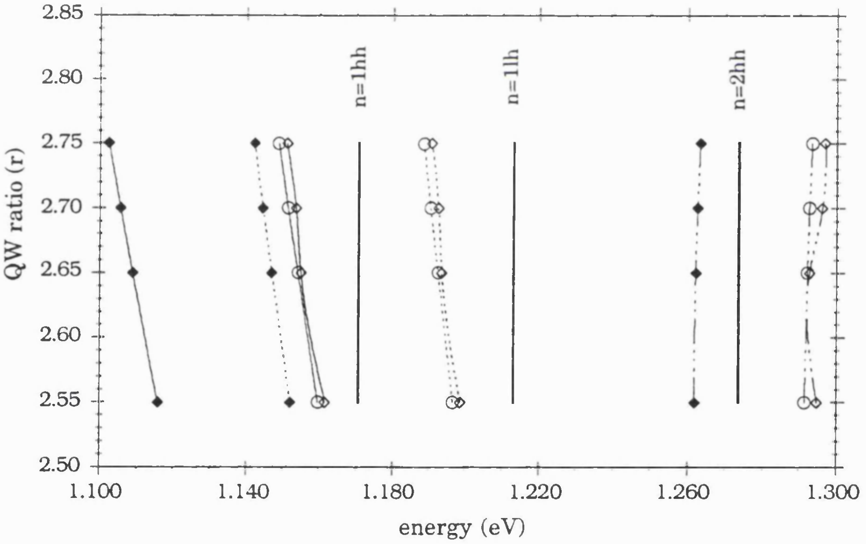

(b)

Figure 5-13. *Comparison of calculated and experimental excitonic transitions for (a) M737 and (b) M738. The vertical lines in both plots are the experimental transitions from the photocurrent spectra. The calculated spectra are labeled n=1hh (solid lines) n=1lh (dotted) and n=2hh (dash-dotted). In addition, structures derived from the three average arsenic values (i),(ii) and (iii) in Table 5-11 are labeled as, (i) open circles, (ii) solid diamonds and (iii) open diamonds. See text for further details on constructing structures, eg. for r=2, M737(i) data gives 105Å/105Å with* $InAs_{0.217}P_{0.783}$ *as the well composition.*

§5.3.4 Relaxation in InAsP/InP MQW Structures.

X-ray diffraction on the samples presented in this chapter, demonstrate some relaxation in the samples has taken place, ie. the measured in-plane lattice constant is not the same as the substrate/barrier, InP (cf. Tables (5-4, 5-10). Despite this, the samples showed good optical and electrical properties with excitonic transitions clearly visible at room temperature. In Chapter 2, (§2.4), two 'popular' relaxation mechanisms were presented (cf. Fig.2.6). In the first, the integrated strain throughout the MQW led to relaxation via dislocations generated at the base of the MQW, ie. forming at the MQW/substrate interface (Fig.2-6a). While for the second case, the individual strained layers are above their critical thickness, and relaxation occurs via dislocations generated at each interface. A key distinction between the two mechanisms is that the internal interfaces of the MQW remain coherent for the first mechanism. For the samples in this chapter, TEM imaging of M395, M396 and M397 showed the MQW layers to be free of dislocations ie. the dislocation density is $<10^7 cm^{-2}$ (X.M. Zhang, private communication). HRXRD from all the samples, revealed between 5 and 8 sharp satellite peaks which is indicative of good MQW structure. Along with the optical measurements, the experimental results from the samples would indicate that relaxation has taken place at the base of the MQW. Moreover, the expected arsenic compositions for all the samples in the well regions are <30%, so that even using the 'conservative' Matthews and Blakeslee model (cf. Fig.2-7a), the well widths used are not expected to exceed the critical thickness.

Establishing that relaxation in the samples is probably by the first mechanism (cf. Fig.2-6a), it is appropriate to recall some further consequences. The in-plane lattice constant in the MQW region, $a_{\|}^{MQW}$, is the same throughout, ie. the interfaces are coherent. However, as relaxation proceeds, $a_{\|}^{MQW}$ tends towards the free standing value, $a_{\|}^{MQW,fs}$ (2.4). This is easily visualized, since in the limit of full relaxation, the MQW is in effect separated from the substrate, ie. the substrate does not influence the layers making up the MQW in any way. As $a_{\|}^{MQW}$ tends towards $a_{\|}^{MQW,fs}$, the strain distribution in the structure changes. For example, in an ideal coherent InAsP/InP structure (Fig.5-14a), for growth on InP only the well layers are required to accommodate the strain, such that $a_{\|}^{MQW} = a_{sub}$. With relaxation, $a_{\|}^{MQW} \rightarrow \bar{a}_{\|}^{MQW}$, which is somewhat between the two limits of no relaxation, a_{sub}, and full relaxation, $a_{\|}^{MQW,fs}$.

$$a_{sub} \leq \bar{a}_{\|}^{MQW} \leq a_{\|}^{MQW,fs} \qquad (5.3)$$

The barrier material (InP), must accommodate some strain to match the in-plane lattice constant, $\bar{a}_{||}^{MQW}$. The increase of strain in the barriers occurs as strain in the well layer reduces, since $\bar{a}_{||}^{MQW} > a_{sub}$, therefore at full relaxation, the structure is essentially strain balanced.

The evolution from ideal coherency to full relaxation is illustrated in figure 5-14. Calculated spectra on the right hand side are for an $InAs_{0.18}P_{0.82}$/InP QW with zero field applied. The three excitonic transitions shown correspond to n=1hh, n=1lh and n=2hh. Broadening values of 12 (5), 24 (10) and 24 (10) meV are used throughout for the FWHM of the peak and associated continuum (in brackets). The aim of the graphs, is to highlight the shift in transition energies one might expect as the degree of relaxation increases. As noted earlier, the separation between the heavy- to light-hole transitions is sensitive to the amount of strain in the well layer. As the strain in the well layer reduces (and increases in the barrier), the separation reduces. However even for full relaxation, there is still some strain in the well layers and hence, an appreciable separation of the heavy and light hole excitonic transitions. This aside, there is an overall shift to longer wavelengths (shorter energies) as the compressive strain in the well decreases. Considering the shift of the n-1hh transition with relaxation illustrates how with some degree of non-uniform relaxation, broadening of the exciton resonance observed in absorption or photocurrent measurements can occur. Throughout all cases, the separation between the two heavy hole transitions (n=1hh, n=2hh), remains approximately constant. The decrease in conduction to heavy hole band gap for the bulk well layer, with decreasing strain, is matched by a similar decrease in the barrier, hence the potential confinement of electron and heavy hole states remains approximately the same. In contrast, the light hole confinement, from an already small value, reduces even further (cf. Fig.5-5).

In the figures, I have deliberately avoided comparing absolute absorption between the three cases, due to the uncertainty in broadening parameters and limitations of the present model. However some comments can be made. Previous studies (eg. Woodward *et al* 1990), and those presented here, consistently demonstrate an increase in FWHM of the n=1hh exciton peak with an increase in relaxation. Therefore for a given oscillator strength, a reduction of the exciton peak absorption would be expected with relaxation, (cf. §4.4.3). However, it can also be stated that with relaxation, the separation between heavy and light hole states reduces, which would have some effect on the valence band in-plane mass, (cf. §2.2.2). For a compressively strained QW, the closer proximity of the first light hole state will typically increase the in-plane heavy hole mass at the top of the valence band. The resulting increase in reduced mass, and decrease in exciton radius, would increase the oscillator strength (§4.4.3). In this case relaxation increases the excitonic area and so for a given linewidth, the peak absorption would increase.

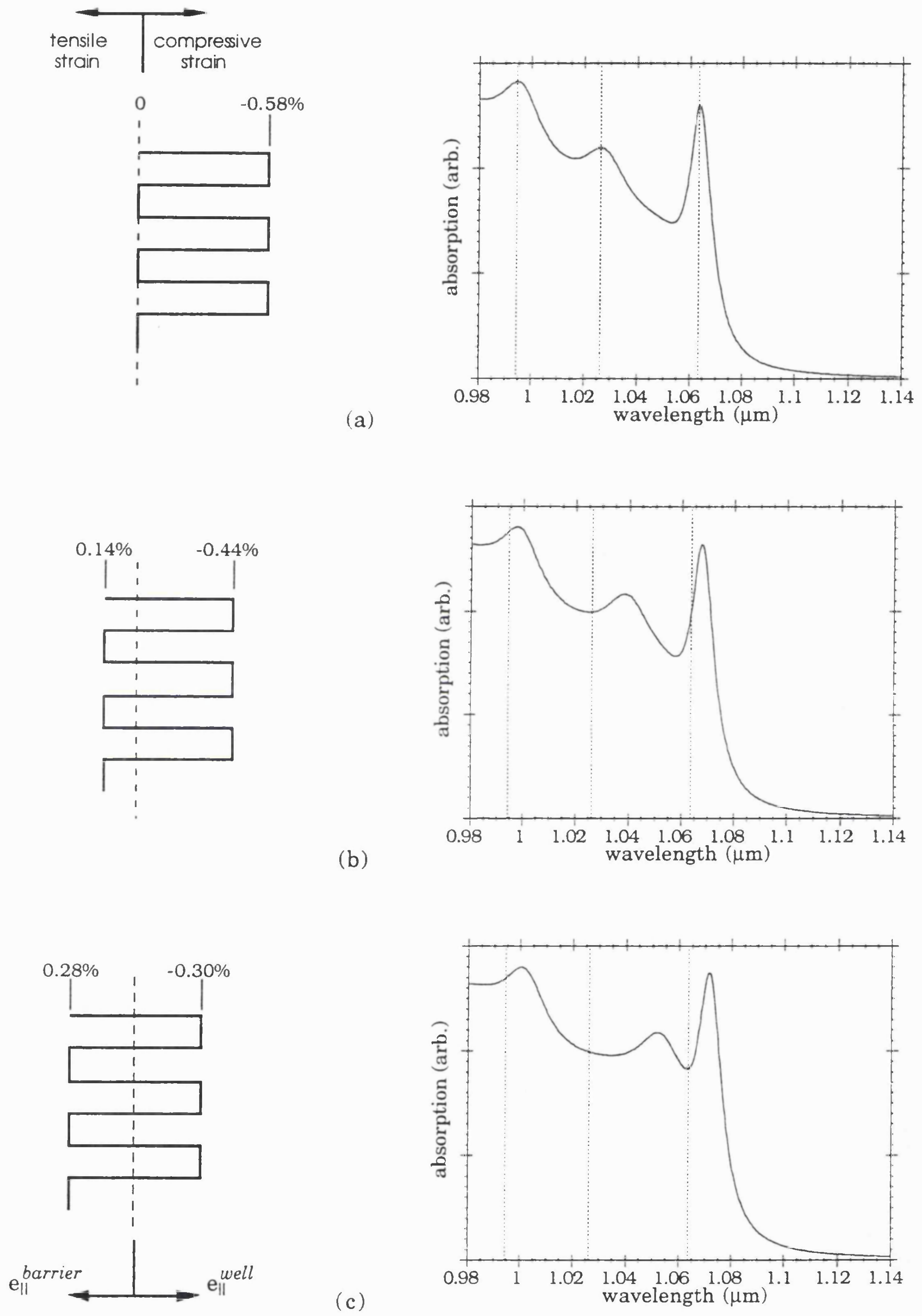

Figure 5-14. *Calculations illustrating the effects of relaxation via the generation of misfit dislocations at the MQW/substrate interface. (a) ideal case, no relaxation* ($\bar{a}_{||}^{MQW} = a_{sub}$)*. (b) 50% relaxation,* ($a_{sub} < \bar{a}_{||}^{MQW} < a_{||}^{MQW,fs}$)*. (c) full relaxation,* ($\bar{a}_{||}^{MQW} = a_{||}^{MQW,fs}$)*. Vertical lines on calculated spectra show n=1hh, n=1lh and n=2hh excitonic transitions from (a).*

To recap, as dislocations are introduced at the base of the MQW, the MQW will relax towards its free standing or equilibrium state. Defining relaxation to be zero for the case in Fig.5-14a, and unity for the case in Fig.5-14c, an intermediate state of relaxation, Fig.5-14b, can be defined as:

$$R = \frac{\left(\bar{a}_{\parallel}^{MQW} - a_{sub}\right)}{\left(a_{\parallel}^{MQW,fs} - a_{sub}\right)} \tag{5.4}$$

Therefore a measure of relaxation is given by the difference in the in-plane lattice constant of the MQW and substrate divided by the difference in the free standing lattice constant and the substrate, ie. this is a measure of how far the MQW has relaxed towards its equilibrium state. This expression is similar to that commonly used in HRXRD analysis on the relaxation of single layers. It has already been noted in §2.4.2, that the free standing lattice constant for the MQW can be shown to be equivalent to the cubic layer value, a_{cubic},which is constructed from the X-ray measurements. [note: It is from the equivalent cubic layer that the average arsenic is determined using Vegard's Law]. Hence, a measure of relaxation can be similarly defined by (M.A.G Haliwell (1990)):

$$R = \frac{\left(\bar{a}_{\parallel}^{MQW} - a_{sub}\right)}{\left(a_{cubic} - a_{sub}\right)} \tag{5.5}$$

The advantage here is that all the parameters are obtained from HRXRD, $\bar{a}_{\parallel}^{MQW}$ is the measured in-plane lattice constant and a_{cubic} is calculated from the measured $\bar{a}_{\parallel}^{MQW}$ and a_z. Using a_{cubic} the uncertainties in the QW ratio, which is required to evaluate (5.4) are avoided. All of the samples so far discussed are listed in Table 5-11 with the relaxation values calculated from (5.5). The total length of the MQW is found by multiplying the measured X-ray period by the number of periods. The calculated misfit (2.16) between the cubic layer and InP substrate is also shown.

Although the structures do not represent a coordinated set designed to specifically investigate MQW relaxation, it is useful to attempt to make some comparisons. By considering the average arsenic in the MQW, ie. over a single period, the different well and barrier widths between the structures are automatically accounted for. In effect we can treat the MQW as a partially relaxed layer, as prescribed in most theories on MQW critical thickness (Hull *et al* 1986, R. People 1986, cf. §2-4).

Table 5-11. *$InAs_x$ P_{1-x}/InP MQW p-i-n samples considered in the present work*

sample	equivalent a_{cubic} (Å)	average % As	%cubic misfit (wrt InP)	MQW length (μm)	%relaxation
M395	5.8834	7.309	0.24	1.365	33.5
M397	5.8892	10.327	0.33	1.350	55.3
M737(i)	5.8901	10.869	0.35	0.630	56.3
M737(ii)	5.8873	9.384	0.30	0.621	44.4
M737(iii)	5.8882	9.835	0.32	0.630	48.2
M738(i)	5.8848	8.029	0.26	0.486	37.5
M738(ii)	5.8879	9.685	0.31	0.492	73.7
M738(iii)	5.8849	8.056	0.26	0.492	39.2

Several interesting points arise, for example when M737(i) and M397 are compared both samples have approximately the same average arsenic in the MQW region and both samples are around 55% relaxed. However the total MQW length of M397 is over *twice* as long that of M737(i). Similarly consider M395, which despite having the thickest MQW region, actually exhibits the least degree of relaxation. These results imply that the total length of the MQW makes little difference to the relaxation. In fact the relaxation appears to depend more on the average arsenic composition, i.e. the misfit with the InP substrate (Fig.5-15). It must be emphasised that without other comparisons between similar structures of different length to infer the universality or this relation may be a little premature, particularly in view of the results from InGaAs/GaAs MQWs on GaAs by Bender and co-workers (1993). Here the authors found that by increasing the number of periods, i.e. 10, 15 and 20, in the samples the relaxation increased. Their relaxation factor was defined with respect to the well layers, eg. M737(i) would be ~29% relaxed in their notation. Apart from the proposed mechanism, which they fail to comment on, a measure of relaxation is only a matter of notation and would not affect the observation of increasing relaxation (factor) for an increasing number of periods (i.e. MQW length). However these results do not necessarily discount the case of M737(i) and M397. For these samples the number of periods is 30 and 50 respectively. A possible explanation is that for a given average arsenic composition above a certain MQW length, an initial relaxation mechanism has proceeded to its maximum, i.e. simply adding more periods does not change the average composition and hence no further relaxation is required for the moment since the structure is stable. The maximum in this case does not correspond to the free standing limit, Fig.5-14c, but rather some point between Fig.5-14b and Fig.5-14c. Taking this picture further, it may be that above some thickness, say 80 periods, the structure will relax again, approaching the free standing limit in stepwise fashion. Of course, with the present set of samples, this can only be viewed as speculation.

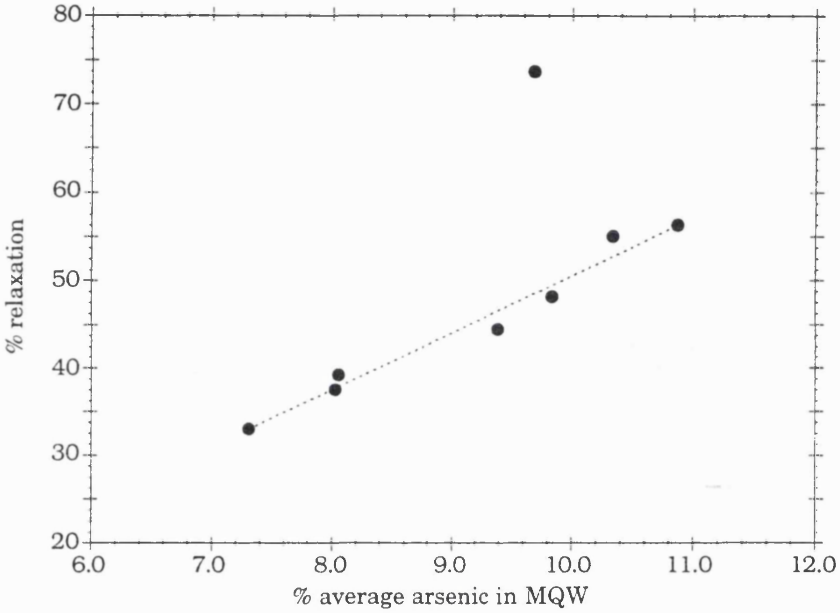

Figure 5-15. *Measured relaxation (defined by (5.5)) against average arsenic composition in the MQW structure. The majority of the results appear to follow a linear relationship, indicated by the straight line.*

So far, the results have been expressed in terms of average arsenic composition, more generally, the above implications can be stated as, increasing relaxation with increasing misfit between the MQW and substrate; the values of which are listed in Table 5-11. For these structures, the misfit strain is proportional to the average arsenic composition, i.e. the arsenic composition averaged over one period. It follows, that by increasing the InP barrier width the average arsenic (and hence misfit) reduces, and from the above arguments the relaxation reduces. As already noted, apart from the expected shift in transition energies with relaxation (cf. Fig.5-14), another factor that seems to be identified with increased relaxation is the increased broadening of the n=1hh exciton peak (Woodward *et al* 1991, Ghisoni *et al* 1994a). This is also observed with the present structures, for example, the HWHM of the n=1hh transition from M395 is ~6.5 meV, while from M737 it measures 7.5 meV. [note: these two structures are chosen because of the similarity of their well widths, since these are also known to effect linewidths.]

Reviewing the salient points mentioned above, for a given well width and well composition, increasing the barrier width reduces misfit strain between the MQW and substrate. From the above results, this suggests the relaxation in the structure reduces and so does the induced broadening of n=1hh transition. For the same excitonic oscillator strength, the expected end result is therefore an increase in the n=1hh excitonic peak absorption (cf. §4.4.3). However, it must be also be recognised that some changes in oscillator strength would be expected, given the sensitivity of the heavy and light hole splitting with relaxation, (Fig.5-14). As already noted with decreasing relaxation, the valence band in-plane mass becomes lighter which ultimately leads to a smaller oscillator strength (cf. §4.4.4). In this sense an interesting question is, would the reduced linewidth (and hence increase in peak absorption) found with reducing strain relaxation, out-weigh the expected increase in oscillator strength (and increase in linewidth) found with increasing relaxation?

The design of future strained MQW devices would clearly benefit from further investigations into MQW strain relaxation (§7.1). For example, some recent work on InGaAs/GaAs structures (on GaAs), with which I have had some involvement, investigated the effect of increasing barrier width while keeping both the well width and composition constant. Three structures comprising twenty periods of nominally 80Å $In_{0.20}Ga_{0.80}As$ wells with 100Å, 200Å and 400Å GaAs barriers were grown (MBE) by Christine Roberts at Imperial College (IRC-SM). The electro-absorption properties for the three structures are shown in Fig.5-16.

The results quite clearly demonstrate an increase in zero field n=1hh peak absorption (for the well material) as the average Indium over one period reduces; the average Indium (and MQW misfit w.r.t GaAs) reduces from Figs.5-16(a) to (c). From HRXRD analysis, the relaxation values for the samples are 56%, 26% and 14% for Figs.5-16 (a), (b) and (c) respectively. Thereby demonstrating that as the misfit w.r.t the substrate over one period reduces, the relaxation of the MQW reduces, which is in agreement with the $InAs_xP_{1-x}$/InP results studied earlier. Furthermore, measurements of the excitonic area, taken at room temperature, indicated an increase in area with relaxation, whichwas also suggested. Although it is worth noting that the decrease in exciton linewidth with reducing relaxation has essentially made up for any decrease in oscillator strength; the improvements in linewidth are therefore the main cause of the higher peak absorption values. With the improved resolution of the peaks a much clearer QCSE is observed. [note: In some respects, the response in Fig.5-16a is similar to that found for M737 , i.e. the reduction in peak height is visible but the shift of the exciton is dominated by broadening (cf. Fig.5-11a)]. However, as noted for Fig.5-10, it is the device absorption which is important. The increase in absorption considering just the well material does not necessarily lead to increased device absorption, which includes the optically inert barrier material. For these devices, it turns out that Fig.5-15a has the larger device absorption, however the improved sharpness of the n=1hh transition between Fig.5-15a and Fig.5-15b, leads to considerable gains in terms of insertion loss and contrast ratio for operation at longer wavelengths than the zero applied field n=1hh transition (Ghisoni *et al* 1994b).

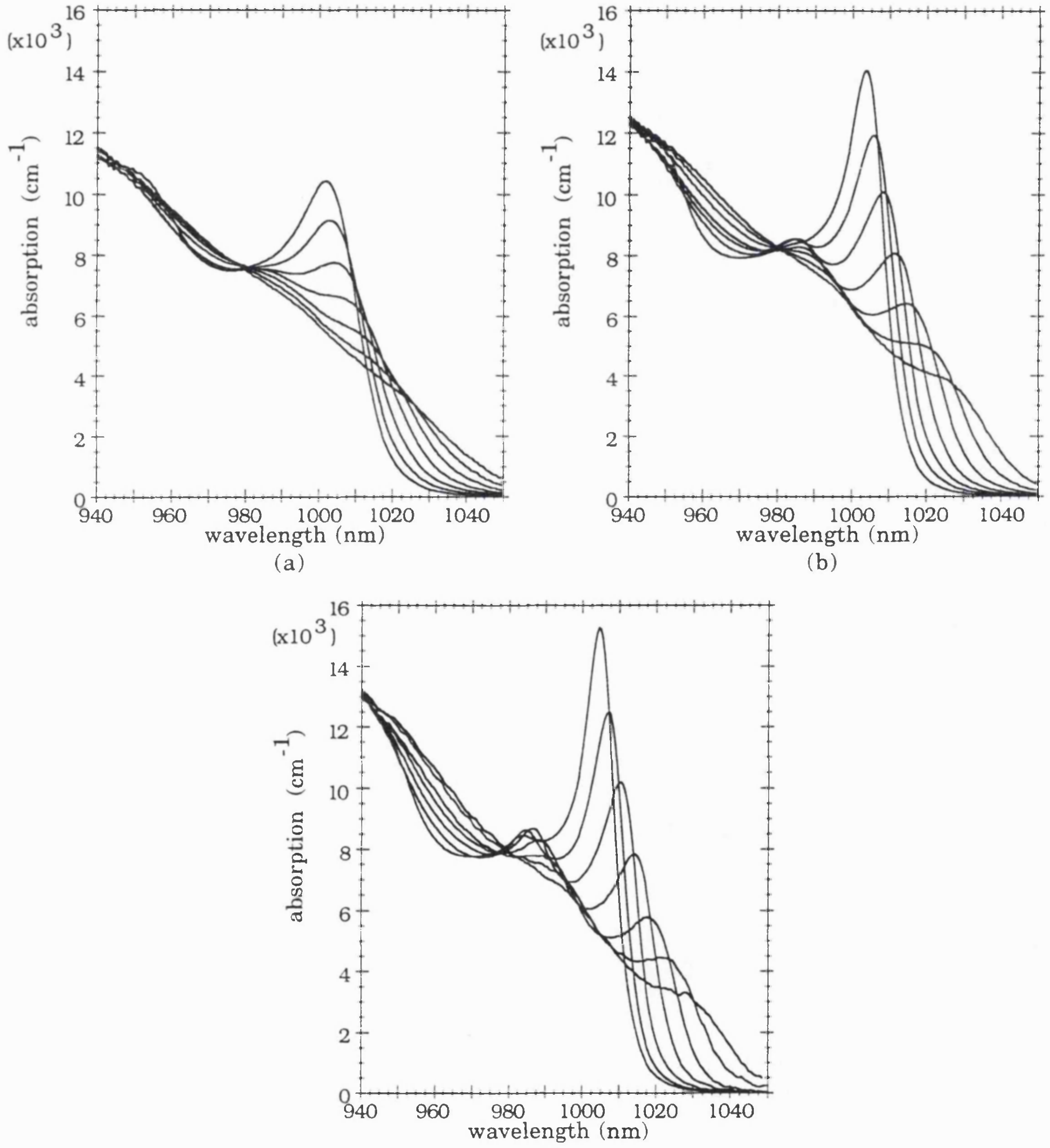

(a)

(b)

(c)

Figure 5-16. *QCSE demonstrated in three twenty period* $In_{0.2}Ga_{0.8}As$ *(80Å) / GaAs p-i-n diodes. (a) using 100Å barriers (b) 200Å barriers (c) 400Å barriers. All the spectra are shown with increasing reverse bias of 0 to -12 V in 2V increments. [measurements by Dr. M. Ghisoni at Oxford (IRC-SM)]*

§5.4 Concluding Remarks.

Above all, this work has demonstrated that $InAs_xP_{1-x}$/InP QW structures can be successfully grown by conventional MBE; structures are at least of comparable quality to those grown by different methods. Use of this material in QW devices is itself relatively new and has already indicated considerable improvements over traditional GaAs and InP based structures operating around 1.06μm and at longer wavelengths (Woodward *et al* 1992, Hou *et al* 1993, Yamamoto *et al* 1994). All of the structures investigated demonstrated clear room temperature excitonic absorption, and with improved MBE solid sources, excellent electrical properties.

On the modelling aspects, it was demonstrated that a main drawback of investigating a new material combination, is the lack of reliable bulk parameters, eg. the deformation potentials. In addition, attempting to calibrate parameters to fit published experimental results, relies heavily on the accuracy of values quoted, particularly the compositions. The majority of published work often determines compositions using X-ray diffraction, however, a straightforward comparative study of X-ray results from partially relaxed InAsP/InP MQW samples, demonstrated how uncertainties in the measured compositions can arise. Using measured QW parameters from X-ray and TEM and accounting for relaxation, the modelling results for the initial structures was shown to predict the measured experimental excitonic transitions reasonably well.

Exploratory calculations using the model, suggested a range of $InAs_xP_{1-x}$/InP QW's samples, differing in well width and composition, could be used to obtain structures operating at the same wavelength. The zero field n=1hh exciton transition and the subsequent electro-absorption characteristics of QW's are known to be strongly dependent on the well width (see eg. Whitehead *et al* 1988). However, the current interest in producing devices that work with neodymium based solid state lasers, requires structures to operate at specific wavelengths. In this sense, by effectively removing the dependence of the well width on the n=1hh transition, devices could chosen for a particular application solely in terms of the electro-absorption characteristics.

As a result of this work, two samples with different well widths and compositions were grown. Experimentally, the electro-absorption characteristics observed agreed well with the theory. The n=1hh exciton peak absorption in the wider well sample rapidly decreased in height as field was applied, while in the narrow well, strong retention of both the shape and height of the n=1hh peak was found. However, the observed n=1hh transitions were not at the same wavelength (~13nm apart). X-ray analysis from several parts of the wafers, revealed the arsenic compositions in both samples was larger

than the nominal values. Moreover, a large variation in arsenic composition across the wafer was evident, the cause of which is not understood at present and was certainly not expected. This has important implications regarding the overall process of obtaining samples and performing characterization (§7.1).
[note: Since the original work here on fixed wavelength design, as part of a IRC-SM project, similar calculations were carried out for InGaAs/GaAs samples. Recently, experimental results from these designs have become available and demonstrate two structures, varying in well width and composition, with zero field n=1hh transitions less than 1nm apart. Electro-absorption responses demonstrate similar results to those presented here (M.Ghisoni, private communication)]

Various degrees of partial relaxation was found in all the MQW samples investigated. Although the good structural and optical properties exhibited suggests this more likely refers to relaxation of the MQW with respect to substrate, ie. the internal structure of the MQW remains coherent. With measurements from X-ray diffraction, the degree of relaxation could be quantified. A surprising result came from comparing two structures with similar average arsenic values (similar misfits) but with different MQW lengths. Despite the difference in length (almost a factor of two), the measured state of relaxation was found to be the same. Typically, a comparison of relaxation in the samples indicated the dominant factor to be the average arsenic composition, ie. the MQW misfit with the substrate. Samples with a larger MQW/substrate misfit exhibited greater relaxation; the majority of the results displaying a linear dependence of relaxation with misfit.

References.

Adams A.R, *"Band Structure Engineering for Low Threshold High Efficiency Semiconductor Lasers"* Electron. Lett. **22**, (1986), pp 249-250.

Brum J.A, and Bastard G, *"Electric-Field-Induced Dissociation of Excitons in Semiconductor Quantum Wells"* Phys. Rev. **B 31**, (1985), pp 3893-3898.

Chiu T-H, Cunningham J.E, Woodward T.K, and Sizer II T. *"Growth of Strain-Balanced InAsP/InGaP Superlattices for 1.06 μm Optical Modulators"*, Appl. Phys. Lett. **62**, (1993), pp 340-342.

Cunningham J.E, Goossen K.W, Williams M, and Jan W.Y, *"Pseudomorphic InGaAs-GaAsP Quantum Well Modulators on GaAs"*, Appl. Phys. Lett. **60**, (1992), pp

727-729.

David J.P.R, Hopkinson M, Hill G, Stavrinou P.N, and Haywood S.K, *"Growth and Characterisation of InAsP/InP SQW and MQW PIN Diode Structures"*, presented at IEEE InP and Related Materials conf., Paris, (1993), pp 167-170.

David J.P.R, Hopkinson M, Hill G, Stavrinou P.N, and Haywood S.K, *"Growth of InAsP/InP MQW Structures by Solid Source Molecular Beam Epitaxy"*, to be submitted to J. Elec. Mat, (1995).

Fewster P.F, and Curling C.J, *"Composition and Lattice-Mismatch Measurement of Thin Semiconductor Layers by X-Ray Diffraction"*, J. Appl. Phys. **62**, (1987), pp 4154-4158.

Fewster P.F, *"X-ray Diffraction From Low-Dimensional Structures"*, Semicon, Sci. Technol. **8**, (1993), pp 1915-1934.

Geshoni D, Temkin H, and Panish M.B, *"Excitonic Transitions in Lattice-Matched* $Ga_{1-x}In_xAs/InP$ *Quantum Wells"*, Phys. Rev. **B 38**, (1988), pp 7870-7873.

Geshoni D, Temkin H, Panish M.B, and Hamm R.A, *"Excitonic Transitions in Strained-Layer* $In_xGa_{1-x}As/InP$ *Quantum Wells"*, Phys. Rev. **B 39**, (1989), pp 5531-5534.

Ghisoni M, Parry G, Hart L, Roberts C, and Stavrinou P.N, *"Room Temperature Characterisation of InGaAs/AlAs MQW P-I-N Diodes"*, Appl. Phys. Lett. **65**, (1994a), pp 3323-3325.

Ghisoni M, Parry G, Hart L, Roberts C, Marinopoulou A, and Stavrinou P.N, *"Effect of Well/Barrier Ratio on the Performance of Strained InGaAs/GaAs Quantum Well Modulators"*, Electron. Lett., **30**, (1994b), pp 2067-2068.

Goodwill D.J, Walker A.C, Stanley C.R, Holland M.C, and McElhinney. M, *"Improvements in Strain-Balanced InGaAs/GaAs Optical Modulators for 1047nm Operation"*, Appl. Phys. Lett. **64**, (1994), pp 1192-1194.

Goosen K.W, Cunningham J.E, and Jan W.Y, *"Excitonic Electroabsorption in Extremely Shallow Quantum Wells"*, Appl. Phys. Lett. **57**, (1990), pp 2582-2583.

Hart L, Ghisoni M, Stavrinou P.N, Roberts C, and Parry G, *"X-ray Characterisation of InGaAs/AlAs Multiple Quantum Well P-I-N Structures"*, submitted to Materials Science and Technology, (1994).

Hou H.Q, and Tu C.W, *"Growth of* $GaAs_{1-x}P_x/GaAs$ *and* $InAs_xP_{1-x}/InP$ *Strained Quantum Wells for Optoelectronic Devices by Gas-Source Molecular Beam Epitaxy"*, J. Elec. Mat. **21**, (1992), pp 137-141.

Hull R, Bean J.C, Cerdeira F, Fiory A.T, and Gibson J.M, *"Stability of Semiconductor Strained-Layer Superlattices"*, Appl. Phys. Lett. **48**, (1986), pp 56-58.

Joyce B, *"Molecular Beam Epitaxy"*, Rep. Prog. Phys. **48**, (1985), pp 1637-1697.

Kopft R.F, Herman M.H, Lamont Schnoes M, Perley A.P, Livescu G, and Ohring M, *"Band Offset Determination in Analog Graded Parabolic and Triangular Quantum Wells of GaAs/AlGaAs and GaInAs/AlInAs"*, J. Appl. Phys. **71**, (1992), pp 5004-5011.

Landolt-Börnstein, edited by Madelung, New Series, Group 3, Vol. 17a, (Springer, Berlin 1982) , pp 281-289; Vol. 22a, (Springer, Berlin 1989) pp 107-116.

Loh W.H, Atkinson D, Morkel P.R, Grey R, Seeds A.J, and Payne D.N, *"Diode-Pumped Self Starting Passively Modelocked Neodymium-Doped Fibre Laser"*, Electron. Lett. **29**, (1993), pp 808-810.

Miller D.A.B, Chemla D.S, Damen T.C, Gossard A.C, Wiegmann W, Wood T.H, and Burrus C.A, *"Electric Field Dependence of Optical Absorption Near the Band Gap of Quantum Well Structures"* Phys. Rev. **B 32**, (1985), pp 1043-1060.

Miller D.A.B, Weiner J.S, and Chemla D.S, *"Electric Field Dependence of Linear Optical Properties in Multiple Quantum Well Structures: Waveguide Electroabsorption and Sum Rules"*, IEEE J. Quantum Electron. vol. **JQE-22**, (1986), pp 1816-1830.

Nicholas R.J, Stradling R.A, and Ramage J.C, *"Evidence for a Reduction in the Momentum Matrix Element P^2 Due to Alloy Disorder in $InAs_{1-x}P_x$"*, J. Phys. C, **12**, (1979), pp 1641-1651.

O'Reilly E.P.O, *"Valence Band Engineering in Strained Layer Structures"*, Semicon. Sci. Technol. **4**, (1989), pp 121-137.

Pearsall T.P, (editor) *GaInAsP Alloy Semiconductors*, John Wiley & Sons, New York, (1982).

Pezeshki B, Lord S.M, Harris Jr. J.S, *"Electroabsorptive Modulators in InGaAs /AlGaAs"*, Appl. Phys. Lett., **59**, (1991), pp 888-890.

Quillec M, Goldstein L, LeRoux G, Burgeat J, and Primot J, *"Growth Conditions and Characterization of InGaAs/GaAs Strained Layers Superlattices"*, J. Appl. Phys. **55**, (1984), pp 2904-2909.

Siegman A.E, *Laser*, chp.27, University Science Books, Mill Hill Valley, California, (1982).

Schneider Jr R.P, and Wessels B.W, *"Monolayer Abruptness in Highly Strained* $InAs_xP_{1-x}/InP$ *Quantum Well Interfaces"*, Appl. Phys. Lett. **54**, (1989), pp 1142-1144.

Schneider Jr R.P, and Wessels B.W, *"Photoluminescence Excitation Spectroscopy of* $InAs_{0.67}P_{0.33}/InP$ *Strained Single Quantum Wells"* J. Elec. Mat. **20**, (1991), pp 1117-1123.

Stavrinou P.N, Haywood S.K, Hart L, Zhang X.M, Hopkinson M, David J.P.R, and Hill G, *"Varying Strain in* $InAs_{1-x}P_x/InP$ *Multiple Quantum Well Device Structures"*, presented at IEEE InP and Related Materials conf., Paris, (1993), pp 652-655.

Stevens P.J.S, Whitehead M, Parry G, and Woodbridge K, *"Computer Modelling of the Field Dependent Absorption Spectrum of Multiple Quantum Well Material"* IEEE J. Quantum Electron. vol. JQE-**24**, (1988), pp 2007-2014.

Tsang W.T, *"Heterostructure Semiconductor Lasers Prepared by Molecular Beam Epitaxy"*, IEEE J. Quantum Electron. vol. QE-**20**, (1984) pp 1119-1132.

Woodward T.K, Sizer II T, Sivco D.L, and Cho A.Y, *"*$In_xGa_{1-x}As/GaAs$ *Multiple Quantum Well Optical Modulators for the 1.02-1.07 μm Wavelength Range"*,Appl. Phys. Lett. **57**, (1990), pp 548-550.

Woodward T.K, Sizer II T, and Chiu T.H, *"*$InAs_yP_{1-y}/InP$ *Multiple Quentum Well Optical Modulators for Solid-State Lasers"*, Appl. Phys. Lett. **58**, (1991), pp 1366-1368.

Woodward T.K, Chiu T-H. and Sizer II T, *"Multiple Quantum Well Light Modulators for the 1.06 μm Range on InP Substrates:* $In_vGa_{1-v}As_xP_{1-x}/InP$, $InAs_xP_{1-x}/InP$ *and Coherently Strained* $InAs_xP_{1-x}/In_vGa_{1-v}P$*"*, Appl. Phys. Lett. **60**, (1992), pp 2846-2848.

Yablonovitch E, and Kane E.O, *"Reduction of Lasing Threshold Current Density by the Lowering of Valence Band Effective Mass"*, J. Lightwave Technol., **LT-4**, (1986), pp 504-506: Errata: J. Lightwave Technol., LT-4, (1986), pp 961-962.

Yamamoto M, Yamamoto N, and Nakano J, *"MOVPE Growth of Strained InAsP/InGaAsP Quantum-Well Structures for Low-Threshold 1.3-μm Lasers"*, IEEE J. Quantum Electron. vol. JQE-**30**, (1994) pp 554-561.

Chapter 6. Investigations into Composite Quantum Well Structures: A three layer basis for an absorption edge blue shift.

The present chapter describes a novel method to obtain blue shifting structures, where an internal field is induced through the band offset ratios within the composite well region. This internal field is then cancelled by an opposing externally applied field resulting in a blue shift of the absorption edge. To achieve the required band offset conditions, one of the constituent layers is a strained layer, hence the structure relies on the ability to accommodate strain. Theoretical calculations, from the model constructed in the earlier chapters, are used throughout to demonstrate the expected blue shift and associated absorption change. A short correspondence about the present work has been recently reported (Stavrinou *et al* 1994). Details of this are included in the present chapter along with a further investigation into the factors which govern the blue shift and ultimately the performance of such structures.

§6.1 Introduction.

§6.1.1 Red or blue shift QW structures?

To date the large body of work on electro-absorption MQW devices has utilized, in some manner, the quantum confined Stark effect (QCSE) for operation. At the band edge, this manifests itself as a decrease in peak height and *red shift* of the n=1hh transition as electric field is applied (Fig. 6-1a). Choosing a fixed operating wavelength near the band edge, the resulting change in absorption with applied field admits a number of possible opto-electronic devices (cf. §1.3.3) One of the most widely studied bistable opto-electronic devices is the self-electro-optic effect device or SEED (see D.A.B Miller (1990) for a review on SEED's). A detailed discussion on SEED devices is beyond the scope of this thesis, and this work will essentially regard SEED's as two state devices which are 'on' when absorption is low and 'off' when absorption is high. The operating wavelength for a SEED device corresponds to the zero applied field n=1hh transition, such that for increasing applied field, the absorption (and hence photocurrent) at this wavelength decreases through the QCSE, (cf. §1.2.3). This decreasing photocurrent with increasing field is the negative resistance that is required for all the various SEED configurations (D.A.B Miller 1990). For practical use of SEED devices in systems, several design optimisations and trade-offs are apparent (R.Grindle 1992). These inevitably depend heavily on the proposed application, for example, a large ratio of the maximum and minimum absorption (ie. off/on contrast ratio) is desirable in telecommunications system for a large extinction ratio between two signal channels. Although the off/on contrast ratio is important, so are the individual absorption levels in the device. For example, maximizing the absorption leads to reduced light transmission in the 'off' state, which is beneficial in cascaded systems in which a number device outputs are essentially summed onto a single input. Whereas minimizing the absorption in the 'on' state, reduces the on state insertion loss and thereby power dissipation, an important consideration in two dimensional arrays of SEED's for use in optical logic planes. For a recent review of SEED devices and application considerations see Lentine and Miller (1993), and references therein.

Traditionally SEED devices are based on decreasing absorption/photocurrent at the operating wavelength arises from the *red shift* of the n=1hh exciton transition (D.A.B Miller 1989). However it was recognized that SEED devices based on a *blue shift* can offer several advantages (eg. J Khurgin 1988, and next section). In a *blue* shifting structure, the band edge absorption (excitonic) shifts to shorter wavelengths (higher energies) on application of an electric field, Fig.6-1 (right). The situation in figure 6-1b can be viewed as having a pre-biased *conventional* QW device, such that on removing the field the excitonic band edge returns to its *conventional* zero applied field wavelength. However a key difference in the blue shift structure is that the field across the device is *increased* to produce the blue shift. Thus if the operating wavelength corresponds to the zero applied field band edge, the decreasing absorption (hence photocurrent) for increasing field will also produce negative device resistance, the condition required for the SEED devices, Fig.6-1 (right).

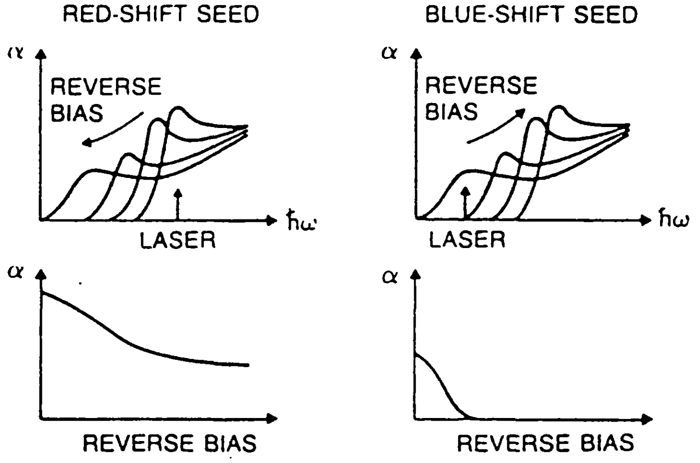

Figure 6-1. *Schematic of SEEDs employing red-shifting (left) and blue-shifting (right) QW structures. [taken from Goossen et al 1990]*

In fact, irrespective of a red or blue shift device, provided the operating wavelength is chosen to be the zero applied field n=1hh transition, applying an electric field will produce the negative device resistance required for SEED configurations. It is only when a SEED application is envisaged that the relative merits of either structure are revealed. That is, although the contrast ratio may be comparable, red shifting SEED's give a high absorbing 'off' state whereas blue shifting SEED's suggest a low absorbing 'on' state (cf. §6.1.2).

The comments so far have been directed mainly towards electro-absorption SEED devices, it should be noted that electro-refraction devices, ie. devices utilizing the accompanying change in refractive index with a change in absorption, are expected to exhibit advantages by using a blue shifting mechanism (Zucker *et al* 1990a). Blue shifting devices allow operation at smaller *detuning* energies from the zero applied field exciton resonance than red shifting devices. Hence large changes in refractive index are available for optical phase modulation with minimal intensity modulation (Zucker *et al* 1990b).

§6.1.2 Obtaining blue shifting structures.

The work by J.Khurgin (1988) and then D.A.B Miller (1989) first established the advantages that could be gained by using blue shifting SEED devices. Operating in the high transmitting 'on' state (ie. with applied field), the residual absorption in the device takes on sub gap values or at least the low absorption in the n=1hh tail. On the other hand, a red shift SEED in its 'on' state still experiences significant absorption from either the e1hh1 continuum or other transitions. For sufficient contrast, a red shift device places the usual demands on the quality of the zero field exciton peak in relation to linewidth and hence peak absorption (cf. §4.4.3). To some extent, this fixes the operating wavelength to the n=1hh peak wavelength. In a blue shift device although the 'off' state absorption is less the contrast ratio can still be the same, due to the small 'on' state absorption. In addition, the operating range of the device is increased and to some extent, less emphasis is placed on good quality exciton peaks (D.A.B Miller 1990).

Many of the blue shifting structures which have been proposed actually exhibit a *quasi*-blue shift of the absorption edge. For example, a net blue shift of the absorption edge was shown to occur in superlattice structures, (cf. §1.3.3), through Wannier-Stark localization (Bleuse *et al* 1988a, Bleuse *et al* 1988b). A similar outcome was demonstrated using symmetric coupled QWs (Onose *et al* 1989). Here the QCSE rapidly diminished the strength of the n=1hh transition, allowing higher energy transitions to dominate, eg. e1hh2. In contrast to these localization induced quasi-blue shifts, structures achieving an *actual* blue shift of the absorption edge have been demonstrated in strained MQWs grown on [111] orientated substrates (Goossen *et al* 1990, Pabla *et al* 1993, 1994); as previously noted in §2.3, such growth leads to piezoelectric fields in the strained MQW region. In operation an electric field is applied in the opposite direction to the internal piezoelectric field, essentially reducing the pre-biased state of the structure. Recently, such structures have been used to demonstrate all-optical bistable switching for an S-SEED configuration (Pabla *et al* 1994). Opposing a built-in field is the underlying principle behind many of the proposed [100] structures. A built in field which is then cancelled by an applied field, can be achieved using either graded gap QWs (Hiroshima and Nishi 1987) or asymmetric coupled QWs (J. Khurgin 1988, D.A.B. Miller 1989). The internal field in these structures is implied from the spatial separation of the ground state electron-hole pair, caused by the asymmetry of the structure. However, the magnitude of the blue shifts in these works is likely to be comparable to phenomena such as excitonic broadening and would therefore be difficult to observe at room temperature (Leavitt and Little 1990). More recently, it was predicted that using a three step asymmetric coupled QW, substantial blue shifts could be obtained, due to the larger internal field generated, ie. larger spatial separation of the electron-hole pair (Susa and Nakahara 1992). Finally, another device that has been shown to exhibit a blue shift is the BRAQWET structure (Wegener *et al* 1990) where the applied electric field sweeps electrons into the well region causing a blue shift of the absorption edge via band filling effects.

As noted, it is with the principle of inducing (and then opposing) an internal field that the present work is concerned. A large blue shift, sufficient for room temperature operation around 1.55 μm, can be achieved.

§6.2 A Three Layer Basis for an Absorption Edge Blue Shift.

The three layer device proposed has an asymmetric well structure resulting in a potential profile of the form shown in Fig.6-2. The composite well region (layers B and C) consists of two materials which are chosen because of the opposite weighting of the band offset parameters, Q_c:Q_v, with respect to the barrier material (layer A). [note: the band offset parameters refer to the percentage share of the total confinement potential between the conduction and heavy hole valence band]. To illustrate this point, consider a structure similar to Fig.6-2, and assume that layers B and C have comparable band gaps. The offset parameters for layers A and B are such that $Q_c^{AB} > Q_v^{AB}$, so the band gap difference is shared in favour of the conduction band. Conversely, the parameters for materials A and C are such that $Q_c^{AC} < Q_v^{AC}$, indicating the difference in band gaps is shared in favour of the valence band. With layer A enclosing the structure, the resulting line-up between the B and C layers is a staggered or type II one. Clearly to obtain this type of profile in practice, requires knowledge of the band offset parameters for various material systems. These have often proved difficult to determine, although recent work suggests that by growth of the appropriate structures they may be found to a high degree of accuracy (Kopf *et al* 1992).

The materials chosen to fulfil the offset conditions expressed above, and provide operation around the 1.55 μm region, are InP as the barrier material (layer A) enclosing a composite well region of $InAs_{0.4}P_{0.6}$ (layer B) and lattice matched $In_{0.53}Ga_{0.47}As$ (layer

C). Growth is taken to be on [100] InP substrates, hence the effects of strain are only considered for the InAsP material which is assumed to accommodate the ~1.3% compressive strain coherently (cf. the single layer critical thickness model of Matthews and Blakeslee, §2.4.2). Cumulative effects of strain in a MQW are for the moment neglected (cf. Chapter 7), noting that the average misfit of one period would be less than that for the well alone and ultimately depend on the dimensions of the lattice matched layers (A and C).

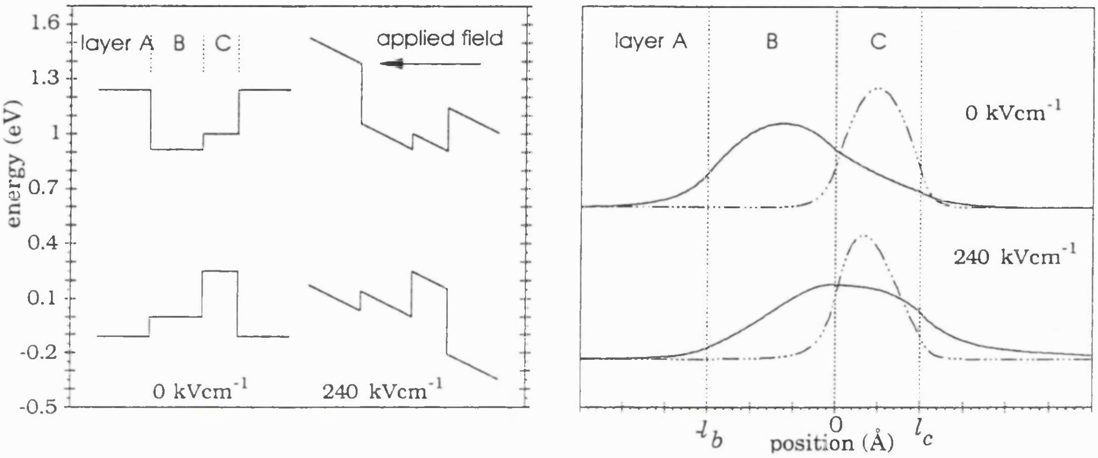

(a) (b)

Figure 6-2. *(a) Potential profile (illustrating only the conduction and heavy hole bands) of a* InP(A)/$InAs_{0.4}P_{0.6}$ (B)/$In_{0.53}Ga_{0.47}As$ (C) *composite structure. The direction of applied field (right diagram) is chosen to produce an blue shift of the absorption edge. (b) Ground state envelope functions, e1 (solid) and hh1 (dash-dotted), for zero applied field and 240 kV/cm.*

A type II line-up between layers B and C, (cf. Fig.6-2a), is due to the contrasting offset parameters with respect to the InP barriers. Initially, these are taken as 75:25 for InAsP/InP (Schneider and Wessels 1991) and 40:60 for InGaAs/InP (Skolnick *et al* 1987). Given that the InAsP/InP offset is the least studied of the two, it is useful to note a type II line-up may still be achieved using an offset of up to 55:45 for InAsP/InP. Naturally, the potential steps between the B and C layers will be reduced, but as demonstrated in the following section, (§6.3.1), the general principle expressed here will still hold. The following results are for a structure with dimensions, 100Å (layer A), 60Å (layer B), and 40Å (layer C). These well widths and compositions are initially chosen simply to demonstrate the general principle of achieving a blue shift.

At zero applied field for the structure of Fig.6-2a, the calculated hh1 state is strongly confined in layer C (cf. upper plot (dash-dotted line) in Fig.6-2b). Whereas the first electron state, e1, is situated in layer B, some 32 meV below the conduction band edge of layer C. At zero applied field, the observed spatial separation of the ground state envelope functions, (upper plot of Fig.6-2b), may also be inferred from the low squared overlap integral, Fig. 6-3a. This situation is analogous to a symmetric square QW with a field applied, the resulting asymmetric potential *polarizes* the states to opposite sides of the well, thereby inducing a spatial separation. This is *imitated* in the three layer structure, with the separation resulting from the asymmetric type II potential profile in the composite well region. Thus, an induced internal field is present in the three layer structure.

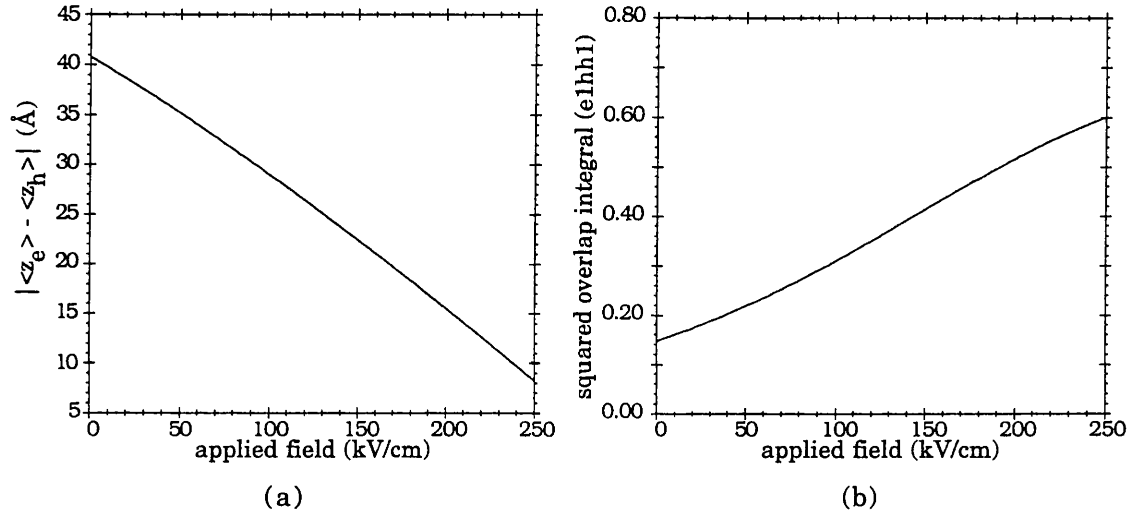

(a) (b)

Figure 6-3. *Calculated performance of the structure in Fig.6-2a with an applied electric field. (a) Spatial separation of the e1 and hh1 envelope functions. (b) Squared overlap integral between e1 and hh1 states.*

In order to achieve a blue shift of the n=1hh transition, an external electric field is applied in the direction illustrated in right hand side of Fig.6-2a. Increasing the applied field in this direction, essentially acts against the internal field and the spatial separation of the electron and hole states reduces, Fig.(6-3a). The resulting QCSE then starts out as a blue shift (D.A.B Miller 1989). The envelope functions, Fig.6-2b, demonstrate the re-distribution of the states as field is applied. The first electron state, e1, is pulled towards the layer C as the potential here gradually lowers with respect to layer B. Less noticeably, the heavy hole, hh1, is pulled towards layer B, however it is still very much confined in layer C due to the large potential barrier it experiences. The decrease in spatial separation is explicitly demonstrated in figure 6-3a, and causes a subsequent increase in the squared overlap integral between the states, Fig.6-3b. The corresponding blue shift of the n=1hh excitonic transition is shown in Fig.6-4a. It can be noted the linear increase in transition energy for low applied fields tends to a quadratic one with high fields. This is opposite to that found in conventional red shift quantum wells (eg. Bastard and Brum 1986), and so supports the idea of an induced internal field which is gradually reduced with applied field. .

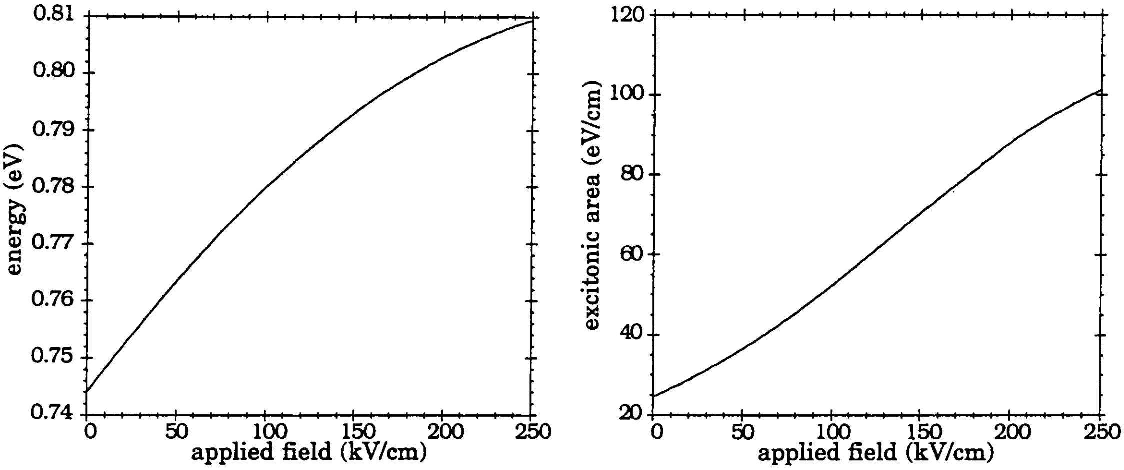

(a) (b)

Figure 6-4. *Calculations of the excitonic properties for the structure in Fig.6-2a under an applied electric field. (a) The n=1hh excitonic transition energy. (b) The n=1hh excitonic area.*

As is the case with calculations in conventional QW structures, many of the excitonic properties, such as the change in oscillator strength (or integrated area) with field, are well described in form by the squared overlap between the individual states (cf. Fig.5-7b and Fig.5-8b and see Miller *et al* 1986). This is demonstrated in figure 6-4b, where the calculated excitonic area, (4.82), is shown to increase with applied field (similar in form to Fig.6-3b). Calculations in the following section will initially use the squared overlap, exploiting its correspondence with the excitonic features, to discuss excitonic absorption. Although not shown, it is noted that the excitonic binding energy for e1hh1 increases with field and the in-plane radius decreases with field; again, exactly the opposite to that found for conventional square QW structures, (cf. Fig.4.9). All of these results for the present composite structure indicate an increase in excitonic absorption as electric field is applied. This is implicit from both the increase of the squared overlap integral *and* the decrease between the expectation values $\langle z_e \rangle$ and $\langle z_h \rangle$ with applied field where,

$$\langle z_i \rangle = \int_{-\infty}^{\infty} f_i^*(z_i) z_i f_i(z_i) dz_i \qquad (6.1)$$

Having demonstrated the basic principle behind the blue shift structure, the next section concentrates on the main parameters affecting the performance, eg. band offsets, and on design optimization, eg. tailoring the 'built-in' field. Specific comments about the modelling are brought in as the situation arises, however some general points common to all calculations can be made:

(i) Despite the composite nature of the structure, the *common* assumption that the Kane matrix element is the same throughout the structure is used (Bastard 1981). However, unlike a conventional symmetric QW (where it is reasonable to assume the value for the well material), for the composite structures I used a weighted average of the two respective well values; the ratio of the layer width to the composite well width was used as the weight.

(ii) For absorption calculations, the real part of the refractive index and the optical matrix element from the *full* model (§3.2.2) are averaged over a two dimensional configuration space (z_e, z_h) weighted by the envelope functions. As with the reduced mass and dielectric constant calculations (§4.4.2), the reasoning behind this method is in the assumption that the exciton resides in some embedding space determined by both electron and heavy hole distributions. Hence:

$$\langle x \rangle = \bar{x} \iint |f_{el}(z_e)|^2 |f_h(z_h)|^2 \, dz_e dz_h \qquad (6.2)$$

with

$$\bar{x} = \frac{1}{|z_e - z_h|} \int_{z_h}^{z_e} x(z) dz$$

where x corresponds to either Ep or n, the matrix element and the real part of the refractive index respectively.

§6.3 A Re-examination of the Governing Factors.

Realizing a blue shifting three layer structure lies in obtaining a spatial separation of the electron and hole ground states at zero applied field. Since the separation is induced by the asymmetric potential of the structure, parameters such as material composition, well widths and offset parameters will significantly effect the degree of spatial separation. In the present section examples of the governing factors are investigated in relation to the blue shifting performance of prospective devices. While by no means exhaustive, these preliminary results demonstrate the electro-absorption properties may be tailored in some fashion towards an optimum design.

§6.3.1 Band offset parameters and compositions.

In the composite well considered in §6.2, it is recognized that the offset parameters for InAsP/InP are the least studied of the two. However, evidence in the literature points to an offset in favour of the conduction band (e.g. Schneider and Wessels 1991, Yamamoto *et al* 1994). To date, two *very* similar parameters have been reported, namely, 75:25 from samples containing ~67% arsenic (Schneider and Wessels 1991) and more recently, 70:30 from samples containing ~21% (Hou and Tu 1994). The slight difference could be attributed to the different compositions and hence different strain in the samples. Although as the previous chapter demonstrated the offset parameter in symmetric QWs can conceivably take on a range of values, (cf. Fig.5-2a), yet still satisfy experimental transition energies due to uncertainties in material parameters.

For the present work, the InAsP/InP offset parameter is varied while still keeping the share of confinement potential in favour of the conduction band. The lattice matched InGaAs/InP offset is fixed at 40:60, since next to the GaAs/AlGaAs system this remains one of the most widely investigated, and hence established, offset parameters for a III-V material system.

For the first example, both well materials are kept as $InAs_{0.4}P_{0.6}$ and $In_{0.53}Ga_{0.47}As$, i.e. the same as in the previous section. Three offset parameters for $InAs_{0.4}P_{0.6}$/InP are chosen which comfortably cover the range suggested in the literature. The second set of calculations uses fixed offset parameters but varies the arsenic composition. For both sets of examples, the constituent widths in the composite well are kept the same, i.e. 60Å (layer B) and 40Å (layer C). Rather than show the potential profiles the essential details of the line-ups can be obtained from Table 6-1.

At zero applied field, the heavy hole potential confinement between layers B and C, ΔE_{hh}^{BC}, is sufficiently large to confine the hh1 state strongly in the C layer. In this sense, $\langle z_h \rangle$ is typically at the centre of layer C for all the above examples, (Fig.6-6a,b). [note: The x-axis zero in figures 6-5a,b represents the B/C interface] Conversely, the changes in offset parameters or composition indicated in Table 6-1 strongly effect the energy of the e1 state in relation to the structure and hence $\langle z_e \rangle$. However, whether the e1 state lies above or below the conduction band edge of the C layer, there is always a significant non-zero spatial separation between the states at zero applied field, i.e. $\langle z_e \rangle - \langle z_h \rangle \neq 0$, (Fig.6-6a,b). Furthermore, since the $\langle z_h \rangle$ is relatively insensitive to the modifications in the structure, the change in spatial separation is almost entirely due to the change in the expected position of e1, $\langle z_e \rangle$.

Table 6-1. *The energy separations between the conduction and valence band of the layers for the example structures considered in this section, i.e. varying offset parameters* $Q_c^{AB}:Q_v^{AB}$ *and layer B composition. Also indicated is the position of the e1 state with respect to the conduction band edge of layer C (for 60Å/40Å composite well). The energy zero is taken to be at the heavy hole band edge of the layer B, and the separations are described as* $\Delta E_i^{xy} = E_i^x - E_i^y$. *Negative values of* ΔE_c^{BC} *and* ΔE_{hh}^{BC} *imply a type II line-up between layers B and C (cf. Fig.6-2a). In all cases, layer C is lattice matched InGaAs and has the same potential offset as illustrated in Fig.6-2a..*

	$InAs_{0.4}P_{0.6}$			$InAs_{0.5}P_{0.5}$	$InAs_{0.3}P_{0.7}$
	75:25	65:35	55:45	75:25	75:25
ΔE_c^{AB}:	328	284	240	399	252
ΔE_c^{BC}:	-82	-38	6	-153	-6
e1:	$<E_c^C$	$>E_c^C$	$>E_c^C$	$<E_c^C$	$>E_c^C$
ΔE_{hh}^{AB}:	-109	-153	-197	-133	-84
ΔE_{hh}^{BC}:	-259	-215	-172	-235	-284

Considering specific structures in relation to a *reference* sample used in §6.2, increasing the valence band share of confinement potential (e.g. from 75:25 to 55:45) produces qualitatively the same results as decreasing the arsenic composition in layer B (e.g. 40% to 30%). In both cases, the e1 state lies above the conduction band edge of the B and C layer and is therefore localised over both layers. As a result, $\langle z_e \rangle$ is closer to the B/C interface which consequently decreases the zero applied field spatial separation (w.r.t reference sample). With these results it can be generally stated that as the potential step in the conduction band between layers B and C increases, $\langle z_e \rangle$ is situated further towards the centre of layer B, (Fig.6-5a,b). Accordingly, the overlap between the ground electron and hole states reduces.

The applied field results for the both example sets all demonstrate varying degrees of n=1hh blue shift and corresponding increase in overlap integral (Fig.6-5). Comparative analysis indicates they can be explained by considering varying strengths of internal field *vis-à-vis* the zero applied field spatial separation. Structures giving rise to a smaller zero applied field spatial separation, either through reducing arsenic composition or increasing the valence band offset parameter, show a smaller n=1hh blue shift across the range of applied fields (Fig.6-5e,f).

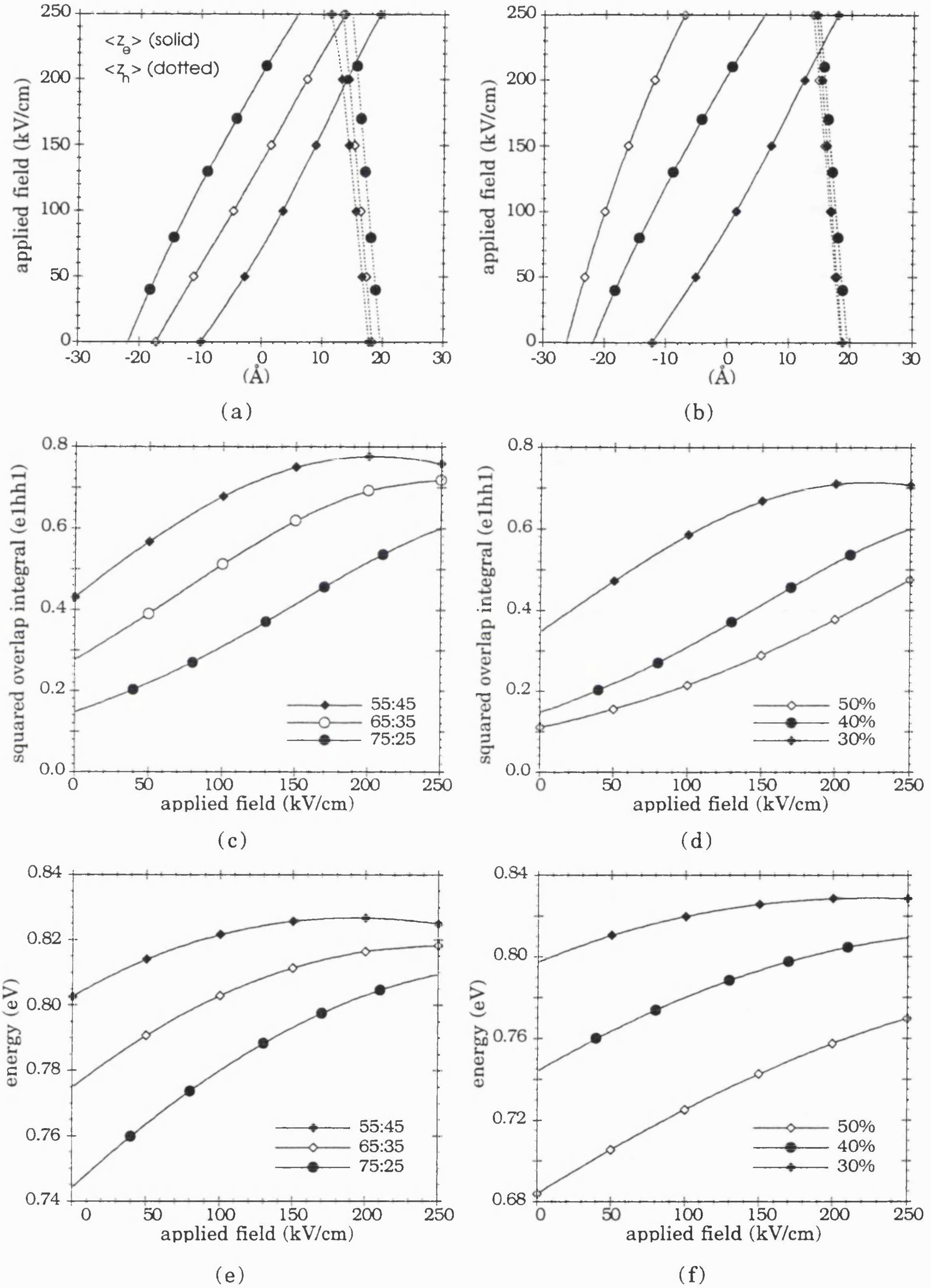

Figure 6-5. *Calculated applied field characteristics for the two example sets in Table 6-1. Left hand graphs are varying* $Q_c^{AB}:Q_v^{AB}$ *for* $InAs_{0.4}P_{0.6}/In_{0.53}Ga_{0.47}As$ *(60Å/40Å). Right graphs are varying x for* $InAs_xP_{1-x}/In_{0.53}Ga_{0.47}As$ *(60Å/40Å) with* $Q_c^{AB}:Q_v^{AB}$ *(75:25). (a) and (b) expectation values for e1 and hh1. (c) and (d) e1hh1 squared overlap integral. (d) and (e) blue shift of n=1hh transition. (labelling in (a) and (b) is the same in associated plots directly below)*

For increasing applied field, the quadratic dependence of the n=1hh the blue shift clearly dominates which in turn reduces the blue shift per unit field, in some cases eventually resulting in a red shift . The respective overlap calculations are similar in form, (Fig.6-5c,d). Recalling the analogy with *pre*biasing a conventional square QW, the *early* quadratic nature of n=1hh blue shift with applied field suggests these structures induce less of an internal field than the reference sample. Similar reasoning applies to the other structures, where the e1 state is increasingly confined in the B layer, ie. e1 state lies below the C layer conduction band edge (cf. Table 6-1). The zero applied field spatial separation is larger and by implication the internal field in these structures is greater. The resulting n=1hh blue shift retains an almost linear dependence with increasing applied field, and only at large fields does the quadratic nature becomes apparent. In this sense, the *late* quadratic nature of the n=1hh blue shift is consistent with a larger internal field in these structures, which was suggested by the larger spatial separation at zero applied field.

The results have shown that even accounting for a larger valance band offset, an n=1hh blue shift and increase in overlap integral with applied field can be achieved, though at a decreased rate since the zero field separation is reduced. To some extent this can be compensated for by increasing the arsenic composition, ie. further reducing the conduction band potential in layer B. Subsequently, through the stronger localization of e1 in the B layer an increase in the zero applied field spatial separation results.

In both sets of structures, where the well widths remain constant, the magnitude of the spatial separation is shown to be proportional to the strength of the internal field induced. This is borne out by considering the form of the n=1hh blue shift with applied field. It is also interesting to note that the n=1hh transition at zero applied field is very sensitive to the offset parameters used, (Fig.6-5e). This suggests an asymmetric structure of this type would be useful in investigating the InAsP/InP offset.

§6.3.2 Well width selection for internal fields.

To investigate the effect of structure dimensions the example system to be considered consists of $InAs_{0.4}P_{0.6}/In_{0.53}Ga_{0.47}As$ as the composite well region. All of the results will assume the offset parameters of 75:25 for the InP/InAsP interface. For the initial study, the zero applied field characteristics of the structure are investigated. The method here consists of varying the width of layer B ($InAs_{0.4}P_{0.6}$) while keeping the width of layer C ($In_{0.53}Ga_{0.47}As$) constant. As suggested in the previous section, the position of the electron state with respect to the bulk band edges plays an important role in these characteristics.

The calculations, over a range of B layer widths, are carried out for two values of layer C, ie. 20Å and 40Å. Increasing the width of layer B causes the first electron state to become more confined in layer B, ie. further below the conduction band edge of layer C, (Fig.6-6a). Accordingly, the expectation value, $\langle z_e \rangle$, moves further away from the B/C interface and tends towards the center of the B layer for large l_B. Consequently, the overlap with the hh1 state reduces as the distribution of the e1 envelope function into the C layer decreases, (Fig.6-6b). To some extent the width of layer C effects the energy position of the conduction band states, with higher energy states found for a smaller C layer, (Fig.6-6a). In many respects the situation is similar to the higher energies found in narrow square QWs, ie. for the present case the smaller C layer reduces the total length of the composite well. As l_B increases the effect of the C layer on the conduction band states reduces, a feature also found in wide square QW's in relation to the small changes in confined state energies as the well width increases. However an additional effect, quite relevant for e1 state in the present structures, is the reduced distribution of this state into the C layer as l_B increases above ~40Å, ie. the C layer essentially becomes potential barrier which has a diminishing effect on the e1 state which is predominantly localised in layer B.

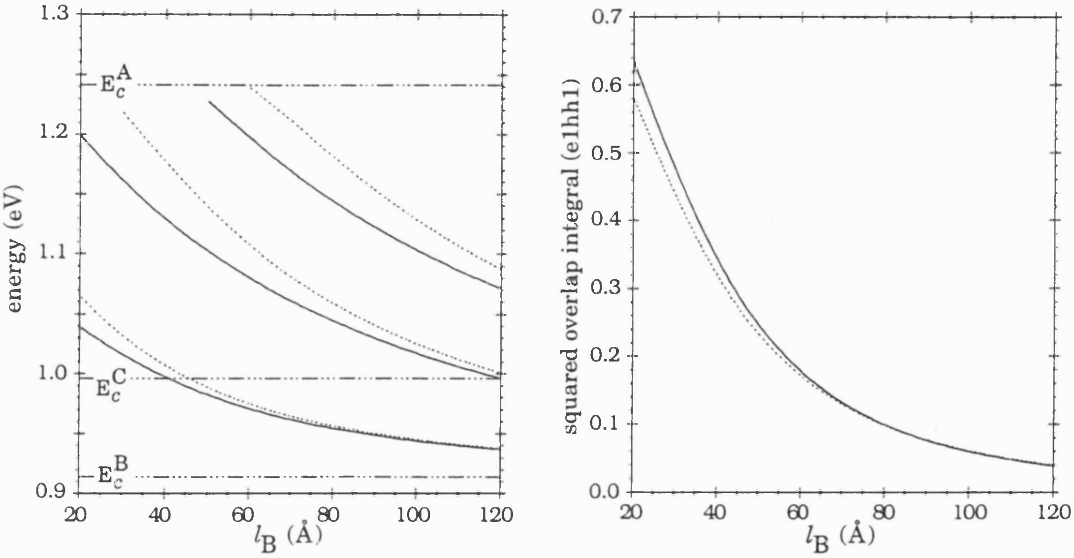

(a) (b)

Figure 6-6. *Calculations for a three layer structures with varying B width and fixed C width, l_C=40Å (solid) and l_C=20Å (dotted) . (a) The conduction band states in relation to the band edges of the structure. (b) The squared overlap integral between e1 and hh1.*

The effect of layer C on the calculated expectation values for the ground states, show for a given l_B, $\langle z_e \rangle$ is situated closer towards the B/C interface for a wider C layer. However, it should be remembered the total lengths of the structures are different for a given l_B, and so is the position of B/C interface in relation to the composite length. The question of comparing spatial separation for different composite lengths is discussed later in relation to the blue shift properties. For increasing l_B, the effect of layer C on $\langle z_e \rangle$ reduces, in a similar manner as found with the e1 energy. Results for hh1 justify the reference to a *strongly* confined hh1 state in layer C. Both the expectation value,$\langle z_h \rangle$, and hh1 energy are unaffected by the width of layer B. However the difference in n=1hh transition energies for the 40Å and 20Å layer C widths is mainly due to the difference in hh1 energy (~50 meV) which is in turn determined by the width of layer C, (Fig.6-7a).

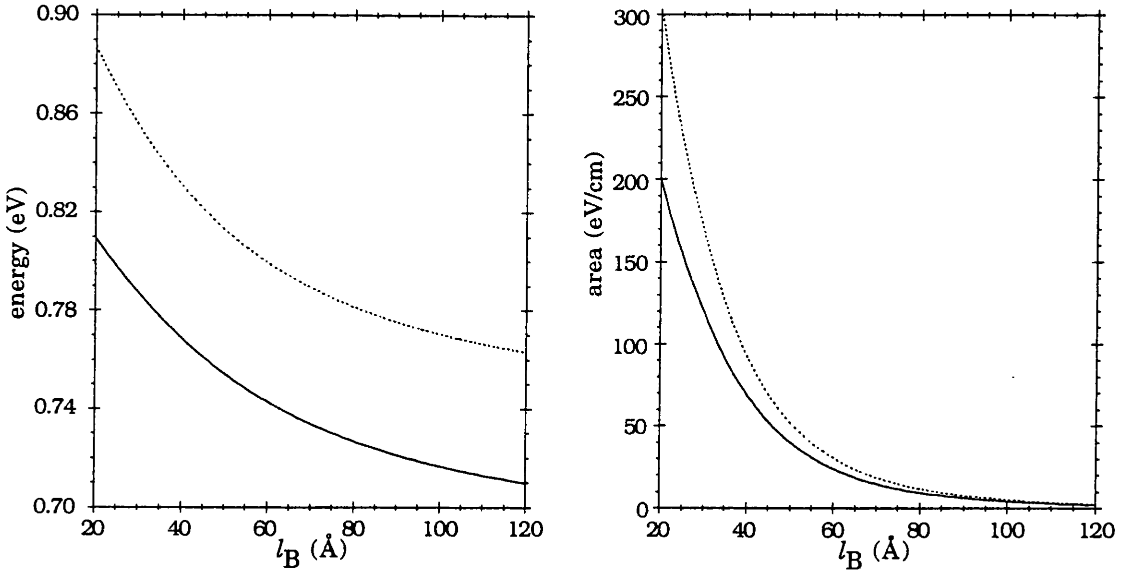

(a) (b)

Figure 6-7. *Calculations for a three layer structures with varying B width and fixed C width, l_C=40Å (solid) and l_C=20Å (dotted). (a) The n=1hh excitonic transition. (b) The n=1hh excitonic absorption area.*

The calculated excitonic absorption area is illustrated in figure 6-8b, and is seen to reduce as l_B increases, in a similar way to the overlap integrals (Fig.6-6b and cf. (4.77)). However, as the last chapter demonstrated, comparing the overlap integral between two dissimilar structures can be misleading, it reveals nothing about the difference in absolute absorption. This is demonstrated by a comparison of figures 6-6b and 6-7b. In figure 6-6b for small l_B, the wider C layer structure produces a higher overlap integral between e1 and hh1; however the calculated excitonic absorption area lower. That is, the overall smaller composite width accompanies a larger calculated absorption area. [note: The increase of absorption area with reducing well width (or in this case composite width) is well established, (cf. Fig.5-8a), although it is also recognized that the overlap integral is an important factor (cf. (4.77).]

In the design of a blue shifting electro-absorption device, eg. a SEED device, the absorption at the operating wavelength for zero applied field is an important consideration (D.A.B Miller 1989). The operating wavelength, λ_{op}, is typically chosen near the zero applied field n=1hh exciton transition, (cf. Fig.6-1b). To a first approximation, the absorption change of the device with field is determined from the zero applied field peak absorption at λ_{op}, assuming that with field the absorption at λ_{op} tends to zero. However the oscillator strength, leading to excitonic absorption, follows the same trend as the squared overlap integral between the states forming the exciton, Fig.6-6b and (cf. §4.3.3 and (4.77)). Clearly a trade off exists between obtaining a reasonable zero applied field absorption, ie. a large overlap integral, and achieving a sufficient n=1hh blue shift, ie. requiring an internal field and hence a reduction in the overlap integral.

In addressing the zero applied field absorption for the present materials, reducing the width of layer B is seen predominantly to increase the overlap (and hence absorption). [note: It may also be recalled an additional way of increasing the overlap integral at zero applied field is to reduce the arsenic composition in layer B (cf. Fig.6-5d)]. The width of the C layer, although importantly governing the zero applied field n=1hh transition, in the following examples is also seen to determine the performance of the n=1hh blue shift, (Fig.6-8a).

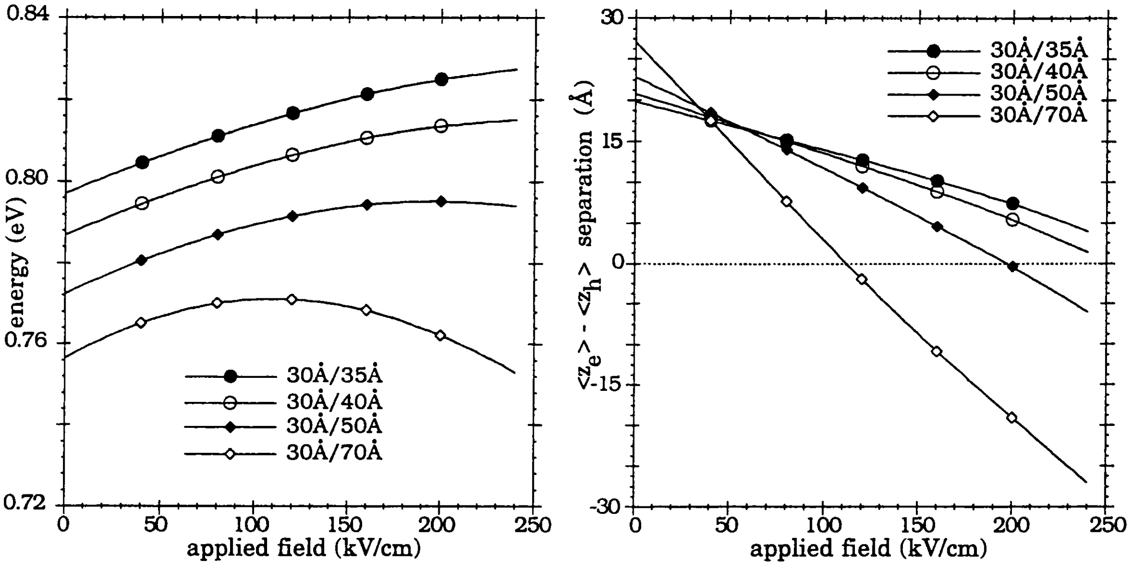

(a) (b)

Figure 6-8. *Calculations for three layer structures with 30Å layer B and varying layer C width. (a) The n=1hh transition energy for applied electric field. (b) The spatial separation of the e1 and hh1 envelope functions.*

For the final examples, $InAs_{0.4}P_{0.6}/In_{0.53}Ga_{0.47}As$ are used for the composite well, the B layer width is fixed at 30Å while the C layer is varied. For all cases, at zero applied field the e1 state is above the conduction band edge of layer C, and for increasing C layer width this resides closer towards the bulk band edge of layer C, (cf. Fig.6-6a). As the composite length increases the spatial separation increases, (Fig.6-8b), which can mainly be attributed to $\langle z_h \rangle$ following the centre of the layer C. In otherwords, the lower potential in the B layer causes $\langle z_e \rangle$ to be reasonably 'pinned' close to the B/C interface, which gradually moves through the interface towards the C layer for larger values of l_C. At a given applied field, the ground states in the wider structure experience a larger change in potential. Consequently, although the zero field spatial separation is larger, the reduction in separation per unit field for the wider composite well is greater, (Fig.6-8b). The maximum blue shift (and maximum increase in excitonic area) occurs for a net zero separation, and a red shift results as $\langle z_e \rangle$ and $\langle z_h \rangle$ effectively pass one another ie. represented as a negative separation. Recalling the analogy with conventional QW's, a zero separation represents a complete cancelling of the internal field by the applied field. The positive spatial separation that still exists at large applied fields in structures with a narrower C layer suggests a residual internal field is still present. Accordingly, the maximum blue shift and increase in absorption area have yet to be achieved, (Fig.6-8b). By considering both the decrease in spatial separation and the form of the blue shifts (and excitonic area) for applied field, it is concluded that structures with a wider C layer induce a smaller internal field.

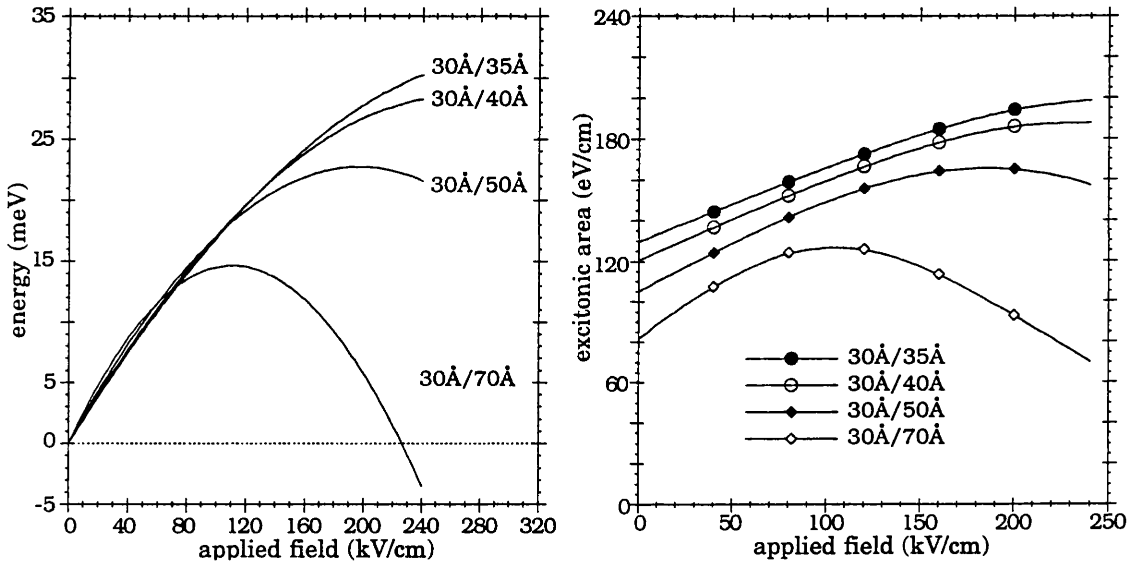

(a) (b)

Figure 6-9. *Calculations for three layer structures with 30Å layer B and varying layer C width. (a) The relative n=1hh shift for applied electric field. [note: positive values denote a blue shift] (b) The n=1hh excitonic area for applied field.*

A potentially confusing point arises from the conclusions made in §6.3.2, in that a larger spatial separation at zero applied field implies a larger internal field, exactly the opposite of what is found here. To unravel this apparent contradiction, it is useful to consider conventional QW structures. For wide wells the spatial separation rapidly *increases* as field is applied, while for a narrow well the rate of increase is somewhat less, such that at a given field a larger separation is found in a wider well. Then for the same *pre*biased field across each QW, simply taking the spatial separation to be a measure of the prebiased (or internal) field yields an incorrect result. The point is the well width is a governing factor in the spatial separation. In fact determining the size of the prebiased field could be achieved by applying an *opposing* field and observing the value that produces zero separation, ie. exactly the method employed here. For the structures in §6.3.2, the composite length was the same and so comparing the zero applied field spatial separation is justified, and consistently agrees with applied field results. To compare structures with different composite widths, the form of the applied field blue shift (and overlap integral) appear to be the best methods along with observing the applied field at which a net zero separation occurs.

For a typical electro-absorption device, the blue shift must be sufficient to reduce the absorption at the operating wavelength. If the zero field n=1hh transition is the operating wavelength, a sensible condition to aim for is the n=1hh blue shift to be at least comparable to the half-width half-maximum (HWHM) of the n=1hh resonance. From the series considered in figure 6-9a, nearly all exhibit blue shifts in excess of 20 meV which is actually larger than the full width half maximum (FWHM) of typical InGaAs/InP QW's (see eg. Sugawara *et al* 1990). Moreover, up to this value, the shift per unit applied field is very efficient essentially following a linear relationship rather than a quadratic one.

To illustrate possible devices operating around the optical fibre low loss window (1.55 μm), the electro-absorption spectra for two structures, ie. 30Å/35Å and 30Å/40Å from figure 6-8a, was calculated and presented in figure 6-10. The spectra assume light propagating perpendicularly to the layers, ie. such as in a transverse MQW device. Only the n=1hh exciton and the corresponding continuum were computed, since the next closest transition for both structures is some 60 meV away, ie. the n=1lh exciton. In both the cases, the InP width (A layer) was taken to be 100Å. For this width, coupling between adjacent composite wells would be negligible, ie. the e1 state has a miniband width of $\sim 10^{-4}$ eV. Further examination with the superlattice dispersions, (§4.2.1), indicate for the well widths used, the InP width could be reduced to 80Å giving a miniband width of ~0.5meV.

At zero applied field the n=1hh transitions are ~19 nm apart, ie. 1.555 μm and 1.574 μm in figures 6-10a,b respectively. The *bunching* of the spectra at large applied fields is a result of the quadratic nature of the blue shift which starts to dominate, (cf. Fig.6-9a). In this regime, the n=1hh transition and absorption strength is less sensitive to changes in applied field. However, before this occurs the linear blue shift is sufficient to allow decreasing absorption for increasing applied field at the chosen operating wavelength, ie. 1.555 μm (Fig.6-10c). Were the structures incorporated in the intrinsic region of a p-i-n diode, the decreasing absorption would give rise to a decreasing photocurrent and hence satisfy the conduction for a SEED configuration. It is noted the calculated change in absorption is larger than the InGaAs/InP square QW devices used by Bar-Joseph and co-workers (1988) to demonstrate bistable operation with a D-SEED configuration.

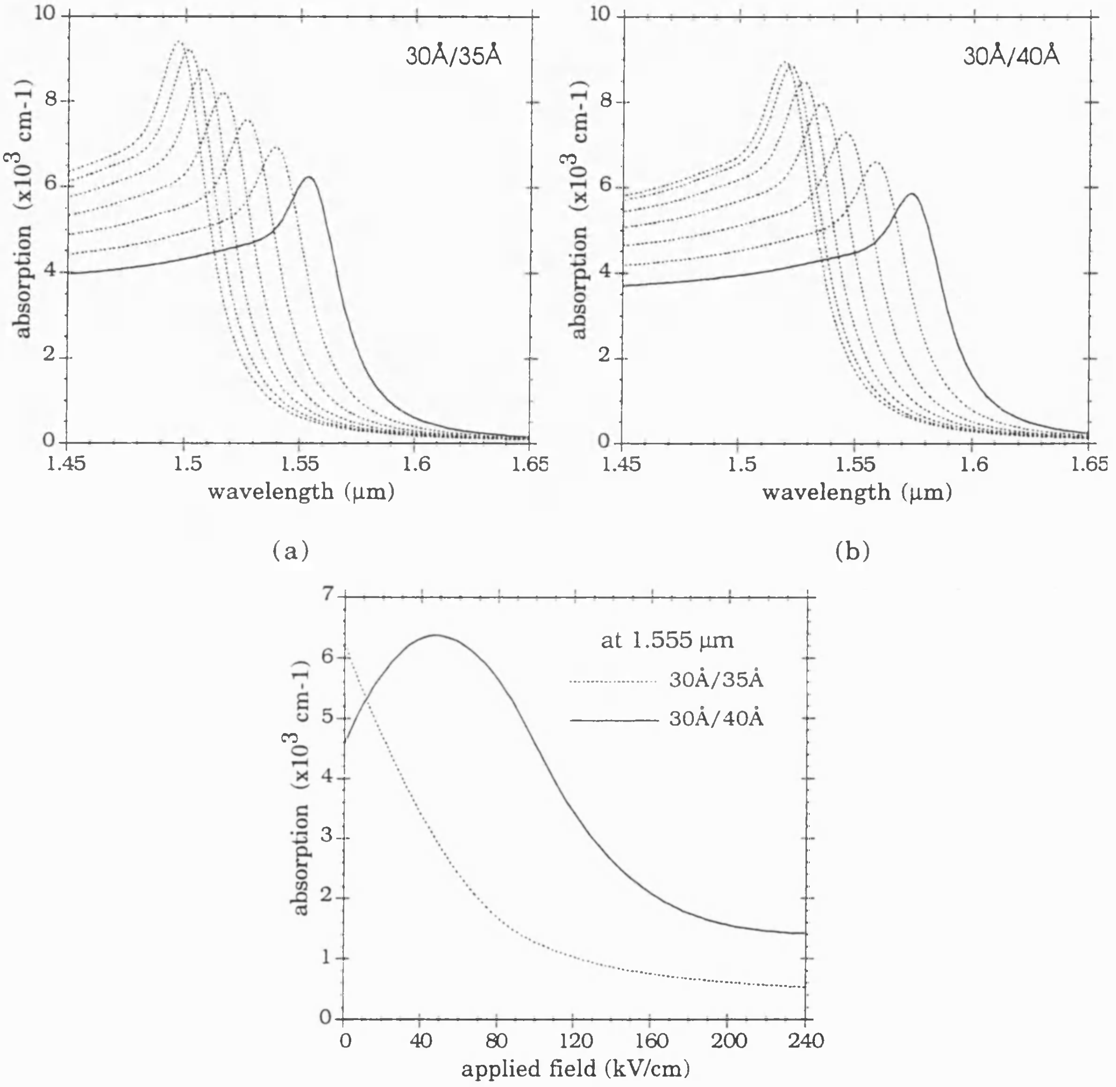

(a) (b)

(c)

Figure 6-10. *Calculated absorption spectra for an applied field (0-240 kV/cm in steps of 40 kV/cm) for two three layer structures. The zero applied field spectra is shown as a solid line, the absorption refers to the composite well region. (a) a 30Å/35Å structure. (b) a 30Å/40Å structure. (c) the absorption with applied field at 1.555 μm which corresponds to the zero applied n=1hh transition of (a). Line widths used are 8 meV (HWHM) for the exciton resonance, and 8 meV for the continuum.*

Although encouraging, the above spectra can only be indicative of the performance, mainly due to the uncertainty in broadening mechanisms contributing to the exciton resonance, eg. alloy broadening and interface roughness. I have attempted to use realistic line widths for structures which are slightly larger than those typically found in

InGaAs/InP MQW structures (see eg. Sugawara *et al* 1990). Although given the different nature of the structures, linewidths from square QW's with a single well layer, may not be representative of a composite one. Another factor that has been previously mentioned in §4.4.3 is the choice of line shape functions for the exciton resonance. The use of Lorentzian functions are well known to exaggerate the absorption in the tail of the resonance (eg. P. Zouganelli 1993). This is particularly relevant for blue shift structures, since the resonance tails effectively set the minimum absorption, and hence contrast ratio. Switching to Gaussian lineshapes which some authors use (eg. Shim and Lee 1993), the problem reverses with the minimum absorption tending to be underestimated (actually becoming zero at 1.555 μm for large applied fields). In addition to this, the peak absorption of the resonance for a given linewidth increases by ~50% (cf. §4.4.3). In this respect the predicted electroabsorption performance of the structures would be substantially improved, simply by changing to a different lineshape function! Similar problems have arisen in device modelling containing square QW's, thereby producing unreliable evaluations of device performance (eg. P. Zouganelli 1993, chp. 3). To circumvent these problems, the tails of a Lorentzian line shape were modified to fit experimental results, and subsequently gave a better indication of device performance. In view of the above comments, it is felt further calculations of the absorption spectra should await experimental results.

§6.4 Concluding Remarks.

In summary, a novel composite structure has been proposed which can provide a blue shift and increase of the n=1hh transition on application of an electric field. A two-layer well region, consisting of materials that exhibit contrasting band offsets (w.r.t InP barrier layer), provides a non-zero spatial separation of the ground states at zero applied field. The direction of the applied field is chosen to reduce this separation, leading to a blue shift of the n=1hh transition and an increase in excitonic absorption. While the underlying principle is common to many previous structures (cf. inducing an *internal* field, §6.1.2), the use of band offset parameters in a composite well to induce the spatial separation had not previously been considered.

With two different constituent materials comprising the well region, the nature of the structure admits a range of independent parameters which were shown to govern the performance. Although the conditions on the band offset parameters are important, it was demonstrated that a range of values could provide blue shifting operation, (Figs.6-5a,c and d). In fact, a structure of this type would be useful for determining the offset parameters given the strong dependence of the ground state transition for fixed dimensions. The compositions of the well layers represented another governing factor, (Figs.6-5b,d and e). Varying the InAsP composition affected the position of the electron state which largely determined the spatial separation of the ground states; the heavy hole state were found to be insensitive to the changes because of the strong localization in the InGaAs layer. Comments on changing composition of the InGaAs layer are made in Chapter 7, giving rise to further design issues.

The final set of parameters studied were the dimensions of the composite well. Although largely exploratory in approach, these latter studies centred on satisfying a typical electroabsorption device specification, suitable for SEED type operation. Such criteria for *blue* shift devices had been previously noted (eg. D.A.B Miller 1989); namely, the need for reasonable zero applied field n=1hh absorption which decreased with applied field *via* the blue shift; with the zero applied field absorption essentially setting the contrast ratio of the device. However, these two conditions are conflicting given that the blue shift arises from the spatial separation of the ground states, which in turn reduces the absorption *vis-á-vis* the overlap integral. [note: This conflicting nature is inherent in all blue shifting structures, and therefore represents a need to tailor the properties carefully (cf. work on (111) structures from Goossen *et al* (1989) and Pabla *et al* (1993)]. In the composite structures, the InAsP width was shown to mainly govern the overlap integral of the ground state transition; a smaller width providing a larger overlap and consequently, a larger excitonic area (Fig.6-6b). The relative unimportance of the InGaAs layer in relation to the zero applied field absorption was further demonstrated by fixing the InAsP layer and performing calculations for an applied electric field on structures with increasing InGaAs width, (Fig.6-9b). However, the maximum attainable n=1hh blue shift *did* exhibit a strong dependence on the width of the InGaAs layer; a smaller width providing a larger maximum blue shift (~30 meV) for applied fields up to 240 kV/cm. By examining the form of the n=1hh blue shift and excitonic area with field, the results suggested the implied *internal* field for these structures can exceed 240 kV/cm. Following the investigations, the absorption spectra from two structures operating around 1.55 μm was computed, (Fig.6-10a,b). Choosing an operating wavelength, at 1.555 μm, both structures demonstrated decreasing absorption with increasing applied field, thereby satisfying the conditions for SEED based devices.

In Chapter 7, some practical issues relating to the growth of these structures are discussed. In addition to this, a further development of these type of structures is noted which can bring further functionality to the present design.

References

Bar-Joseph I, Sucha G, Miller D.A.B, Chemla D.S, Miller B.I, and Koren U, *"Self-Electro-Optic Effect Device and Modulation Converter with InGaAs/InP Multiple Quantum Wells"*, Appl. Phys. Lett., **52**, (1988), pp 51-53.

Bastard G, and Brum J.A, *"Electronic States in Semiconductor Heterostructures"*, IEEE J. Quantum Electron., **QE-22**, (1986) pp 1625-1644.

Bleuse J, Bastard G, and Voisin P, *"Electric-Field-Induced Localization and Oscillatory Electro-Optical Properties of Semiconductor Superlattices"*, Phys. Rev. Lett. **60**, (1988a), pp 220-223.

Bleuse J, Voisin P, Allovon M, and Quillec M, *"Blue Shift of the Absorption Edge in AlGaInAs-GaInAs Superlattices: Proposal for an Original Electro-Optical Modulator"*, Appl. Phys. Lett. **53**, (1988b), pp 2632-2634.

Goossen K.W, Caridi E.A, Chang T.Y, Stark J.B, and Miller D.A.B, *"Observation of Room Temperature Blue Shift and Bistability in a Strained InGaAs-GaAs <111> Self-Electro-Optic Effect Device"*, Appl. Phys. Lett. **56**, (1990), pp 715-717.

Grindle R, *"Self-Electro-Optic Effect Devices and their use in Optical Switching and Communication Systems"*, chp.5, PhD Thesis, University of London, (1993).

Hiroshima T, and Nishi K, *"Quantum-Confined Stark-Effect in Graded-Gap Quantum Wells"*, J. Appl. Phys. **62**, (1987), pp 3360-3365.

Hou H.Q, and Tu C.W, *"Optical Properties of InAsP/InP Strained Quantum Wells Grown on InP (111)B and (100) Substrates"*, J. Appl. Phys. **75**, (1994), pp 4673-4679.

Kopft R.F, Herman M.H, Lamont Schnoes M, Perley A.P, Livescu G, and Ohring M, *"Band Offset Determination in Analog Graded Parabolic and Triangular Quantum Wells of GaAs/AlGaAs and GaInAs/AlInAs"*, J. Appl. Phys. **71**, (1992), pp 5004-5011.

Kurgin J, *"Novel Configuration of Self-Electro-Optic-Effect-Device Based on Asymmetric Quantum Wells"*, Appl. Phys. Lett. **53**, (1988), pp 779-781.

Leavitt R.P, and Little J.W, Comment on *"Optical Bistability in Self-Electro-Optic Effect Devices with Asymmetric Quantum Wells"* and *"Novel Configuration of Self-Electro-Optic-Effect-Device Based on Asymmetric Quantum Wells"*, Appl. Phys. Lett. **57**, (1990), pp 1363-1365.

Lentine A.L, and Miller D.A.B, *"Evolution of the SEED Technology-Bistable Logic Gates To Optoelectronic Smart Pixels"*, IEEE J. Quantum Electron. vol. JQE-**29**,

(1993), pp 655-669.

Miller D.A.B, Weiner J.S, and Chemla D.S, *"Electric-Field Dependence of Linear Optical Properties in Quantum Well Structures: Waveguide Electroabsorption and Sum Rules"*, IEEE J. Quantum Electron. vol. QE-**22**, (1986), pp 1816-1830.

Miller D.A.B, *"Optical Bistability in Self-Electro-Optic Effect Devices with Asymmetric Quantum Wells"* , Appl. Phys. Lett. **54**, (1989), pp 202-204.

Miller D.A.B, *"Quantum-Well Self-Electro-Optic Effect Devices"*, Opt. & Quant. Electron. **22**, (1990), pp S61-S98.

Onose H, Yoshima H, and Sakaki H, *"Field-Induced Decoupling of Quantized Levels and Blue Shift of Absorption Edge in a Potential Inserted Quantum Well Structure"*, Appl. Phys. Lett., **54**, (1989), pp 2221-2223.

Pabla A.S, Sanchez-Rojas J.L, Woodhead J, Grey R, David J.P.R, Rees G.J, Hill G, Pate M.A, Robson P.N, Hogg R.A, Fisher T.A, Willcox A.R.K, Whittaker D.M, Skolnick M.S, and Mowbray D.J, *"Tailoring of Internal Fields in InGaAs/GaAs Multiwell Structures Grown on (111)B GaAs"*, Appl. Phys. Lett., **63**, (1993), pp 752-754.

Pabla A.S, Woodhead J, Grey R, Rees G.J, David J.P.R, Pate M.A, and Robson P.N, *"All-Optical Bistable Switching in a Strained Piezoelectric Self-Electro-Optic Effect Device"*, Electron. Lett., **30**, (1994), pp 1521-1522.

Schneider Jr R.P, and Wessels B.W, *"Photoluminescence Excitation Spectroscopy of* $InAs_{0.67}P_{0.33}/InP$ *Strained Single Quantum Wells"*, J. Elec. Mat. **20**, (1991), pp 1117-1123.

Shim S, and Lee E-H, *"Optimization of InGaAsP/InP Quantum Well Heterostructures for Enhanced Excitonic Electroabsorption Effects at 1.55 μm"*, Appl. Phys. Lett., **63**, (1993), pp 2387-2389.

Skolnick M.S, Taylor L.L, Bass S.J, Pitt D, Mowbary D.J, Cullis A.G, and Chew N.G, *"InGaAs-InP Multiple Quantum Wells Grown by Atmospheric-Pressure Metalorganic Chemical Vapor-Deposition"*, Appl. Phys. Lett. **51**, (1987), pp 24-26.

Sugawara M, Fujii T, Yamazaki S, and Nakajima K, *"Theoretical and Experimental Study of the Optical-Absorption Spectrum of Exciton Resonance in* $In_{0.53}Ga_{0.47}As/InP$ *Quantum Wells"*, Phys. Rev. **B 42**, (1990), pp 9587-9597.

Susa N, and Nakawara T, *"Large Blue Shifts Induced by Stark-Effect in Asymetric Coupled Quantum Well"*, Electron. Lett., **28**, (1992), pp 941-943.

Wegener M, Zucker J.E, Chang T.Y, Sauer N.J, Jones K.L, and Chemla D.S, *"Absorption and Refraction Spectroscopy of a Tunable-Electron-Density Quantum Well and Reservoir Structure"*, Phys. Rev. **B 41**, (1990), pp 3097-3104.

Yamamoto M, Yamamoto N, and Nakano J, *"MOVPE Growth of Strained InAsP/InGaAsP Quantum-Well Structures for Low-Threshold 1.3-μm Lasers"*, IEEE J. Quantum Electron. vol. JQE-**30**, (1994) pp 554-561.

Zouganeli P, *"Design and Assessment of Fabry-Perot Quantum Well Electro-absorption Optical Modulators"*, chp.3, PhD Thesis, University of London, (1992).

Zucker J.E, Chang T.Y, Wegener M, Sauer N.J, Jones K.L, and Chemla D.S, *"Large Refractive Index Changes in Tunable-Electron-Density InGaAs/InAlAs Quantum Wells"*, IEEE Photonics Technol. Lett., **2**, (1990a), pp 29-31.

Zucker J.E, Wegener M, Jones K.L, Chang T.Y, Sauer N, and Chemla D.S, *"Optical Waveguide Intensity Modulators Based on a Tunable Electron Density Multiple Quantum Well Structure"*, Appl. Phys. Lett., **56**, (1990b), pp 1951-1953.

Chapter 7. **Future Directions.**

§7.1 $InAs_xP_{1-x}$/InP Multiple Quantum Wells.

It is quite clear, even from the existing work in the literature, that the $InAs_xP_{1-x}$ material shows considerable promise for use in InP based heterostructures. With the work in Chapter 5, heterostructures comprising InAsP/InP quantum wells have now been grown, and devices demonstrated, by all the major growth techniques. Above all the present work has highlighted the flexibility of InAsP/InP design, particularly for the wavelength range specified by the commercially available high power and compact neodymium based solid state lasers. The study into this heterostructure combination, ie. where the InAsP layer is nominally strained w.r.t the InP substrate, deliberately concentrated on multiple quantum well (MQW) samples. Relaxation due to the cumulative strain in the structures was investigated and highlighted several interesting features that have a direct bearing on the optical quality devices. It is felt further work with this material combination should look at the question of relaxation in more detail. From this point of view, several sets of wafers could be studied, for example:

(i) For a given composition and period, investigate the effect of increasing the number periods. Using, say 10, 30, and 50 periods, it may be possible to observe the onset of relaxation as the number of periods is increased. The set would also be able to identify any 'clamping' of relaxation between two samples that have already relaxed, ie. verify the implications from M737(i) and M395 results.

(ii) For a given composition, well width and number of periods, investigate the effect of increasing the barrier width in successive samples. In effect this reduces the average arsenic composition over one period. Again, if the initial results on relaxation presented here are representative, then a decrease of relaxation would be expected as the barrier width increased.

From each case, a better understanding of relaxation in MQW structures will follow which is directly relevant to the design of these types of strained MQW structures. For example, one issue raised by work on InGaAs/GaAs (on GaAs) MQW devices (Ghisoni *et al* 1994), is the improved resolution of the exciton peak as relaxation reduces, ie. a reduction in linewidth. A question arises as to whether the improved sharpness of the exciton (and hence absorption in the well, cf. Fig.5-16) translates to an *overall* improvement in absorption of the structure. Clearly a trade off exists between increasing the barrier width to reduce relaxation and simultaneously increasing the amount of optically inert material in the intrinsic region. Studying case (ii), above should go some way to determine the optimum barrier thickness.

It is also clear from the present work, that the process in which the samples are characterized should be changed. In future, some form a wafer mapping would be beneficial. Growth on double polished substrates would allow transmission measurements to be taken in which the n=1hh transition can be easily observed. Since the thickness variation appears to be small, (cf. Table 5-10), any shift of the n=1hh transition is likely to arise from a variation in arsenic and/or strain relaxation. Through mapping, areas can be selected for fabrication into mesas for photocurrent measurements. In addition, this would indicate the uniformity of the wafers in relation to the n=1hh transition energy. Large areas exhibiting uniform n=1hh transitions are desirable if arrays of electro-optical devices, eg. SEED's, are to be envisaged. Of course HRXRD would be an ideal mapping technique, although in practice, the duration of the scans may limit this to selected parts of the wafer or wafers.

Keeping with the $InAs_xP_{1-x}$ well material, another option is to investigate using $In_xGa_{1-x}P$ as the barrier material (Woodward *et al* 1992). Recall, that for the present work, the implication of increasing relaxation with increasing average arsenic is more correctly stated, as increasing relaxation with increasing misfit strain between a_{sub} and $a_{\|}^{MQW,fs}$. Without growing on a pseudo-substrate (ie. buffer layer), another other way of reducing the misfit is to use a barrier material under *tensile* strain with respect to InP. It follows from (2.4), that for a given $InAs_xP_{1-x}$ well width, a suitable $In_xGa_{1-x}P$ barrier width can result in $a_{\|}^{MQW,fs} = a_{sub}$, or at least a reduced misfit, thereby reducing MQW relaxation. However, an overriding consideration would be the ease of growth in the present MBE system, given the limited number of sources. It is worth emphasizing, an attractive feature of InAsP/InP QW's is that only two III-V materials are used throughout, with the wells being effectively defined by modulating the arsenic shutter.

To conclude, immediate recommendations focus on relaxation in strained MQW structures. Any advantages of using strain balanced structures will become more obvious following a coordinated study of the effects of relaxation on device performance. Depending on the application, it may be the case that accommodating a certain amount relaxation is not necessarily detrimental to device performance. In this sense, the emphasis would shift to *reducing* relaxation rather than attempting to avoid it.

§7.2 Composite Structures.

The work in Chapter 6 introduced the idea of using composite structures to provide a blue shift of the n=1hh transition for an applied electric field. Clearly a future direction for this work would be to experimentally verify the predictions. A set of structures, based on compositions described in §6.2 with varying InAsP width, are currently waiting to be grown. Although with the limited cells available on the MBE kit at Sheffield the structures are somewhat difficult to grow (M. Hopkinson, private communication). The $InAs_xP_{1-x}$ (x=0.4) layer requires a controlled low arsenic flux, with the As fraction approximately given by (As/In $\approx$0.4). The growth of the next layer, $In_zGa_{1-z}As$ requires almost four times the arsenic level, with (As/(In+Ga) $\approx$ 1.5; where In$\approx$Ga for InGaAs). Difficulties arise due to the instability of the arsenic flux from layer to layer, as the arsenic fraction is switched from a low value (InAsP) to a high value (InGaAs). Currently, the MBE kit at Sheffield is being overhauled, including installation of a new valved cracker arsenic cell to provide better control of the arsenic flux.

As for as the structures themselves, further work should concentrate on optimizing for different applications by adjusting parameters such as well width and composition. Throughout the study, there was little mention of the strain in the structures. For all the examples, strain was assumed to be accommodated solely in layer B (InAsP), with the effect on the bulk band structure included. In essence, the development of the asymmetric potential profile rested on the ability to *accommodate* strain, rather than using it as a means to tailor band structure properties, (cf. §2.2.2). It is acknowledged the distinction is a subtle one, since with strain the band structure does change. However the essential point is that by accommodating strain, this allowed different materials to be used (with different offset parameters) which gave rise to the necessary asymmetric potential. In addition, it could also be argued that the relevant valence band states in the structure are localised in the unstrained lattice matched InGaAs layer. Further work might look at using strain effects on the band structure to both to increase the flexibility of the design and/or improve the stability of the structure from the viewpoint of cumulative effects of strain.

To demonstrate these latter points, consider the effect of changing the composition in the InGaAs layer from the lattice matched values, (x=0.53), to values which result in a tensile strain (w.r.t InP substrate), ie. x<0.53. The valence band potential of the structure would resemble that illustrated in figure 7-1.

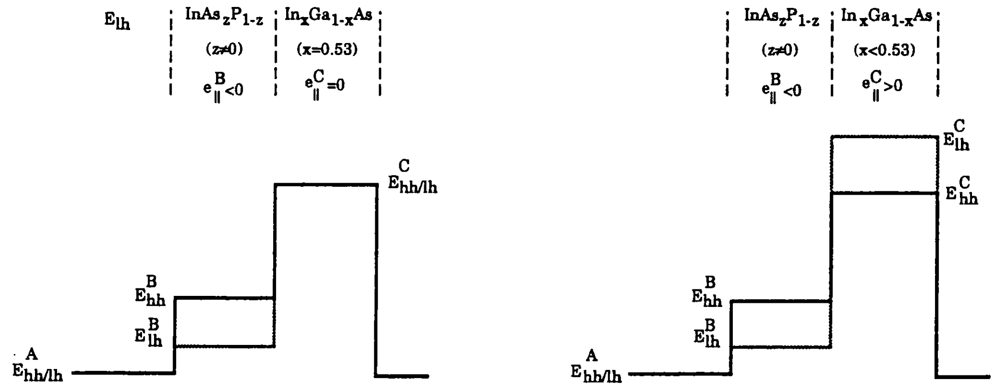

Figure 7-1. *Schematic illustrating the valence band profile in a composite structure. Unstrained InGaAs layer (left), InGaAs layer under tensile strain (right).*

With compressive strain in the InAsP layer and tensile strain in the InGaAs layer, in principle the *net* strain in the composite well region could be made zero. However, rather than simply balancing the in-plane strain tensors in each material, the dimensions of the materials would need to be considered, since it is the strain energy that should be balanced. The approach I have taken for the following results, is to use the Matthews and Blakeslee expression ie. (2.4), which predicts the in-plane lattice constant that results from two lattice mismatched bulk layers, ie.

$$a_{\|} = \frac{a_o^B G_B l_B + a_o^C G_C l_C}{G_B l_B + G_C l_C}$$

or rewritten as,

$$r = \frac{l_B}{l_C} = \frac{G_C\left(a_o^C - a_{\|}\right)}{G_B\left(a_{\|} - a_o^B\right)} \tag{7.1}$$

The subscripts, B and C, represent layers B (InAsP) and C (InGaAs) in the composite structure. The term 'r' is introduced to denote the ratio of the layer widths forming the well region, as before the G's are the shear moduli and a_o^i's are the bulk lattice constants of each layer, (cf. (2.4)). Since growth is on InP, the in-plane lattice constant, $a_{\|}$, that is usually calculated is this time set equal to the InP lattice constant.

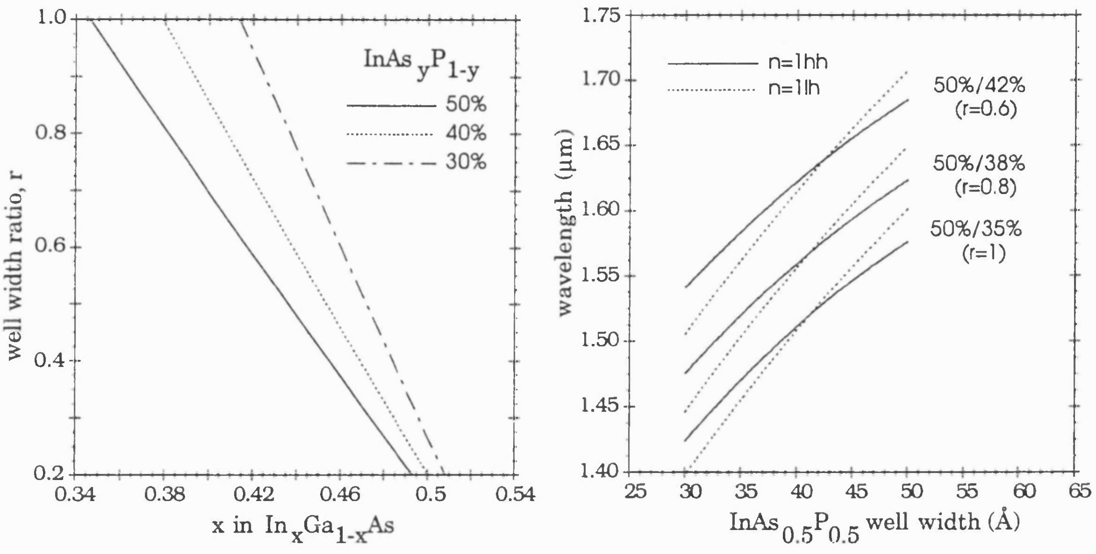

(a) (b)

Figure 7-2. *(a) Evaluation of equation (7.1) for three arsenic compositions. (b) Calculated n=1hh (solid) and n=1lh (dotted) transitions for three composite width ratios. Band offsets parameters used are 75:25 and 40:60, see text for further details.*

By choosing the compositions in each layer, equation (7.1) provides the correct layer width ratio to ensure the combined misfit of layers B and C with the substrate (and layer A) is zero; referred to hereafter as the *balanced* ratio. In figure 7-2a, (7.1) is evaluated for three arsenic compositions in layer B. Any point along the line can be projected to each axis to establish the indium fraction in layer C and the ratio of the layer dimensions required. The results in Fig.7-2a, show that for a given ratio in the composite well, increasing the arsenic composition in the B layer (ie. increasing the compressive strain) would require a decreasing indium composition in layer C (ie. increasing tensile strain). It is useful to express these conditions in terms of the layer widths since it was shown that they determine the blue shifting properties of the structures, (cf. §6.3.2). [For example, the structures in Fig.6-9 would correspond to $r \approx 0.86$ (30Å/35Å), $r=0.75$ (30Å/40Å), $r=0.6$ (30Å/50Å) and $r \approx 0.43$ (30Å/70Å)]

A further consequence of employing a tensile strain InGaAs layer, is the resulting closer proximity of the n=1lh transition in relation to the n=1hh transition, (Fig.7-2b). Choosing an arsenic composition for layer B, ie. InAs$_{0.5}$P$_{0.5}$, three indium compositions for layer C are found corresponding to a *balanced* layer ratio, ie. 42%In ($r \approx 0.6$), 38%In ($r \approx 0.8$) and 35%In ($r \approx 1$). For reducing indium in layer C (increasing tensile strain), the separation between the heavy and light hole band edges increases, with the light hole band edge higher in energy, (cf. §2.2.2 and Fig.7-1). As noted in §2.2.2, the splitting between the hh1 and lh1 states, confined in layer C, will reduce, and can result in lh1 becoming the highest valence band state. A feature which is demonstrated by calculating both the n=1hh and n=1lh transitions for a range of structures, (Fig. 7-2b). [note: The structures are formed from a given InAsP width which then specifies the InGaAs width prescribed by the *balanced* ratio. The compositions used are those discussed earlier.] In Fig.7-2b, a potentially useful situation arises for layer widths of 40Å (B) and 50Å (C), ie. (r=0.8), where both zero applied field transitions occur around 1.55 μm. As discussed in §2.3 structures exhibiting this feature can overcome several difficulties relating to the polarization sensitivity of a device (in waveguide configuration). Benefits may also be present for transverse devices, where enhanced absorption can be found.

Although experimental verification must take precedent in the development of the composite structures. This rather limited study has clearly hinted at the *further* design issues that are available. I believe several of these are worth pursuing; eg. a strain-balanced blue-shifting polarization-insensitive structure. In this sense, some comments should be made about improving the level of modelling, eg. to include in-plane mixing. This is particularly important if further study into the merging of the n=1hh and n=1lh transitions is undertaken. For example, it is well known that when the light-and heavy-hole states are close together, in-plane mixing can cause the light -hole dispersion to exhibit an electron-like curvature resulting in a negative value for the in-plane effective mass (eg. E.P O'Reilly 1989). With the subsequent increase in the heavy hole mass, the diagonal approximation is clearly becoming too severe an approximation.

References

Ghisoni M, Parry G, Hart L, Roberts C, Marinopoulou A, and Stavrinou P.N, *"Effect of Well/Barrier Ratio on the Performance of Strained InGaAs/GaAs Quantum Well Modulators"*, Electron. Lett., **30**, (1994b), pp 2067-2068.

O'Reilly E.P, *"Valence Band Engineering in Strained-Layer Structures"*, Semicon. Sci. Technol., **4**, (1989), pp 121-137.

Woodward T.K, Chiu T-H. and Sizer II T, *"Multiple Quantum Well Light Modulators for the 1.06 μm Range on InP Substrates:* $In_yGa_{1-y}As_xP_{1-x}/InP$*,* $InAs_xP_{1-x}/InP$ *and Coherently Strained* $InAs_xP_{1-x}/In_yGa_{1-y}P$*"*, Appl. Phys. Lett. **60**, (1992), pp 2846-2848.

Appendix A. Material Parameters.

Unless otherwise stated all parameters obtained from the Landolt-Börnstein compilations.

	$InAs_xP_{1-x}$	$In_xGa_{1-x}As$
Lattice constant (Å)	$5.8696 + (0.18943\,x)$[a]	$5.6533 + (0.40573\,x)$[a]
Elastic moduli (10^{11} dyn/cm^2)		
C_{11}	$10.11 - (1.78\,x)$	$11.88 - (3.55\,x)$
C_{21}	$5.61 - (1.08\,x)$	$5.38 - (0.85\,x)$
Deformation potentials (eV)		
a_{gap}	$-8.6 + (1.9918\,x)$[b]	$-8.3768 + (1.7686\,x)$
b	$-2.0 + (0.2\,x)$	$-1.7 - (0.1\,x)$
Conducion band effective mass (m_0)	$0.084 - (0.0621\,x)$	$0.0665 - (0.0446\,x)$
Luttinger parameters		
$\gamma_{1,L}$	$4.95 + (14.72\,x)$	$6.85 + (12.82\,x)$
$\gamma_{2,L}$	$1.65 + (6.72\,x)$	$2.1 + (6.27\,x)$
Spin-orbit splitting, Δ (eV)	$0.11 + (0.12\,x) + (0.15\,x^2)$[c]	$0.341 - (0.09\,x) + (0.14\,x^2)$
Bulk band gap (300K), E_g (eV)	$1.351 - (1.315\,x) + (0.32\,x^2)$[c]	$1.424 - (1.5\,x) + (0.4\,x^2)$
Kane matrix element, E_P, (eV)	$19.7 + (2.5\,x)$[d]	$28.8 - (6.6\,x)$[d]
refractive index, n	$[3.279 - 0.442\,\hbar\omega + 0.382(\hbar\omega)^2$ $+ (0.1244 + 0.4184\hbar\omega + 0.2165(\hbar\omega)^2\,x)]$[e]	$[3.33 - 0.133\,\hbar\omega + 0.229(\hbar\omega)^2$ $+ (0.1244 + 0.4184\hbar\omega + 0.2165(\hbar\omega)^2\,x)]$[f]
dielectric constant, ε, (ε_0)	$12.56 + (2.59\,x)$	$12.53 + (2.62\,x)$

notes on material parameters.

[a]: Lattice constants provided by Dr. Linda Hart from *High Resolution Simulation*, 1st ed, Phillips Electronics NV, Sept. 1993. The values determined at standard temperatures and pressure.

[b]: The values used here are derived from measured pressure dependence of the bulk band gap, $^{dE_g}\!/_{dP}$ (10^{-6} eV/bar). Explicitly,

$$a_{gap} = -\frac{1}{3}(C_{11} + 2C_{12})\, ^{dE_g}\!/_{dP} \tag{A.1}$$

(note: 10^{11} dyn/cm^2 x 10^{-6} eV/bar = 0.1 eV)

[c]: Nicholas *et al* (1979)

[d]: Corzine *et al* (1993)

[e]: Fitted polynomial of each binary covering the energy range, $1.4 \geq \hbar\omega \geq 0.9$ (eV), then linear interpolation. Binary values obtained from E.D Palik (1991).

[f]: Fitted polynomial of each binary covering the energy range, $1.4 \geq \hbar\omega \geq 0.35$ (eV). Binary values obtained from E.D Palik (1991).

References.

Corzine S.W, Yan R.H, and Coldren L.A, in *Quantum Well Lasers*, Chapter 1, ed. P.S Zory, Academic Press, New York, (1993), pp 17-96.

Landolt-Börnstein, edited by Madelung, New Series, Group 3, Vol. 17a, (Springer, Berlin 1982), pp 281-289; Vol. 22a, (Springer, Berlin 1989) pp 107-116.

Nicholas R.J, Stradling R.A, and Ramage J.C, "*Evidence for a Reduction in the Momentum Matrix Element* P^2 *Due to Alloy Disorder in* $InAs_{1-x}P_x$", J. Phys. C, **12**, (1979), pp 1641-1651.

Palik E.D (editor), *Handbook of Optical Constants of Solids II*, (1991).

Acknowledgements.

First of all I would like to thank my supervisor, Dr. Stephanie Haywood, for her constant support, guidance and enthusiasm at all times. I would also like to thank Professor Gareth Parry (now at Oxford), not only for his comments and encouragement but for also nurturing an excellent working environment.

Several people from outside U.C.L have made valuable contributions to all aspects of the work. I would like to thank Dr. David Guy from D.R.A (Malvern) for his interest and many valuable suggestions in all stages of the work. Thanks are also due to Dr. Richard Warburton (formerly at Oxford) for his helpful comments on the modelling (and introducing me to the **k.p** method). For the growth, processing and characterisation of the samples, the expert assistance and contribution from Dr's Mark Hopkinson, John David, Geoff Hill and Malcom Pate from Sheffield University is gratefully acknowledged. I would also like to mention several people from the Semiconductor Interdisciplinary Research Center, based at Imperial College, for their valuable support and useful discussions; Dr's Linda Hart, Xiao Mei Zhang and Ray Murray.

Closer to home, a rather large round of applause must go to all (past and present) members of the Digital Optics Group for various contributions over the last four years. *The sphere lives* co-starred Marco Ghisoni, Robert Grindle, Paul Barnes, David Atkinson, Mark Whitehead, Evi Zouganelli, Abid Khan, Farah Mansoor, Peter Poon, Chee Fai Tang and Petra Guy.

Finally, I would like to thank both the U.K Science and Engineering Council and the Electronics Sector of the Defence Research Agency at Malvern for financial support during the period of my thesis.

Publications.

as first author,

Stavrinou P.N, Haywood S.K, Zhang X.M, Hopkinson M, Claxton P.A, David J.P.R, and Hill G, *"Photoconductivity of a Strained InAs / InP Superlattice in the 1.0-1.5 μm region"*, Proc. 4th IEEE International Conference on InP Related Materials, Newport, Rhode Island, U.S.A, March (1992), pp 569-572.

Stavrinou P.N, Haywood S.K, Hart L, Zhang X.M, Hopkinson M, David J.P.R, and Hill G, *"Varying Strain in* $InAs_{1-x}P_x$ */ InP Multiple Quantum Well Device Structures"*, Proc. 5th IEEE International Conference on InP Related Materials, Paris, France, April (1993), pp 652-655.

Stavrinou P.N, Haywood S.K, and Parry G, *"Use of a Three-Layer Quantum-Well Structure to Achieve an Absorption Edge Blueshift"*, Appl. Phys. Lett., **64**, (1994), pp 1251-1253.
[registered as invention record No. 4400 by Defence Research Agency, Malvern]

as contributing author,

David J.P.R, Hopkinson M, Hill G, Stavrinou P.N, Haywood S.K, *"Growth and Characterisation of InAsP / InP SQW and MQW PIN Diode Structures"*, Proc. 5th IEEE International Conference on InP Related Materials, Paris, France, April (1993), pp 167-170.

Ghisoni M, Parry G, Hart L, Roberts C, Stavrinou P.N, *"Room Temperature Characterisation of InGaAs / AlAs Multiple Quantum Well P-I-N Diodes"*, Appl. Phys. Lett. **65**, (1994a), pp 3323-3325.

Hart L, Ghisoni M, Stavrinou P.N, Roberts C, Parry G, *"X-Ray Characterisation of InGaAs / AlAs Multiple Quantum Well P-I-N Structures"*, presented at 1st International Conference on Materials for Microelectronics, Barcelona, Spain, October (1994); accepted for publication in Materials Science and Technology, (1994).

Ghisoni M, Parry G, Hart L, Roberts C, Marinopoulou A, and Stavrinou P.N, *"Effect of Well / Barrier Ratio on the Performance of Strained InGaAs / GaAs Quantum Well Modulators"*, Electron. Lett., **30**, (1994b), pp 2067-2068.

Wang H, LiKamWa P, Ghisoni M, Parry G, Stavrinou P.N, Roberts C, Miller A, *"Ultrafast Recovery in a Strained InGaAs / AlAs MQW PIN Modulator"*, accepted for publication in Photon. Technol. Lett., February issue 1995.